Parasite proliferation and host cell phenotype drive *Leishmania* exit from infected macrophages

Dissertation

zur Erlangung des Grades

Doktor der Naturwissenschaften

am Fachbereich Biologie

der Johannes Gutenberg-Universität Mainz

Moritz Jaedtka

geb. am 28.11.1992 in Frankfurt am Main

Mainz, 2024

Diese Doktorarbeit wurde vom 01.12.2020-31.05.2024 in der Abteilung Immunologie am Paul-Ehrlich-Institut, Bundesinstitut für Impfstoffe und biomedizinische Arzneimittel erstellt. Die experimentelle Arbeit wurde betreut durch

1. Betreuer:

2. Betreuer:

3. Betreuer:

Dekan: Prof. Dr. Eckhard Thines

Institut für Molekular Physiologie

Johannes Gutenberg-Universität Mainz

1. Berichterstatter:

2. Berichterstatter:

Tag der mündlichen Prüfung: 05.11.2024

Table of Contents

List of Figures

List of Tables

Abbreviations

%	percent
°C	degree Celsius
µg	microgram
µl	microliter
µm	micrometre
µM	micromolar
µs	microsecond
1-MT	1-methyltryptophan
AAM	Alexander’s Amastigote medium
Ab	antibody
AF	AlexaFluor
Akt	protein kinase B
ASC	apoptosis-associated speck-like protein containing a caspase recruitment domain
ATP	adenosine triphosphate
B-ALL	B cell acute lymphoblastic leukemia
Bax	Bcl-2-associated X
Bcl-2	B-cell lymphoma 2
BM	BLaER1 medium
BMDM	bone marrow-derived macrophage
Cas9	CRISPR-associated protein 9
caspase	cysteine aspartyl proteases
CD	cluster of differentiation
CDS	coding sequence
CF	carboxy fluorescein
CL	cutaneous leishmaniasis
Cl^-	chlorine
CLSM	confocal laser-scanning microscope

cm	centimetre
CM	complete medium
cm2	cubic centimetre
CRISPR	clustered regularly interspaced short palindromic repeats
CXCL	chemokine (C-X-C motif) ligand
DAMP	damage-associated molecular pattern
DC	dendritic cell
DMSO	Dimethyl sulfoxide
DNA	deoxyribonucleic acid
EDTA	ethylenediaminetetraacetic acid
eGFP	enhanced green fluorescence protein
ER	oestrogen receptor
ERK	extracellular-signal regulated kinase
FA	formaldehyde
FADD	FAS-associated death domain
FCS	fetal calf serum
FRAC	fluorescence recovery after conversion
FSC	forward scatter
fwd	forward
g	gram
g	fold gravitational acceleration
GM-CSF	granulocyte macrophage colony stimulating factor
GOI	gene of interest
GSDMD	gasdermin D
h	hour
HBSS	Hank’s balanced salt solution
hMDM	human monocyte-derived macrophage
IDO1	indoleamine 2,3 dioxygenase
IF	immunofluorescence

IFN	interferon
IL	interleukin
iNOS	inducible nitric oxide synthase
K^+	potassium
KBMA	killed but metabolically active
KO	knockout
KYNU	kynureninase
L.	*Leishmania*
LDH	lactate dehydrogenase
Lm	*Leishmania major*
LM	Leishmania medium
LPG	lipophosphoglycan
LPS	lipopolysaccharide
M(-)	non-activated hMDM
M(IFNγ)	hMDM activated by IFNγ
M(IL-10)	hMDM activated by IL-10
M(IL-4)	hMDM activated by IL-4
M(M-CSF)	hMDM activated by M-CSF
MACS	magnetic activated cell sorting
MCL	mucocutaneous leishmaniasis
MCL-1	myeloid cell leukemia 1
M-CSF	macrophage colony stimulating factor
MFI	median fluorescence intensity
mg	milligram
min	minute
ml	millilitre
MLKL	mixed lineage kinase domain like pseudokinase
mm	millimetre
mM	millimolar

MOI	multiplicity of infection
mRNA	messenger RNA
ms	millisecond
n.s.	not significant
NAD^+	Nicotinamide adenine dinucleotide
NINJ1	Ninjurin-1
NLR	NOD-like receptor
NLRP3	NLR family pyrin domain containing 3
NO	nitric oxide
NOD	nucleotide-binding oligomerization domain
NOS2	nitric oxide synthase 2
nt	nucleotide
PAMP	pathogen-associated molecular pattern
PBMC	peripheral blood mononuclear cell
PCR	polymerase chain reaction
pI	post infection
PI	propidium iodide
PI3K	phosphoinositid-3-kinasen
PKDL	post kala-azar dermal leishmaniasis
PtdSer	phosphatidylserine
rev	reverse
RIPK	receptor-interacting serine/threonine-protein kinase
RNA	ribonucleic acid
ROS	reactive oxygen species
RPMI	Roswell Park Memorial Institute
s	second
SD	standard deviation
SE	succinimidyl ester
sgRNA	single guide RNA

SSC	sideward scatter
TAE	tris-acetate-EDTA
TAM	Tyro3, Axl, MerTK
TAM	Tyro3, Axl, MerTK
tdBM	transdifferentiation BM
TDO	tryptophan 2,3-dioxygenase
TGF	transforming growth factor
TLR	Toll-like receptor
TNF	tumor necrosis factor
U	unit
UTR	untranslated region
V	volt
v/v	volume per volume
VL	visceral leishmaniasis
w/v	weight per volume
WB	wash buffer
WHO	World Health Organisation
Z-DEVD	carbobenzoxy-Asp-Glu-Val-Asp(OMe)-fluoromethylketone (Z.DEVD-FMK)
Z-VAD	carbobenzoxy-Val-Ala-Asp(OMe)-fluoromethylketone (Z-VAD-FMK)

1 Abstract

Leishmaniasis is a tropical neglected disease caused by the protozoan parasite of the genus *Leishmania* (*L.*). Infections by the species *L. major* (*Lm*), actuator for a majority of annual reported cases, manifests in ulcerating and sore lesions of cutaneous membranes termed cutaneous leishmaniasis. Parasites are transmitted in their flagellated promastigote form to the upper dermis of the human host during the blood meal of an infected phlebotomine sandfly. After their uptake by macrophages, promastigotes reside in the acidifying phagolysosome, where they transform into their lysis-resistant and replicative amastigote form. The interplay of macrophage and parasite is shaped by the inflammatory or regulatory stimulation of the afflicted macrophage population, determining the control or progression of the infection. In order to expand the infection and counter the adaptive immune response, intracellular amastigotes need to exit their primary host and enter yet uninfected cells. Although this process is likely a critical step for *Lm* infectivity, the mechanism facilitating the transmission between host cells is vastly unknown. A recent study first reported evidence for an involvement of apoptosis in the exit process of *Lm* parasites, which was in line with preliminary data of our research group. I hypothesized that the underlying mechanisms for both, *Lm* pathogen exit and entry into new host cells is the induction of host cell death depending on the proliferation of infecting amastigotes and the host cell phenotype. By using human monocyte-derived macrophages (hMDM), I established a fluorescence-based co-incubation assay to quantify cell-to-cell transfer events via flow cytometry. With this, I could show that the transfer of *Lm* parasites is associated with the transfer of cellular material from the initially infected host cell to the recipient cell. This finding was complemented by an increased caspase-3 activity of axenic amastigote infected cells, both indicating an involvement of apoptosis in the transmission mechanism. The implementation of a proliferation reporter system expressed by *Lm* parasites revealed that the share of high proliferating parasite populations positively correlates with the increase of exit. The inflammatory stimulation of hMDM with IFNγ resulted in elevated parasite proliferation rates in comparison to regulatory stimuli IL-4 and M-CSF. Consequently, the higher parasite proliferation translated to more exit events under the IFNγ stimulation, while especially IL-4 stimulated hMDM were able to suppress the transmission of *Lm* to new host cells. The present work expands the current understanding of *Lm* parasite exit by linking the direct cell-to-cell transmission of parasites in hMDM with the induction of apoptosis that is triggered by high proliferating parasite populations. Moreover, the data shows that both, the macrophage phenotype and the parasite tailors exit, and an inflammatory stimulation of host cells can contribute to an expansion of the infection by increased transmission events. Interestingly, phenotype variations of individual donors for hMDM in response to *Lm* infection under IFNγ stimulation unraveled a previously unknown role of the kynurenine pathway in parasite exit and proliferation, uncovering a relevant mechanism for exit and infection progression in humans.

2 Zusammenfassung

Leishmaniose ist eine durch den Parasiten *Leishmania* (*L.*) hervorgerufene Erkrankung, die durch die Sandmücke *Phlebotominae* übertragen wird. Infektionen durch die Spezies *L. major* (*Lm*), die einen Großteil der jährlich registrierten Erkrankungen ausmacht, führen zu der Bildung von schmerzhaften Läsionen der Haut an der Einstichstelle. Übertragene Promastigoten werden final durch Makrophagen aufgenommen, wo sie sich innerhalb des Phagolysosoms in Amastigoten umwandeln, welche resistent gegenüber dem sauren Milieu des Kompartiments sind und sich innerhalb der Zelle vermehren können. Dabei wird die Wechselwirkung zwischen Parasiten und der Wirtszelle stark von der inflammatorischen oder regulatorischen Stimulation der betroffenen Makrophagenpopulation bestimmt, die darüber entscheiden kann, ob sich eine *Lm* Infektion ausbreiten kann oder vom Wirt kontrolliert wird. Um die Infektion auszuweiten, müssen die intrazellulären Parasiten die Wirtszelle verlassen und weitere, vormals uninfizierte Zellen, infizieren. Obwohl dieser Schritt wahrscheinlich kritisch für die Infektiosität von *Lm* ist, wurde der zugrundeliegende Mechanismus der einen Zell-Zell-Transfer ermöglicht bisher kaum erforscht. Kürzlich erschienene Daten legen nahe, dass der apoptotische Zelltod und eine erhöhte Parasitenreplikationsrate in Zusammenhang mit einer Übertragung zwischen Zellen stehen. Auf Basis dessen habe ich die Hypothese formuliert, dass der Zellaustritt und die Reinfektion von unifizierten Makrophagen mittels Apoptose induziert wird, in Abhängigkeit von dem Metabolismus des Parasiten und dem Phänotyp der Wirtszelle. Mittels Makrophagen, die aus Monozyten von humanen Blutspendern differenziert werden, konnte ich einen fluoreszenzbasierten Assay etablieren der eine Detektion von Übertragungsevents im Durchflusszytometer ermöglichte. Mit diesem Assay konnte ich zeigen, dass die Übertragung von Parasiten mit einem Übertrag von Zellmaterial der vorherig infizierten Zelle einhergeht. Die Caspase-3 Aktivität in Makrophagen war zudem erhöht in Folge einer *Lm* Infektion, was zusammen deutlich auf einen apoptotischen Zelltod von primärinfizierten Zellen hinweist. Durch die Verwendung eines Proliferationsreporters, der von den infizierenden Parasiten exprimiert wird, war es möglich zu messen, dass die Übertragung zwischen Zellen von stark intrazellulär proliferierenden *Lm* abhängt. Interessanterweise war diese Population sowie die generelle Proliferation von Parasiten in Makrophagen erhöht, wenn sie mit dem inflammatorischen Signalmolekül IFNγ stimuliert wurden, während eine anti-inflammatorische Aktivierung der Makrophagen durch IL-4 oder M-CSF zu einer Reduktion der Proliferation führte. Im Einklang mit den vorigen Ergebnissen war die erhöhte Proliferation unter IFNγ Stimulation mit vermehrtem Zell-Zell Transfer von Parasiten verbunden, während im besonderen IL-4 Stimulation eine Übertragung verminderte. Die vorliegende Arbeit trägt damit zu Erweiterung des Verständnisses über die Übertragung von *Lm* zwischen Zellen bei, indem sie eine enge Verknüpfung zwischen Parasitentransfer, -proliferation und apoptotischen Zelltod der Wirtszelle herstellt. Die Daten zeigen in Übereinstimmung mit der Hypothese, dass der Phänotyp der infizierten Makrophage Einfluss

auf die Proliferation und die Übertragung nimmt und dadurch auf die Kontrolle oder die Verbreitung der Infektion wirkt. Interessanterweise führten Spendervariationen in dem inflammatorischen Phänotyp durch die Infektion mit *Lm* unter der Stimulation mit IFNγ dazu, dass eine vorher unbekannte Rolle des Kynurenin Stoffwechselwegs in der Übertragung von Parasiten beschrieben werden konnte, die zum Verständnis des Austrittsmechanismus von *Lm* und der Expansion von Infektionen im Menschen beiträgt.

3 Introduction

3.1 *Leishmania*: parasite and disease

Leishmaniasis is a vector-borne disease caused by the pathogen *Leishmania* (*L.*) and is transmitted by the bite of an infected phlebotomine sandfly [1]. In humans, the neglected tropical disease has different clinical manifestations, namely cutaneous (CL), mucocutaneous (MCL), and visceral leishmaniasis (VL), occurring in dependence on the infecting *L.* species and the immune response of the affected individual [2,3]. VL is the most severe form, resulting in swelling of the spleen and liver, causing weight loss, fever, and anemia, with a fatal outcome if the symptoms remain untreated. In addition, recovered patients can develop post-kala-azar dermal leishmaniasis, a cutaneous variant of the disease that forms a macular or maculopapular rash that expands from the face to the extremities [4]. VL occurs upon infection by the species *L. donovani* in the Old World (Eastern Hemisphere) and *L. infantum* in the New World (Western Hemisphere), causing 50'000 to 90'000 new cases per year, dominantly in South Asia, Sudan, and Brazil. CL is a less severe but vastly more abundant form of the disease, with 600'000 to 1 million cases annually caused by multiple species, including *L. major* (*Lm*) (Old World) and *L. mexicana*, *L. amazonensis*, and *L. braziliensis*, with most cases reported in Central Asia, North Africa, and South America. [3,5]. CL manifests as an ulcerating skin lesion localized to the site of the sandfly bite that is self-healing but leaves behind scars stigmatized in many cultures [3]. Despite the self-healing of lesions, treatment is needed to prevent complications arising during infections by *Lm* that can cause relapses with multiple lesions and scarring of affected patients [6]. MCL, as well as diffuse CL are chronic forms of CL causing severe skin lesions of soft tissue in the nose and mouth or multiple non-ulcerating lesions, respectively, that can occur simultaneously with a localized CL or months after recovery [2,7].

Leishmaniasis is a poverty-related disease. Risk factors for becoming diseased are a weakened immune system and malnutrition. Poor housing and low hygiene standards improve the propagation of the sandfly vector, increasing transmission rates. All these factors mostly inflict impoverished populations in rural and suburban areas. Access to diagnosis and medication varies greatly between different health-care systems but is often hard to get and costly [8,9]. Moreover, treatment with miltefosine and amphotericin B causes several mild to moderate adverse effects, and increasing resistance of the *L.* parasite to the established drugs is reported [10,11]. Vaccines, which have proven to be very successful for intervention strategies in third-world countries for multiple endemic diseases, are not yet available for any form of leishmaniasis in humans [12–14]. This urges the need for continuous research in the field of *L.* infection to find potential parasitic mechanisms that can be exploited for the development of medications and vaccines [6,11].

3.2 The life cycle of *Lm* parasites

Apart from the symptoms, there are numerous differences in the course of infection caused by different *L.* species *(spp.).* This present work and introduction focusses on the research of *Lm* infections, but similarities and deviations with other *spp.* are discussed if they are relevant for the context or to draw conclusions. As with all other *L. spp.*, *Lm* has a biphasic life cycle that ensures the parasites survival and replication through a morphologic change of the parasite during the transit between vector and host (Figure 1) [15,16].

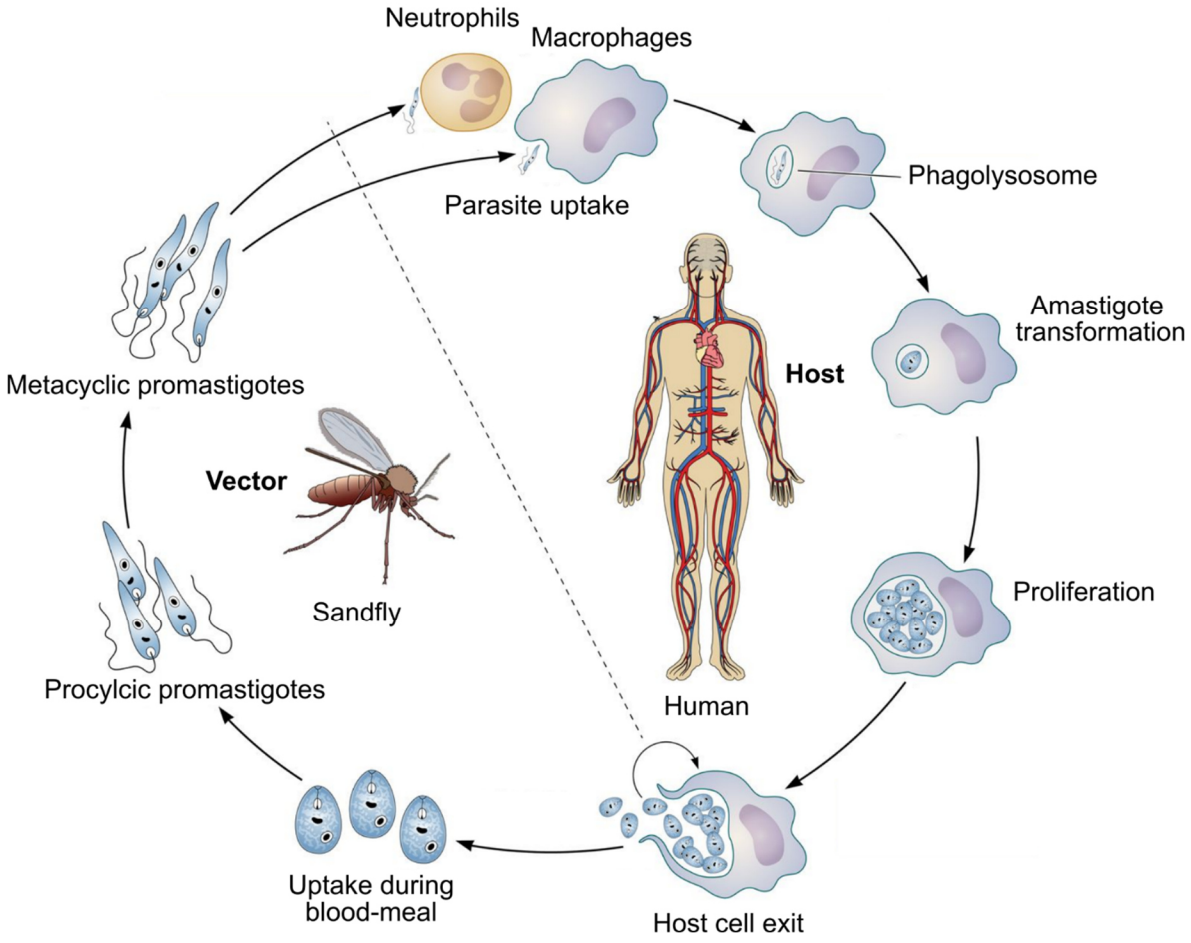

Figure 1: Biphasic life cycle of *Lm* parasites.
Transmission of metacyclic promastigotes to the upper dermis of human hosts by the phlebotomine sandfly vector ultimately results in infection of macrophages. Within the maturated phagolysosome, *L.* parasites transform into their amastigote form, which is resistant to the harsh environment, proliferate intracellularly, and eventually infects infiltrating monocyte-derived macrophages. The life cycle closes with the uptake of amastigotes during a blood meal on a host after their transformation into promastigotes in the sandfly's midgut [17].

During the blood meal of a parasitized vector, metacyclic promastigotes are transmitted in the upper dermis of host organisms. Mechanistically, the transmission is facilitated by a plug, formed with promastigote secretory gel in the stromodeal valve that forces the sandfly to regurgitate this plug alongside highly metacyclic promastigotes infective into the opened wound to free up the proboscis [18]. At the site of the sandfly bite, promastigotes are taken up by neutrophils invading the inflicted tissue or by tissue-resident macrophages. During the

infective route via neutrophils, intracellular promastigotes prolong the lifespan of these short-lived host cells by inhibiting apoptotic cell death. Later, and after macrophage recruitment, the parasites transfer to the newly recruited cells alongside the dying neutrophil, resulting in a silent transmission between host cells, resembling a 'trojan horse' to outwit the innate immune response [19,20]. Upon reaching the ultimate host cell, the macrophage, parasites reside within the phagosome. With the change of the pH during the maturation of the compartment and due to the higher temperature in the human host, promastigotes transform into non-flagellated amastigotes [21]. Amastigotes are more resistant to the anti-microbial conditions within the phagolysosome and are able to proliferate intracellularly [22]. To maintain and propagate the established infection, amastigotes infect newly recruited monocyte-derived macrophages invading the inflamed tissue [23]. Although, a functional host cell exit strategy and re-infection of a new host cell is likely a critical process to uphold the infection and counter the adaptive immune response in patients being diseased by CL between 2 to 18 months, the underlying mechanism is poorly understood [24]. Finally, the life cycle is closed with a sandfly feasting on an infected host, eventually ingesting amastigotes which then retransform into procyclic promastigotes within the midgut of the vector.

3.3 Response of the immune system

Infections by *Lm* trigger an immune response that is initiated by cells of the innate immune system after getting into contact with the metacyclic promastigotes and pro-inflammatory contents of the sandfly's saliva at the site of infection. The uptake of parasites by phagocytic host cells induces anti-microbial mechanisms on the cellular level of whom many are derailed by the infecting parasite [25]. The subsequent activation of the adaptive immune system by antigen presenting cells (APCs) coordinates the systemic response which is crucial for the fate of infection. Corner stone of the infection process are macrophages that play a bivalent role in exaggeration and control of the infection [2]. On one hand, macrophage populations are the reservoir and proliferation niche for parasites during established infections [26]. On the other hand, macrophages induce the adaptive immune response and can control the infection as effector cells initiating anti-microbial mechanisms [27].

3.3.1 Macrophages

Macrophages were first described by Ilja Iljitsch Metchnikoff in the late 1900th century as a cell, capable of phagocytosis and he already proposed that its functions are part of an immune response. Indeed, macrophages are in the first line of the hosts defense, the innate immune system, engaging infecting pathogens and exert microbicidal effector mechanisms [28]. As APCs they are also crucial for the initiation of an adequate innate immune response. Macrophages express a multitude of pattern recognition receptors (PPRs) mediating pathogen recognition. The most important receptor protein family are toll-like receptors (TLR) that bind to various pathogen-associated molecular pathogens patterns (PAMPS). They are present on

the cell surface and in the endosome of macrophages [29]. Additionally, they attribute for the recognition of damage-associated pathogen patterns (DAMPS), endogenous signals of cells undergoing a lytic form of cell death. This function is complemented by nucleotide-binding oligomerization domain (NOD)-like receptors (NLRs) accounting for the reception of cytosolic PAMPS and DAMPS that, upon activation exert inflammasome signaling [30]. An activation of TLRs induces the expression and release of pro-inflammatory cytokines like type 1 interferons (IFN). Other PPRs also contribute in the recognition and uptake of pathogens like CD14 and the mannose receptor CD206 [31,32]. Subsequent to an exogenous stimulus of PPRs and cytokine signaling, macrophages serve as effector cells for pathogen clearance by a respiratory burst [33]. By contrast, macrophages also contribute to restoring the steady state after inflammation by tissue repair mechanisms and anti-inflammatory signaling, mainly driven by IL-4 signaling. Lastly, macrophages uphold homeostasis in steady-state situations by the removal of dying cells and debris by phagocytosis in the presence of IL-10 or e.g. immunocomplexes (Figure 2) [34,35].

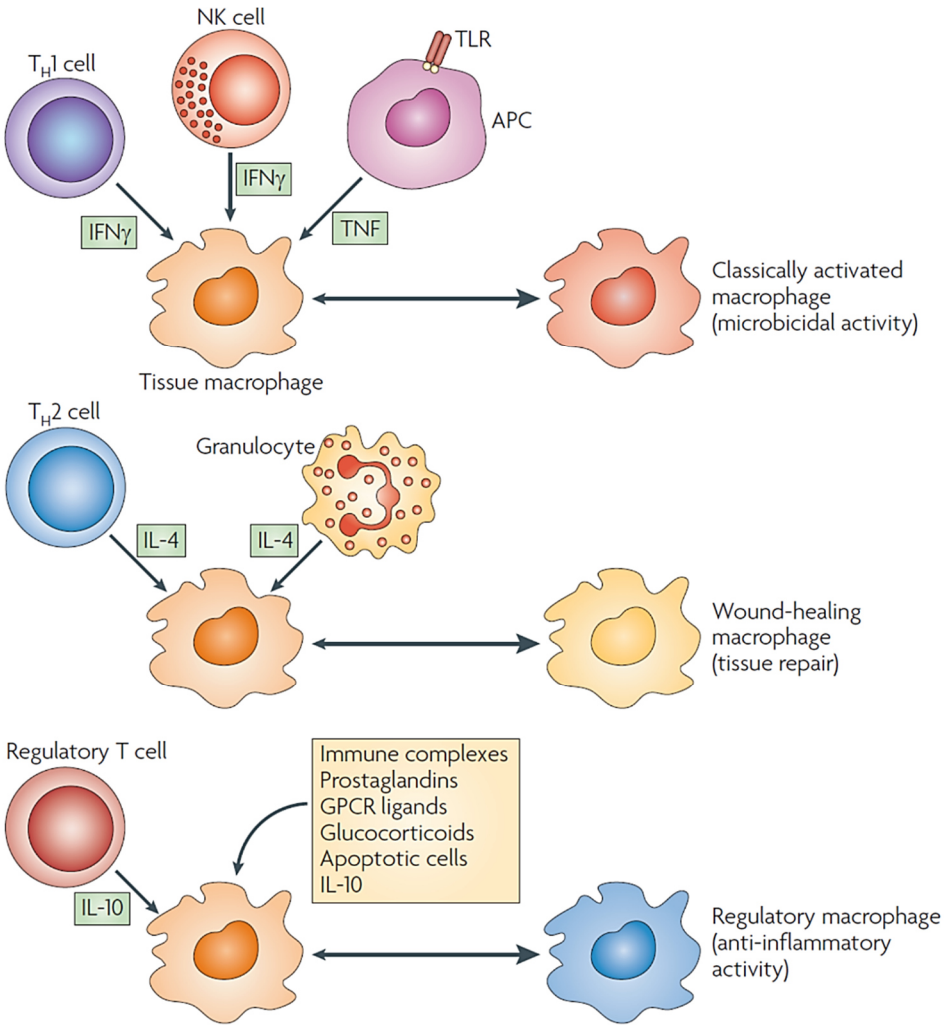

Figure 2: Activation spectrum of macrophages.
Stimuli of the adaptive immune response and other immune cells tailoring the macrophage phenotype to attribute for tasks in pathogen control (classically activated macrophages), recovery (wound-healing macrophages) and homeostasis (regulatory macrophages). *In vivo* the shown stimuli are supplemented by various other stimuli resulting in a nuanced set of subpopulations of each presented phenotype [34].

Macrophages originate from different progenitors, dividing its population into resident and recruited cells. Tissue-resident macrophages are present in most organ tissues, account for tissue homeostatic processes through all life stages and coordinate the initial immune response to infection. Monocyte-derived macrophages are recruited during an infection and differentiate during the transit from the blood to the inflicted tissue to a variety of phenotypes in dependence on local stimuli. According to the state of inflammation, they account to all previously described tasks despite having a shorter life span than the resident macrophage population, and their numbers diminish during steady-state situations (reviewed in [36]).

Historically and to account for different cell functions, macrophages were categorized into classically activated (M1) and alternatively activated (M2) macrophages which refers to the helper T-cell responses (Th1 and Th2) that are forms the respective macrophage phenotype. This scheme was introduced by Charles D. Mills describing the two phenotypes based on the catabolism of arginine by the regulation of two contending enzymes. Either by the upregulation of inducible nitric oxide synthase (iNOS) for the generation of nitric oxide (NO) in pro-inflammatory M1 macrophages or by anti-inflammatory activity of M2 macrophages with an upregulation of arginase producing L-ornithine [37]. This rigid classification was pried open with studies showing a more nuanced set of functions carried out by macrophage cell populations. The diversification of macrophage phenotypes resulted from the manifold combinations of stimuli *in vivo* as well as a plasticity of activated macrophages, allowing a cell to account for different tasks in dependence of the tissue requirements [34,38]. While pro-inflammatory macrophages activated by IFNγ are still referred to as M1, the terminology was expanded to additional phenotypes of anti-inflammatory or regulatory macrophages: M2a, activated by IL-4 or IL-13; M2b, derived by the reception of immunocomplexes and TLR activation or IL-1β; M2c, by the stimulation with IL-10; and M2d, activated by TLR antagonists [39,40]. Because of the plethora of co-stimuli acting on these cells [35], the activation of macrophages can even better be described by an activation spectrum within the categories, inflammatory (classically activated) macrophages, wound-healing macrophage, and regulatory macrophage (Figure 2) [34,41].

3.3.2 Activation of macrophages by the onset of infection

After their transmission to the dermis, *L.* promastigotes are engaged by neutrophils and tissue-resident macrophages [42,43]. While the role of neutrophils as “trojan horse” has briefly been described previously, the role of macrophages requires a deeper analysis. Macrophages inherit the two central anti-leishmanial effector mechanisms, the respiratory burst that produces radical oxygen species (ROS) and the generation of NO catalyzed by NOS [20,44,45]. The respiratory burst is activated through the enzyme NADPH oxidase 2 (NOX2) and is a prompt reaction to the parasite uptake. *L.* parasites are able to intervene with the ROS activity mediated by the cell surface molecule lipophosphoglycan (LPG) present on metacyclic

promastigotes [26,46]. The production of the effector molecule NO is induced by the reception of IFNγ which is mainly provided by natural killer cells during the innate immune response before the onset of an adaptive immune response. Despite the activation of both effector mechanisms in macrophages, the innate immune response is unable to control the infection progress due to the persistence of *L.* parasites for the harsh microbicidal conditions within the phagolysosome [25].

3.3.2.1 Heterogeneity of macrophage phenotypes during the adaptive immune response

Even though *L.* parasites are able to dampen the pro-inflammatory cytokine release by phagocytes (reviewed in [47]), *L. spp.* infections by ultimately trigger the release of type 1 interleukins (IL), IL-6 and tumor necrosis factor α (TNFα) and induce a T cell response [48,49]. A response by $CD4^+$ Th1 cells can provide a sustained and systematic stimulation with IFNγ and TNFα that triggers a prolonged production of ROS and NO [44,50]. *L.* Infections in mice show opposed results regarding resolution or exacerbation of the disease severity by the adaptive immune response in dependence on whether the BALB/c or C57BL/6 murine model is employed. C57BL/6 mice are able to control the infections by most *L. spp.* by an IL-12 mediated Th1 response that induces the cytokine release of IFNγ and TNFα and therewith the production of ROS and NO in monocyte-derived macrophages [51]. On the other side of the spectrum, BALB/c mice induce a Th2 immune response during infection leading to an alternative activation of recruited monocytes by IL-4 and IL-13 and non-healing lesions [44,52]. This established a paradigm between susceptibility and resistance to infection mediated by contrary T-cell responses and the corresponding alternative or classical activation of infected macrophages. Yet, these differences in the adaptive immune response were not translatable to the disease progressions during human infections, contradicting this paradigm, and the role of macrophages during infections was further analyzed, to improve the understanding of an infection progression and disease [2]. More recent studies in mice showed that a local cytokine milieu of IL-4 and IL-10 can sustain a parasite reservoir of tissue-resident macrophages [53]. Also, $Ly6C^+CCR2^+CD11c^+$ macrophage phenotypes were shown to provide an effective replication niche for *Lm* despite a Th1 immune response which further refutes the Th1/Th2 paradigm [23]. In addition, an alternatively activated $CD11b^+MHCII^+PDL2^+Arg1^+$ macrophage phenotype was identified in the absence of IL-4 in *L.* infected skin tissue [27]. The release of IFNγ during the onset of Th1 immunity was found to account for the recruitment of monocytes by MCP-1, CXCL9 and CXCL10 which directly translates to high number of infected $Ly6C^+CCR2^+$ monocytes and monocyte derived macrophages although iNOS is active [27,54,55]. The controversial role of pro-inflammatory monocytes acting as permissive host cells, as well as effector cells controlling the infection during the Th1 response shows that likely a balance by the IFNγ signaling is needed to limit the monocyte recruitment and still induce NO production (Figure 3) [27].

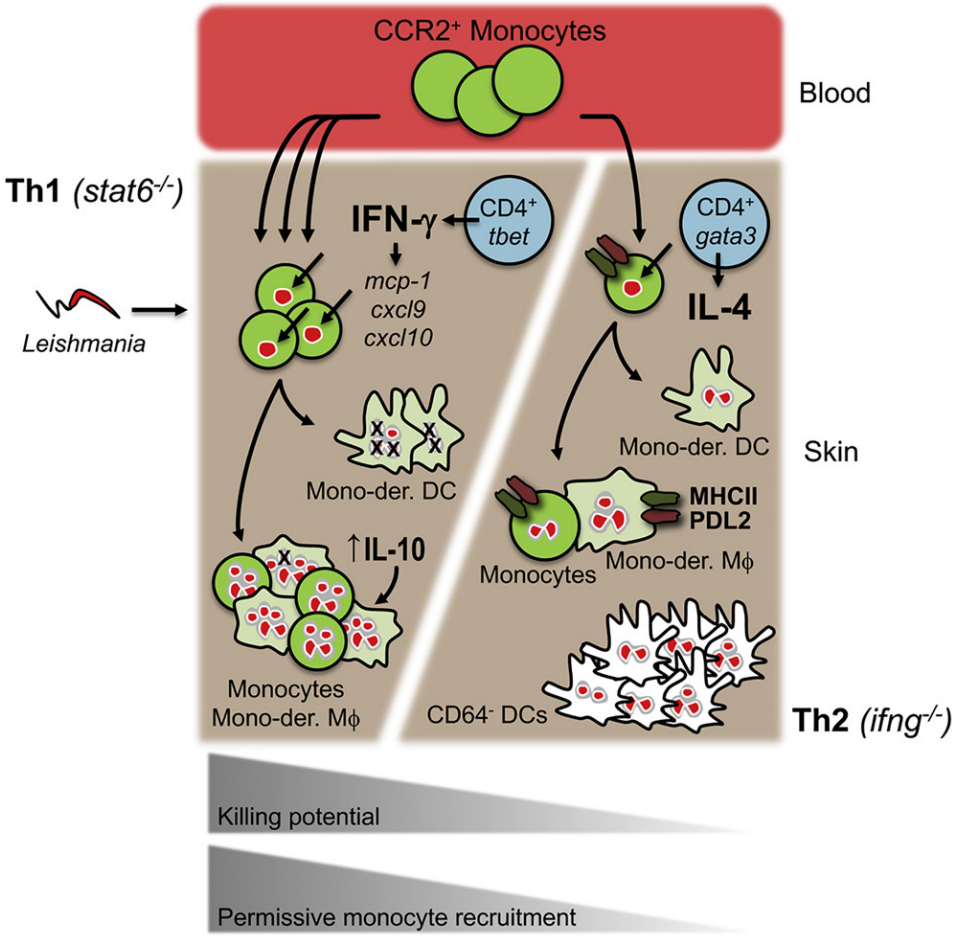

Figure 3: Cross regulation of monocyte recruitment during Th1 and Th2 immune response. An isolated Th1 response through the ablation of transcription factor *stat6* causes an IFNγ dominated stimulation (left side). This induces a high monocyte recruitment from the blood to the tissue by the *mcp-1*, *cxcl9* and *cxcl10* expression and translates to high numbers of infected monocytes and monocyte-derived macrophages. While IFNγ stimulation activates iNOS to control the infection, the concomitant upregulation of IL-10 allows the formation of parasite reservoirs. An isolated Th2 response due to the ablation of *ifnγ* yields a stimulation by IL-4 (right side). In that scenario the recruitment of monocytes is limited. Therewith the number of infected cells is controlled, yet iNOS is not upregulated leading to the infection progression in alternatively activated MHCII$^+$PDL2$^+$ monocyte-derived macrophages and DCs (Mono-der. DC). In addition, the IFNγ mediated parasite killing by CD64$^-$ DCs is suppressed. (Mono-der. Mϕ) monocyte-derived macrophages [27].

Interestingly, NO itself was shown to limit the monocyte recruitment and thereby contributes to this balance [56]. In further contrast to the Th1/Th2 paradigm, a limited monocyte recruitment was observed during the Th2 response mediated by IL-4 signaling which provides a certain protection against exaggerated infection progression by lowering the number of infected cells. Additionally, the intracellular parasite titer was not altered by the ablation of the IFNγ receptor and the simultaneous absence of CD11b$^+$iNOS$^+$ cells early during the infection [27]. The prominent role of monocyte recruitment for the infection progression currently lacks a cellular mechanism, explaining the transmission of infecting parasites to the newly recruited cells and how this mechanism might also be affected by the macrophage host cell phenotype. Initial results restricted to observations in resistant C57BL/6 mice suggest that the parasite proliferation is determinant for the cell-to-cell transfer [23]. The versatile role of macrophage

phenotypes in the infection progression might therefore also affect the parasite exit mechanism. Besides these results from mouse infection models, the human disease variant CL showed a more divers immune response, that did not confer to either Th1 or Th2, but resolving of the infection relied on an interplay of both, indicating the involvement of a diverse macrophage population afflicted by parasites [2].

3.3.2.2 The kynurenine pathway

Apart from the arginine catabolism another amino acid catabolic pathway might be involved in intracellular *L.* parasite control. This kynurenine pathway is the *de novo* synthesis pathway which generates the metabolite Nicotinamide adenine dinucleotide (NAD^+) from L- tryptophan. NAD^+ and NADH are important metabolites fueling processes like glycolysis, oxidative phosphorylation, and β-oxidation as electron carrier. The pathway is strongly upregulated under pro-inflammatory stimulation to cover the increased energy consumption during inflammatory situation resulting from oxidative stress and DNA repair among others [57,58]. The rate-limiting step of the pathway, the degradation of L- tryptophan to *N*-formyl kynurenine further to L-kynurenine, is catalyzed by tryptophan 2,3-dioxygenase (TDO) or indoleamine 2,3 dioxygenase 1 and 2 (IDO) (Figure 4).

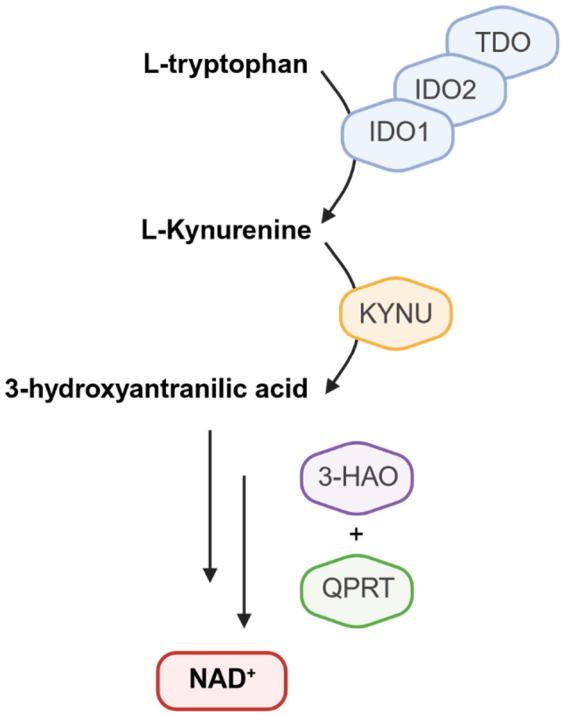

Figure 4: Simplified kynurenine pathway.
L-tryptophan is catabolized to L-kynurenine by IDO1/IDO2/TDO and further metabolized to 3-hydroxyanthranilic acid by KYNU. 3-hydroxyanthranilic acid is then oxidized by 3-HAO to 2- amino-3-carboxymuconic-6-semialdehyde that reacts spontaneously to quinolinic acid. From quinolinic acid, nicotinic acid is synthesized by QRPT which is further processed to NAD^+ by the Preiss-Hanssler pathway. (IDO) indoleamine 2,3 dioxygenase, (KYNU) kynureninase, (3-HAO) 3-hydroxyamino oxidase; (QPRT) quinolinate phosphoribosyltransferase, (NAD^+) nicotinamide adenine dinucleotide.

While TDO is mostly expressed in the liver, IDO1 can be expressed by a multitude of cells but is specifically upregulated in primary human macrophage during the stimulation by IFNγ [59]. Vice versa, IL-4 and IL-13 downregulate the kynurenine pathway, even after induction by IFNγ [60]. Downstream of the catalytic activity of IDO/TDO, kynureninase (KYNU) catabolizes L-kynurenine further ultimately forming nicotinamide which then enters the Preiss-Hanssler pathway and results in NAD^+. Interestingly, *L.* parasites are auxotroph for the *de novo* synthesis of NAD^+ and need to salvage the metabolites nicotine amide, nicotinic acid or nicotinamide riboside from its hosting cell to produce NAD^+, that is required for the parasites' proliferation [61]. An ablation of the salvage pathway in *L. infantum* parasites results in a growth lag during an *in vitro* culture and a reduced parasite burden during infections of THP-1 cells. This phenotype is recovered by the addition of exogenous nicotinic acid [61]. Regulation of IDO1 and the kynurenine pathway are implicated with several infectious diseases, with positive or negative outcome for the pathogen [62]. Parasite burdens in skin lesions from CL patients infected by *Lm* negatively correlated with the expression of TDO. This conferred to an increase in parasitic mRNA obtained from *in vitro* infected monocyte-derived macrophages with inhibition of TDO [63]. Besides the *de novo* synthesis of NAD^+, IDO1 also has a T cell suppressive effect when it is expressed in plasmacytoid DCs [64]. Infection of mice by *Lm* revealed an increased expression of IDO1 in DCs within the lymph node, resulting in the suppression of a T-cell response. The inhibition of IDO by 1-methyltryptophan (1-MT) consequently reduced the severity of footpad swelling and the parasite burden [65,66]. Moreover and in well accordance, the infection of human myeloid-derived DCs by *Lm* and *L. donovani* both induced the expression of IDO [67].

3.4 The importance of pathogen exit

An important mechanism in regard of pathogenicity is the exit of intracellular protozoan parasites, fungi, and bacteria (reviewed in [68–70]). By their intracellular lifestyle, these pathogens obtain a niche that after withstanding effector mechanisms of the host cell, provides nutrients and protection from both the innate and the adaptive immune response. While processes and dynamics facilitating the initial transmission, infection and immune subversion of pathogens were extensively studied by researchers, the occurrence of pathogen exit from infected cells was mostly seen as passively occurring event. [70] Though, more recent studies from multiple intracellular parasites suggest that exit pathways are often tightly regulated mechanisms, influenced by factors from both, the host cell, and the pathogen, representing a second cycle of transmission between cells. Understanding these pathways holds great potential for the discovery of new medication strategies infectious diseases, as the successful transmission from cell-to-cell can be related to chronicity and expansion of infections. Already characterized exit strategies can be grouped into three different categories proposed by Flieger *et al.*: induction of regulated cell death (1), active host cell membrane destruction (2) and

membrane-dependent exit without destruction (3) (Figure 5) [70]. This overview including examples for a multitude of pathogens emphasizes for the diverse set of exit strategies emerged from the co-evolution of pathogen and host.

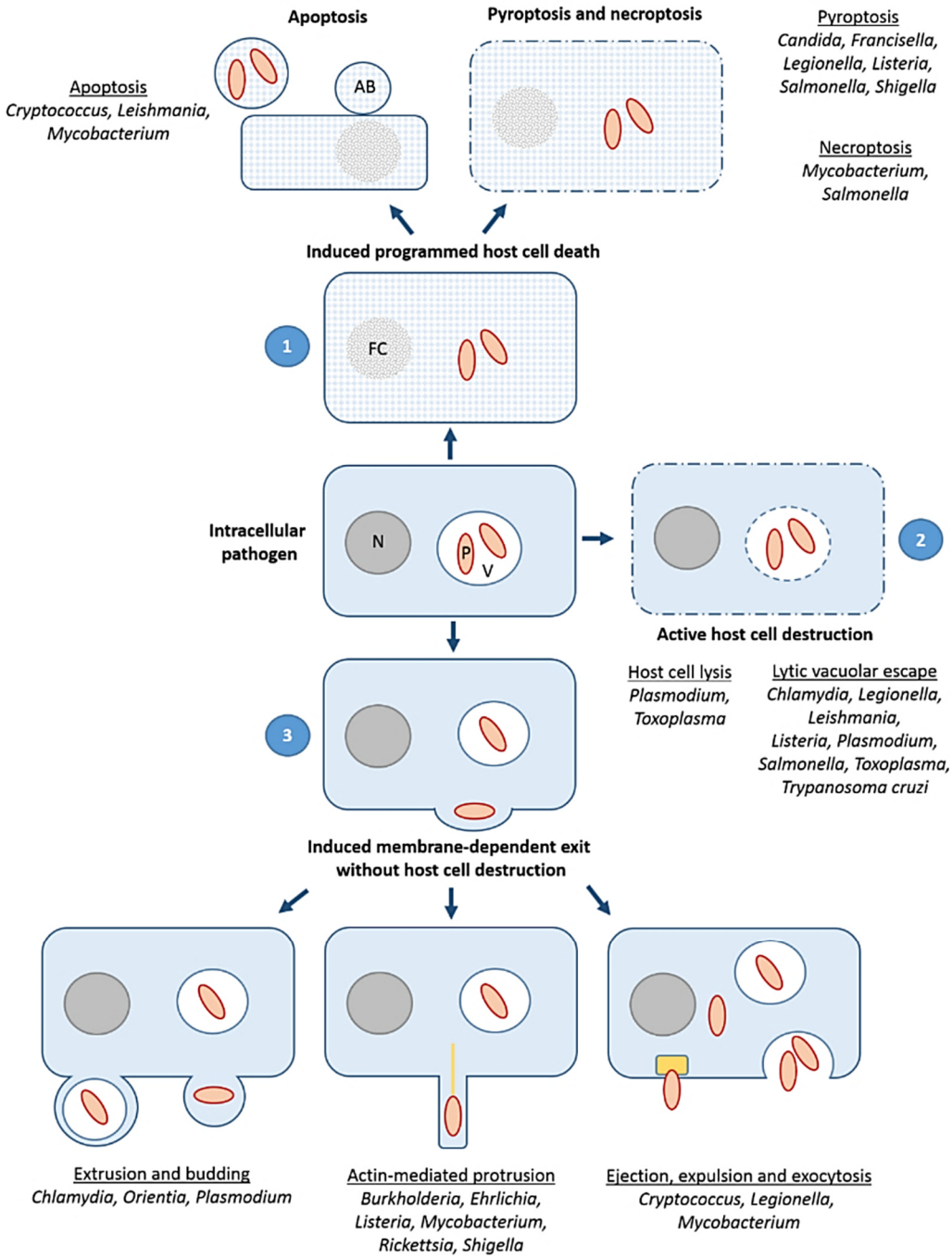

Figure 5: Exit strategies of intracellular pathogens.
Exit strategies in three categories with pathogen examples engaging the described pathway. (1) Induction of regulated cell death, either non-lytic via apoptosis or lytic via pyroptosis and necroptosis. (2) Membrane destruction of the pathogen containing compartment or the host cell membrane. (3) Membrane-dependent exit without cell membrane destruction by an uncontained release of pathogens, protrusion of the cell membrane or extrusion of a membrane surrounded compartment. (N) nucleus, (FC) fragmented chromatin, (AB) apoptotic body, (P) pathogen, (V) vacuole [70].

In regards of *L.* exit pathways, mechanisms from all three categories have been proposed or implicated by previous studies. More than 50 years ago, analyses from histological preparation of CL patients described the occurrence of extracellular parasites evaded from lysed macrophages. The researchers already described limited amounts of extracellular amastigotes associated with increased damage of connective tissue in Brazilian patients (New World) compared to patients from the Old World, with parasitized, necrotic macrophages but without extracellular parasites and no connective tissue damage [71]. Around the same time, microscopic observations of *in vitro* cultured mouse macrophages infected by *L. tropica* presented unhindered amastigote proliferation and ruptured cells after prolonged incubation times resulting in the release of intracellular parasites [72]. Later, murine peritoneal macrophages were observed to exocytose *Lm* parasites after 5 days of infection, whereby the membrane was shriveled but not ruptured [73,74]. In accordance, low-dose infection of mice presented a silent propagation of parasites for 4 to 5 weeks prior to the onset of an acute inflammatory phase [75]. A potential lytic exit pathway for *L. amazonensis* and *L. guyanensis* might be provided by the pore-forming cytolysin leishporin. Leishporin is catalytically active at pH of 5.0 to 5.5 but also at pH 7.0, suggesting a function within the phagolysosome and an exit of parasites into the cytoplasm but also yield the potential to permeate the cellular membrane in order to escape the host cell [76,77]. Results observing a de facto exit of *L. amazonensis* and *L. guyanensis* parasites from host cells driven by leishporin are yet missing and leishporin is not expressed by other *L. spp.* Besides evidence for host cell membrane destructing- and non-destructing strategies, interference of *L.* parasites with different forms of regulated cell death, especially apoptosis and inflammasome activation are evident in recent studies which requires a more comprehensive analysis of both hereinafter.

3.4.1 Apoptosis

Apoptosis is a non-lytic, regulated form of cell death that is crucial for tissue homeostasis and preventing the onset of inflammation. In the apoptotic process, cells retain their membrane integrity and contribute to their clearance by phagocytes [78,79]. As briefly described before, hallmarks of apoptotic cells are a shriveled and blebbing membrane, fragmentation of chromosomal DNA and the exposure of presented phosphatidylserine (PtdSer) on the outer leaflet of the lipid membrane [80,81]. Apoptosis can be catalyzed by an extrinsic, and, more importantly in the context of intracellular pathogens, by an intrinsic pathway. In vital cells, the anti-apoptotic B-cell lymphoma 2 (Bcl-2) protein family members antagonize the pro-apoptotic effector proteins Bcl-2-associated X protein (Bax/Bac). During the intrinsic or mitochondrial induction of apoptosis, this balanced regulation is disturbed by BH3-only protein members that are activated and subsequently inhibit anti-apoptotic Bcl-2 proteins, removing the blockage of Bax/Bac. This dysregulation can be triggered by a plethora of factors including nutrient deprivation, a lack of growth factors and ROS [82]. Bax/Bac facilitate the release of Cytochrome *c* from the mitochondrion and the oligomerization of Apaf1 [83]. This complex

triggers the activation of pro- cysteine aspartyl proteases (caspase)-9 by auto-catalytical cleavage which in turn activates caspase-3 as the central effector protease, accounting for the induction of all apoptosis hallmarks [84,85].

Apoptotic cells are recognized and engulfed by professional phagocytes, mainly macrophages which display receptors for the recognition PtdSer on dying cells surface [86]. This reception is essential for their clearance by efferocytosis [81,87]. PtdSer can be bound by the soluble protein milk fat globulin-E8 (MFG-E8) which functions as an adapter between presented PtdSer and Integrin ($\alpha_v\beta_3$, $\alpha_v\beta_5$) localized in the membrane of macrophages [87,88]. Another PtdSer binding complex is formed by the TAM receptors (Tyro3, Axl, MerTK) and the adapter proteins ProS and Gas6 [89–92]. TAM mediated efferocytosis is accompanied by secretion of anti-inflammatory molecule release (TGF-β, IL-10 and prostaglandin E2) and reduced production of endotoxin-induced pro-inflammatory cytokines (IL-6, TNF-α) [93–95].

3.4.1.1 Induction and inhibition of apoptosis by *L.* parasites

The beneficial circumstances of a silent transfer between cells are apparent for *L.* parasites, yet contrasting results describing apoptosis inhibition, as well as apoptosis induction during infection were reported over the years. Murine bone marrow derived macrophages (BMDM) infected by *L. amazonensis* presented PtdSer on the cell surface, showed a loss of nucleic DNA integrity and were active for caspase-3 within the first 3 days post-infection (pI). Conversely, all these hallmarks of apoptotic regulated cell death were not apparent during infections by *L. guyanensis* [96]. Especially *L. donovani* but also *Lm* are associated with an inhibition of host cell apoptosis induction in RAW264.7 macrophage like-cells. During infection, the parasites upregulated the survival signaling via the phosphoinositid-3-kinasen/protein kinase B (PI3K/Akt) pathway and the expression of the anti-apoptotic protein Bcl-2 [97–99]. In addition, the infection by *L. donovani* was also shown to increase the protein production of myeloid cell leukemia 1 (MCL-1) that inhibits the dimerization of Bax and thereby the apoptosis induction through the release of Cytochrome *c* [100]. Vice versa, long term infection experiments with *L. amazonensis* resulted in a membrane blebbing of the same infected RAW 264.7 cells and a cell-to-cell transfer of evaginated amastigotes to co-cultivated, uninfected cells [101].

Considering that exit mechanisms in general are described as dependent on the pathogen life stage as well as the type and activation status of the host cell, these in parts contradictory results can be explained and even co-exist [70]. Moreover, the varying counts of extracellular parasites observed in biopsies from patients parasitized by Old and New World species and the occurrence of apoptosis hallmarks in *L. amazonensis* infected BDMD but not *L. guyanensis* infected BDMD indicate conserved, inter-species differences [71,96]. The best described exit strategy of *L.* parasites implicating apoptosis is the transfer of promastigotes from infected neutrophils to tissue-resident macrophages [19,20,43]. Still, a pathway unraveling cues and

triggers for an exit induction, especially of *L.* in their amastigote form and during the infection of macrophages is lacking. Observations from wide field microscopy of infected BMDM revealed a blebbing of host cells prior to a direct transfer of the parasite to a new host cell [23]. Accordingly, in fluorescent microscopy, imaging of human monocyte-derived macrophages (hMDM) from our group showed membrane blebbing of a *Lm* infected cell and a subsequent transfer to an uninfected cell with limited exposure to the extracellular milieu (Figure 6).

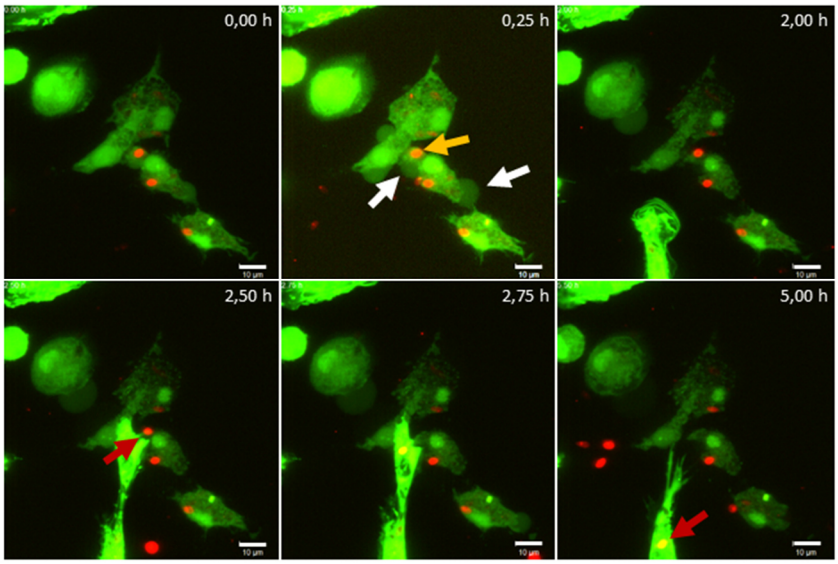

Figure 6: Parasite cell-to-cell transfer in hMDM.
Wide field microscopy observation of hMDM stained by a green-fluorescent dye (green) infected with *Lm* expressing a DsRed fluorophore (red). The infected cell shows a blebbing membrane (white arrow) with a parasite in the evaginated area (orange arrow). The dying cell and the parasite are approached by another hMDM, and the infecting amastigote is transferred to approaching cell (red arrow).

3.4.2 Inflammasome activation and pyroptosis

The second important form of regulated cell death in the context of *L.* infections is pyroptosis. This form of cell death is linked to an integral part of the innate immune response to infections, an activation of the NOD-like receptor family pyrin domain-containing 3 (NLRP3) inflammasome [102]. Pyroptosis is a lytic form of cell death, dependent on the pore formation by gasdermin protein family. In the process, cells shed the cytokines IL-1β and IL-18 and release DAMPs during membrane rupture, both inflammatory mediators in the afflicted tissue [103,104]. To date, three distinct induction cascades of the NLRP3 inflammasome are described, with substantial differences between human and mice (Figure 7) [105]. The canonical activation of the NLRP3 inflammasome requires two sequential stimuli, an initial stimulation by PAMPS, for example by an TLR2 or TLR4 agonist like bacterial lipopolysaccharide (LPS) or LPG from *L.* primes the expression of pro-IL1β and pro IL-18 by NF-κB and the post-translational modification of NLRP3 [106,107]. The second stimulation can result from various signals including potassium (K^+) or chlorine (Cl^-) efflux, ROS or lysosomal contents in the cytosol and induces the formation of the NLRP3 inflammasome consisting of NLRP3, ASC and the pro-caspase-1 [105,108]. After the autocatalytic activation, caspase 1

catalyzes the pore formation by gasdermin D (GSDMD) and the maturation IL1β and IL-18 which are released through the formed pores [109]. Downstream of the pore formation by GSDMD, a hallmark of pyroptotic cell death, ninjurin-1 (NINJ1) is recruited to the cell membrane and induces the cell lysis [110,111]. During the non-canonical inflammasome activation, the effector caspase-4/5 in human or their ortholog caspase-11 in mice sense inflammatory stimuli in the cytosol [112,113]. Caspase-4/5/11 are capable to directly cleave GSDMD and the resulting pore formation leads to K^+ efflux and a subsequent formation of the NLRP3 inflammasome and NINJ1 recruitment. Importantly, caspase-4/5 is constitutively expressed in humans as cytosolic sensors, while mice require a TLR4 priming by LPS to upregulate the expression of caspase-11 [114,115]. The third pathway, the alternative activation pathway of the NLRP3 inflammasome is absent in mice but exists in humans and other mammals. In that pathway, inflammatory cytokine release is induced by the activation of a receptor-interacting serine/threonine-protein kinase-1-FAS-associated death domain protein-caspase-8 (RIPK1-FADD-caspase-8) complex by a singular stimulation of TLR4 by LPS. As in the canonical pathway, NF-κB induces the expression of pro-IL1β and pro IL-18 that are released after the caspase-1 dependent pore formation, yet a NLRP3 inflammasome complex is not assembled and lytic cell death is not observed downstream of the activation [116].

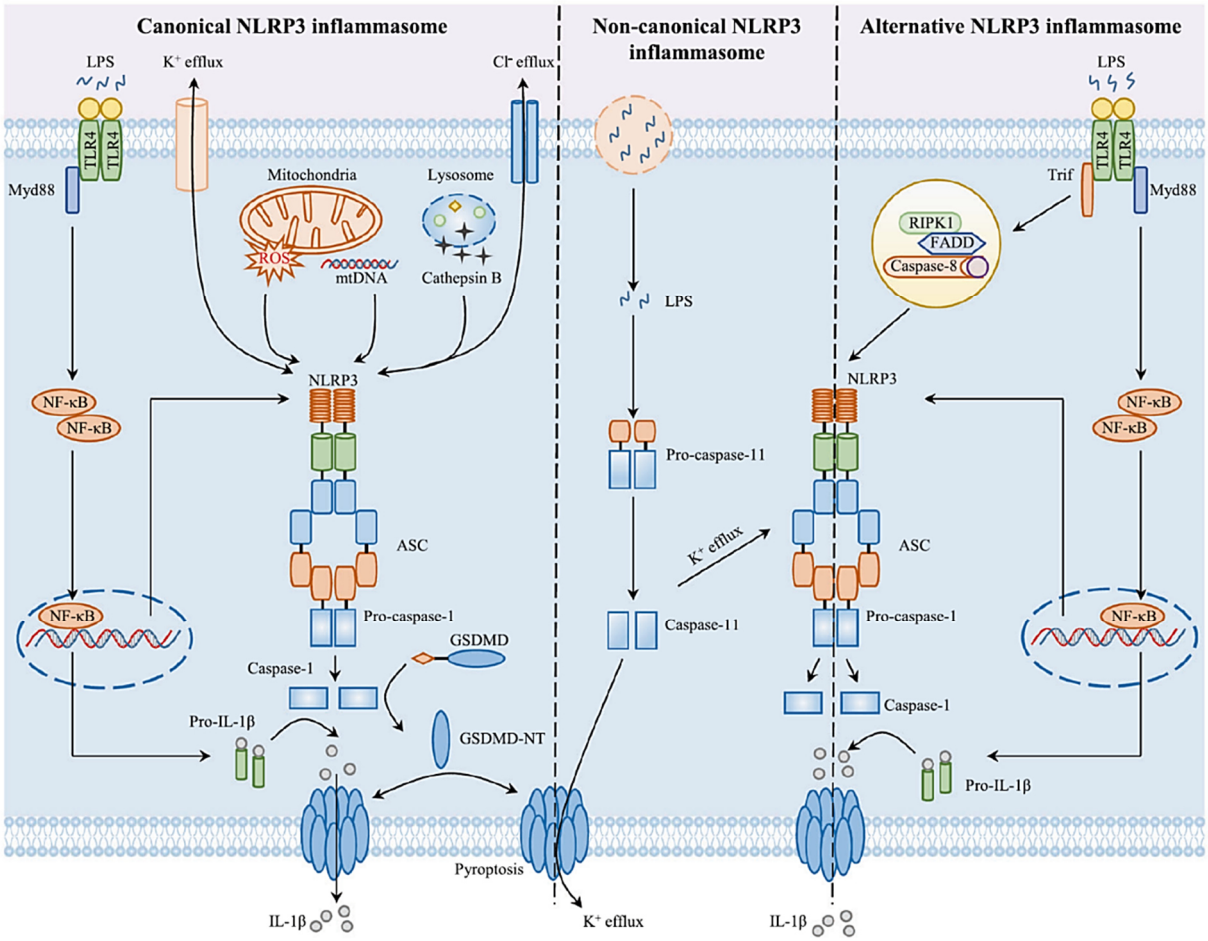

Figure 7: NLRP3 inflammasome activation pathways.
The canonical activation (left) is primed in this example by an activation of TLR4 by LPS activating the transcription factor NF-κB via the adapter protein Myeloid differentiation primary response 88 (Myd88) that induces the production of Pro-IL-1β and NLRP3 inflammasome components. A second stimulus activates the assembly of NLRP3, Apoptosis-associated speck-like protein containing a CARD (ASC) and Pro-caspase-1. The activated caspase-1 maturates pro- IL-1β and cleaves GSDMD, leading to pore formation in the cell membrane, the release of IL-1β and subsequent pyroptosis. In the non-canonical activation (middle), cytosolic LPS activates pro-caspase-11 (in mice, caspase-4/5 in human) that cleaves GSDMD and results in a pore formation. K^+ efflux by the formed pore induces the formation of the NLRP3 inflammasome and induces pyroptosis. The alternative activation (right) is induced by LPS binding to TLR4 leading to the Myd88 dependent activation of NF-κB and the formation of the RIPK-FADD-caspase-8 complex by the adaptor protein Toll/interleukin-1 receptor domain-containing adapter-inducing interferon-β (Trif). In this pathway, the inflammasome is not assembled but all components are required for a caspase-1 dependent pore formation and IL-1β release, despite no induction of pyroptosis [105].

3.4.2.1 Inflammasome activation by *L.* parasites

Inflammasome activation is evident as cellular response to *L.* parasites due to the release IL-1β by infected cells. The release is shown to be dependent on the presence of all NLRP3 inflammasome components demonstrated by its absence by the ablation of NLRP3, ASC and caspase-1 [117,118]. While the release of IL-1β is associated with a parasite resistance by acting directly on the induction of NO in *L. amazonensis* and *L. braziliensis* infections [118], studies with a non-healing variant of *Lm* Seidman strain and C57BL/6 mice associated the NLRP3 inflammasome activation with exacerbated neutrophil recruitment and lesion

expansion [118,119]. In humans, the expression of IL-1β and NLRP3 was detected in lesions from CL patients infected by *L. braziliensis* and *L. mexicana* [120,121]. According to a non-protective role proposed in non-healing infection of mice, IL-1β serum levels correlated positively with disease severity and the abundance of infecting parasites within lesions [119,120,122]. Although the systemic effect of the NLRP3 activation and the IL-1β release have been subject of research studies, there is limited knowledge on the fate of parasitized cells after inflammasome activation and the eventual induction of pyroptosis. In addition to the release of DAMPs during lytic cell death, the regulated cell death by pyroptosis can contribute to the control of intracellular pathogens by dampening the availability of the susceptible niche and mediate uptake and clearance by phagocytes [123]. Since *L.* parasites infect phagocytes as a replicative niche, pyroptosis is a potent exit mechanism to transfer parasites between cells. In line with that, the canonical activation of the NLRP3 inflammasome by LPS and the DAMP ATP induces pyroptosis in *L. amazonensis* infected BMDM and the process results in the exposure of vital amastigotes to the extracellular milieu associated with the remains of the lysed cell [124].

3.4.3 Parasite proliferation

The intracellular parasite replication tailors the acute and chronic phase of leishmaniasis while its control by the immune system is associated with a resolution of the infection [2]. The proliferation of *L.* parasites is inevitably tied to the phenotype of the hosting cell [23]. Experimentally, alternatively activated macrophages are connected with high parasite burdens [27,53,125,126]. In addition, the local exposure of macrophages to IL-10 during Th1 responses efficiently formed parasite reservoirs loaded with amastigotes, despite the activation of microbicidal effector mechanisms [27,53]. Vice versa, Th1 responses of the immune system and IFNγ stimulation lead to reduced parasite titers [27,127]. Contrary to the interpretation that high parasite burden is a result of increased parasite proliferation due to limited effector mechanism activation, measurements of the dynamic process of parasite proliferation show that parasites in high burdened cells replicate slower than parasites in cells with low burdens [23]. Consistently, low burdened $Ly6C^{+}CCR2^{+}$ monocytes constitute a permissive niche for increased parasite proliferation [27]. A control of the proliferation in *Lm* infected C57BL/6 is ultimately achieved by NO which dampens the parasites proliferation and the recruitment of new monocytes to the site of infection without directly exert killing of intracellular parasites [128,129]. Summarized, *L.* parasites exert different replication modes, with exaggerated proliferation during the early phase of infection resulting in high numbers of infected recruited monocytes and monocyte derived macrophages driven by IFNγ on one hand. On the other hand, low-proliferating parasites residing in long-lived macrophage subpopulations result in high parasite burden and titers with an overall lower number of infected cells linked to persistence and chronicity of the infection mediated by IL-4 and IL-10 stimulation. Experimentally, the proliferation of parasites can be impaired by chemical treatment or

genetical modification [130,131]. The chemical blockage of pathogen replication can be achieved by the compound amotosalen that intercalates with DNA and crosslinks base pairs, a property that is used to protect blood plasma products from pathogen growth [132]. The method has been successfully used to generate proliferation-incompetent *L. infantum* and *Lm* parasites termed killed but metabolically active (KBMA) [130,133]. A replication deficiency by gene modification has been achieved with an ablation of the *centrin* gene in multiple *L. spp.* [134–137]. The ablation results in a stage specific arrest of replication confined to the amastigote stage of the parasite [131,134].

3.4.3.1 mKikume proliferation reporter

Müller *et al.* have shown that the application of the fluorescent reporter protein mKikume, constitutively expressed by parasites during the infection, unravels the dynamic process of parasite proliferation by *intravital* imaging of mice [129]. Mechanistically, the reporter bases on a change of red to green fluorescence dependent on the parasites' proliferation. The mKikume protein emits green fluorescence that is switched to red fluorescence emission upon photoconversion of the protein by the illumination with violet light [138]. In the subsequent fluorescence recovery after conversion (FRAC), the fission of parasites dilutes the fluorophore emitting red fluorescence and in addition, unconverted, green fluorescent protein is reproduced, altering the ratio of both. Because the mKikume gene expression is regulated by the promotor of a ribosomal subunit, the synthesis of green fluorescent protein is also a measure for the metabolic activity [129]. The ratio of red and green fluorescence emission of parasites after the FRAC allows a conclusion on the proliferative state of the parasite (Figure 8).

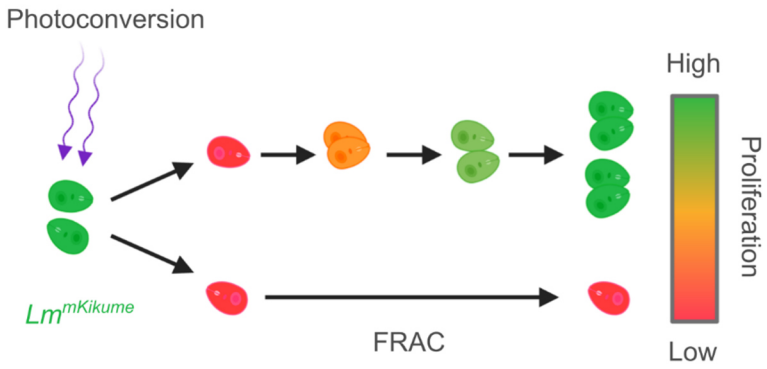

Figure 8: Change of the fluorescence signal by the proliferation reporter mKikume after photoconversion.
Lm parasites expressing the mKikume fluorescent protein can be photoconverted by violet light. During the FRAC, high proliferating parasites dilute the red fluorescence of the converted protein by cell division and reproduce unconverted, green fluorescent protein. Low proliferating parasites do not reduce the converted protein and barely reproduce unconverted protein due to a low metabolic activity.

3.5 Limitations of infection models

Although the murine model contributes greatly to the understanding of *L.* infections, considerable differences occur in the inflammation capacity and immune response in comparison to human hosts [139]. As previously described, the use of clonal murine strains coined the bias of the Th1 and Th2 paradigm that does not translate to human disease progression. In addition, the role of the central microbicidal effector molecule NO is less pronounced in human CL patients and the infection control relies more on the production of ROS (see 3.3.2.1). The use of clonal or isogenic models, meaning animal models or cell lines with practically identical genes, for infectious diseases also underrepresents the effect of natural variation in the innate immune response of individual hosts, limiting the explanatory power if only certain murine strains are employed [140]. Furthermore, and as mentioned above, the non-canonical activation of the NLRP3 inflammasome in mice requires a priming by LPS for the expression of the effector caspase-11, while the orthologous caspase-4/5 is constitutively expressed by humans. Plus, the alternative activation pathway is entirely absent in mice (see 3.4.2). While IL-1β plays an ambiguous role during infections of mice, either providing protection against disease progression or exaggerating the disease, the effect of increased IL-1β expression and serum level was adverse and worsened the infection outcome in CL patients (see 3.4.2.1). Overall, these findings urge the use of human *in vitro* infection models to complement important findings in the murine infection model.

3.5.1 hMDM as human infection model

The differentiation of $CD14^+$ monocytes with the granulocyte/macrophage colony stimulating factor (GM-CSF) or macrophage colony stimulating factor (M-CSF) to render hMDM has been successfully used as *L.* infection model [141–143]. These primary human macrophages are susceptible to infections by *Lm* promastigotes cultivated *in vitro* in biphasic Novy, McNeal and Nicolle (NNN) medium and by amastigotes from axenic culture [141,144–146]. The use of isolated monocytes from individual healthy human donors introduces a naturally occurring variation to inflammatory stimulation to experiments which better reflects disease responses in humans [140]. Moreover, the *in vitro* model of hMDM is expanded by various stimuli to derive various macrophage phenotypes, increasing the applicability of this cell model [147,148]. To allow better comparability between studies and to incorporate limitations that result from single stimulus application *in vitro* comparing to multiplexed stimulations *in vivo*, a nomenclature for *in vitro* generated macrophages was proposed by Murray *et al.* is used in the present work, stating the used stimuli for differentiation and activation (Figure 9) [38,41].

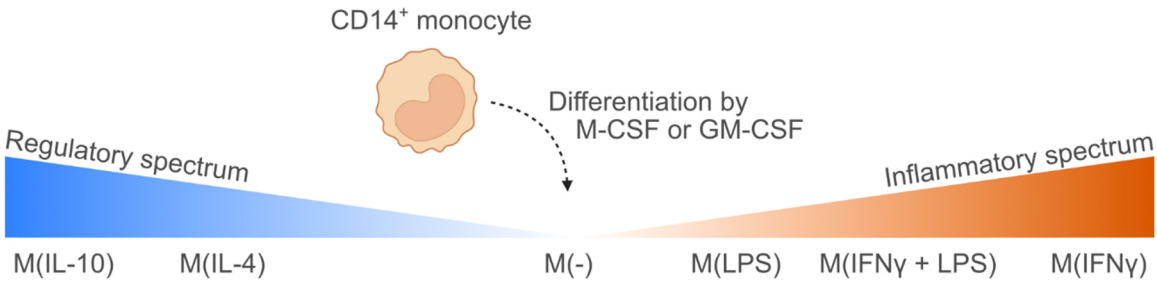

Figure 9: Activation spectrum of *in vitro* macrophages with exemplary stimuli.
hMDM that were differentiated by GM-CSF or M-CSF can be further stimulated by indicated stimuli *in vitro*. To account for differences in the phenotype caused by concentration of stimuli, time of activation and co-stimulatory molecules, the activation of macrophages can be better described by a spectrum in the inflammatory or regulatory range.

3.5.2 BLaER1 macrophage-like cell line

Macrophage-like cell lines provide another experimental tool for the analysis of *L.* infections, with the advantage of gene modifications. Yet, cell lines like THP-1 that are regularly employed as *L.* infection model are not fully capable of the inflammasome assembly, especially in the context of *L.* infections, and unlike primary macrophages show high tolerance to the stimulation by LPS [149,150]. Moreover, the alternative activation of THP-1 cells by IL-4 shows variations in the cell surface marker expression compared to hMDM [151]. The more recently introduced BLaER1 macrophage-like cell line combines the sensitivity for LPS with intact inflammatory activation pathways and was used to discover the formerly unknown alternative activation pathway of the NLRP3 inflammasome [116,152]. The BLaER1 cell line bases on a B cell acute lymphoblastic leukemia cell line RCH-ACV that was modified by transduction of the master regulator in myeloid differentiation, CEBPα. Its transcription is under the control of a promotor which is induced by the binding of an activated estrogen receptor. BLaER1 cells in their pre-B cell state can be trans-differentiated to a macrophage-like cell by β-Estradiol, aided by the viability signaling molecules M-CSF and IL-3. Trans-differentiated BLaER1 cells (hereafter termed BLaER1) gain adherence to cell culture plates, conduct phagocytic activity and express macrophage cell surface markers CD14 and CD11b among others [152,153]. In addition, Kerren Volkmar from our group showed in his experiments that BLaER1 cells are susceptible to *Lm* infections [154].

4 Hypothesis and aim

Infections with the protozoan parasite *Leishmania* pose a threat to the health of people in tropical and subtropical areas, especially affecting the poor. To date, no vaccination has been developed and only costly medication is available for the majority of the diseased people. The path of infection after the transmission of parasites by sandflies has been extensively studied, while the transmission between host cells during established infections lack further insight, despite cumulative evidence that exit mechanisms are a key element of a pathogen's immune subversion strategy and are probably tightly regulated (Figure 10).

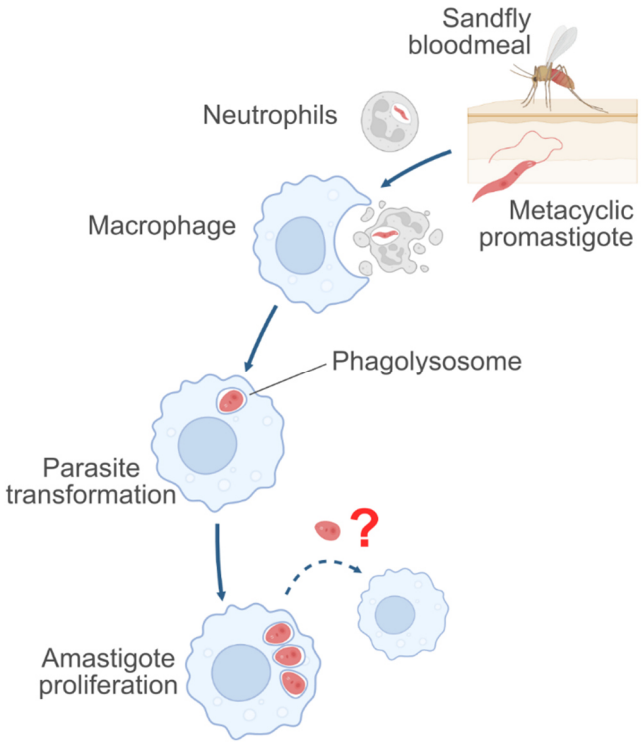

Figure 10: *Lm* exit strategy as part of the parasites' life cycle.

Infected human and murine macrophages displayed membrane blebbing prior to a transfer of intracellular parasites to a recipient cell. In addition, *L.* parasites undergoing the transmission between macrophage host cells showed elevated proliferation rates. Interestingly, the proliferation behavior of parasites is dependent on the phenotype of the infected cell and endogenous stimulation during the adaptive immune response. From the culminated available data, the following hypothesis was derived for the present work:

The underlying mechanisms for both, *Lm* pathogen exit and entry into new host-cells is the induction of cell death depending on the proliferation of infecting amastigotes and the host cell phenotype.

To test this hypothesis I aimed to,

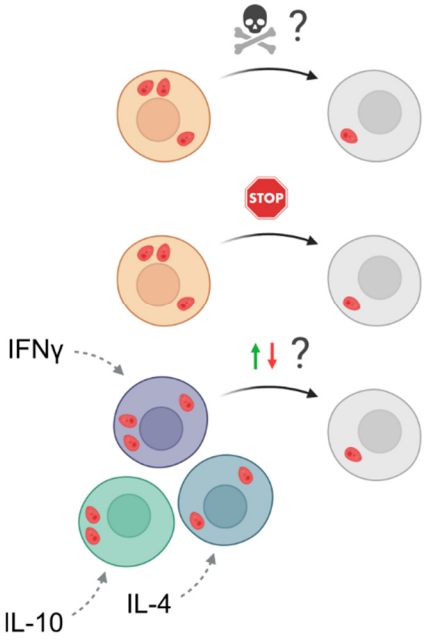

(1) elucidate possible modes and dynamics of cell death associated with Lm exit and transfer to new host cells *in vitro* by establishing assay to detect parasite transfer.

(2) manipulate the identified candidate cell-to-cell transfer mechanism in order to prevent the exit and dissemination of the parasite *in vitro*.

(3) analyze the influence of different inflammatory and regulatory stimuli on human primary macrophages for the parasites proliferation and exit behavior.

5 Material and methods

5.1 Material

5.1.1 Devices

Device	Manufacturer
AxioVert 25 wide field microscope	Carl Zeiss Microscopy
CASY® Cell Counter Model TT	OLS OMNI Life Science
Centrifuge 5430 and 5430R	Eppendorf
Centrifuge J2-MC	Beckman Coulter
Centrifuge Megafuge 40R with BIOLiner swinging bucket rotor and buckets (75003670, 75003668)	Thermo Fisher Scientific
CLARIOstar Plus microplate reader	BMG Labtech
ECL and fluorescence imager Chemostar	Intas
FACS LSR Fortessa	BD Bioscience
FACS LSR II SORP	BD Bioscience
FACS Symphony A3 Cell Analyzer	BD Bioscience
Gel Doc XR+	Bio-Rad
Horizontal electrophoresis system Sub-Cell Model 192 Cell	Bio-Rad
LED Diode Array 3x3 (λ=415 nm)	Paul-Ehrlich-Institut
Light Cycler 480 System	Roche Applied Science
Live-7 confocal microscope	Carl Zeiss Microscopy
MACS Chill Rack	Miltenyi Biotec
MACS multistand	Miltenyi Biotec
MidiMACS Magnet	Miltenyi Biotec
MidiMACS Separator	Miltenyi Biotec
Mini centrifuge Sprout	Biozym Scientific GmbH
Nalgene Mr. Frosty freezing container	Thermo Fisher Scientific
Neubauer counting chamber improved, depth 0.02 mm	VWR

Device	Manufacturer
Neubauer counting chamber improved, depth 0.1mm	VWR
pH meter PB -11	Sartorius
Pipette controller (accu-jet® pro)	BRAND
Pipette Research Plus 1-channel (1-10 µl, 10-100 µl, 20-200 µl, 100-1000 µl)	Eppendorf
Pipette Research Plus 8-channel/12-channel (1-100µl)	Eppendorf
Pipette Transferpette S 8-channel (10-100 µl, 20-200 µl, 30-300 µl)	BRAND
PowerPac HC power supply	Bio-Rad
PrimoStar-1 wide field microscope	Carl Zeiss Microscopy
Spectrophotometer NanoDrop 2000c	Thermo Fisher Scientific
TCS SP8 confocal fluorescence microscope	Leica Microsystems
Thermal cycler S-1000	Bio-Rad
Thermomixer comfort with thermoblock	Eppendorf
UV-Torchlight 15F	Trotec

5.1.2 Consumables

Consumables	Manufacturer
CASY cups	OLS OMNI Life Science
CASY tubes	OLS OMNI Life Science
Cell culture flasks with filter (T25 = 25cm2 and T75 = 75cm2)	Sarstedt
Cell culture plates (6 well F-bottom, 12 well F-bottom, 24 well F-bottom, 48 well F-bottom, 96 well F/U/ V-bottom)	Sarstedt
Cell scraper (S, M)	Sarstedt
Centrifuge tubes (1.5 ml, 2.0 ml)	Eppendorf, Hamburg, GER
Centrifuge tubes PCR Tube Multiply® Pro (0.5 mL)	Sarstedt
Chamber µ-slides (8-well, 12-well with removable gasket)	Ibidi

Consumables	Manufacturer
Conical tubes, 15ml, 50ml	Greiner Bio-One
Cover slip (#1.5)	Thermo Fisher Scientific
Cryos Freezing Tube, 2 ml, round bottom	Greiner Bio-One
Electroporation cuvettes (2 mm)	VWR
FACS micronic tubes, 1.4 ml, U-bottom	Micronic
FACS tube, 5 ml	BD labware
Falcons (15 mL, 50 ml)	BD labware Europe, Le Pont de Claix, FRA
Light Cycler 96-well-plates white	Roche Applied Science
MACS column, LS	Miltenyi Biotec
Microcentrifuge tubes (1.5ml, 2ml)	Eppendorf
Millipore Express® PLUS Membrane Filters, polyether sulfone, 0.22 µm; 0.45 µm	Merck Millipore
Nunc™ cell culture plates with UpCell™ surface (12 well F-bottom, 24 well F-bottom, 48 well F-bottom)	Thermo Fisher Scientific
Pipette tips (0.5-10 µl; 2-200 µl; 50-1000 µl)	Biozym Scientific, Hessisch Oldendorf, GER
Pipettes (Research plus: 0.5-10 µl; 10-100 µl, 20-200 µl, 100-1000 µl)	Eppendorf
Serological pipettes, sterile (2.5 ml; 5 ml; 10 ml; 25 ml)	Greiner Bio-One
Stericup™ Quick Release-GP Sterile Vacuum Bottle Top Filtration Systems	Merck Millipore
Sterile filter (0.22 µm, 0.45 µm)	VWR

5.1.3 Reagents

Reagents	Manufacturer
(L)-glutamine	Biochrom
660-YVAD-FMK	Abcam
Acetic acid (CH3COOH)	Roth
Agarose LE	Biozym Scientific

Reagents	Manufacturer
AlexaFluor 405-SE	Thermo Fisher Scientific
Ammonium chloride (NH4Cl)	Merck
Aqua bidest. (ddH2O)	Paul-Ehrlich-Institut
Blasticidin	InvivoGen
Bovine Serum Albumin (BSA)	AppliChem
Calcium acetate (Ca(OAc)2)	Sigma-Aldrich
Carboxyfluorescein-SE	Thermo Fisher Scientific
CD14 MicroBeads	Miltenyi Biotec
CellTracker CMFDA	Thermo Fisher Scientific
CellTracker Deep Red	Thermo Fisher Scientific
Disodium phosphate (Na2HPO4)	Merck, Darmstadt
Ethanol (EtOH, 96%)	Paul-Ehrlich-Institut
Ethylenediaminetetraacetic acid (EDTA)	Paul-Ehrlich-Institut
Fetal Calf Serum (FCS)	Sigma-Aldrich
Formaldehyde (FA) 4%	Cell Signalling
Glutaraldehyde (GA)	Sigma-Aldrich
Glycine	Sigma-Aldrich
HEPES (4-(2-hydroxyethyl)-1-piperazineethanesulfonic acid	Merck
High-purity water	Sigma-Aldrich
Histopaque 1.077 g/ml	Sigma-Aldrich
Human AB serum	DRK Blutspendedienst Hessen/ Baden-Württembergs
Hydrochloric acid (HCl)	Roth
Hygromycin	InvivoGen
Immersion oil	Leica Microsystems
Latex beads red (2 µm diameter)	Invitrogen
LEUKINE® (sargramostim) Granulocyte-Macrophage Colony-Stimulating Factor (GM-CSF)	Sanofi

Reagents	Manufacturer
LPS, E. coli O111:B4	Sigma-Aldrich
Magnesium acetate (Mg(OAc)2)	Sigma-Aldrich
Magnesium chloride (MgCl2)	Merck
Methanol (MeOH)	Paul-Ehrlich-Institut
Mowiol 4-88	Sigma-Aldrich
Nigericin	Biomol
NucView® 405	Biotium
Paraformaldehyde (PFA) 4% (w/v)	Sigma-Aldrich
Penicillin/ Streptomycin solution	Biochrom
Poly-L-lysine	Sigma-Aldrich
Poly-L-ornithine	Sigma-Aldrich
Potassium chloride (KCl)	Sigma-Aldrich
Potassium dihydrogen phosphate (KH2PO4)	Merck
Puromycin	InvivoGen
Rabbit blood, defibrinated	Elocin-Lab/ Paul-Ehrlich-Institut
Recombinant Human Macrophage Colony-Stimulating Factor (M-CSF)	R&D Systems
rhIFN-γ	Sigma-Aldrich
rhIL-10	PeproTech
rhIL-3	PeproTech
rhIL-4	Invitrogen
Sodium chloride (NaCl)	Sigma-Aldrich
Sodium hydroxide (NaOH)	Merck
Staurosporin	AdipoGen
Sucrose	Sigma-Aldrich
SytoxBlue	Thermo Fisher Scientific
TMB (Tetramethylbenzidine) solution (ELISA substrate solution)	Biozym Scientific

Reagents	Manufacturer
Tris	Paul-Ehrlich-Institut
Triton X-100	Sigma-Aldrich
Ultracomp eBeads™ Plus Compensation Beads	Invitrogen
ViaFluor® 405-SE	Biotium
Z-DEVD-FMK	Santa Cruz Biotechnology
Zombie Aqua™, Yellow™, NIR™ viability dye	Biolegend
Z-VAD-FMK	Santa Cruz Biotechnology
β-Estradiol	Sigma-Aldrich
β-Mercaptoethanol	Sigma-Aldrich

5.1.4 Media

Media	Components
Alexander's Amastigote medium (AAM) pH 5.5 by hydrochloric acid sterile filtered	RPMI-1640 medium 10% FCS (v/v) 4 mM L-glutamine 100 U/mL penicillin 100 µg/mL streptomycin
BLaER1 medium (BM)	RPMI 1640 10% (v/v) FCS 2 mM L-glutamine 100 U/mL penicillin 100 µg/mL streptomycin 10 mM HEPES buffer
Complete medium (CM)	RPMI-1640 medium 10% FCS (v/v) 10.0 mM HEPES-Buffer 2.0 mM L-glutamine 100.0 U/ml penicillin 100.0 µg/ml streptomycin 50.0 µM β-mercaptoethanol

Media	Components
LB medium Prepared by media kitchen (Paul-Ehrlich-Institut)	2. 5% LB bouillon (Miller) ddH_2O
LB_{AMP} agar plates Prepared by media kitchen (Paul-Ehrlich-Institut)	3.7% LB agar 100 µg/mL ampicillin ddH_2O
Leishmania medium (LM)	RPMI-1640 medium 5% FCS (v/v) 10.0 mM HEPES-Buffer 2 mM L-glutamine 100.0 U/ml penicillin 100.0 µg/ml streptomycin 50.0 µM β-mercaptoethanol
Liquid *Leishmania* medium (LLM)	M199 medium 20% FCS (v/v) 20 mM HEPES buffer 100 µM adenine 0.05% hemin (w/v) 0.041% biotin (w/v) 100 U/mL penicillin 100 µg/mL streptomycin
Novy-Nicolle-McNeal agar	16% rabbit blood defibrinated 16% PBS 3.4% brain heart infusion agar 66.2 U/mL penicillin 66.2 µg/mL streptomycin
SOC medium pH 7.0	20 µg/ml Bacto Tryptone 5 µg/ml Bacto Yeast extract 0.5 µg/ml NaCl 2.5 µl/ml 1 M KCl 10 µl/ml 1 M MgCl2 20 mM D-glucose
Medium 199 (M199) Sigma-Aldrich	According to manufacturer

Media	Components
Roswell Park Memorial Institute (RPMI) 1640 Biowest/ Sigma-Aldrich	According to manufacturer

5.1.5 Buffer solutions

Buffer/ solution	Composition
Ammonium chloride solution Prepared by media kitchen (Paul-Ehrlich-Institut)	ddH_2O 150.0 mM NH_4Cl
ELISA wash buffer pH 7.4	PBS 0.05% Tween 20
IF blocking buffer pH 7.1	PBS 10% FCS (v/v) 10% human AB Serum (v/v)
IF permeabilization buffer pH 7.1	PBS 1% FCS (v/v) 1% human AB Serum (v/v) 0.5% Triton X-100
IF washing/ staining buffer pH 7.1	PBS 1% FCS (v/v) 1% human AB Serum (v/v)
MACS buffer pH 7.1 Prepared by media kitchen (Paul-Ehrlich-Institut)	PBS pH 0.5% BSA (w/v) 0.5 mM EDTA
Mowiol mounting solution pH 8.5	ddH_2O 25% Glycerin 10% Mowiol 4-88 100 mM Tris
Phosphate-buffered saline (PBS) pH 7.1/ pH 7.4 w/o Mg^{2+} and Ca^{2+} Prepared by media kitchen (Paul-Ehrlich-Institut)	ddH_2O 140.0 mM NaCl 6.5 mM Na_2HPO_4 2.7 mM KCl 1.5 mM $KH_2PO_4 \cdot 2H_2O$

Buffer/ solution	Composition
Reagent diluent pH 7.1	PBS 1% BSA
Tris-Acetat-EDTA (TAE) buffer 10x	ddH_2O 400.0 mM Tris 1.1% acetic acid (v/v) 10.0 mM EDTA
Wash buffer (WB) pH 7.1	PBS 10% macrophage complete medium (v/v)
Zimmermann buffer pH 7.0	132.0 mM NaCl 8.0 mM KCl 8.0 mM Na_2HPO_4 1.5 mM KH_2PO_4 0.5 mM $Mg(OAc)_2$ 90 µM $Ca(OAc)_2$
NEB buffer r3.1 (10x) New England Biolabs	According to manufacturer
FACS Flow Prepared by media kitchen (Paul-Ehrlich-Institut)	PBS 0.1 % (v/v) sodium azide
FACS Clean BD Biosciences	According to manufacturer
FACS Rinse BD Biosciences	According to manufacturer
CASYton OLS OMNI Life Science	According to manufacturer
DNA loading buffer (10x) New England Biolabs	According to manufacturer
Trypsin Prepared by media kitchen (Paul-Ehrlich-Institut)	PBS, pH 7.1 1 % (v/v) EDTA 0.05 % (w/v) trypsin
Buffer RLT Plus Qiagen	According to manufacturer

5.1.6 Ready to use kits

Kit	Manufacturer
CyQUANT™ LDH Cytotoxicity-Assay	Invitrogen
DNeasy™ extraction Kit blood and tissue	Qiagen
human IL-1β ELISA MAX deluxe	Biolegend
ImProm-II™ Reverse Transcription System	Promega
QIAprep Spin Miniprep Kit	Qiagen
RNeasy extraction Kit	Qiagen
Takyon™ No ROX SYBR 2X MasterMix blue dTTP	Eurogentec
TaqMan™ Fast Advanced Master Mix for qPCR, no UNG	Fisher Scientific

5.1.7 Enzymes

Kit	Manufacturer
SwaI	New England Biolabs
PWO Master Mix	Roche Applied Science
TaqMan Advanced Mix	Thermo Fisher Scientific

5.1.8 Antibodies

Specificity	Species reactivity	Host species	Clone	Conjugate	Manufacturer
α-CD11b	Human	Mouse	ICRF44	PE/Cy7	Biolegend
α-CD14	Human	Mouse	63D3	APC/Cy7	Biolegend
α-CD16	Human	Mouse	3G8	BV421	Biolegend
α-CD19	Human	mouse	SJ25C1	PerCP-Cy5.5	Biolegend
α-CD86	Human	Mouse	2331 (FUN-1)	FITC	Biolegend
α-CD163	Human	Mouse	GHI/ 61	BV605	Biolegend
α-CD206	Human	Mouse	15_2	BV711	Biolegend
α-MerTK	Human	Mouse	590H11G1E3	AF647	Biolegend

Specificity	Species reactivity	Host species	Clone	Conjugate	Manufacturer
α-*Lm* polyclonal IgG Serum	*Lm*	Rabbit	polyclonal	-	Kindly provided by Uwe Ritter, Regensburg
α-IgG	Rabbit	Chicken	polyclonal	AF647	Thermo Fisher Scientific

5.1.9 Plasmids

Name	Origin
pLEXSY-mKikume-hyg2.0 [129]	kindly provided by Prof. Andreas J. Müller
pTPuro [155]	kindly provided by Tom Beneke
pTBlast [155]	kindly provided by Tom Beneke

5.1.10 Oligonucleotides

Primers used for *Leishmania* gene knock out employing the CRISPR/Cas9 system were ordered according to sequences provided by the LeishGEdit tool [155]. All primers were purchased from Eurofins MWG Operon, except for TaqMan probes, which were ordered from Thermo Fisher Scientific by the respective Assay ID.

Name	Sequence/ Assay ID	Used for
IL12A	Hs01073447_m1	qPCR with TaqMan Probe
ARG1	Hs00163660_m1	qPCR with TaqMan Probe
NOS2	Hs01075529_m1	qPCR with TaqMan Probe
Hyg_fwd	ACTCGTCCGAGGGCAAAGGA	Confirmation PCR
3'SSU_rev	CAGTGTGGACTACAATGGTC	Confirmation PCR
5'SSU_fwd	CATTCCGTGCGAAAGCCGG	Confirmation PCR
Blast_fwd	GCCGCATCTTCACTGGTGTCAA	Confirmation PCR
Centrin4_CDS_fwd	GGATGAGCAGATTCGCGAGG	Confirmation PCR
Centrin4_CDS_rev	GCAGCATCACGCTCTTGAAC	Confirmation PCR
Centrin4_UTR_rev	GGGCAGGTAAAGCGACAAGG	Confirmation PCR
HPRT1	Hs02800695_m1	qPCR with TaqMan Probe
HPRT1_ fwd	CCT GGC GTC GTG ATT AGT GA	qPCR with SYBR green

Name	Sequence/ Assay ID	Used for
HPRT1_ rev	CGA GCA AGA CGT TCA GTC CT	qPCR with SYBR green
IDO1_fwd	GCCTGATCTCATAGAGTCTGGC	qPCR with SYBR green
IDO1_rev	TGCATCCCAGAACTAGACGTGC	qPCR with SYBR green
TGFβ	Hs00998133_m1	qPCR with TaqMan Probe
KYNU_fwd	GTTGGCTTTGATCTAGCACATGC	qPCR with SYBR green
KYNU_rev	TGAAGGCACCAGCAATTCCTCC	qPCR with SYBR green
mKikumeUTR_rev	CCGAGAAGGCGACGTGAAAGG	Confirmation PCR
Puro_fwd	TATCCGCGGCTTCACAACGCTTG	Confirmation PCR
Scaffold DNA	AAAAGCACCGACTCGGTGCCACTT TTTCAAGTTGATAACGGACTAGCCT TATTTTAACTTGCTATTTCTAGCTCT AAAAC	CRISPR/Cas9 based gene knock-out

5.1.11 *Leishmania* strains

***Leishmania major* isolate MHOM/IL/81/FEBNI:**

Originally isolated from a skin biopsy of an Israeli patient and kindly provided by Dr. Frank Ebert (Bernhard Nocht Institute for Tropical Medicine, Hamburg, Germany)

***Leishmania major* isolate MHOM/IL/81/FEBNI^{DsRed}**

Parasite strain with stable expression of genes encoding the protein DsRed and the selective marker Hygromycin generated in our group.

***Leishmania major* isolate MHOM/IL/81/FEBNI^{eGFP}**

Parasite strain with stable expression of genes encoding the protein eGFP and the selective marker Hygromycin generated in our group.

***Leishmania major* isolate MHOM/IL/81/FEBNI^{mKikume}**

Parasite strain with stable expression of genes encoding the protein mKikume and the selective marker Hygromycin. The strain was generated by me using the plasmid pLEXSY-mKikume-hyg2.0 kindly provided by Prof. Andreas J. Müller (Otto-von-Guericke-Universität, Magdeburg, Germany) [129].

***Leishmania major* isolate LRC-L137^{mKikume}**

Parasite strain with stable expression of genes encoding the protein mKikume and the selective marker Hygromycin kindly provided by Prof. Andreas J. Müller (Otto-von-Guericke-Universität, Magdeburg, Germany) [129].

***Leishmania major* isolate MHOM/IL/81/FEBNI$^{Cas9/T7}$**

Parasite strain with stable expression of genes encoding Cas9 endonuclease and T7 RNA polymerase and the selective marker Hygromycin. The strain was generated and kindly provided by Celia López Gutiérrez (Laboratory of Antonio Jiménez Ruiz in Alcalá de Henares, Spain)

5.1.12 Bacteria strains

***E. coli* TOP10 F' cells**

Chemically competent *E. coli* strain for transformation with plasmids.

5.1.13 BLaER1 cell lines

BLaER1

BLaER1 cell line without expression of a fluorescence marker. The strain kindly provided by Holger Heine (Research Center Borstel)

BLaER1^{eGFP}

BlaER1 cell line with constitutive expression of the fluorescence marker eGFP. The strain kindly provided by Holger Heine (Research Center Borstel)

BLaER1$^{eGFP\ x\ GSDMD\ -/-}$

BlaER1 cell line with ablation of the gene coding for pore forming protein GSDMD with constitutive expression of the fluorescence marker eGFP. The strain kindly provided by Holger Heine (Research Center Borstel)

BLaER1$^{GSDMD-/-}$

BlaER1 cell line with ablation of the gene coding for pore forming protein GSDMD. Generated by Kerren Volkmar in our group.

5.1.14 Software

Software	Manufacturer
Citavi v6.12.0.0	Swiss Academic Software
FACSDiva v9.0.1	BD Biosciences
FlowJo v10.7.1	BD Biosciences
Fiji	[156]
Image Lab v6.0.1.34	Bio-Rad
Inkscape v1.2.0	The Inkscape Project
LabImage1D	Intas

Software	Manufacturer
LAS X v3.5.19976.5	Leica Microsystems
Mars v4.01 R2	BMG Labtech
Office package v2016 and v2019	Microsoft
Prism v9.2.0.332	GraphPad Software Inc.
SnapGene v6.0	GSL Biotech LLC
ZEN (black edition) 3.1	Carl Zeiss Microscopy

5.2 Methods

5.2.1 General remarks

All methods handling living cells were performed in sterile conditions and under a laminar flow hood graded with biosafety level 2. BLaER1 cells and hMDM were cultured at 37°C, 5% CO_2, *Lm* promastigotes were cultured at 27°C, 5% CO_2 and axenic amastigotes were cultured at 33°C, 5% CO_2. If not stated otherwise, hMDM and PBMCs were centrifuged at 200 *g*, 8 minutes (min), BLaER1 cells at 100 *g*, 10 min, *Lm* promastigotes and axenic amastigotes at 2400 *g*, 8 min, each at room temperature.

5.2.2 Primary human cell culture and treatment

5.2.2.1 Isolation of peripheral blood mononuclear cells (PBMCs) and CD14$^+$ monocyte magnetic-activated cell sorting (MACS)

PBMCs were isolated from blood concentrates (30-50 ml) from anonymized human donors (DRK Blutspendedienst Hessen/ Baden-Württemberg). The blood concentrate was replenished with PBS to a final volume of 100 ml and layered on prewarmed leukocyte separation medium 1077 (1.077 g/ml) in falcon tubes. Erythrocytes were separated from peripheral blood mononuclear cells by centrifugation at 573 *g* for 30 min. PBMCs precipitated on the separation medium were harvested, cell debris was removed by centrifugating and resuspending twice in wash buffer (WB). Remaining erythrocytes were lysed by incubating the cells for 10 min in 10 ml cold 0.15 M ammonium chloride solution. The solution was diluted in WB, the cells were pelleted again, resuspended in MACS buffer and the cells were counted (5.2.2.2).

To isolate CD14$^+$ monocytes, pelleted cells were resuspended in 95 µl MACS and 5 µl CD14 MicroBeads per $10*10^6$ cells and incubated for 20 min at 4°C. The cells were washed and loaded in a volume of 3 ml MACS buffer onto a LS column installed in a MidiMACS Separator.

The columns were washed three times with MACS buffer, before the positively selected cells were eluted and differentiated to human monocyte derived macrophages (hMDM) (5.2.2.3).

5.2.2.2 Automated cell counting

PBMCs and hMDM were counted using the CASY automatic cell counter. 10 µl of a cell suspension were diluted in 10 ml CASYton buffer and subjected to a light scatter-based measurement in a 150 µm capillary. The measurement yielded the cell viability, cell count per ml and aggregation factor, which were documented for each donor. Cells with a viability below 50% were not used for further experiments.

5.2.2.3 Macrophage differentiation and activation

The eluted $CD14^+$ PBMCs were counted (5.2.2.2) and seeded to T75 flask with 20-25*10^6 monocytes per flask in 15 ml in complete medium (CM). The cell culture was supplemented by either 50 ng/ ml M-CSF or 30 ng/ ml GM.CSF for 5-7 days. The differentiated cells were detached from the tissue culture flasks by incubating 30 min on ice and scraping. The cells were pelleted once and resuspended in fresh CM, counted (5.2.2.2), and their concentration was adjusted to 1*10^6 cells/ ml. These non-activated macrophages M(-) were then seeded to tissue culture dishes for further experiments. To activate the macrophages, they were supplemented after seeding by either 50 ng/ml IFN-γ, 20 ng/ml IL-4, 10 ng/ml IL-10 or, as a control, 10 ng/ml M-CSF for 24 h.

5.2.2.4 Inhibitor treatment of macrophages

Caspase inhibition – For caspase inhibition in uninfected cells, M-CSF derived M(-) were seeded to 24-well UpCell plates with 0.5*10^6 cells per well and incubated for 1 h. The M(-) were then treated with a final concentration of 20 µM or 50 µM Z-DEVD-FMK (Z-DEVD) or Z-VAD-FMK (Z-VAD) solved in DMSO. As controls, an untreated sample, a sample treated by 1 µM Staurosporine and samples treated by 0.2 % or 0.5 % volume percent DMSO. Samples were incubated for 20 h, harvested from UpCell plates according to manufacturer's protocol, and were subjected to staining by Apotracker green (5.2.7.2) and SytoxBlue (5.2.7.1) prior to flow cytometry analysis (5.2.10.2).

For the co-incubation experiments under caspase inhibition, the respective inhibitor was added in concentration of 20 µM or 50 µM to the primary infected cells, 1 h before the uninfected batch of cells was added for co-incubation (5.2.6.3).

IDO1 inhibition – The inhibition of IDO1 by 1-MT was performed using a final concentration 200 µM per application in a series for up to three applications. To analyze the parasite burden of infecting amastigotes, M(IFNγ) were seeded to a 24-well plate with 0.5*10^6 cells per well and infected by Lm^{DsRed} axenic amastigotes (5.2.6.1). In distinct samples, 1-MT was applied as follows:

- 1x, 2 h pre infection for one sample analyzed 3 h pI,
- 1x, 22 h pI for one sample analyzed 44 h pI,
- 2x, 3 h pI and 22 h pI for one sample analyzed 44 h pI,
- 3x, 2 h pre infection, 3 h pI and 22 h pI for one sample analyzed 44 h pI.

For each sample, a respective control was included, where cells were treated with the same volume percent of 0.1N NaOH which was used as solvent for 1-MT. Samples were harvested, stained by SytoxBlue (5.2.7.1) and analyzed by flow cytometry (5.2.11). For the inhibition by 1-MT during co-incubation experiments, 1-MT was applied accordingly, also including controls treated with NaOH (5.2.6.3).

5.2.3 Parasite cell culture and treatment

5.2.3.1 *Lm* promastigote cell culture

Lm promastigotes were cultivated in a 96-well flat bottom plate in a biphasic Novy-McNeal-Nicolle medium [145]. The solid phase was prepared by 50 µl rabbit blood agar, covered by 100µl the liquid phase of parasites in *Leishmania* medium (LM). *Lm* parasites were passaged to fresh blood agar plates after 7-10 days of culture and to maximum of eight passages. Therefore, parasites from the previous passage were pooled from three wells and counted with a Neubauer improved counting chamber with a depth of 0.02 mm. The concentration was adjusted to $1*10^6$ viable and dead parasites *Lm* promastigotes/ ml in LM, supplemented by a selective antibiotic in dependence of the strain (5.1.11) and re-seeded to a fresh blood agar plate. Cultured *Lm* isolate MHOM/IL/81/FEBNI promastigotes show a logarithmic growth phase at day 3-4 and a stationary growth phase at day 6-8.

5.2.3.2 Generation of axenic *Lm* amastigotes

Lm promastigotes from the logarithmic growth phase were pooled from 16 wells and transferred to 20 ml *Leishmania* liquid medium (LLM) in aT75 flask and supplemented by 2 ml fetal calf serum (FCS) for incubation over three days. Then, promastigotes were washed twice with Alexander's amastigote medium (AAM) and resuspended in AAM. The concentration was adjusted to $20*10^6$ viable promastigotes/ ml and seeded to 24-well with 1 ml parasite culture per well [144]. The parasites transformed from pro- to amastigotes within10-14 days of cultivation and were used in subsequent experiments.

5.2.3.3 Generation of KBMA parasites

For the generation of KBMA axenic amastigotes, viable parasites were harvested and transferred to a falcon tube, pelleted and resuspended in LM with 20*106 parasites/ml (5.2.3.2). Conditioned AAM from the axenic culture was saved sterile filtered and stored until further use. amotosalen was added to a final concentration of 1 µM, 2 µM or 3 µM and the culture was incubated 30 min at 33°C. Amastigotes were washed once in LM, pelleted again and resuspended in conditioned and sterile filtered AAM with $10*10^6$ parasites/ml. Amastigote

suspension was transferred to 24-well plate with 1 ml per well and each well was illuminated for 40 sec by UV-A light using a UV-Torchlight 15F (Trotec) from a distance of 25 cm above the well and a radiation of 30 mm. For parasite counting and proliferation analysis of the *in vitro* culture, AMT- and UV-treated amastigotes were seeded to a 96-well plate with 200 µl per well. For infection experiments, treated parasites were washed in CM once and used for infection (5.2.6.1).

5.2.4 BLaER1 cell culture and treatment

5.2.4.1 BLaER1 cell culture

BLaER1 cells were cultured in suspension using T75 culture flasks with 20 ml BLaER1 medium (BM). The cells were passaged twice a week by harvesting the total culture and determining the viable cell concentration by loading 10 µl of cell suspension in a 1:9 trypan blue dilution onto a Neubauer counting chamber with a diameter of 0.1 mm. The cells were then pelleted and resuspended in fresh BM with $10*10^6$ cells/ml. $0.1\text{-}0.5*10^6$ cells/ ml were re-seeded into a new T75 flask and further incubated.

5.2.4.2 Culture dish coating for BLaER1 cell culture

To improve the adherence of BLaER1 cells during trans-differentiation, 96- or 24- culture plates were coated by poly-L-ornithine, by incubating each well with 50 µl (96-well plate) or 200 µl (24-well plate) of 0.05 mg/ ml poly-L-ornithine solution for 2 h at 37°C, prior to washing three times with ddH_2O.

For seeding of BLaER1 cells after trans-differentiation, 96-well culture plates and 8-well chamber slides were coated with poly-L-lysine by incubating each well with 50 µl (96-well plate) or 150 µl (8-well chamber slide) of 0.05 mg/ml poly-L-lysine solution for 1 h at room temperature, prior to washing three times with PBS.

5.2.4.3 BLaER1 cell trans-differentiation

BLaER1 cells were trans-differentiated in uncoated 6-well culture plates or poly-L-ornithine coated 24-well and 96-well culture plates in BM conditioned with, 10 ng/ml M CSF, 10 ng/ml rhIL-3 and 200 nM β-estradiol (tdBM).

In 6-well plates, $0.33*10^6$ cells/ml were seeded with a total volume of 3 ml per well, half of the culture medium was replaced each 2-3 days by fresh tdBM. The completely trans-differentiated cells were harvested after 7 days by resuspension in fresh BM with a pipette, counted (5.2.4.1), and seeded to a poly-L-lysine coated culture plate in the desired concentration for further experiments in tdBM.

In coated 24-well and 96-well plates $0.5*10^6$ cells/ml were seeded with a total volume of 0.5 ml or 0.1 ml per well, respectively. Half of the culture medium was replaced each 2-3 days by fresh tdBM. BLaER1 cells were completely transdifferentiated after 7 days. Three wells were

harvested, pooled and counted (5.2.4.1) to derive the cell concentration per well. The medium of the adherent cells in the remaining wells was replaced by fresh tdBM and used in subsequent experiments.

5.2.4.4 Canonical inflammasome activation and pyroptosis induction in BLaER1 cells

In general, inflammasome and pyroptosis induction was achieved by addition of LPS in a final concentration of 200 ng/ml for 3 h 45 min and with or without subsequent treatment by 4 µM nigericin.

To measure the susceptibility to inflammasome and pyroptosis activation of uninfected BLaER1 and BLaER1$^{GSDMD-/-}$, cells were transdifferentiated on 96-well plates (5.2.4.3) and stimulated as described. For analysis of the viability and PtdSer presentation, cells were harvested by trypsinization with 0.05% trypsin–EDTA at the respective time-points and stained by SytoxBlue (5.2.7.1) and Annexin V (5.2.7.2) prior to analysis by flow-cytometry (5.2.11). Supernatants of the same culture were used for subsequent analysis of IL-1β release by ELISA (5.2.9.2).

5.2.5 Microbiology, parasitology and molecular biology methods

5.2.5.1 Transformation and plasmid isolation

An aliquot of 50 µl chemically competent *E. coli* TOP10 Prime cells were thawed on ice. 5 ng of pLEXSY-mKikume-hyg2.0 (5.1.9) plasmid DNA were added to the bacteria and incubated for 20 min on ice. Heat shock was applied for 60 sec at 42°C with subsequent incubation on ice for 2 min. *E. coli* were resuspended in 950 µl SOC media and 20 µl of the suspension were plated on LB_{AMP} agar plates with subsequent incubation overnight at 37 C. A single clone was picked with a sterile pipette tip and transferred to 5 ml LB media supplemented by 100 µg/ml ampicillin in a culture tube. The bacteria culture was grown overnight at 37°C, shaking with 300 rpm. The culture was harvested by pelleting the bacteria at 5000 *g* for 10 min, followed by cell lysis plasmid preparation using the QIAprep Spin Miniprep Kit according to the manufacturers protocol. The concentration of resulting plasmid DNA was measured by spectral photometer NanoDrop 2000c and stored at 4°C until further use.

5.2.5.2 Gene integration by homologous recombination

The mKikume gene and the adjacent resistance marker for hygromycin, both encoded on the pLEXSY-mKikume-hyg2.0, were stably integrated into the 18S rRNA (SSU) locus of *Lm* by homologous recombination. To this end, 15 µg pLEXSY-mKikume-hyg2.0 (5.1.9) were linearized using SwaI for 3 h at 37 °C. Subsequently, the restriction enzyme was heat-inactivated at 80 °C for 20 min and success of the restriction digest was confirmed by gel-electrophoresis of a reaction aliquot (5.2.5.10) (data not shown). The remaining linearized plasmid was sterilized for 5 min at 95°C and used for nucleofection (Lonza Nucleofector 2b) of

Lm (5.2.5.4) and subsequent selection by antibiotic resistance and limiting dilution to receive a single cell clone (5.2.5.5).

5.2.5.3 CRISPR-Cas9 based gene knockout in *Lm*

For CRISPR-Cas9-mediated gene knockout using $Lm^{Cas9/T7}$, parasites were transfected by linear DNA fragments. Two DNA fragments (5' and 3' sgRNA templates) are *in vivo transcribed in*to a guide RNA sequences complementary to the 5' and 3' end of the target gene, respectively, determining the Cas9 cleavage sites. A donor DNA containing a resistance marker and 5' and 3' UTR regions of the target gene replace the Cas9-cleaved target gene by homologous recombination [155].

The sgRNA templates for *LmjF22.14.10 (centrin)* were generated in in two separate PCR reactions by polymerase chain reaction (PCR), coding for the 3' and the 5' end of the gene of interest (GOI) and including a primer for the *in vivo* translation by T7RNA polymerase. Each reaction contained either the 5´-forward or the 3´-reverse primer and the scaffold DNA, serving as the complementary primer (Table 1) in the shown PCR program (Table 2). The DNA fragments were analyzed by gel-electrophoresis after the PCR reaction (5.2.5.10).

Table 1: PCR mix for the sgRNA template.

Component	Initial concentration	Volume
Scaffold DNA	10.0 µM	4.0 µl
sgRNA_primer_5' sgRNA_primer_3'	20.0 µM	4.0 µl
H_2O (nuclease free)	-	0.65
PWO Master	-	10 µl
Total	-	18.65 µl

Table 2: PCR program for the sgRNA-template.

Step	Temperature	Time	
Initial denaturation	98°C	30 s	
Denaturation	98°C	10 s	
Annealing	60°C	30 s	35 cycles
Elongation	72°C	15 s	
Storing	4°C	continuous	

In a third PCR reaction, a linear DNA fragment was produced, encoding a selective marker and a homologous region (HR) to the untranslated regions (UTRs) flanking *Centrin4* in *Lm.* The selective marker was amplified from the plasmids *pTPuro* or *pTBlast* (5.1.9) using primers introducing the 5' and 3' HR (Table 3) in the shown PCR program (Table 4). 2 µl of the resulting PCR products were analyzed by gel-electrophoresis (5.2.5.10) and the remaining DNA was sterilized for 5 min at 95°C prior to electroporation and subsequent selection by antibiotic resistance and limiting dilution to receive a single cell clone (5.2.5.5).

Table 3: Reaction mix composition for the HR-PCR reaction.

Component	Initial concentration	Volume
pTPuro/ pTBlast	10.0 µM	2.0 µl
HR_primer_fwd	20.0 µM	2.0 µl
HR_primer_rev	20.0 µM	2.0 µl
DMSO	3%	0.6 µl
MgCl2	1.375 mM	2.75 µl
H_2O (nuclease free)	-	0.65
PWO Master	-	10 µl
Total	-	20 µl

Table 4: Program for the HR-PCR reaction.

Step	Temperature	Time	
Initial denaturation	94°C	5 min	
Denaturation	94°C	30 s	
Annealing	65°C	30 s	40 cycles
Elongation	72°C	2 min 15 sec	
Final Elongation	72°C	7 min	
Storing	4°C	continuous	

5.2.5.4 Nucleofection of *Lm* promastigotes

For the nucleofection of $Lm^{T7/Cas9}$ or *Lm* wildtype *Lm*, $60*10^6$ promastigotes were taken from the logarithmic phase, washed once in Zimmermann buffer and resuspended in 200 µl Zimmermann buffer. The parasite solution was the transferred to an electroporation cuvette for the transfection of linearized DNA fragments. For the gene knockout using $Lm^{T7/Cas9}$, 7.5µl of both the 3' and 5' sgRNA templates and HR (5.2.5.3) were added to the cuvette. For the stable insertion of genes, 15µl of linearized DNA from the SwaI digestion mix were added to the

cuvette (5.2.5.2). Parasites were electroporated using the Nucleofector 2b (Lonza) and a program with three 100 µs-pulses of 1600 V, in 500 ms intervals. As mock control *Lm*$^{as9/T7}$ were transfected solely with the sgRNA templates. After transfection, promastigotes were seeded to a T25 flask with prewarmed LM and placed in the incubator.

5.2.5.5 Resistance selection and limiting dilution

The day after electroporation, the putative *Lm* mutants were supplemented with 10% FCS (v/v) and the corresponding antibiotic was added (30 µg/ml puromycin, 10 µg/ml blasticidin for *Lm*$^{LmjF22.1410-/-}$ or 30µg/ml hygromycin for *Lm*^{mKikume}) to positively select clones with a successful insertion of the resistance marker. Growth of viable parasites under the selective antibiotic was examined periodically by wide-filed microscopy. To isolate a single clone, $0.1*10^6$ viable parasites/ml were transferred to wells in the first row of a 96 well blood agar plate. With each following row, parasites were repeatedly 1:3 in LM row by row. Mathematically, the sixth dilution step contains only a single clone of the putative *Lm* mutant. The plate was incubated 7 to 10 days and populations growing in row seven or higher were subjected DNA isolation (5.2.5.6) and confirmation PCR (5.2.5.7).

5.2.5.6 DNA isolation from *Lm* parasites

4 wells of *Lm* parasites in their logarithmic growth phase were taken from a 96-well blood agar plate and expanded in 5 ml liquid *Leishmania* media (LLM) in a T25 flask for 7 days. Genomic DNA from the parasites was isolated with the Qiagen DNeasy Blood and Tissue Kit used according to the manufacturer's protocol. The concentration of the yielded DNA was determined by spectral photometer NanoDrop 2000c.

5.2.5.7 PCR-based confirmation of gene modification

Replacement of a GOI by a selection marker after a CRISPR/Cas9 based gene knockout or stable insertion of GOI was tested by PCR (Table 5) in the shown PCR program (Table 6).

Table 5: Reaction mix composition for the Confirmation PCR reaction.

Component	Initial concentration	Volume
Genomic DNA	~50 ng/µl	1.0 µl
Fwd_primer	20.0 µM	0.75 µl
Rev_primer	20.0 µM	0.75 µl
PWO Master	-	2.5 µl
Total	-	5 µl

Table 6: Program for the Confirmation PCR reaction.

Step	Temperature	Time	
Initial denaturation	94°C	5 min	
Denaturation	94°C	30 s	
Annealing	60-62°C	30 s	25 cycles
Elongation	72°C	2 min 15 sec	
Final Elongation	72°C	7 min	
Storing	4°C	continuous	

For the confirmation of the *LmjF22.1410* knockout on both alleles in $Lm^{Cas9/T7}$, four separate PCR reactions were performed (Table 7). As control, genomic DNA of *Lm* wildtype was used as a template.

Table 7: List of PCR reactions for *LmjF22.1410* knockout confirmation.

PCR reaction	Fwd_primer	Rev_primer
1	Centrin4_CDS_fwd	Centrin4_CDS_rev
2	Centrin4_CDS_fwd	Centrin4_UTR_rev
3	Blast_fwd	Centrin4_UTR_rev
4	Puro_fwd	Centrin4_UTR_rev

For the confirmation of the stable insertion of *mKikume* in *Lm*, three separate PCR reactions were performed (Table 8). As control, genomic DNA of *Lm* wildtype was used as a template.

Table 8: List of PCR reactions for *mKikume* insertion confirmation.

PCR reaction	Fwd_primer	Rev_primer
1	5'SSU_fwd	mKikume_UTR_rev
2	5'SSU_fwd	3'SSU_rev
3	Hyg_fwd	3'SSU_rev

5.2.5.8 RNA isolation and complementary DNA (cDNA) generation

For the quantitative PCR (qPCR) analysis of infected M(IFNγ), GM-CSF derived M(-) were seeded to 24-well plate with $0.5*10^6$ cells per well, stimulated by IFNγ (5.2.2.3), infected by *Lm* axenic amastigotes MOI 2 (5.2.6.1) and incubated until 24 h pI or 44 h pI. Samples of uninfected GM-CSF derived M(-) and M(IFNγ) were included as controls. For mRNA isolation, cells were washed once in cold PBS and lysed in buffer RLT Plus. RNA was isolated by RNeasy extraction Kit (Qiagen), according to the manufacturer's protocol. The resulting RNA concentration was measured by the spectral photometer NanoDrop 2000c. The RNA integrity was checked by mixing 5 µl RNA sample with 2.5 µl 2x RNA loading dye, thermal treatment with 70°C for 5 min and 4°C for 10 min with subsequent gel electrophoresis (5.2.5.10) on a 2 % agarose gel. Gels were imaged by Gel Doc XR+ and intact RNA was identified by two distinct bands for the 28S and 18S rRNA. Subsequently, cDNA was synthesized from equal amounts of mRNA using the ImProm-II™ Reverse Transcription System according to the manufacturer's protocol and was stored at -20°C until further use.

5.2.5.9 qPCR

Reactions were performed with primers listed in 5.1.10. For primers without probes, qPCR reactions were performed using the kit Takyon™ No ROX SYBR 2X MasterMix blue dTTP according to the manufacturer's protocol and with the cycler program (Table 9). As negative controls, a water sample, and a sample from cDNA synthesis without reverse transcriptase were taken along.

Table 9: LightCycler 480 program for Takyon™ No ROX SYBR 2X MasterMix blue dTTP.

Step	Temperature	Time	°C/sec
Activation	95°C	5 min	4.4
Amplification (40 Cycles) Denaturation	95°C	15 sec	4.4
Annealing and Elongation	60°C	1 min	2.2
Melting Curve	95°C	10 sec	4.4
	65°C	1 min	2.2
	95°C	continuous	0.11

For primers with Taqman probes, qPCR reactions were performed using the kit TaqMan™ Fast Advanced Master Mix for qPCR, no UNG according to the manufacturer's protocol and with the following cycler program (Table 10). As negative controls, a water sample, and a sample from cDNA synthesis without reverse transcriptase were included.

Table 10: TaqMan™ Fast Advanced Master Mix for qPCR, no UNG.

Step	Temperature	Time	°C/sec
Activation	95°C	10 min	4.4
Amplification (40 Cycles) Denaturation	95°C	15 sec	4.4
Annealing and Elongation	60°C	1 min	2.2
Melting Curve	95°C	10 sec	4.4
	65°C	1 min	2.2
	95°C	continuous	0.11

With the cycle threshold (Ct) resulting from qPCR measurement, the ΔΔCt value was calculated as a measure of the relative gene expression level by using HPRT1 as housekeeping gene for human primary macrophages in the following formula:

$$\Delta Ct = Ct_{gene\ of\ interest} - Ct_{housekeeping\ gene}$$
$$\Delta\Delta Ct = \Delta Ct_{sample} - \Delta Ct_{control} \quad (1)$$

5.2.5.10 Analytical gel-electrophoresis

Electrophoretic separation of DNA samples was performed in a TAE buffered horizontal electrophoresis system at 100 V, 400 mA for 40 min. Therefore, 2 µl DNA samples were mixed with 0.5 µl 6x DNA loading dye and loaded on a 1% agarose (w/v) gel with 0.002% ethidium bromide (v/v). DNA bands were visualized by the ChemiDoc XRS+ BioRad system with an epi-white light and trans-UV (302 nm) lamp.

5.2.6 Human cell biological methods

5.2.6.1 Infection of primary human macrophages and BLaER1 cells

Generally, cells were infected by *Lm* by adding parasites in CM to the cell culture and incubated for 3 h at 37°C, 5% CO_2. Then, the adherent cells were washed by removing CM and carefully rinsing twice with WB. The CM was replenished and, in dependence of the experiment, was supplemented by stimuli or inhibitors. This time point is referred to as 0 h post infection (pI) for all subsequent experiments. The protocol was conducted accordingly for all used *Lm* strains.

For the infection with promastigotes, parasites were harvested from the stationary growth phase (d 6-8), and viable and dead parasites were counted. The parasites were pelleted and

adjusted to 10*10^6 parasites/ml in CM, prior to their application to the cell culture with a multiplicity of infection (MOI) of 10.

For the infection with amastigotes, parasites were harvested by removing the supernatant of the amastigote culture (5.2.3.2) and resuspending the slightly attached parasites from the bottom of the culture dish in CM. Viable amastigotes were counted, pelleted and their concentration was adjusted to 10*10 promastigotes/ml in CM. They were applied with a MOI of 2 or 5, which is specified for each experiment.

5.2.6.2 Intracellular parasite proliferation measured by fluorescent reporter protein mKikume

The proliferation of *Lm* parasites can be analyzed using the fluorescent proliferation reporter protein mKikume. The fluorescence emission wavelength of this protein can be photoconverted from green to red by illumination with violet light. When parasites proliferate during the fluorescence recovery after conversion (FRAC), their red fluorescent emission is reduced by fission and new, green fluorescent protein is produced. Sample fluorescence was analyzed simultaneously by flow-cytometry in two channels, mKikume green (FITC channel) and mKikume (PE channel) and the median fluorescence intensity (MFI) was derived for each channel (MFI_{green}, MFI_{red}). The ratio of green to red fluorescence can be normalized to an unconverted control (maximum green fluorescence) and a control converted 0 h before analysis (maximum red fluorescence) yielding the proliferation index by the following formula:

$$\text{Index} = 1 - \frac{mKikume_{Sample}\left(\frac{MFI_{red}}{MFI_{green}}\right) - mKikume_{Unconverted}\left(\frac{MFI_{red}}{MFI_{green}}\right)}{mKikume_{0\ h\ converted}\left(\frac{MFI_{red}}{MFI_{green}}\right) - mKikume_{Unconverted}\left(\frac{MFI_{red}}{MFI_{green}}\right)} \qquad (2)$$

For the analysis of intracellular parasite proliferation over time, 0.4*10^6 M-CSF derived M(-) were seeded per well in a 12-well plate and separately infected with *Lm*^{mKikume} promastigotes with an MOI of 10 and amastigotes with an MOI of 5 (5.2.6.1). Four samples for each form of parasites were photoconverted 24 h (FRAC) prior to analysis at 0 h, 24 h, 48 h and 72 h pI, by illumination from below the culture plate for 60 s with a 3x3 LED diode array (λ=415 nm). For normalization by formula (2), an unconverted control and 0 h converted control of promastigote and amastigote infected cells was analyzed at 24 h pI. At the timepoints 24 h, 48 h, 72 h and 96 h pI the respective samples were harvested and transferred to microcentrifugation tubes. The harvested cells were washed once in MACS buffer, resuspended in 200 µl MACS buffer and then transferred to FACS micronic tubes for flow cytometry analysis (5.2.11).

For the proliferation analysis of intracellular parasites in M(IFN-γ), M(M-CSF), M(IL-4) and M(IL-10), the cells were infected after stimulation (5.2.6.1) by *Lm*^{mKikume} amastigotes with an

MOI of 2 (5.2.6.1). Both normalization controls were prepared separately for each stimulation and used for the calculation of the proliferation index.

High proliferating subpopulations were quantified by introducing the following equation for relative proliferation to the tool “Derived Parameter” in the FlowJo software:

$$Relative\ proliferation = 100 - 10 * \left(\frac{mKikume^{red}}{mKikume^{green}}\right) \quad (3)$$

The unconverted control and the 0 h converted control served as gating assistant to define a ranged gate for the high proliferating subpopulation within infected cell samples (Figure 11).

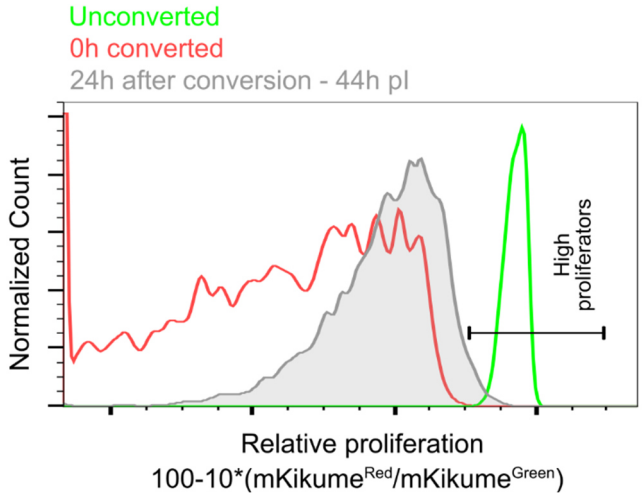

Figure 11: Relative proliferation for the gating of high proliferating parasite populations. Histogram of the relative proliferation by formula (3) of *Lm*^{mKikume}. Shown is a representation samples of M(-) infected by axenic amastigotes 24 h after conversion, 0 h after conversion and unconverted. High proliferators are gated by a ranged gate.

5.2.6.3 Co-incubation assay with primary human macrophages

The co-incubation assay was used to detect parasite transfer between primary infected cells and initially uninfected cells in a flow cytometry-based analysis. Therefore, GM-CSF and M-CSF derived macrophages of an individual donor where split. The first batch of cells was fluorescently labeled (5.2.7.4) and seeded to a 12-well culture plate with 0.4*10^6 cells per well in 500 µl CM. After gaining adherence, they were infected by *Lm*^{DsRed} promastigotes or amastigotes with an MOI of 10 or 5, respectively (5.2.6.1) and further incubated.

The second batch of macrophages (only M-CSF derived) from the same donor were re-seeded uninfected to a 6-well plate with 3*10^6 cells per well in 1 ml CM supplemented with 30 ng/ml M-CSF and incubated. Before starting the co-incubation, the uninfected cells were also labeled with a fluorophore with a distinct emission spectrum then the infected cells (5.2.7.4). The co-incubation was started 24 h or 72h pI by adding 0.4*10^6 uninfected cells to the infected cells and incubating for additional 20 h. Uninfected, co-incubated cells were included as negative

control. Cells were harvested by placing the cells on ice for 30 min with subsequent detaching by a cell scrape or by trypsinization with trypsin buffer. The cells were then washed once in MACS buffer, resuspended in 200 µl MACS buffer and transferred to FACS micronic tubes for flow cytometry analysis (5.2.11). The protocol was adapted for different experimental demands as follows:

For the co-incubation experiments including proliferation analysis with *Lm*^{mKikume} amastigotes in primary infected cells and cells infected after exit, the MOI was reduced to 2. The primary infected cells remained unlabeled or were stained by CellTracker™ Deep Red. The mKikume protein was photoconverted 20 h pI and the co-incubation was started 24 h pI for additional 20 h. Primary infected cells with unconverted and 0 h converted parasites were included for normalization to the proliferation index. Prior to the flow-cytometry analysis, cells were stained with the live/dead stain Zombie Near Infrared™ (NIR) (5.2.7.1). A sample of viable cells spiked by cells heated to 65°C for 10 min (non-viable) and an incubation on ice was included as gating control. The fluorescent labelling had no influence on the mKikume fluorescence in the red and green channel (Figure 12).

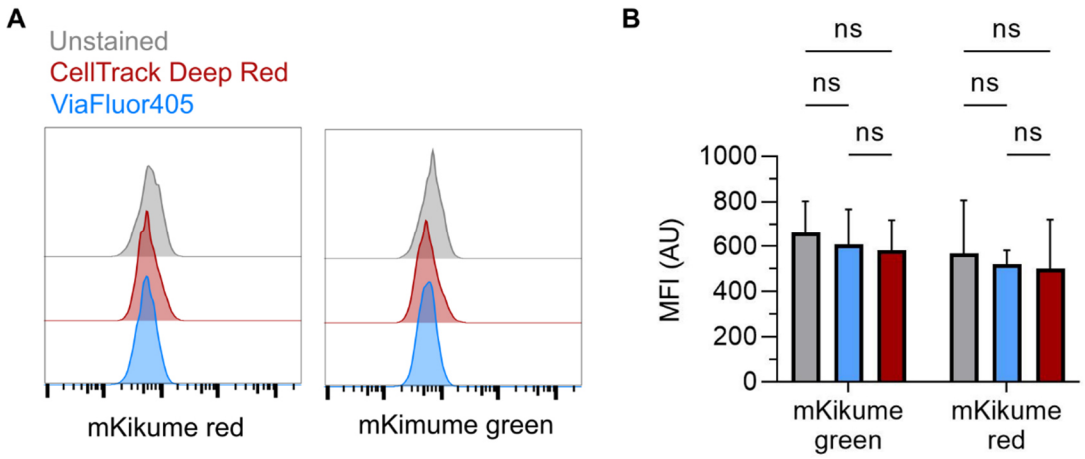

Figure 12: No fluorescent crosstalk into the mKikume detection channels by fluorescent labels. Fluorescent signal of uninfected M(-) labelled with ViaFluor405, CellTracker Deep Red and an unstained control used for uncompensated experiments with *Lm*^{mKikume}. Shown are histograms of a representative sample **(A)** and the MFI of as mean value + SD of three individual donors, N=2. Significance was determined by 2way ANOVA with multiple comparison correction by Holm-Šidák test, ns – not significant.

For the co-incubation assay with M(IFN-γ), M(M-CSF), M(IL-4) and M(IL-10), the cells were seeded and infected after stimulation (5.2.2.3) by *Lm*^{DsRed} amastigotes with an MOI of 2, without being fluorescently labeled. As a control, the same set of cells was incubated with red fluorescent latex beads equally sized to amastigotes with an MOI of 10 for 3 h at 37°C, 5% CO_2. All cells were co-incubated with M-CSF derived macrophages, which were stained with ViaFluor405 (5.2.7.4) before being seeded to microcentrifugation tubes with $1*10^6$ cells/ml and incubated till the co-incubation was started. The live/dead stain was also included as described previously.

For visualization of the transfer of cellular material by confocal laser scanning microscopy (CLSM), cells were stained with CellTracker CMFDA and $0.05*10^6$ cells were seeded per well in a 12 well µ-slide for CLSM. The cells were infected by *Lm* wildtype amastigotes with an MOI of 5. The initially uninfected cells were stained by CellTracker Deep Red and also $0.05*10^6$ cells per well were added for co-incubation at 24 h pI. The co-incubation was stopped by paraformaldehyde (PFA) fixation at 44 h pI, and it was proceeded by immunolabeling for CLSM (5.2.10.2).

5.2.6.4 Co-incubation assay with BLaER1 and BLaER1$^{GSDMD-/-}$ cells

BLaER1 and BLaER1$^{GSDMD-/-}$ were differentiated in a 24-well plate (5.2.4.2) and infected after transdifferentiation by *Lm*^{DsRed} stationary-phase promastigotes with an MOI of 5 or axenic amastigotes with an MOI of 2 (5.2.6.1). After removing extracellular parasites, cells were further incubated for 1 h and $0.25*10^6$ uninfected BLaER1$^{eGFP\ GSDMD-/-}$ were added per well. At 18 h pI, samples were stimulated as described (5.2.4.4), including an untreated control. Respective samples were harvested 120 min, 180 min, or 240 min post-treatment by nigericin and analyzed by flow cytometry (5.2.11).

5.2.7 Viable cell staining

5.2.7.1 Live/dead cell staining

Zombie dyes – For the staining with membrane impermeable, amine-reactive fluorescent Zombie dyes, cells from the respective experiment were washed once in cold PBS (pH 7.4) and then resuspended in Zombie dye diluted 1:500 in cold PBS (pH 7.4) using 100 µl per $0.2*10^6$ cells. Cells were stained 15 min at 4°C, washed once in MACS buffer and resuspended in again in MACS buffer prior to analysis. As gating controls, a sample of viable cells spiked with cells heated to 65°C for 10 min with subsequent incubation on ice was included, resulting in two distinct live/dead populations in the flow-cytometry analysis.

SytoxBlue – For the staining with membrane impermeable SytoxBlue fluorescent dye with high nucleic acid affinity, 100 mM SytoxBlue staining solution was added 1:100 to respective samples in FACS tubes solved in MACS buffer prepared for the analysis by flow-cytometry. Samples were incubated 5 min on ice and immediately analyzed by flow-cytometry.

5.2.7.2 Apoptosis staining

NucView405 – To analyze caspase-3 activity, M-CSF derived M(-) or M(IFNγ), M(M-MCSF), M(IL-4) were seeded to UpCell plates with $0.4*10^6$ cells per well (5.2.2.3). Subsequently, M(-) by *Lm*^{DsRed} promastigotes with an MOI of 10 and axenic amastigotes with an MOI of 5 and M(IFNγ), M(M-MCSF), M(IL-4) were infected by *Lm*^{DsRed} axenic amastigotes with an MOI of 2 (5.2.6.1). At 24 h pI, 2.5 µM NucView405 reporter peptide were added to cell culture and incubated for 20 h. Cells were harvested at 44 h pI according to manufacturer's protocol from UpCell plates, transferred to a 96 well V-shape plate and washed once by pelleting cells at

339 *g,* 4 min at 4°C and resuspending in cold PBS. M(-) were pelleted again, resuspended in 100 µl MACS buffer and subsequently analyzed by flow-cytometry, including an uninfected and unstained control. M(IFNγ), M(M-MCSF), M(IL-4) were subjected to a staining by Apotracker green and a live/dead staining by Zombie NIR (5.2.7.1) followed by flow cytometry analysis (5.2.11). As controls, FMO samples, uninfected samples of each stimulus and samples induced by 1 µM Staurosporine for 4 h were included.

Apotracker green – Prior to the staining by Apotracker green, cell samples were washed once in cold PBS and then stained in Apotracker staining solution with 400 nM in PBS using 100 µl for $0.4*10^6$ cells. Samples were incubated for 20 min at room temperature, then, cells were washed once in MACS buffer, resuspended in 100 µl MACS buffer and subjected to flow-cytometry analysis (5.2.11) including a FMO control.

Annexin V – For the staining with Annexin V, BLaER1 samples were washed once in Ringer solution and stained by 1 µl per $1*10^6$ cells Annexin V-AF647 diluted 1:1000 in Ringer solution. Cells were incubated protected from light for 20 min on ice. Samples were washed once Ringer solution and then resuspended in 100 µl Ringer solution for analysis by flow-cytometry (5.2.11).

5.2.7.3 Pyroptosis staining

660-YVAD-FMK – To analyze caspase-1 activity, M(IFNγ), M(M-MCSF), M(IL-4) were seeded to UpCell plates with $0.4*10^6$ cells per well (5.2.2.3). Subsequently, M(IFNγ), M(M-MCSF), M(IL-4) were infected by Lm^{DsRed} axenic amastigotes with an MOI of 2 (5.2.6.1). At 36 h pI, 660-YVAD-FMK diluted was added to the culture with a final dilution 1:300 from stock in 300 µl culture media with $0.4*10^6$ cells and incubated for 8 h. Cells were harvested at 44 h pI according to manufacturer's protocol from UpCell plates, transferred to a 96 well V-shape plate and washed once by pelleting cells at 339 *g,* 4 min at 4°C and resuspending in cold PBS. M(IFNγ), M(M-MCSF), M(IL-4) were subjected to a staining by a live/dead staining by Zombie aqua (5.2.7.1) followed by flow-cytometry analysis (5.2.11). As controls, Fluorescence minus one (FMO) samples, uninfected samples of each stimulus and samples induced by 200 ng/ml for 6 h subsequent addition of 10 µM nigericin for additional 1 h were included.

5.2.7.4 Fluorescent labelling of viable cells

Viable cells were labeled for the respective experiments with different membrane permeable amine-reactive dyes by washing cells once in warm PBS (pH 7.4) and subsequent resuspension in staining solution using 0.5 ml solution per $1*10^6$ cells. Samples were then incubated for 20 min at 37°C. The amine reactive group of the dyes was quenched by the addition CM in a ratio of 1:1 to the staining solution. Cells were washed once in WB and then resuspended in CM at the desired concentration for subsequent use in experiments. The respective dyes were used in the final concentration in PBS as follows: CFSE – 10 µM,

CellTracker CMFDA – 5 µM, AF405 – 10 µM, ViaFluor405 – 10 µM, CellTracker Deep Red – 0.5 µM.

5.2.8 Immunological assays

5.2.8.1 Immunostaining of cells for flow cytometry

To analyze the immunophenotype of differently stimulated M(-), 0.5*10^6 cells were seeded per well in a 24-well UpCell plate, stimulated (5.2.2.3) and infected by *Lm*^{DsRed} axenic amastigotes (5.2.6.1). At 44 h pI, cells were harvested according to manufacturer's protocol from UpCell plates, pelleted at 400 *g*, 5 min in Eppendorf tubes and transferred in PBS (pH 7.1) to a 96 well V-shape plate. Cells were pelleted at 339 *g,* 4 min at 4°C, resuspended in IF blocking buffer and incubated for 15 min at 4°C. Then, cells were stained by a solution of α-CD14, α-CD16, α-CD86, α-CD163, α-CD206 and α-MerTK antibodies in IF staining buffer (5.1.8) for 30 min at 4°C. Cells were washed once by PBS (pH 7.4) and subsequently stained by Zombie yellow as live/dead (5.2.7.1). For compensation, compensation beads were stained separately by 0.5 µl of each antibody, Zombie yellow was compensated by a sample of viable cells spiked with cells cooked at 65°C for 10 min with subsequent incubation on ice. DsRed was compensated using *Lm*^{DsRed} axenic amastigotes from *in vitro* culture that include dead parasites resulting in a DsRed positive and negative population. Cells and compensation controls were washed twice in MACS buffer, resuspended in 100 µl MACS buffer and subjected to flow cytometry analysis (5.2.11).

5.2.8.2 Immunolabeling of *Lm* for CLSM

For CLSM, the fixed samples on the 12-well ibidi from the co-incubation experiment (5.2.6.3) were washed twice PBS (pH 7.1). All following steps were performed at room temperature. The cells were permeabilized by IF permeabilization buffer for 15 min and blocked by IF blocking buffer for 15 min. Intracellular parasites were stained by rabbit α-*Lm* Serum diluted 1:100 in IF staining buffer for 1 h. Then, cells were washed three twice by IF staining buffer, a AF647-conjugated chicken α-rabbit antibody diluted 1:1000 in IF staining buffer was added and incubated for 1 h. Cells were washed twice with PBS (pH 7.1) and incubated with DAPI at a final concentration of 300 nM for 5 min and washed again twice by PBS (pH 7.1). As controls, an uninfected sample, an infected sample not stained by the primary antibody (FMO DsRed) and an infected sample not stained by DAPI (FMO DAPI) were included. Residual liquid was removed, the cells were embedded in Mowiol mounting solution and covered by a #1.5 coverslip. The slide was sealed with nail polish and stored at 4°C till CLSM analysis (5.2.10.2).

5.2.9 Colorimetric assays

5.2.9.1 Quantification of lactate dehydrogenase (LDH) release

Macrophages were seeded to a 96-well plate with 75'000 cells per well, stimulated (5.2.2.3) and infected by *Lm*^{DsRed} axenic amastigotes with an MOI of 2 (5.2.6.1). To measure time

dependent LDH release, the medium was replaced at the beginning for each interval from 0 h - 4 h pI, 4 h - 24 h pI and 24 h - 44 h pI and harvested at the end of the interval. The cell culture supernatant was then analyzed for the released LDH by using the CyQUANT™ LDH Cytotoxicity Assay according to the manufacturer's protocol. The LDH release was measured by fluorescence signal with excitation at 560 nm and emission at 590 nm. The background fluorescent was measured in a sample with CM and subtracted from all values. The LDH release in percent was derived from obtained values normalized to a lysed (maximal release) and uninfected (minimal release) control, included in the assay according to the following formula:

$$LDH\ release\ (\%) = \left(\frac{LDH_{Sample} - LDH_{Uninfected}}{LDH_{Lysed} - LDH_{Uninfected}}\right) * 100 \quad (4)$$

5.2.9.2 IL-1β enzyme linked immunosorbent assay (ELISA)

Harvested cell culture supernatants were transferred to a 96-well V-bottom plate and exempt from cells and cell debris by centrifugation at 2400 *g*, 8 min. Supernatants were transferred to a new 96-well plate and analyzed by human IL-1β ELISA MAX deluxe according to the manufacturers protocol. Concentrations were calculated based on a standard curve generated form a serial dilution by performing a 4-parameter logistic regression in Mars (ClarioStar).

5.2.10 Microscopic methods

5.2.10.1 Live-cell imaging for parasite release from BLaER1 cells.

To detect parasite release 0.15*10^6 BLaER1 or BLaER1$^{GSDMD-/-}$ cells per well were seeded to poly-d-lysine-coated 8-well ibidi slide (5.2.4.2) and infected by *Lm*^{DsRed} promastigotes with an MOI of 5 (5.2.6.1). The cells were treated as described (5.2.4.4) after 18 h pI and the image acquisition was started upon addition of nigericin, recording a single frame every 2.5 min of three distinct positions per sample for 12 h in total. *S*amples were imaged with the Zeiss LSM 7 LIVE confocal laser scanning microscope using the Plan-Apochromat 40x/0.95 Korr M27 objective, beam splitter at 565 nm excitation with lasers at 488 and 561 nm, and emission detection using the filters BP 495–555 (eGFP), or BP 575–615 + LP 655 (DsRed). Image acquisition was controlled with the Zen black software (Carl Zeiss Microscopy), images series were exported analyzed using Fiji software [156]. To analyze parasite release, infected cells were tagged and traced manually over the acquisition time. Events pre-exit (white numbers) were defined by a visual GFP signal (green) surrounding the parasites' DsRed signal (red). Parasite exit was timely defined by the frame where the GFP signal was lost, and parasites reached the extracellular space (orange numbers) (Figure 45).

5.2.10.2 Confocal laser scanning microscopy

Confocal LSM images were acquired by the Leica SP8 DMi microscope using an apochromatic 63x/1.4 oil objective Oil. Fluorescence signals were detected using line averaging of two scans: Line 1 with excitation by laser lasers at 405 nm and 633 nm, detecting signals by PMT detector with a filter 410-480 nm (DAPI) and by HyD detector with a filter 672-784 nm (AF647) Line 2 excitation by laser lasers at 488 nm and 633 nm, detecting signals by PMT detector with a filter 501-550 nm (CMFDA) and by HyD detector with a filter 794-799 nm (CellTracker Deep Red). Image acquisition was controlled with the LAS X software (Leica Microsystems), images of single channels were exported and overlaid by Fiji software [156].

5.2.11 Flow cytometry

Samples were analyzed by the flow cytometry devices BD FACS Fortessa, BD FACS Symphony or BD FACS LSR II SORP. The gating strategy for acquisition was done with FACSDiva software. In general, a minimum of 10’000 single cell events were recorded or a minimum of 5’000 infected cells. Resulting raw data was exported as fcs files and analyzed by FlowJo software. The same software was used to generate plots and histograms for gating strategies. Gated ratios and median fluorescence intensity values were exported in excel files and graphically analyzed subsequently (5.2.12).

5.2.12 Graphical and statistical analysis

Graphical analysis and depiction of data was performed by GraphPad PRISM software. Statistical tests were also performed using GraphPad PRISM software. In general. a standard distribution was assumed for technical replicates from the same sample conditions. Data obtained from differently treated samples was seen independent. Therefore, unpaired parametric statistic tests were used to determine significant differences between groups. For comparisons of three or more groups, a correction for multiple comparisons by statistical hypothesis testing was included. The first exceptions were the comparisons of groups resulting from uniformly treated samples (*e.g.* infected and uninfected cells from the same culture dish), where paired parametric statistic tests were used to determine significant differences. The second exception were comparisons of two groups that resulted from splitting of one standard distributed group, where unpaired non-parametric tests were used to determine significant differences. The exact respective test and multiple comparison correction is specified for each experiment in the figure text. Schemes and illustrations were created with biorender.com. Image corrections and figure assembly was done with Inkscape software.

6 Results

6.1 Quantification of parasite exit from primary human hMDMs

The research on *Lm* parasites exit mechanism has recently been advanced by utilizing BMDMs from mice in live-cell microscopy, showing a transfer of parasites from on cell to another with no or very limited time of exposure to the extracellular milieu [23]. Accordingly, our group observed membrane blebbing of primary human host cells prior to a parasite release in preliminary fluorescence microscopic analysis (Figure 6). Therefore, the first part of the hypothesis for this thesis is that the parasite exit is a direct transfer from an infected cell to a new host cell, driven by the cell death of the initially infected cell. An indicator for an apoptotic cell death during pathogen egress is the transfer of cellular material from previously infected cells [157]. In order to assess the parasite egress and its abundance, I first sought to establish a fluorescence-based assay to quantify exit events in a co-incubation experiment via flow cytometry. The assay was conceptualized to detect exit events as a result of a two stepped process, beginning with the parasite egress and followed by the uptake by the co-incubated, receiving cell, whose infection can then be detected by flow cytometry. The two steps can be separated timely and spatially (secondary infections) or occur successively as a continuous process (direct transfer). With this assay at a hand, I was able to experimentally compare several factors potentially impacting *Lm* exit comprising the time post-infection (pI), form of the infecting parasite and different stimuli for host cell differentiation.

6.1.1 Co-incubation of adherent hMDMs allows the detection of parasite exit by flow cytometry

Because hMDM are phagocytic cells, they ingest material that is recognized as not-self [28], a transfer of cellular material can potentially be detected by a co-incubation of viable cells with fixed cells, labeled by fluorophores with distinct emission wavelength (Figure 13). Therefore, fluorescent succinimidyl ester (SE) dyes were employed that label primary amines of proteins and are non-toxic to living cells under regular culture conditions. . The fixed AlexaFluor405-SE (AF405) labelled cells were added onto the adherent, viable carboxyfluorescein-SE (CFSE) labeled cells for co-incubation and subsequent analysis by flow cytometry (Figure 13 B)

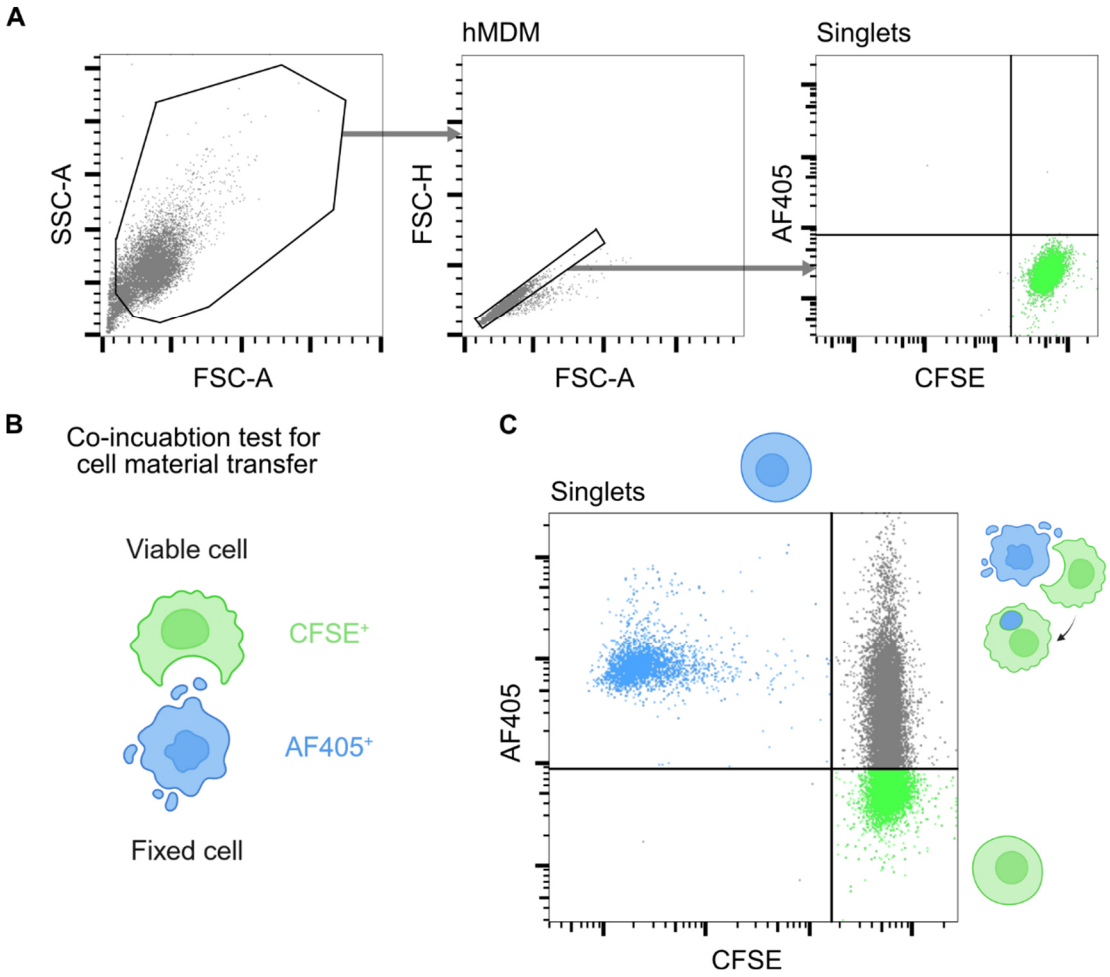

Figure 13: The transfer of cellular material can be measured by flow cytometry.
One batch of M-CSF derived and unstimulated hMDMs (M(-)) was stained by carboxyfluorescein succinimidyl ester (CFSE) and subsequently seeded to a tissue culture plate. Another batch of unstimulated hMDMs (M(-)) was stained with AlexaFluor405 succinimidyl ester (AF405), fixed and added to the adherent $CFSE^+$ M(-) for co-incubation. After 18 h, M(-) were harvested and analyzed by flow cytometry. Non-co-incubated samples of $CFSE^+$ (shown in **(A)**) and $AF405^+$ M(-) (not shown) were included as gating controls. **(A)** Gating strategy for $CFSE^+$ M(-). **(B)** Schematic of the co-incubation of viable and fixed M(-). **(C)** Two-parameter plot with a four-quadrant gate to detect the distinct cell populations: fixed M(-) ($AF405^+$, upper left), viable M(-) with uptake of cellular material after co-incubation ($CFSE^+$ and $AF405^+$, upper right) and viable M(-) without uptake of cellular material ($CFSE^+$ and $AF405^-$, lower left).

A sample of $CFSE^+$ M(-) resulted in a distinct population in the CFSE channel with a uniformly high fluorescence intensity and without fluorescence spill-over into the AF405 channel (Figure 13 A). In the co-incubated sample, an $AF405^+$ but $CFSE^-$ cell fraction was observed. Additionally, two $CFSE^+$ populations that remained uniformly high in their fluorescence intensity were detected. A first one was negative for AF405 in the lower right gate as the non-co-incubated sample (Figure 13 C). The second population was also positive for AF405 with distributed intensities, likely resulting from the uptake of fixed, $AF405^+$ cells. Conclusively, the detection of transferred material is possible by fluorescent labelling during a co-incubation experiment of hMDMs.

Next, a co-incubation assay was designed to detect and quantify parasite cell-to-cell transfer from a primary infected cell to an initially uninfected cell (Figure 14). Therefore, a common *in vitro* cell model of primary M-CSF and GM-CSF derived hMDMs was used that can be infected by different forms of *Lm* after differentiation [144]. By using the previously developed staining technique and gating strategy for co-incubation assay, parasite cell-to-cell transfer events can be characterized whether they occur with or without the transfer of cellular material (Figure 14 A).

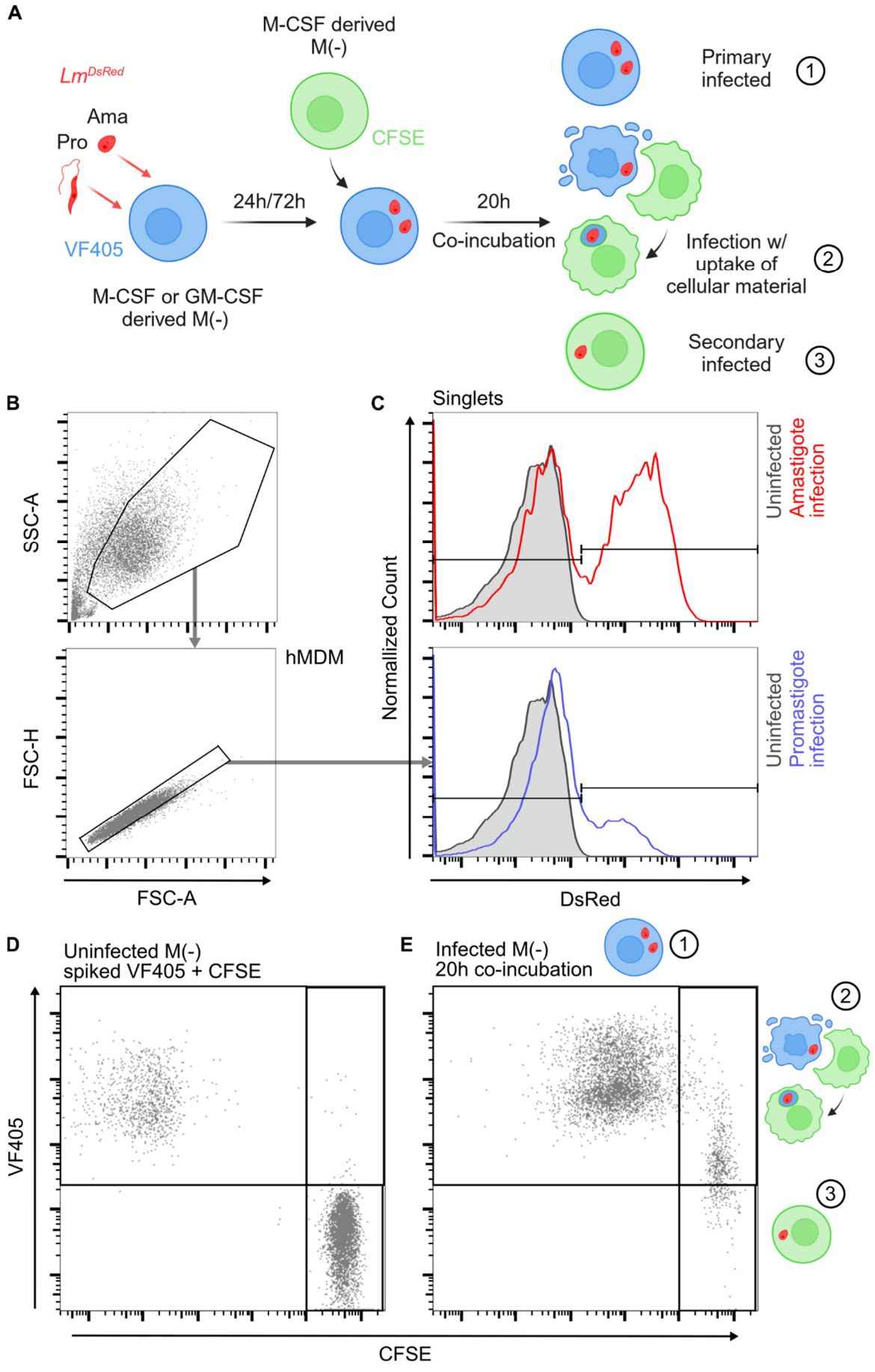

Figure 14: Co-incubation of primary infected and uninfected M(-) results in parasite cell-to-cell transfer.

To Fig. 14 – **(A)** Scheme of the co-incubation assay with VF405$^+$ M(-), primary infected by either *Lm^{DsRed}* promastigotes or axenic amastigotes, subsequent addition of uninfected, CFSE$^+$ cells from the same individual donor and analysis by flow cytometry. **(B)** Gating strategy of events from a representative infected and co-incubated sample with detection of intact cells in the *SSC-A x FSC-A* plot and singlets in the *FSC-H x FSC-A* plot. **(C)** Detection of infected cells in the DsRed channel for amastigote (red line) and promastigote (blue line) infected samples gated based on an uninfected negative control (grey line). **(D)** Gating control for the four-quadrant gating strategy with an uninfected sample of spiked VF405$^+$ cells and CFSE$^+$ cells. **(E)** Four-quadrant of an infected and co-incubated sample to dissect the populations of primary infected cells (1), cells infected after parasite transfer with uptake of cellular material (2) and secondary infections (3). (Pro) Promastigotes, (Ama) Amastigotes.

As in the previous experiment, the analyzed cells were gated for single cells, followed by the detection of infected subpopulations, which had a distinct peak caused by an increased fluorescence intensity in the DsRed channel as compared to the uninfected population (Figure 14 B, C). Promastigote infections showed lower infection rates and decreased fluorescence intensity in the DsRed channel, compared to amastigotes. A composite sample of VF405- and CFSE-stained cells showed a neglectable number of events appearing in the double positive gate, confirming the applicability of the used gating strategy (Figure 14 D). The gating strategy allowed a categorization of infected cells into three different populations: primary infected, infection with uptake of cellular material and infection without uptake of cellular material. Firstly, the assay yielded events of parasite transfer from primary infected to the initially uninfected cells. In addition, a share of CFSE$^+$ and infected cells was also positive for the cellular material of primary infected cells (Figure 14 E).

The sum of cell-to-cell transfer events with and without transfer of cellular material are also termed exit rate in subsequent experiments, describing the percentage of all transferred parasites from all infected cells.

6.1.2 Amastigote infections result in higher parasite exit rates and spreading

In order to find the most relevant condition for parasite exit in the *in vitro* infection of primary human hMDMs, the factors like differentiation stimuli, time pI and life stage of infecting parasite were tested and compared in the co-incubation assay (Figure 15). The co-incubation time with M-CSF derived M(-) was uniformly with 20 h prior to the analysis. For one set of samples the co-incubation interval started at 24 h pI, where infecting promastigotes readily transformed to amastigotes within the cells, for the other set of samples the co-incubation began 72 h pI. Still, the infection routes of promastigotes and axenic amastigotes are different *in vitro*, urging the relevance to test both in our infection system. The second time-point used, was rather limited by the survival of the M-CSF differentiated cells that remained uninfected for the co-incubation.

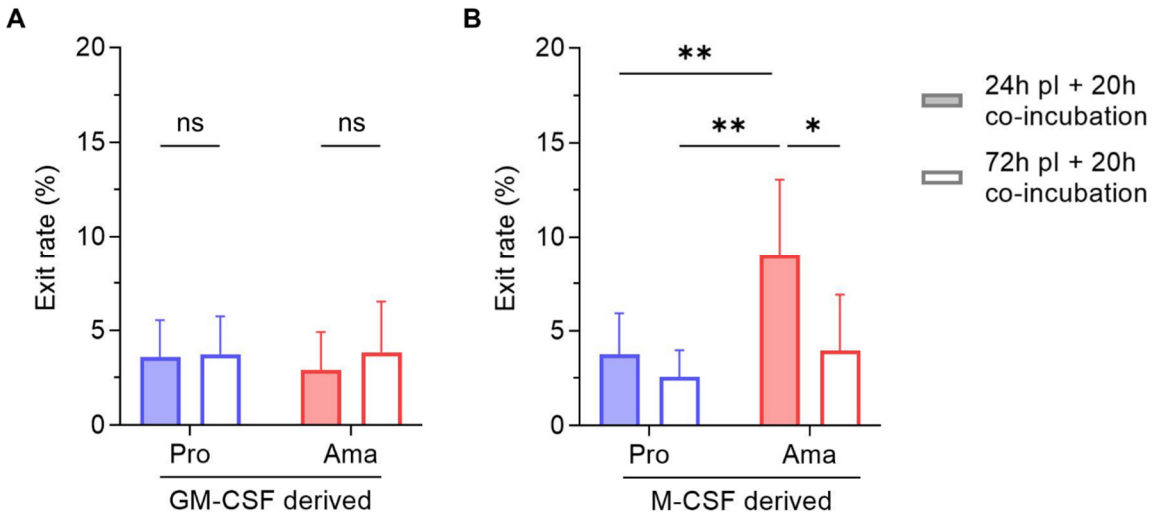

Figure 15: Dependency of parasite exit during co-incubation on differentiation cytokine, parasite stage and post-infection time.
The exit rate of *Lm*^{DsRed} 24 h pI + 20 h of co-incubation or 72 h pI + 20 h of co-incubation with uninfected M(-) in percent analyzed by flow cytometry as described in Figure 14. **(A, B)** Shown are the exit rates from GM-CSF derived M(-) **(A)** and M-CSF derived M(-) **(B)** after promastigote infection (Pro) and amastigote infection (Ama) with the mean ± standard deviation (SD) for six to seven individual donors, N=4. Significance was determined by 2way ANOVA with multiple comparison correction by Holm-Šidák test, ns – not significant, *$p < 0.05$, **$p < 0.01$. (Pro) Promastigotes, (Ama) Amastigotes.

None of the assessed conditions by GM-CSF derived M(-) yielded an exit rate above 5 % and no significant deviation was observed between different time points and the pro- or amastigote form of the parasite used for the initial infection (Figure 15 A). The same observation holds true for the M-CSF derived M(-), except for the exit of LmDsRed from M-CSF derived M(-) infected by axenic amastigotes after 24 h pI + 20 h co-incubation. Here, the exit rate was significantly increased with 9.0 ± 4.0 % compared to promastigote infections with 3.8 ± 2.2 % (24 h pI, Pro) or 2.6 ± 1.4 % (72 h pI, Pro) and to amastigote infections at the later time-point with 4.0 ± 3.0 % (72 h pI, Ama) (Figure 15 B).

In addition, it was of interest if the parasite burden of the infected cells after 24 h pI + 20 h of co-incubation was changed when comparing primary infected cells and cells infected after exit. The parasite burden can be derived from the MFI of DsRed recorded by the same set of primary cell donors experimentally used in Figure 14 and which is constitutively expressed by the parasites (Figure 16).

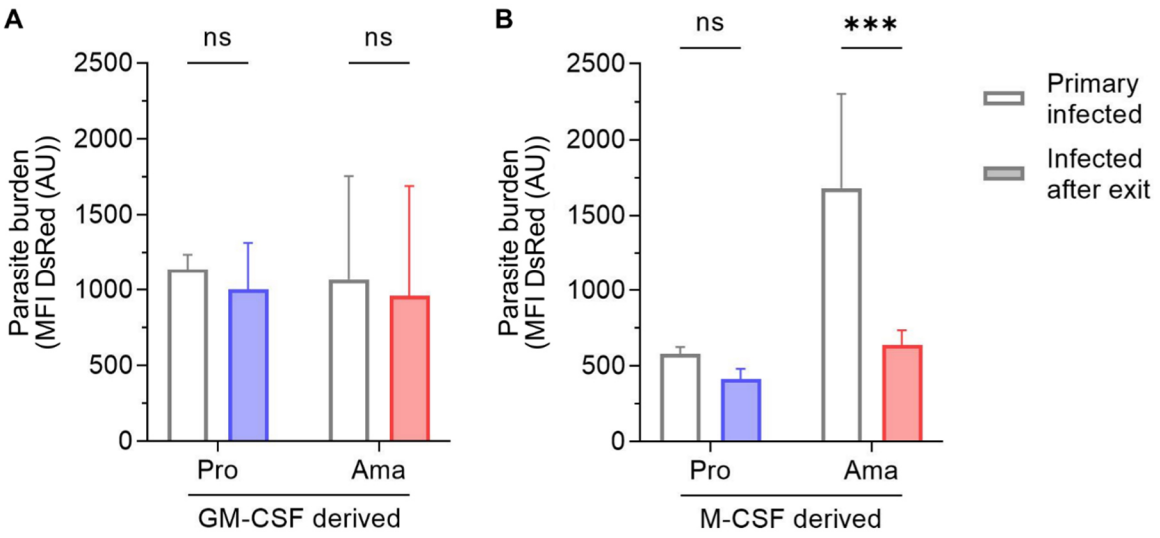

Figure 16: The parasite burden is reduced upon exit from M-CSF derived M(-) after primary axenic amastigote infections.
Parasite burden derived from the DsRed MFI emitted by intracellular parasites and measured by flow cytometry at 24 h pI + 20 h co-incubation. **(A)** MFI of promastigotes (Pro) and Amastigotes (Ama) in primary infected GM-CSF derived M(-) and M-CSF derived M(-) after exit. **(B)** MFI of promastigotes (Pro) and Amastigotes (Ama) in primary infected M-CSF derived M(-) and M-CSF derived M(-) after exit. Shown is the mean ± SD for six to seven individual donors, N=4. Significance was determined by 2way ANOVA with multiple comparison correction by Holm-Šidák test, ns – not significant, ***$p < 0.001$. (Pro) Promastigotes, (Ama) Amastigotes.

M(-) were evenly burdened by parasites in samples, when the initially infected cells were GM-CSF derived, independent of whether they were detected in primary infected cells or in cells infected subsequent to an exit event (Figure 16 A). After the initial infection of M-CSF derived M(-) by promastigotes, the parasite burden of primary infected cells and cells infected after exit was nigh on equal. In contrast, the parasite burden for M(-) infected after parasite exit was significantly reduced compared to the primary infected cell population in samples initially infected by axenic amastigotes (Figure 16 B).

6.1.3 Parasite exit is a direct transfer alongside host cell material

With the introduced gating strategy, it was possible to dissect the share of parasite exit events associated with the transfer of cellular material from the initial host cell to the receiving cell (Figure 17). Accordingly, the relevant time point of 24 h pI and 20 h co-incubation was analyzed for direct transfer events (Figure 17 A).

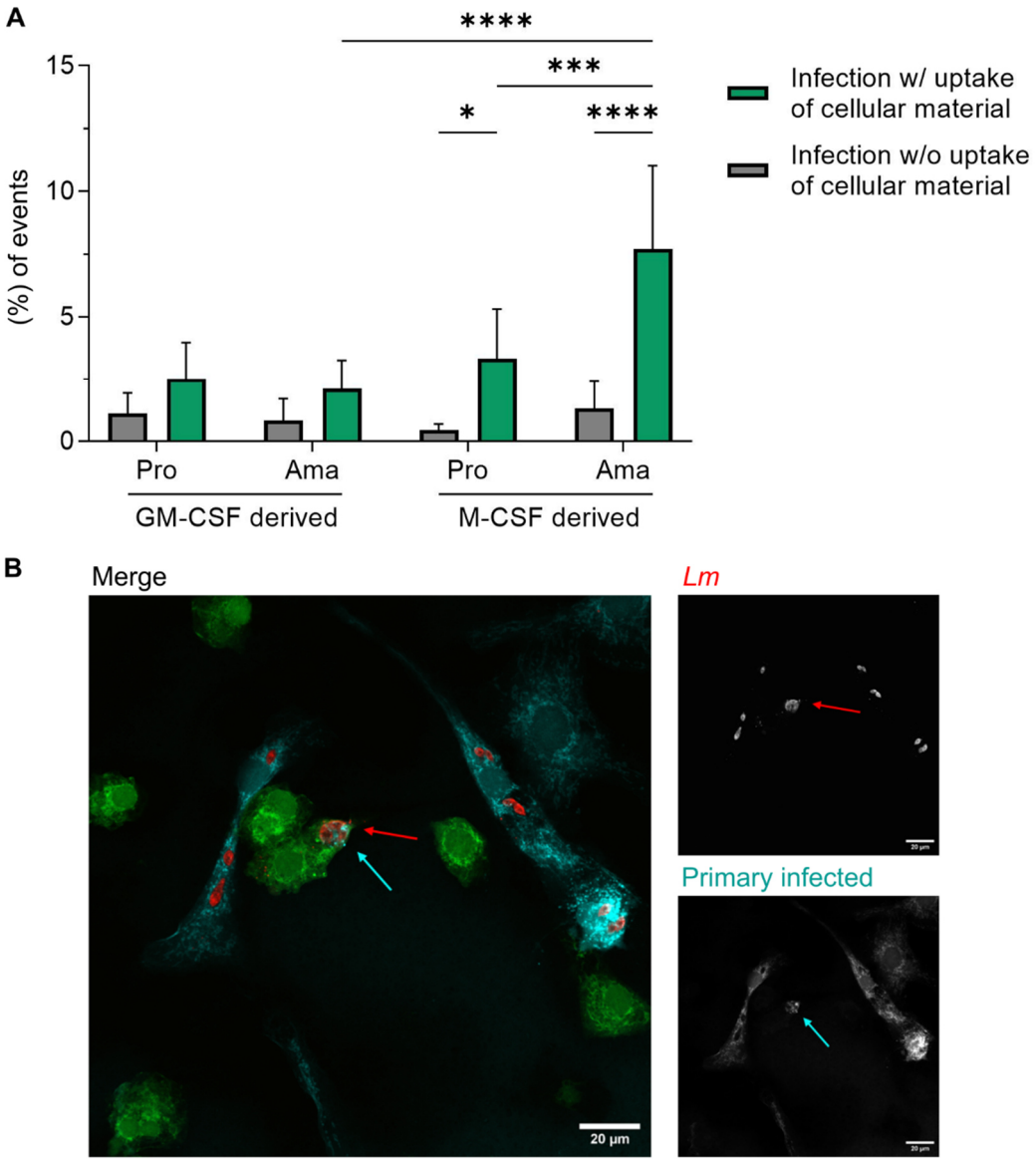

Figure 17: Amastigote exit from M-CSF derived M(-) results mostly from cell-to-cell transfer with cellular material from initially infected cells.
(A) Exit rate of *Lm*^{DsRed} promastigotes (Pro) and amastigotes (Ama) divided to events with uptake of cellular material and without cellular material in percent after 24 h pI + 20 h co-incubation with M-CSF derived M(-). Shown is the mean ± SD for six to seven individual donors, N=4. Significance was determined by 2way ANOVA with multiple comparison correction by Holm-Šidák test, *$p < 0.05$, ***$p < 0.001$, ****$p < 0.0001$. **(B)** Co-incubation experiment for confocal laser scanning microscopy (CLSM), with primary infected cells stained by VF405 prior to the infection with axenic amastigotes and CMFDA staining of the co-incubated cells for the co-incubation. After 24 h pI + 20 h co-incubation, cells were fixed, permeabilized and intracellular parasites were stained by rabbit α-*Lm* serum and a secondary α-rabbit AF647 antibody. Images were acquired at 63x magnification, 0.5 optical zoom and two-times line averaging. Shown is a single transfer event as merge with primary infected cells (blue), co-incubated cells (green) and parasites (red) and highlighting of a transferred parasite (red arrow) and cellular material from a primary infected cell (blue arrow). Additionally, single fluorescence channels for AF647 and the VF405 are shown. The scale bar equals 20 µm. Depicted is a representative micrograph from two individual donors. (Pro) Promastigotes, (Ama) Amastigotes.

The occurring exit events resulted mainly from infections with transfer of cellular material in all conditions, yet, for GM-CSF derived M(-), only a non-significant increase was observed for the overall low exit rates. For M-CSF derived M(-) infections by promastigotes, events with transfer

of cellular material were significantly increased from 3.3 ± 2.0 % compared to 0.4 ± 0.2 % secondary infections. An even more drastic increase from 1.3 ± 1.0 % without transfer of cellular material to 7.7 ± 3.3 % with transfer of cellular material was observed for amastigote infections (Figure 17 A). In a control experiment employing CLSM, exit events with co-localization of cellular material from the initially infected cell (blue arrow) and parasites (red arrow) within the same phagolysosome of a co-incubated cell were observed (Figure 17 B). While the microscopic observations for two individual donors does not allow a quantification of exit events, it demonstrates that exit events with transfer of cellular material can result from a transfer of parasite and cell debris in a single event, opposed to distinct uptake events of parasite and cellular material. These results strongly indicate a direct transfer without exposure of the parasite to the extracellular space, opposed to secondary infection whereby the parasite reaches the extracellular milieu for a certain period of time. To test whether the measured parasite exit is influenced by variations in infection rate or by donor-specific behavior, the data obtained by flow cytometry from the co-incubation experiments with M-CSF derived M(-) at 24 h pI + 20 h co-incubation were analyzed further (Figure 18).

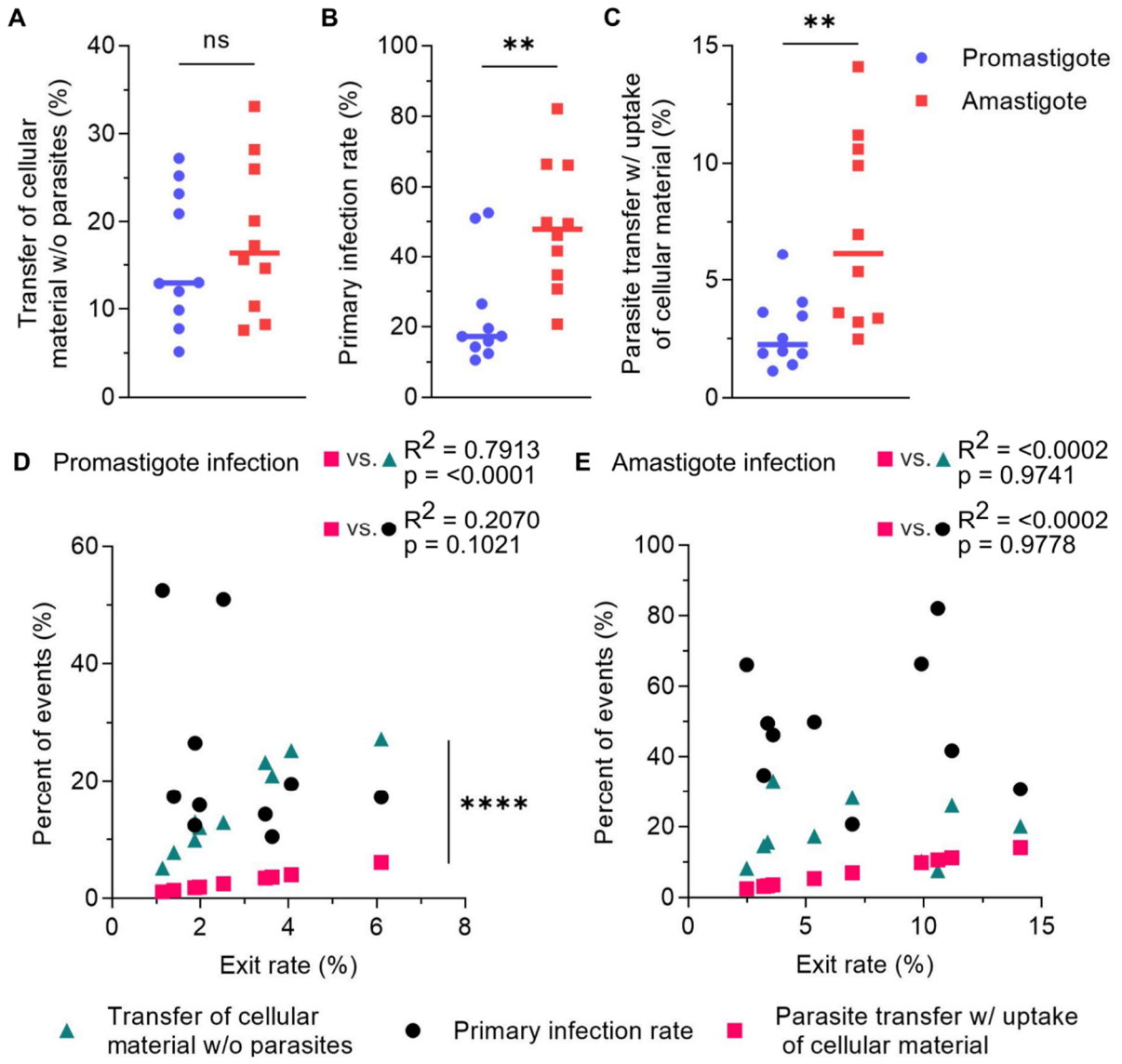

Figure 18: Exit observed for promastigote infected samples is caused by parasite independent uptake of cells.
Further analysis of parasite exit from M-CSF derived M(-) at 24 h pI + 20 h co-incubation with three additional individual donors pooled with data from the previous experiment. The metrics transfer of cellular material by uninfected cells in infected samples, the primary infection rate, and the parasite transfer with uptake of cellular material were derived from the flow cytometry data. **(A-C)** Quantification of uptake of cellular material in the uninfected cell fraction **(A)**, the primary infection at the end of the co-incubation **(B)** and the parasite transfer with uptake of cellular material **(C)** for promastigote and amastigote infections. Each dot represents an individual donor with a total of 10 individual donors, N=5. Mean values are shown by the colored lines for A-C. Significance was determined by two-tailed unpaired t-test, ns – not significant, $^{**}p < 0.01$ **(A-C). (D, E)** Linear correlation of the exit rate with the other metrics described in A-C for promastigote infections **(D)** and amastigote infections **(E)** by Pearson correlation coefficient with the strength of correlation shown by the coefficient of determination R^2**.** Significance of the linear correlation tested with a two-tailed Pearson correlation coefficient, not significant correlation $p > 0.05$, significant correlation $p < 0.05$, $^{****}p < 0.0001$.

The cells derived from individual donors showed a large variation in their uptake of cellular material during co-incubation, independently of a parasite transfer, ranging from 5.2 % to 33.1 % (Figure 18 A). On average, there was no significant difference in the measured uptake of cell material without parasites in samples infected with pro- or amastigotes. Yet, differences

were detected in the primary infection rate, as well as the parasite transfer with uptake of cellular material, as already shown in Figure 17 (Figure 18 B, C). The primary infection rate with promastigotes averaged 23.7 % of the cells, while amastigote infections resulted in a mean infection rate of 48.8 % (Figure 18 B). The increased infection rate had no impact on the direct comparison of the promastigote and amastigote exit rates, as the exit rate is a share of the total infection, including the primary infection rate and thereby normalizing for the varying infection rates (Figure 18 C). In addition, I took into account that differences in the exit rate by individual donors do not base on a parasite-related mechanism but on variations in the primary infection rate or the transfer of cellular material. Therefore, the named metrics were correlated with the exit rate for promastigote and amastigote infection (Figure 18 D, E). Interestingly, the exit rate of promastigotes correlated positively with increasing transfer of cellular material without parasites, indicating that this exit is not specifically driven by the infecting parasites. In contrast, amastigote exit rates correlated neither with the primary infection rate nor the transfer of cell material without parasites, suggesting that another, parasite-specific mechanism causes variations between donors.

In summary, the *Lm* parasite exit was dominantly observed in M-CSF derived M(-) during infection with axenic amastigotes and at 24 h pI. Thereby, the exit occurs as a direct transfer from cell to cell, seen by the transfer of cellular material from the initially infected cell.

6.2 The role of apoptosis in parasite infection and exit

6.2.1 Upregulation of caspase-3 activity and inhibition during parasite infections

The uptake of cellular material by macrophages is usually associated with previous apoptosis of the phagocytosed cell. Therefore, apoptosis was subsequently investigated as a potential driver mechanism for cell-to-cell transmission under conditions where parasite exit was observed *in vitro*. A hallmark for apoptotic cell death that can be measured by fluorescent labelling is the activity of the key protease caspase-3. Here the reagent NucView405 was used that upon cleavage by an active caspase-3 liberates a fluorophore, increasing the fluorescent signal of cells undergoing apoptosis. For the measurement of caspase-3 activity during infection, M-CSF derived M(-) were infected according to previous experiments and the NucView405 substrate was added 24 h pI for 20 h prior to the analysis by flow cytometry (Figure 19).

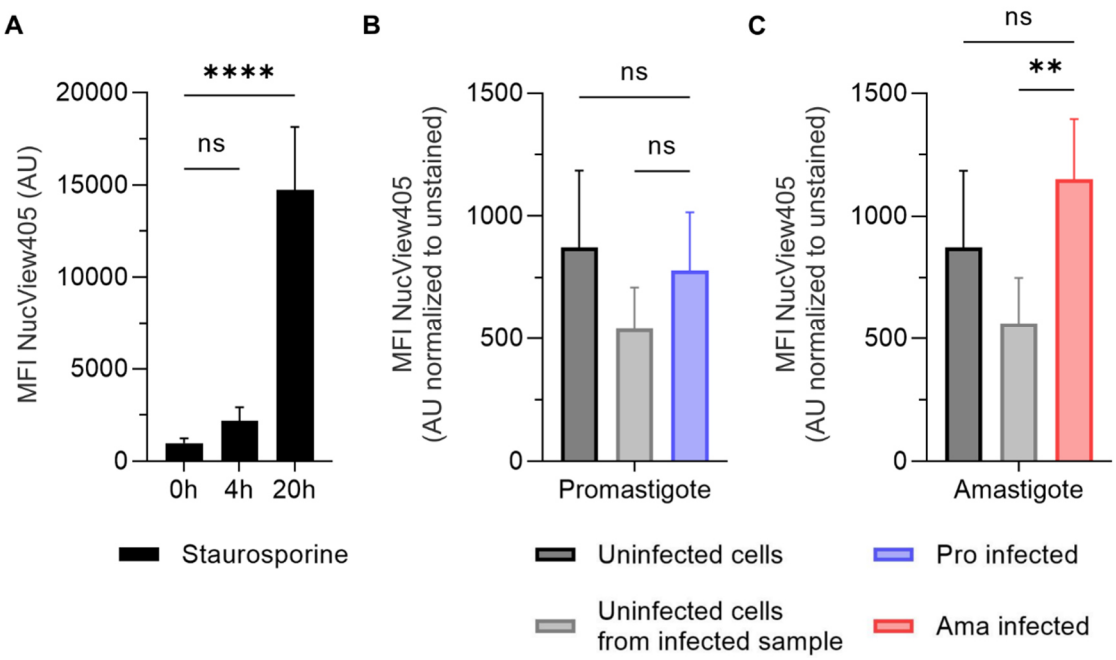

Figure 19: Caspase-3 activity is increased in amastigote infected M(-).
M-CSF derived M(-) were incubated with 2.5 µM of the fluorescent caspase-3 substrate NucView405 24 h pI for 20 h and analyzed by flow cytometry at 44 h pI. The caspase-3 activity was derived by the MFI of the fluorescent dye that was released upon caspase-3 cleavage. **(A)** As a positive control for the staining, apoptosis was induced by the addition of 1 µM Staurosporine during incubation with NucView405 0 h, 4 h or 20 h prior to analysis. Absolute MFI values of singlets are shown. **(B, C)** M(-) were infected by promastigotes **(B)** and amastigotes **(C)** and incubated with NucVIew405 at 24 h pI for 20 h. The MFI of NucView405 was measured in a single uninfected M(-) sample depicted in B and C, the uninfected subpopulation of an infected sample and the infected subpopulation of the same sample. The MFI was normalized with the respective unstained control by subtraction of the MFI value. Shown is the mean ± SD for six individual donors, N=3. Significance was determined by ordinary one-way ANOVA with multiple comparison correction by Dunnet test, ns – not significant, $^{**}p < 0.01$, $^{****}p < 0.0001$.

The incubation with 1 µM Staurosporine, an established inducer of apoptotic cell death, confirmed that the NucView405 caspase substrate leads to increased fluorescence intensities of analyzed M(-) cells during apoptosis (Figure 19 A). To test the caspase-3 activation by pro- or amastigotes, the MFI of NucView405 was measured in infected and compared to uninfected cells, either from an entirely uninfected sample or the uninfected subpopulations from an infected sample. It was observed that infected and unstained samples already displayed elevated NucView405 MFI in comparison to uninfected and unstained cells (data not shown), therefore, the values from stained samples were subtracted by the MFI of their respective unstained control (Figure 19 B, C). The subpopulation of promastigote infected cells showed slightly but not significantly increased levels of caspase-3 activity compared to the subpopulation of uninfected cells. The entirely uninfected sample showed higher caspase-3 activity than promastigote infected cells (Figure 19 B). In contrast, amastigote infected cells had an elevated caspase-3 activity compared to the uninfected cells also shown in Figure 19 B and to the uninfected subpopulation of the amastigote infected sample, whereby only the latter was significant (Figure 19 C).

In order to directly link the observed caspase-3 activity with an induction of parasite transfer from one cell to another, the co-incubation assay was utilized to measure exit while inhibiting caspase-3 activity by the specific inhibitor Z-DEVD or the pan-caspase inhibitor Z-VAD (Figure 20).

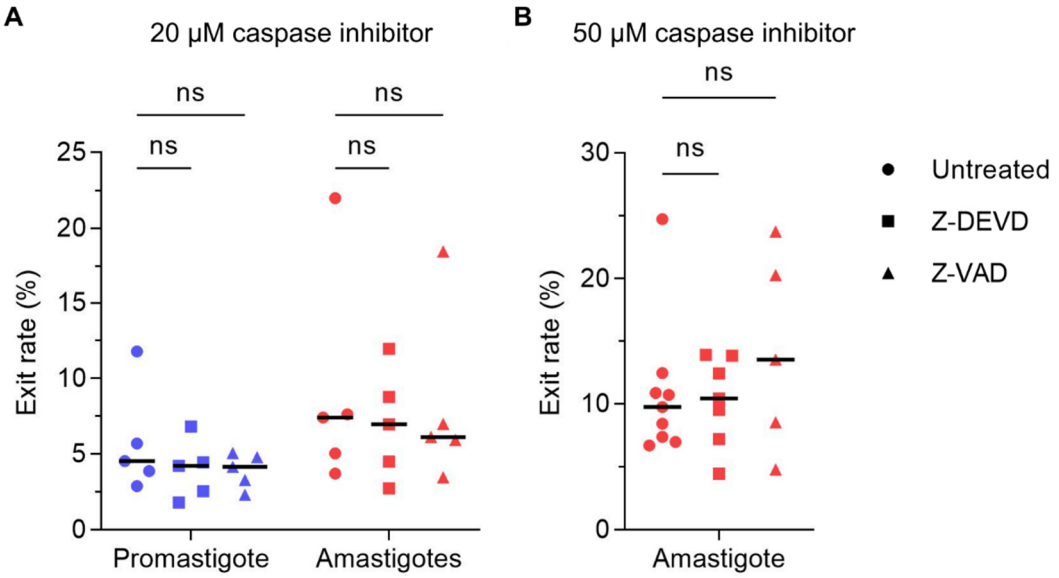

Figure 20: Exit is not reduced by caspase inhibitors during co-incubation.
Caspase-3 inhibitor Z-DEVD or pan-caspase inhibitor Z-VAD were added to the co-incubation assay at 24 h pI, a control sample remained untreated. The exit rates were analyzed by flow cytometry 24 h pI+ 20 h co-incubation. **(A)** Primary infections were done by *Lm*^{DsRed} promastigotes (blue) or amastigotes (red) and 20 µM of the respective inhibitor was used during co-incubation with uninfected M(-). Each dot represents an individual donor with a total of 5 individual donors, N=3. **(B)** Primary infections were done by *Lm*^{mKikume} amastigotes (red) and 50 µM of the respective inhibitor was used during co-incubation with uninfected M(-). Each dot represents an individual donor with a total of nine to five individual donors, N=3-5. Shown are additionally the mean values (black line) for A and B. Significance was determined by ordinary one-way ANOVA with multiple comparison correction by Dunnet test, ns – not significant.

The incubation with 20 µM of either of the inhibitors did not reduce the measured exit rates for promastigotes significantly, with 5.8 %, 4.0 % and 3.9 % for the untreated sample, Z-DEVD and Z-VAD treated sample, respectively. The exit rates of amastigotes were again on a higher level, yet there was no decrease of exit with 9.2 %, 7.0 % and 8.2 % for the samples in the previous order (Figure 20 A). It was apparent that the measurement of exit rates was also subjected to large donor variations, which required a measurement of the untreated sample alongside each treated primary cell sample from the same donor to ensure comparability. Still, with an increased inhibitor concentration of 50 µM, no reduction of exit was observed, even an increase of exit to 14.2 % was measured with the pan-caspase inhibitor Z-VAD, compared to 10.9 % in the untreated and 10.2 % in the Z-DEVD treated sample (Figure 20 B). The donor variation in samples treated by 50 µM Z-VAD ranged from 4.8 % to 23.7 % raising the question whether the inhibitor had an adverse effect on the cells from specific donors.

6.2.2 Inhibition by caspase inhibitors Z-DEVD and Z-VAD occasionally induces cell death

To test if the inhibitors Z-DEVD and Z-VAD impacted the viability of M-CSF derived M(-), M-CSF derived M(-) were incubated with the respective inhibitor or the volume percentage of DMSO, wherein the inhibitors were solved, for 20 h and stained with the PtdSer detecting antibody Apotracker and the live/dead stain Zombie NIR, probing the cell permeability by flow cytometry (Figure 21).

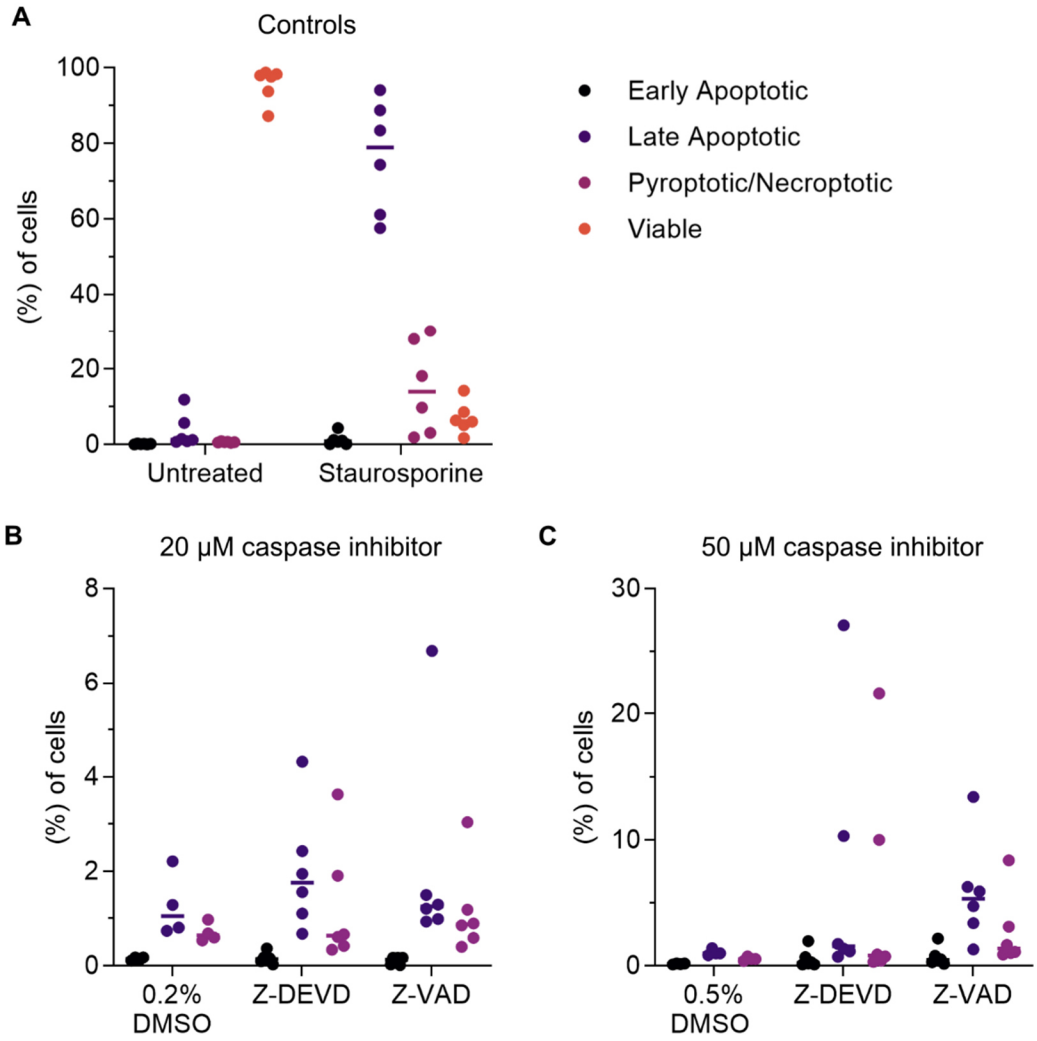

Figure 21: Incubation of hMDMs with caspase inhibitors induces cell death for individual donors. Flow cytometry analysis of uninfected M-CSF derived M(-) incubated with caspase-3 inhibitor Z-DEVD or pan-caspase inhibitor Z-VAD for 20 h and subsequent staining by PtdSer antibody Apotracker green and live/dead stain Zombie NIR. Acquired samples were gated for single cells and categorized by a four-quadrant gate in a bivariate plot of the Apotracker green channel and the Zombie NIR channel to early apoptotic (Apotracker green$^+$, Zombie NIR$^-$), late apoptotic (Apotracker green$^+$, Zombie NIR$^+$) pyroptotic/necroptotic (Apotracker green$^-$, Zombie NIR$^+$) and viable (Apotracker green$^-$, Zombie NIR$^-$). FMO controls served as gating controls. **(A)** As controls, an untreated sample and an apoptosis induced sample treated by 1 µM Staurosporine for 20 h were included. **(B, C)** Samples with 20 µM inhibitor **(B)** and 50 µM **(C)** inhibitor and a control with the respective concentration of the solvent DMSO. Shown is the mean value (colored line) and each dot represents an individual donor with a total of six individual donors, N=3. This experiment was conducted by Bianca Walber under my supervision.

In untreated conditions, a majority of cells was viable, still for some donors a share of late apoptotic cells was detected. The incubation with Staurosporine resulted in 76.5 % late apoptotic cells on average, while 15.2 % were pyroptotic or necroptotic, confirming that the staining procedure is sensitive for the detection of cell death (Figure 21 A). An incubation with 0.2 % DMSO resulted in neglectable shares of late apoptotic and pyroptotic/necroptotic cells. On average, comparable shares were observed for the cells treated with Z-DEVD or Z-VAD, yet some individual donors reacted more sensitive to the treatment with increased cell death rates (Figure 21 B). The same holds true for an increased concentration of the inhibitors, where single donors reacted to the treatment with strongly increased cell death rates, with up to 27.1 % late apoptotic and 21.6 % pyroptotic/necrotic cells with 50 µM Z-DEVD or 13.4 % late apoptotic and 8.3 % pyroptotic/necrotic cells with 50 µM Z-VAD. In addition, Z-VAD induced a more conserved reaction resulting in 7.1 % of late apoptotic cells on average, as opposed to 1.1 % in DMSO treated cells and 5.8 % in Z-DEVD (Figure 21 C).

By addressing apoptosis as a potential mechanism for the amastigote parasite transfer from cell to cell, it was demonstrated that the key enzyme of apoptotic cell death caspase-3 is slightly upregulated in amastigote infected M (-). However, the exit could not be inhibited by the caspase inhibitors Z-DEVD or Z-VAD, administered during the co-incubation. A viability staining of cells treated with said inhibitors revealed adverse effects on M(-) of certain donors in *in vitro* cell culture, resulting in increased cell death rates in comparison to the receptive control condition.

6.3 Parasite proliferation as a driver of exit

The second part of this projects' hypothesis focused on the parasite's proliferation within the host cell as indicator and inducer of parasite exit, which based on the observations by Heyde *et al.* that showed elevated proliferation rates of parasites residing in cells infected after an exit event [23]. The most advanced method for an analysis of *Lm* proliferation is the mKikume reporter protein system [129]. It allows to directly analyze the dynamic process of intracellular proliferation for a defined period of time during infection. To date, data on the parasite's proliferation on a cellular level is lacking in a human infection model and the infection progression has only been derived from measurements of the parasite burden by qPCR or flow cytometry. Therefore, I sought to establish an mKikume expressing *Lm* strain and analyze the parasites proliferation in M(-) infection and its role in exit from human host cells.

6.3.1 Establishing a *Lm*^{mKikume} proliferation reporter strain for *in vitro* infections

I received the *Lm* isolate LRC-L137 with stable expression of the *mKikume* gene from the group of Andreas Müller. In a first attempt to set up the reporter strain in our laboratory, it was

tested whether the newly received strain can be photoconverted, can adapt to the cultivation in biphasic Novy-McNeal-Nicolle medium and is infective for hMDM (Figure 22).

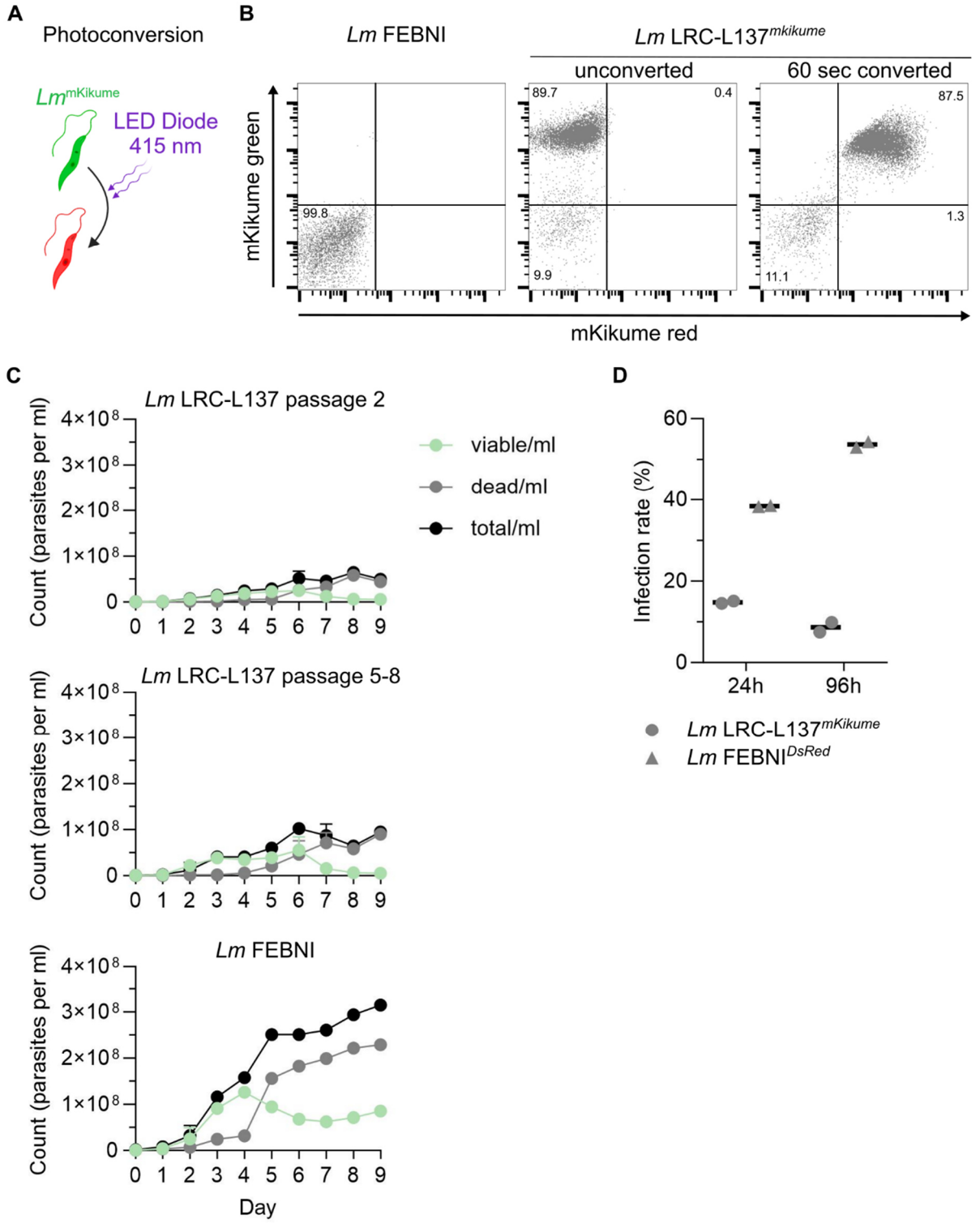

Figure 22: Strain *Lm*^{mKikume} LRC-L137 could not adapt to the culture conditions in blood agar. **(A)** Scheme of the photoconversion of the mKikume fluorescent protein from green to red expressed by *Lm*. **(B)** Flow cytometry analysis of a non-fluorescent *Lm* FEBNI wildtype, an unconverted and converted *Lm* LRC-L137^{mKikume} sample (left to right) from day 3 (d 3) promastigote cultures. **(C)** Growth curves of *Lm* LRC-L137^{mKikume} and *Lm* FEBNI wildtype in promastigote *in vitro* culture, counted manually in a 1:10 dilution using a Neubauer improved counting chamber. Shown are the values from a single count or mean values + SD if samples were counted twice. **(D)** Infection rate analyzed by flow cytometry after infection of M-CSF derived M(-) by *Lm* LRC-L137^{mKikume} or *Lm*^{DsRed} promastigotes from the stationary phase at 24 h and 96 h pI. Shown are mean values (black line) and dots for each individual donor, N=1.

By the photoconversion with violet light, the mKikume protein can be converted from green to red fluorescence (Figure 22 A) [138]. To confirm a constitutive expression and test the set-up for photoconversion, *Lm*^{mKikume} LRC-L137 promastigotes were illuminated for 60 sec with violet light and analyzed by flow cytometry. Illuminated *Lm* FEBNI wildtype promastigotes and unconverted *Lm*^{mKikume} LRC-L137 promastigotes were used as controls (Figure 22 B). *Lm* FEBNI wildtype promastigotes showed neither a fluorescent signal in the green nor the red fluorescence channel for 99.8 % of the recorded events, the unconverted sample was dominantly detected in the green fluorescence channel with 89.7 % of the events, 9.9 % were detected in the non-fluorescent gate which likely resulted from dead parasites in the sample. The converted sample with *Lm*^{mKikume} LRC-L137 promastigotes showed a shift to a red fluorescence for the majority of events, a share of 11.1 % was detected in the non-fluorescent gate, again likely corresponding to a dead subpopulation of parasites (Figure 22 B). In this experiment, the parasites retained a green fluorescence signal despite the conversion, likely due to an incomplete conversion of the produced mKikume protein. Reasons for this could be (i) the conversion of parasites in suspension where parasites diffuse freely and (ii) the use of medium with phenol red that partly absorbs the conversion light.

The cultivation of *Lm*^{mKikume} LRC-L137 promastigotes in biphasic Novy-McNeal-Nicolle medium resulted in a linear increase of viable parasites during their 2nd passage, reaching its peak at d 6 after the last passage with 2.5*10^7. The total parasite count reached a plateau at the same d with a maximum of 6.5*10^7 total parasites. At later passages, a steeper increase of viable parasites was observed that reached a higher peak again at d 6 with 5.6*10^7 parasites. The total number of parasites increased to 1.0*10^8. The *Lm* FEBNI wildtype strain, which is regularly cultivated in biphasic Novy-McNeal-Nicolle medium and used for *in vitro* infection of hMDM, grew in a logarithmic phase and reached its peak already at d 4 and a count of 1.3*10^8 viable parasites. A plateau of the total parasite was reached at d 5 and a maximum of 3.1*10^8 (Figure 22 C). In comparison, the *Lm*^{mKikume} LRC-L137 promastigotes grew slower and without a sigmoidal phase, also the total parasite number was only a third or less of the regularly used *Lm* FEBNI wildtype strain. A single realization of an infection experiment with M-CSF derived M(-) also showed strongly decreased infection rates at 24 h pI and a decrease instead of an increase of said rate at 96 h pI of the *Lm*^{mKikume} LRC-L137 strain compared to a *Lm* FEBNI^{DsRed} strain (Figure 22 D). Moreover, the *Lm*^{mKikume} LRC-L137 were unable to transform into amastigotes under axenic culture conditions.

As a mitigation strategy, it was tried to introduce the *mKikume* gene into the 18S rRNA (SSU) locus of the customary *Lm* FEBNI wildtype strain by homologous recombination upon transfection with linearized DNA coding for the reporter protein (Figure 23).

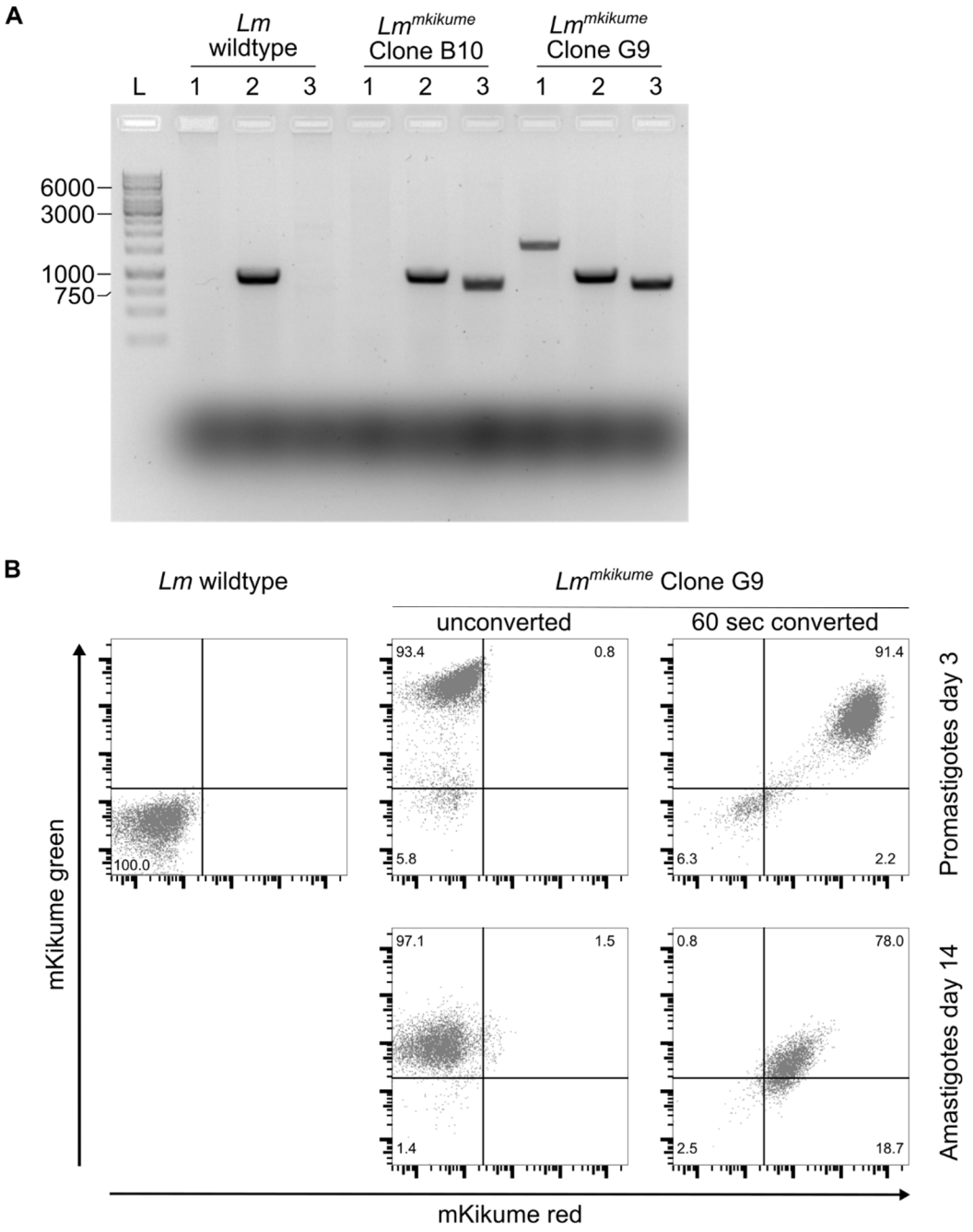

Figure 23: Integration of the *mKikume* gene into the 18S rRNA locus of *Lm* FEBNI.
(A) Analytical gel electrophoresis of PCR products by DNA of *Lm* wildtype, *Lm*^{mKikume} clone B10 and G9 and primers binding to the upstream UTR and *mKikume* (1) (5'SSU_fwd, mKikume_UTR_rev), in the up- and downstream UTR (2) (5'SSU_fwd, 3'SSU_rev) and in the resistance cassette (3) (Hyg_fwd, 3'SSU_rev). 4 µl of the PCR product plus 2 µl loading dye were loaded on a 1% agarose gel and separated at 100 V, 400 mA for 40 min. GeneRuler 1 kb is applied as DNA size ladder (L), the size of the reference fragments is indicated in bp. **(B)** Flow cytometry analysis of a non-fluorescent *Lm* wildtype, an unconverted and converted *Lm*^{mKikume} clone G9 sample (top row, left to right) from d 3 promastigote culture and d 14 axenic amastigote culture (bottom row, left to right).

After transfection of d 3 *Lm* FEBNI wildtype promastigotes, resistance selection and limiting dilution, the two potential clones *Lm*^{mKikume} B10 and G9 were isolated, and their genetic modification was probed by PCR. The first reaction assessed the full insertion of the *mKikume* gene and with the primers used, a fragment of 1715 base pairs (bp) was expected. A

corresponding signal was only observed for the clone G9 but not in clone B10 and, as expected, not in the *Lm* wildtype (Figure 23 A(1)). The second reaction assessed the presence of an intact 18S locus with an expected fragment length of 968 bp and theoretically for an 18S locus with an insertion of *mKikume* and the resistance marker with an expected length of 4871 bp. The first fragment was observed in all three probed samples, the insertion for clone G9 was therefore likely heterozygous insertion. The second fragment was not detected for both clones, even though an insertion of *mKikume* was seen in the first PCR in clone G9 which likely resulted from an insufficient elongation time for this large fragment (Figure 23 A(2)). The third reaction tested the insertion of the selective marker into the 18S locus with an expected length of 847 bp. Corresponding signals were observed for both potential clones (Figure 23 A(3)). The presence of the selective marker for clone B10 explains that it surpassed the resistance selection and limiting dilution, yet because of the missing *mKikume* gene, only the clone G9 was continued.

The presence of the mKikume protein in *Lm*^{mKikume} clone G9 promastigotes was evaluated by its ability for photoconversion analyzed by flow cytometry (Figure 23 B). *Lm* wildtype promastigotes were negative in both, the red and green fluorescence channel. An unconverted sample of *Lm*^{mKikume} clone G9 was solely positive for the green fluorescence channel, with 93.4 % of the recorded events. The photoconversion shifted the 91.4 % of analyzed events to a red fluorescence, whereby the mKikume green fluorescence intensity was slightly decreased compared to the unconverted control (Figure 23 B, upper panel). *Lm*^{mKikume} clone G9 parasites were also able to transform to amastigotes in axenic culture and a signal of unconverted mKikume protein was detected for 97.1 % of the recorded events. After conversion, 78.0 % of the measured amastigotes shifted to a red fluorescence and 16.7 % of the events were solely positive for the red, converted mKikume protein fluorescence (Figure 23 B, lower panel). Again, the conversion appeared incomplete with only slight reduction of the green fluorescence signal, which is attributed to the described reasons for Figure 22 B. With the *mKikume* gene insertion and its expression tested by photoconversion and fluorescence, the *Lm*^{mKikume} clone G9 was confirmed successful and is hereafter termed *Lm*^{mKikume}.

6.3.2 *Lm*^{mKikume} allows analysis of intracellular parasite proliferation in human M(-)

With the *Lm*^{mKikume} strain at hand, it was possible to determine the parasites proliferation rate after infection and within time increments of 24 h from 0 h to 72 h pI, which includes the relevant time intervals from the previous exit experiments (Figure 24). The parasite proliferation is measured as a ratio of green and red fluorescence after a fluorescence recovery after conversion (FRAC), wherein the parasites can reduce the red fluorescent mKikume protein by fission and increase the green fluorescent protein by a reproduction of mKikume protein. For comparability, the proliferation is normalized to values from 1 to 0 by an unconverted sample (maximal proliferation, “1”) and a sample converted prior to the analysis (minimal proliferation, “0”) (Figure 24 A). Because the proliferation is analyzed by flow cytometry, the green and red fluorescence is measured per infected cell and is an average of multiple parasites’ fluorescence if the cell is burdened with more than one parasite. In other words, the resolution of proliferation is not on the parasite level but on the host cell level, potentially including proliferation of multiple parasites per cell.

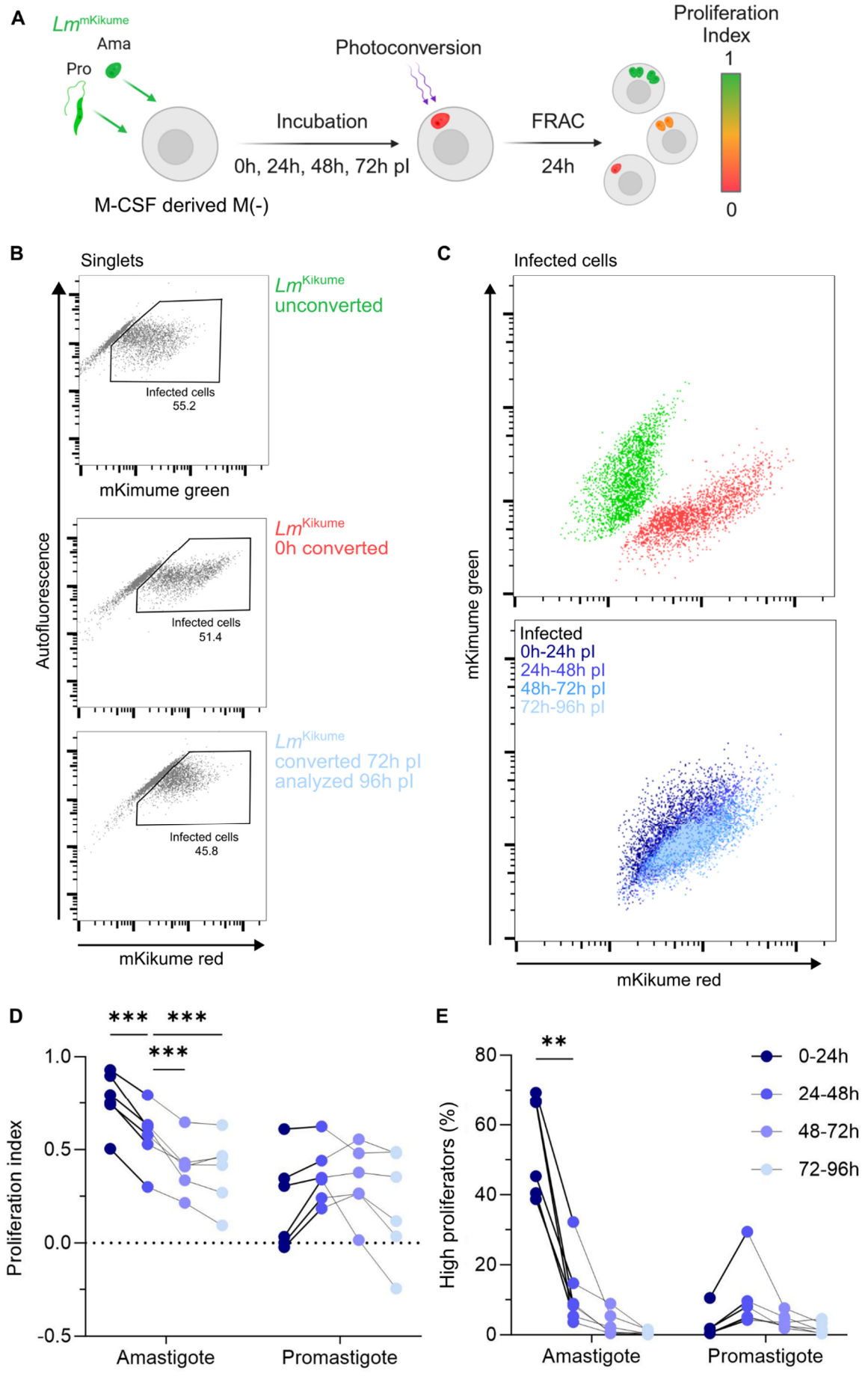

Figure 24: The protein reporter mKikume allows analysis of intracellular parasite proliferation in *in vitro* infections of human M(-).

To Fig. 24 – **(A)** Scheme for the flow cytometry analysis of the parasite proliferation after initial infection of M-CSF derived M(-) by promastigotes or axenic amastigotes during the fluorescence recovery after conversion (FRAC) of 24 h. **(B)** Gating for the detection of infected, single cells in dot plots of *Autofluorescence x mKikume green* for the unconverted control and *Autofluorescence x mKikume red* for the 0h converted control and all samples after 24 h FRAC. **(C)** Dot plot of infected cell displaying the fluorescence ration in *mKikume green x mKikume red* of the unconverted control (green) and the 0 h converted control (red), as well as the samples from 0-24 h pI to 72-72 h pI (light to dark blue). Shown are representative samples of a single individual donor **(B, C)**. **(D)** Proliferation index calculated by Formula (2) of infecting parasites over time for promastigote and amastigote infections in M(-). **(E)** Share of high proliferating parasite populations according to gating in Figure 11 of infecting parasites over time for promastigote and amastigote infections in M(-). Shown are values for individual donors connected by lines with a total of six individual donors, N=3 **(D, E)**. Significance was determined by 2way ANOVA with multiple comparison correction by Holm-Šidák test, $^{**}p < 0.01$, $^{***}p < 0.001$.

At the respective time points, the infected samples were analyzed by flow cytometry and the recorded events were gated for singlets as in previous experiments (plots not shown). Infected cells were then gated by using a dot plot of autofluorescence and either mKikume green (unconverted control) or mKikume red (0h converted control, all samples) (Figure 24 B). It was shown before that the signal ratio of cells in the autofluorescence channel and the mKikume green or mKikume red channel, respectively, is changed differently upon infection, allowing a more precise gating of infected cells [129]. The exemplarily shown plots from amastigote infected M(-) showed comparable infection rates from 55.2 % in the unconverted control to 45.8 % in the last analyzed time point at 96 h pI (Figure 24 B). Even though parasites show fluorescence in both channels, mKikume green and red, infected events of all samples analyzed 24 h after conversion were gated via the mKikume red channel, a back-gating in the mKikume green channel confirmed that all infected cells were reliably detected (plots not shown). Both controls showed a distinct ratio of green and red fluorescence in representative amastigote infected samples (Figure 24 C, upper plot), confirming that the photoconversion within the cells was successful and allows a normalization of the values from the other samples. Already in the dot plot of amastigote infected cells, it can be observed that the events from earlier time points shift towards a higher green and lower red fluorescence (Figure 24 C, lower plot, dark blue), an effect that is gradually decreased to the later pI time points (light blue), indicating a higher proliferation shortly after infection.

Indeed, the proliferation index of intracellular amastigotes was the highest within the first 24 h of infection and decreased significantly and linearly within the next 48 h for each donor. The proliferation level then stabilized from 72 h to 96 h pI, with slight in- or decrease in dependence of the individual donor (Figure 24 D). In promastigote infected samples, variations between individual donors for the proliferation index were observable, yet two different trends occurred. One group of three donors showed no proliferation within the d 1 of infection, which was then increased for the time from 24 h to 72 h pI and decreased 96 h pI. In the other group of donors, parasites had a proliferation index above 0.25 within 24 h pI and the proliferation remained stable over the following 72 h of infection, without the drop-off at d 4 that was seen for the other group (Figure 24 D).

Lastly, the share of cells harboring high proliferating parasites was determined by the gating shown in Figure 11. In well accordance with the proliferation index, 69.3 % to 38.7 % of the infecting amastigotes were high proliferators in the first 24 h. Their share then decreased steeply and significantly after 48 h pI, a trend that was proceeded but weakened for the next 48 h. In promastigote infections, the share of high proliferators was overall low, but uniformly showed an increase at 48 h pI with up to 29.4 %, which decreased below 10 % for all donors at 72 h and 96 h pI (Figure 24 E).

6.3.3 Increased amastigote proliferation is an inducer of parasite transfer

To elucidate the role of proliferation in the parasites' cell to cell transfer, I used the *Lm*^{mKikume} proliferation reporter strain in the established co-incubation assay and analyzed the proliferation index in initially infected M(-) and M(-), which were infected after exit (Figure 25).

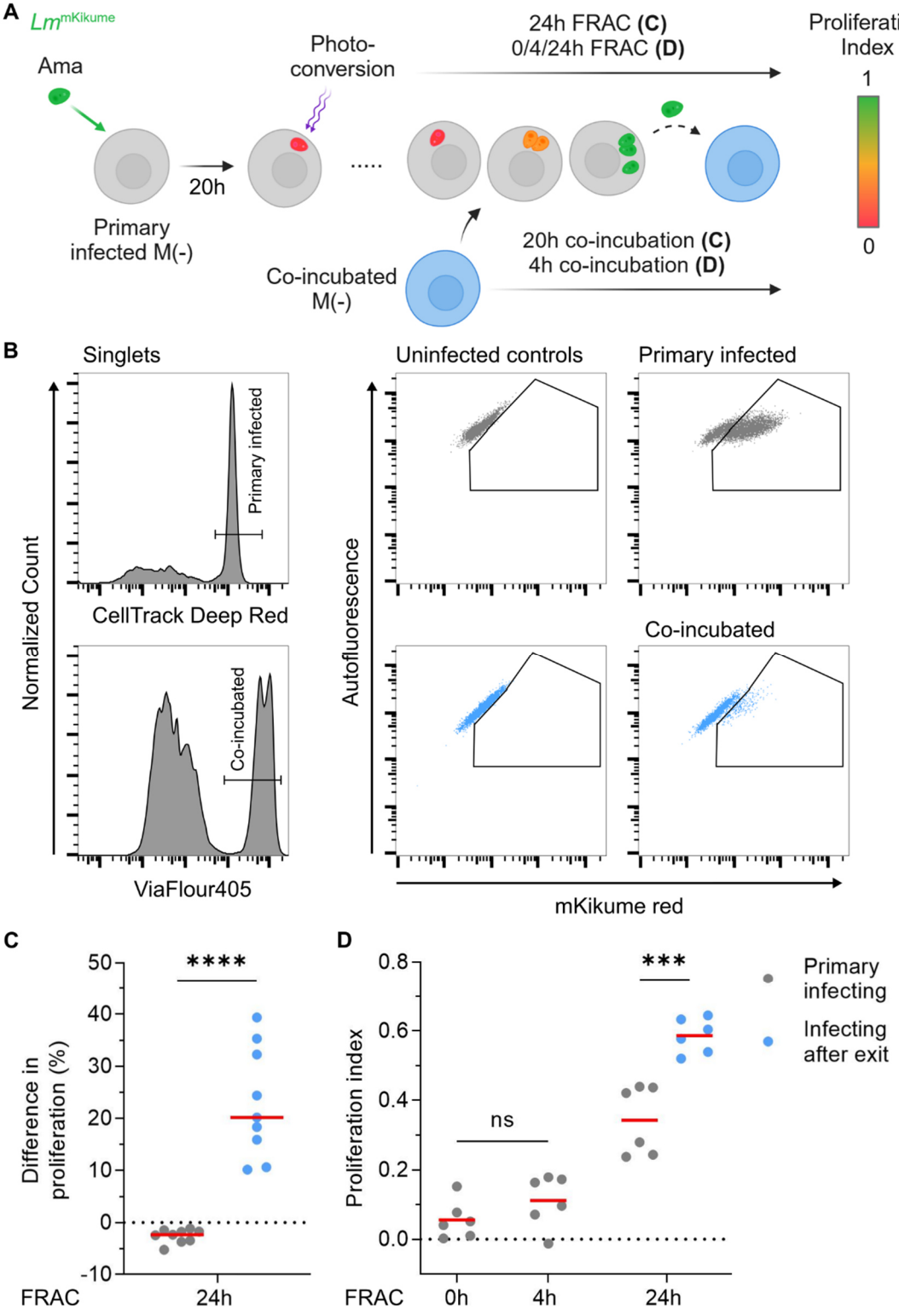

Figure 25: Parasite proliferation is increased prior to amastigote exit.
(A) Schematic of the co-incubation assay with axenic amastigote of proliferation reporter strain *Lm*^{mKikume} in primary infected and recipient M(-) by flow cytometry analysis. **(B)** Adapted gating strategy for single, primary infected cells (CellTracker Deep Red^{+}) and co-incubated cells (ViaFluor405^{+}), as well as the infected cell fraction of both (mKikume red^{+}). **(C)** In- or decrease of proliferation in either primary infected cells (CellTracker Deep Red^{+} in grey) or cells infected after exit (ViaFluor405^{+} in blue) calculated by Formula (2) at 24 h pI plus 20 h of co-incubation. Each dot represents an individual donor plus the mean value (red line) with a total of nine donors, N=5 **(D)** Pathogen proliferation calculated by Formula (2) in the respective cell population 40 h pI plus 4 h of co-incubation and after the indicated time for FRAC. Each dot represents an individual donor plus the mean value (red line) with a total of six individual donors, N=3. Significance was determined by two-tailed unpaired t-test, ns not significant, ***$p < 0.001$, ****$p < 0.0001$.

M(-) labeled by CellTracker Deep Red were primary infected by axenic *Lm*^{mKikume} amastigotes, which were converted 20 h pI. At 24 h pI, VF405-labeled M(-) were added for 20 h of co-incubation (24 h FRAC) (Figure 25 A). Afterwards, the cells were analyzed by flow cytometry and the differently labelled M(-) were separately analyzed by a range gate in the respective channel (Figure 25 B, left panel). Then, infected cells were gated in both populations and the proliferation of intracellular parasite was determined (Figure 25 B, right panel). A separate experiment demonstrated that the different fluorescent labels used for M(-) had no effect on the fluorescence of mKikume red and green (Figure 12)

After 20 h co-incubation, on average, the proliferation of parasites infecting after exit was significantly increased by 22.9 % over the baseline from all infecting parasites, while primary infected cells were decreased by 2.6 % (Figure 25 C). With the long incubation time, it cannot be determined whether the proliferation is increased prior to the exit or after residing in cells after the transfer. Therefore, the co-incubation time was shortened to 4 h (Figure 25 D) in order to limit the time for parasite proliferation after uptake into the new host cells. Within that time period no significant increase in the proliferation was measured, demonstrated by samples converted at the end (0 h FRAC) or at the beginning (4 h FRAC) of the co-incubation. If the cells were converted 24 h (24 h FRAC) prior to the analysis and co-incubated cells were added for the last 4 h of that period, the significant difference in the proliferation rate in primary infected cells versus cells infected after exit was restored which confirmed that the proliferation must have been upregulated prior to the parasites transfer, as the proliferation during the 4 h co-incubation time itself can be neglected.

From the co-incubation experiment with *Lm*^{mKikume} amastigotes we were also able to derive the exit rates, with the experimental advantage to be able to correlate proliferation with the measured exit (Figure 26).

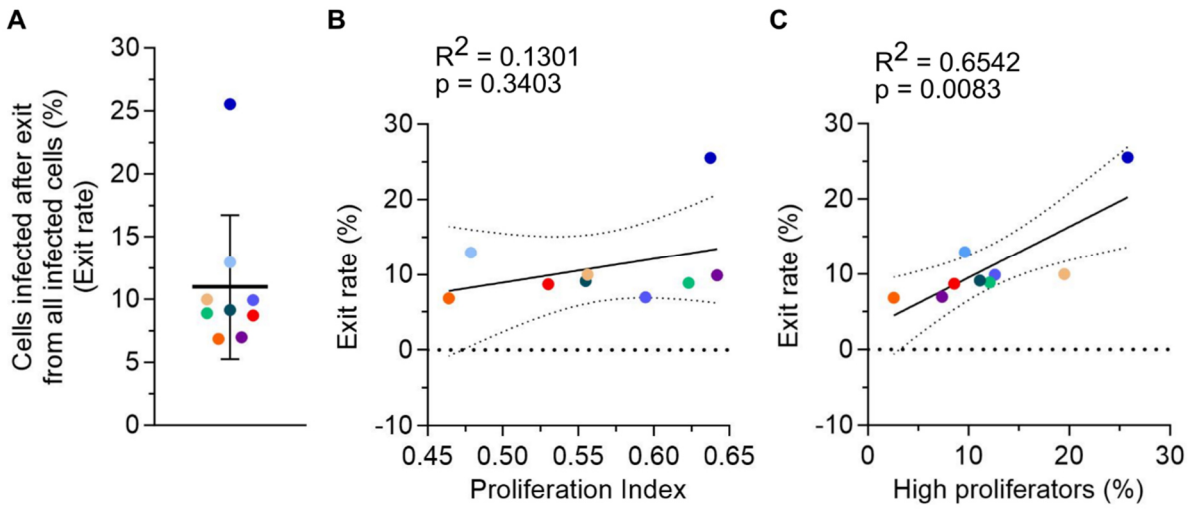

Figure 26: Correlation of proliferation and parasite exit.

To Fig. 26 – **(A)** Quantification of exit from co-incubation experiments with *Lm*^{mKikume} axenic amastigote infected M(-) from experiments shown in Figure 25. Shown is the mean value + standard deviation. **(B, C)** Scatter plots of the exit rate versus parasite proliferation index in primary infected M(-)**(B)** and the share of high proliferating populations according to gating in Figure 11 **(C)**. Each dot represents an individual donor with a total of nine individual donors, N=5, for A to C. Linear correlation by Pearson correlation coefficient with the strength of correlation shown by the coefficient of determination R^2. Significance of the linear correlation tested with a two-tailed test, not significant $p > 0.05$, significant $p < 0.05$ correlation **(B, C)**.

The exit rates of individual donors from the same experiment shown in Figure 25 averaged an exit rate of 11.0 ± 5.7 % but it ranged from 25.5 % to 6.8 % resulting in a large standard deviation (Figure 26 A). Yet, higher proliferation indices of certain donors did not correlate significantly with their respective exit rate (Figure 26 B). Strikingly, the correlation of high proliferating parasite populations with exit revealed a strong and significant dependence of both metrics (Figure 26 C). This indicates that not the average proliferation of a whole sample is relevant for the occasion of exit but explicitly the share of high proliferating parasite populations determines whether increased or decreased levels of exit are observed.

6.3.4 Cells positive for caspase-3 activity harbor parasites with higher proliferation

After connecting exit rates with increased parasite proliferation and caspase-3 activity with amastigote infected M(-), I sought to connect the apoptosis with increased proliferation as well. Therefore, *Lm*^{mKikume} infected cells were converted 20 h pI and incubated with caspase-3 substrate NucView405 from 24 h pI to 44 h pI, according to the experimental setup in Figure 26 A. The proliferation index was calculated for the caspase-3$^+$ and caspase-3$^-$ fraction and compared (Figure 27). As described in the methods section, the proliferation index is derived from the ratio of green and red fluorescence of a specimen, normalized to the same ratio of the unconverted control and the 0h converted control (Formula (2)). The in-depth analysis of the controls revealed that ratio of the 0h converted control is significantly different in the small caspase-3$^+$ cell fraction compared to all cells or caspase-3$^-$ cells (Figure 27 A). The fluorescence ratio of the unconverted control was unaffected of this phenomenon. In conclusion, proliferation index values were calculated using the fluorescence ratio of the controls that were also either caspase-3$^+$or caspase-3$^-$, respectively.

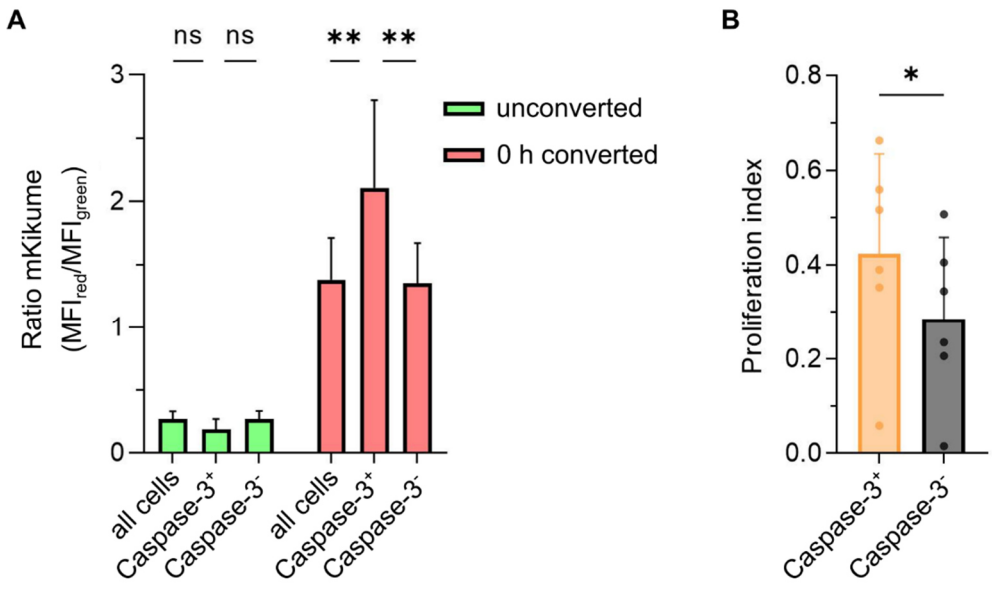

Figure 27: Parasite proliferation is increased in cells displaying caspase-3 activity.
Flow cytometry analysis of proliferation and caspase-3 activity in infected M(-). Cells were infected by *Lm*^{mKikume} axenic amastigote, 20 h pI intracellular parasites were photoconverted and 24 h pI caspase-3 reporter NucView405 was added with a concentration of 2.5 µM. Samples were analyzed 44 h pI. **(A)** Ratio of the mKikume fluorescence MFI_{red} to MFI_{green} that is used in Formula (2) for the unconverted control (green) and the 0 h converted control, analyzed for all cells, only caspase-3$^+$ and caspase-3$^-$ cells. **(B)** Proliferation index of parasites in caspase-3$^+$ and caspase-3$^-$ cells, calculated by Formula (2) using the respective normalization controls derived from caspase-3$^+$ and caspase-3$^-$ populations shown in (A). Shown are mean values + SD of six individual donors, N=3. Significance was determined by 2way ANOVA with multiple comparison correction by Holm-Šidák test **(A)** and two-tailed paired t-test **(B)**, ns not significant, *$p < 0.05$, **$p < 0.01$.

The proliferation for both populations showed vast differences between replicates, giving proliferation indices of 0.42 ± 0.21 for the caspase-3$^+$ fraction and 0.29 ± 0.17 for the negative. By the statistical comparison, the proliferation index in cells showing caspase-3 activity was significantly higher than in those negative for caspase-3 activity at 44 h pI (Figure 27 B).

In summary, the presented data show a conclusive correlation of the parasites' proliferation with the occurrence of exit, as well as with the induction of caspase-3 activity. Yet, the infection system with axenic amastigotes lacks a control to validate that the parasite's ability of high proliferation is indeed the causative process for its exit. Therefore, the additional, methodical aim arose during this project, to establish amastigote infection system with non-proliferating but viable parasites.

6.4 Attempt to establish an amastigote infection model with parasites unable to proliferate

6.4.1 Generation of killed but metabolically active amastigotes

As a strategy to hinder various pathogen replication in medical blood and plasma products is the cross-linking of DNA by the reagent amotosalen and radiation by UVA light [132]. More specifically for *L.* parasites, amotosalen was utilized to generate non-replicating promastigotes for the genus *L. infantum*, called 'killed but metabolically active' (KBMA) [130]. To test whether proliferation can be impaired in amastigotes as well, I adapted the amotosalen treatment for *Lm* axenic amastigote culture and counted the parasites post-treatment (Figure 28).

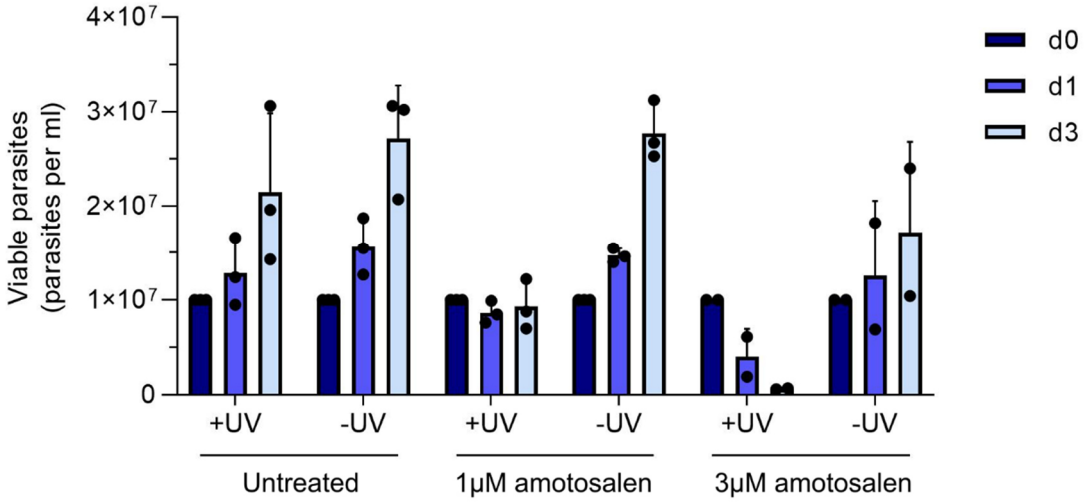

Figure 28: KBMA treatment of axenic amastigotes arrests proliferation *in vitro.*
Quantification of viable amastigotes after KBMA treatment. Amastigotes were incubated with 1 µM or 3 µM amotosalen or remained untreated for 30 min and were subsequently illuminated by UVA light for 40 s. The respective controls were not illuminated by UVA light. Amastigotes were counted manually using a Neubauer improved counting chamber and were adjusted to $1*10^7$ parasites/ml at d 0 and counted again at d 1 and d 3. Shown are the mean values + SD and the counting results of each replicate, N=3 (Untreated, 1 µM amotosalen) or N=2 (3 µM amotosalen).

Independent of the UVA radiation, amastigotes not treated with amotosalen remained proliferative after reseeding $1*10^7$ parasites per ml to the axenic culture, with a viable parasite count of $1.28*10^7 \pm 0.36*10^7$ at d 1 and $2.1*10^7 \pm 0.83*10^7$ at d 3 for the radiated population, while the non-radiated population had $1.56*10^7 \pm 0.30*10^7$ and $2.71*10^7 \pm 0.56*10^7$ at the same time points. When treated with 1 µM amotosalen and radiation by UVA light, the count of viable parasites stagnated around the reseeded number of viable parasites with an average of $0.87*10^7 \pm 0.12*10^7$ at d 1 and $0.93*10^7 \pm 0.26*10^7$ at d 3. The parasites without UVA light were still able to proliferate like the entirely untreated sample, reaching $2.77*10^7 \pm 0.31*10^7$ at d 3 post-treatment. A treatment with 3 µM amotosalen resulted in a loss of viable parasites at d 1 and d 3 after the UVA treatment, while the same amotosalen concentration without UVA treatment caused unchanged viable parasite counts for d 3 in one replicate and allowed

proliferation in the other replicate indicating adverse effect of the amotosalen treatment alone (Figure 28). Because no increase in viable parasite counts were observed in samples treated with 1 µM amotosalen and UVA light, this condition was used in subsequent experiments as KBMA treatment.

6.4.2 KBMA treatment of axenic amastigotes does not change infection rate, proliferation and exit rate compared to untreated parasites

To test if the impaired proliferation ability of amotosalen treated parasites has implications on their cell-to-cell transfer, their infectivity in M(-) *in vitro* was measured by flow cytometry, followed by the co-incubation assay for the exit measurement with KBMA amastigotes versus untreated amastigotes (Figure 29).

In the gating strategy for the detection of infecting parasites by the DsRed fluorophore, a bivariate graph of the DsRed channel against the autofluorescence channel was used granting a more sensitive detection of infected cells as shown by mKikume red gating, in case the KBMA treatment would reduce the parasites fluorescence signal (Figure 29). Yet, both samples, M(-) infected by Lm^{DsRed} KBMA amastigotes or untreated Lm^{DsRed} amastigotes, respectively, gave an equally distinct fluorescent signal separated from the uninfected population (Figure 29 A). The infection rates were continuous over time averaging 67.1 ± 10.3 %, 63.7 ± 11.0 % and 67.6 ± 12.2 % after 3 h, 24 h and 48 h pI, respectively by the untreated Lm^{DsRed}. The rates for Lm^{DsRed} KBMA parasites were slightly reduced in comparison to untreated Lm^{DsRed} with an average of 58.7 ± 13.2 %, 49.9 ± 12.5 % and 54.6 ± 13.2 %. However, the infection was stable over time, without significant loss of intracellular parasites (Figure 29 B). With the positive outcome of the preliminary experiment, I proceeded with the exit measurement by co-incubation. The experimental procedure was refined by an additional live/dead staining that was included into the gating strategy (Figure 29 C).

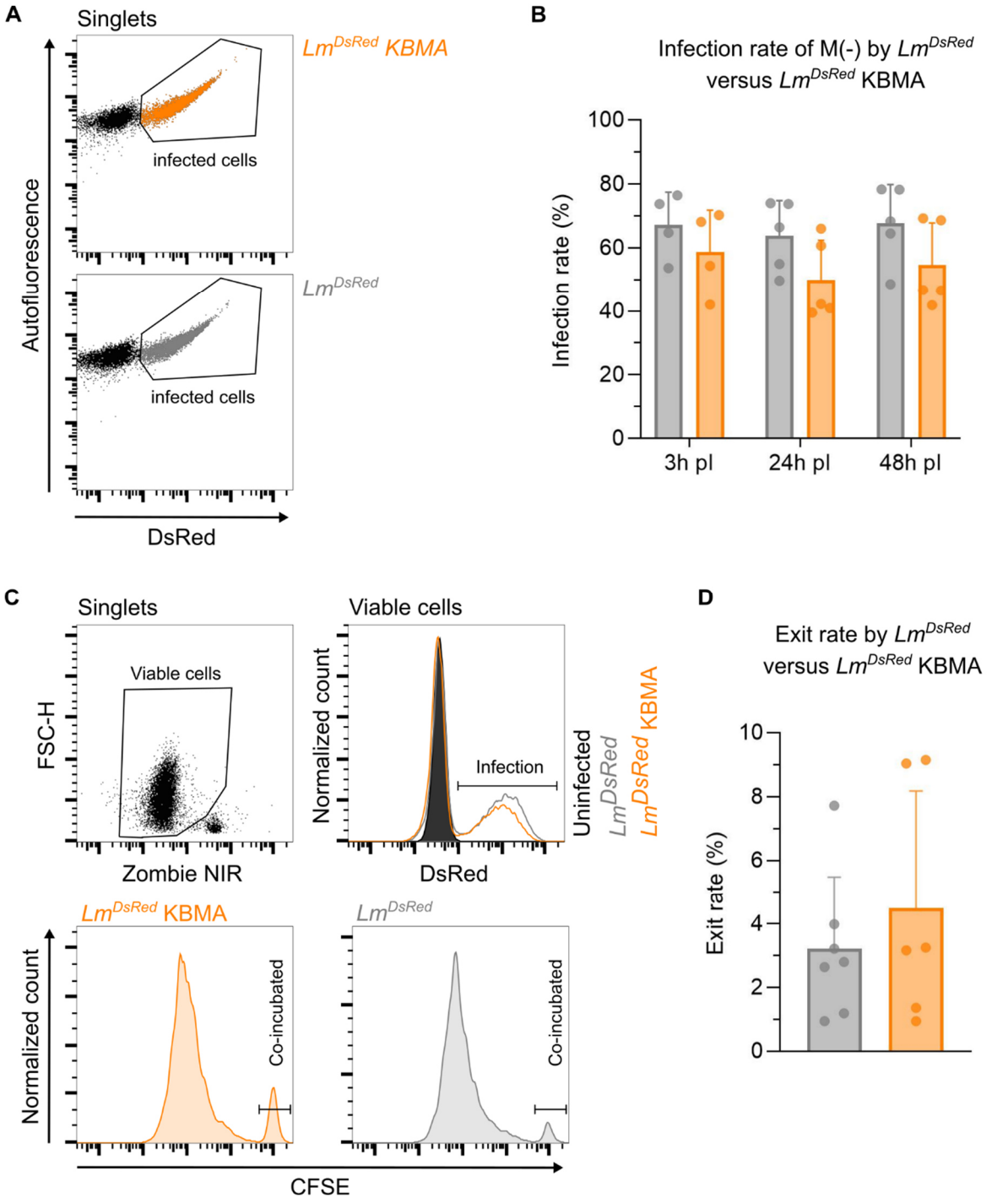

Figure 29: KBMA treatment of amastigotes has no influence on the infection rate and exit from hMDM.
(A) Gating of infected cells based on representative samples of M(-) infected by *Lm*^{DsRed} (orange) or *Lm*^{DsRed} (grey) KBMA amastigotes 24 h pI using a bivariate graph of *Autofluorescence x DsRed*. **(B)** Infection rate of *Lm*^{DsRed} or *Lm*^{DsRed} KBMA amastigotes at 3 h, 24 h and 48 h pI, analyzed by flow cytometry. Shown is a bar graph with mean values + SD and dots for each individual donor with a total of four donors, N=2. **(C, D)** Co-incubation assay of M(-) infected by axenic *Lm*^{DsRed} or *Lm*^{DsRed} KBMA amastigotes and addition of uninfected M(-) at 24 h pI with subsequent flow cytometry analysis at 44 h pI **(C)** Adapted gating strategy for the co-incubation assay with detection of viable cells (Zombie NIR^{-}), infected cells (DsRed^{+}) and subsequent detection of the infected, co-incubated fraction (CFSE^{+}). **(D)** Exit rate from the co-incubation assay shown as bar graph with mean values + SD and dots for each individual donors with a total of six to seven donors, N=3.

The dot plots from the previous experiment showed that the autofluorescence channel was not necessary to detect KBMA parasites (Figure 29 A) and the infected populations were gated in a histogram followed by a detection of exit events by co-incubated M(-) ($CFSE^+$) in subsequent experiments (Figure 29 C). Untreated parasites averaged exit rates of 3.2 ± 2.3 % with a vast variation between donors ranging from 0.9 % to 7.7 %. For the KBMA parasites, the average exit rate was 4.5 ± 3.7 % with a comparable donor variation from 0.9 % to 9.2 % (Figure 29 D). Contrary to the expectations, the exit rate of KBMA parasites was rather increased instead of decreased compared to untreated parasites, raising the question whether counting viable parasites after KBMA treatment is sufficient to describe their proliferative behavior and if the treatment is capable of preventing proliferation of parasites intracellularly. Therefore, instead of DsRed-expressing parasites, the mKikume proliferation reporter system was employed to further analyze the proliferative behavior of KBMA parasites post-treatment (Figure 30).

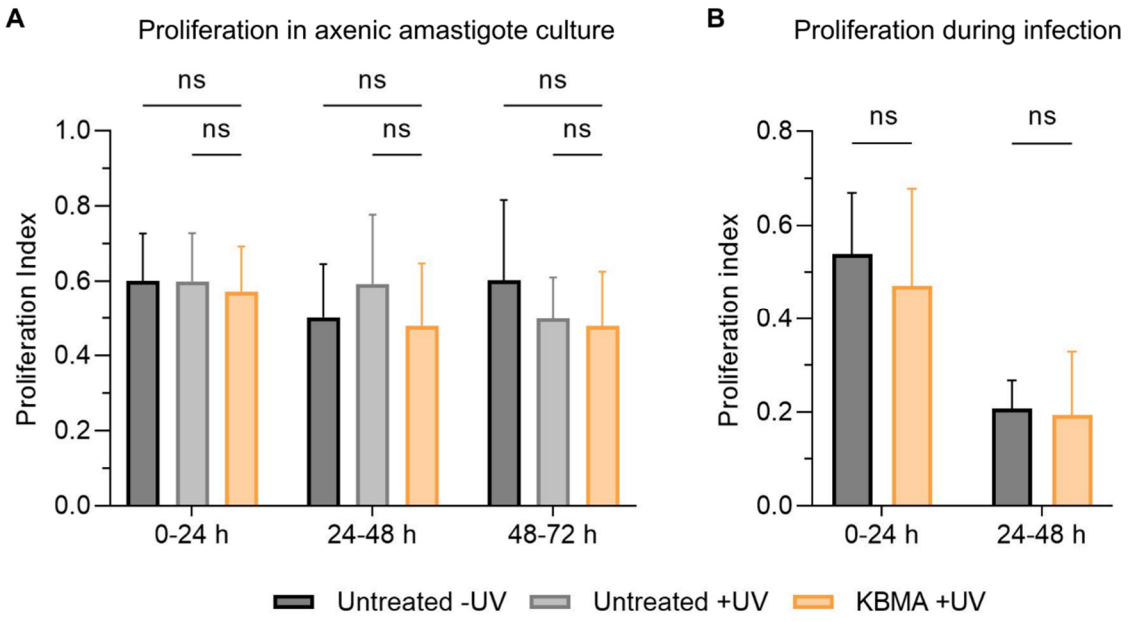

Figure 30: Proliferation reporter mKikume reveals unchanged replication of amastigotes after KBMA treatment.
(A) Amastigote proliferation in *in vitro* culture analyzed by flow cytometry. *Lm*^{mKikume} amastigotes were treated with 1 µM amotosalen and illuminated by UV light or remained untreated with and without illumination by UV light. The mKikume parasites were photoconverted at 0 h, 24 h and 48 h after treatment and mKikume fluorescence was measured after a FRAC of 24 h, the proliferation index was calculated by Formula (2) using the respective controls (not shown). Shown are mean values + SD, N=3. **(B)** Intracellular amastigote proliferation after infection of M(-). *Lm*^{mKikume} amastigotes were treated with 1 µM amotosalen and illuminated by UV light or remained untreated without illumination by UV light and were used for infection of M-CSF derived M(-). Intracellular parasites were photoconverted 0 h and 24 h pI and samples were analyzed after 24 h FRAC. The proliferation index was calculated by Formula (2) using the respective controls (not shown). Shown are mean values + SD of 6 individual donors, N=3. Significance was determined by 2way ANOVA with multiple comparison correction by Holm-Šidák test, ns – not significant. Experiment conducted by Lisa Müller.

The proliferation index was determined for the 72 h after the treatment and reseeding into axenic amastigote culture in 24 h intervals. The resulting data showed a relatively constant proliferation within that period for the untreated parasites with and without illumination by UV

light (Figure 30 A). Surprisingly, the KBMA treatment of parasites did not result in a significant reduction of the proliferation index at any given time-point compared to the controls. Intracellular parasites presented a proliferation index of 0.54 ± 0.13 in the first 24 h pI that dropped to 0.47 ± 0.21 in the second 24 h of infection (Figure 30 B). Again, the KBMA treated parasites had the same proliferative behavior after infection as the untreated control. In conclusion, the treatment of axenic amastigotes by 1 µM amotosalen and subsequent UV illumination was insufficient to produce KBMA parasites.

6.4.3 Generation of non-proliferating parasites by a gene knockout of *LmjF22.1410*

In parallel and as a mitigation strategy, a proliferation arrest in parasites was attempted by specific genetic modification of *Lm* parasites. A previous publication revealed that the knockout of a *centrin* gene in *L. braziliensis* leads to attenuated parasites unable to proliferate in their amastigote form [134]. A homolog protein is expressed in *Lm* by the gene *LmjF22.1410*. By using a CRISPR-Cas9 based gene knockout approach [155], an ablation of the gene was attempted in $Lm^{Cas9/T7}$ parasites (Figure 31).

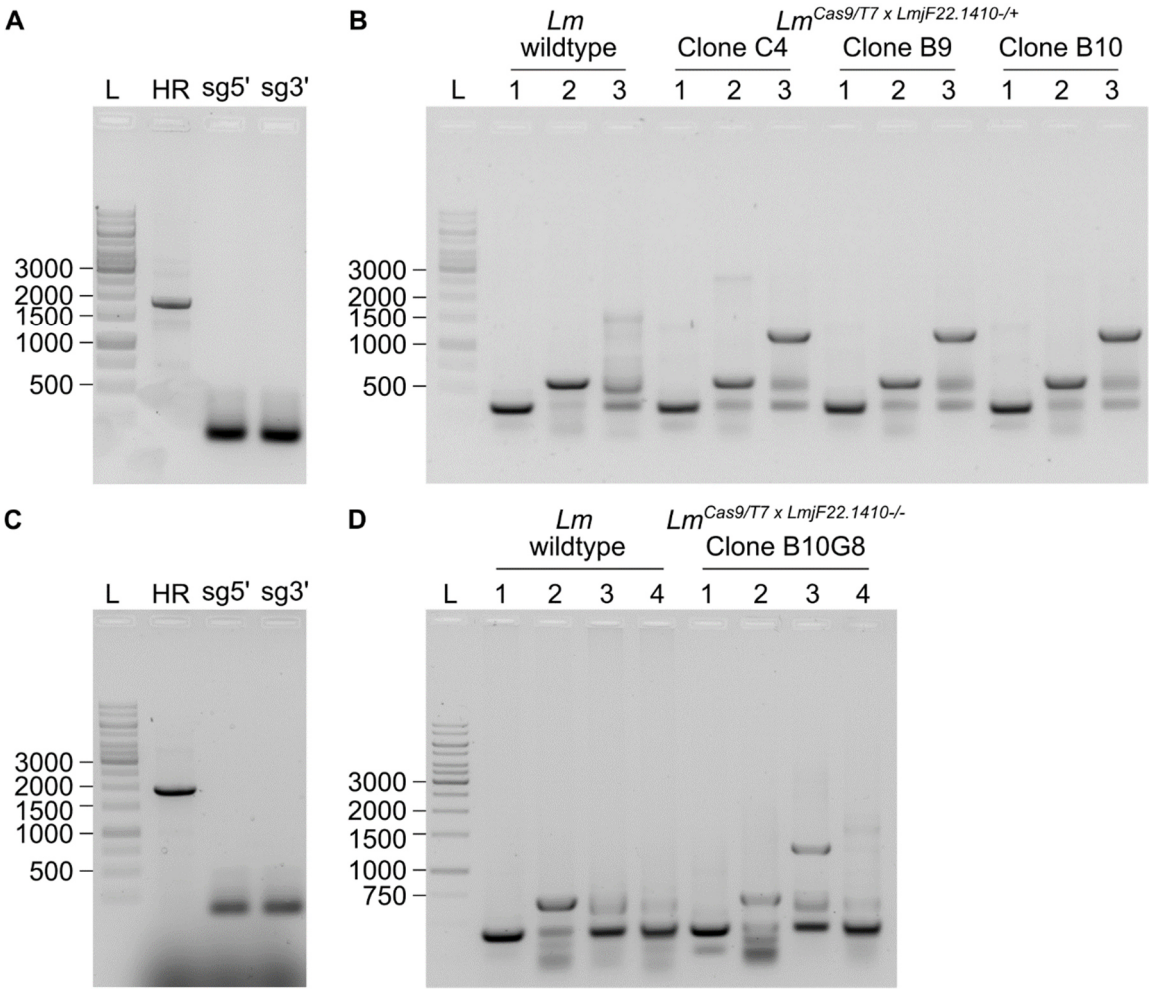

Figure 31: CRISPR/Cas9 based knockout of the gene *LmjF22.1410.*

To Fig. 31 – **(A)** Analytical gel electrophoresis of PCR products for the HR and sgRNA templates. To knockout the GOI, two distinct sgRNAs were amplified from a scaffold for Cas9 binding to target the 3' and the 5' end (sg5', sg3'). Additionally, the HR fragment was amplified with the plasmid *pTBlast* to replace the targeted gene by a blasticidin resistance gene. **(B)** Analytical gel electrophoresis of PCR products by genomic DNA of *Lm* wildtype and *Lm*$^{Cas9/T7\ x\ LmjF22.1410-/+}$ clone C4, B9 and B10 and primers binding in the CDS of *LmjF22.1410* (1) (Centrin4_CDS_fwd, Centrin4_CDS_rev) in the CDS and the downstream UTR of *LmjF22.1410* (2) (Centrin4_CDS_fwd, Centrin4_UTR_rev) and in the resistance cassette of blasticidin and the downstream UTR of *LmjF22.1410* (3) (Blast_fwd, Centrin4_UTR_rev). **(C)** As described in **(A)** except the HR fragment was amplified with the plasmid pTPuro to replace the targeted gene by a puromycin resistance gene. **(D)** As described in **(B)** with *Lm* wildtype and *Lm*$^{Cas9/T7\ x\ LmjF22.1410-/-}$ clone B10G8 and an additionally PCR with primers binding in the resistance cassette of puromycin and the downstream UTR of *LmjF22.1410* (4) (Puro_fwd, Centrin4_UTR_rev). 4 µl of the PCR product were loaded on a 1% agarose gel and were separated at 100 V, 400 mA for 40 min. GeneRuler 1 kb is applied as DNA size ladder (L), the size of the reference fragments is indicated in bp **(A-D)**.

The HR with the selective marker for blasticidin, as well as the DNA fragments to target the GOI, with expected fragment sizes of 1783 bp (HR) and 124 bp (sg5', 3'), were successfully generated (Figure 31 A). After transfection and clone selection, the gene knockout was probed by three independent PCRs, the first to amplify the CDS of *LmjF22.1410* with an expected fragment size of 419 bp and the CDS together with a part of the 3' UTR with expected fragment of 661 bp length. The *Lm* wildtype and all selected clones showed corresponding signals after gel electrophoresis (Figure 31 B). In the third reaction, the sequence of the resistance marker for blasticidin together with the same 3' UTR as before was amplified 3' UTR to confirm the insertion in the selected clones. The respective signal was seen for all clones but not for the wildtype parasites. The presence of the selective marker as well as the coding sequence for *LmjF22.1410* in all clones indicates that the gene was only ablated on one of two alleles and a full knockout was not achieved.

In order to knockout the second copy of *LmjF22.*1410, the clone B10 *Lm*$^{Cas9/T7\ x\ LmjF22.1410-/+}$ was transfected by the targeting sequences and the coding homologous region with the selective marker for puromycin with fragment sizes of 1914 bp (HR) and 124 bp (sg5', 3') (Figure 31 C). Again, a single clone was isolated and genetic modifications were tested by PCR. In addition to the three reactions performed with the single allele knockout, a fourth PCR was performed, now amplifying the selective sequence for puromycin and the UTR. As expected, in the *Lm* wildtype corresponding signals were seen for the CDS of *LmjF22.1410* but not for the resistant markers. Still, the isolated clone B10G8 showed signals for amplified fragments from the CDS of *LmjF22.1410* at 419 bp and 661 bp, as well as for the resistant marker blasticidin but not puromycin (Figure 31 D). Despite repetition of the transfection and clone selection, no clone negative for *LmjF22.1410* CDS was obtained, and the generation of a double allele knockout was not successful. Thus, exploring the effect of non-proliferating parasites on their exit from host cells remains open to further examination.

6.5 Dependence of parasite exit on the host cell phenotype

As comprehensively described in the literature by utilizing the murine infection model, the type of T cell response and its tailoring of the parasite host cells phenotype has an immense impact on the course of *L.* infections [2,26]. Yet, there is a lack of understanding how cellular mechanism like proliferation and parasite exit contribute to the systemic outcome of infection, especially in the human host system. The assays established during this work now allow an exploration of how inflammatory or regulatory stimulation of hMDM affect the parasite proliferation and exit on a cellular level.

6.5.1 Phenotype characterization of hMDMs after stimulation and infection by axenic amastigotes

To expand our *in vitro* infection model for the analysis of intracellular proliferation and exit of *Lm*, hMDM were stimulated by inflammatory or regulatory cytokines and their phenotype was examined by an immunostaining of cell surface markers of infected cells, commonly used for the distinction of hMDMs (Figure 32) [147,158]. In detail, $CD14^+$ monocytes were differentiated either by GM-CSF or M-CSF for 6 days and subsequently simulated by IFNγ or IL-4, M-CSF and IL-10, respectively to comprise the range of the activation spectrum as it is described by the literature and has relevance in *Lm* infections Figure 32 A) [27,41,159]. Resulting differences in the phenotypes were analyzed by the cell surface markers MerTK, CD14, CD86, CD16, CD163 and CD206, of cells stimulated for 24h and subsequently infected for 44h before the analysis.

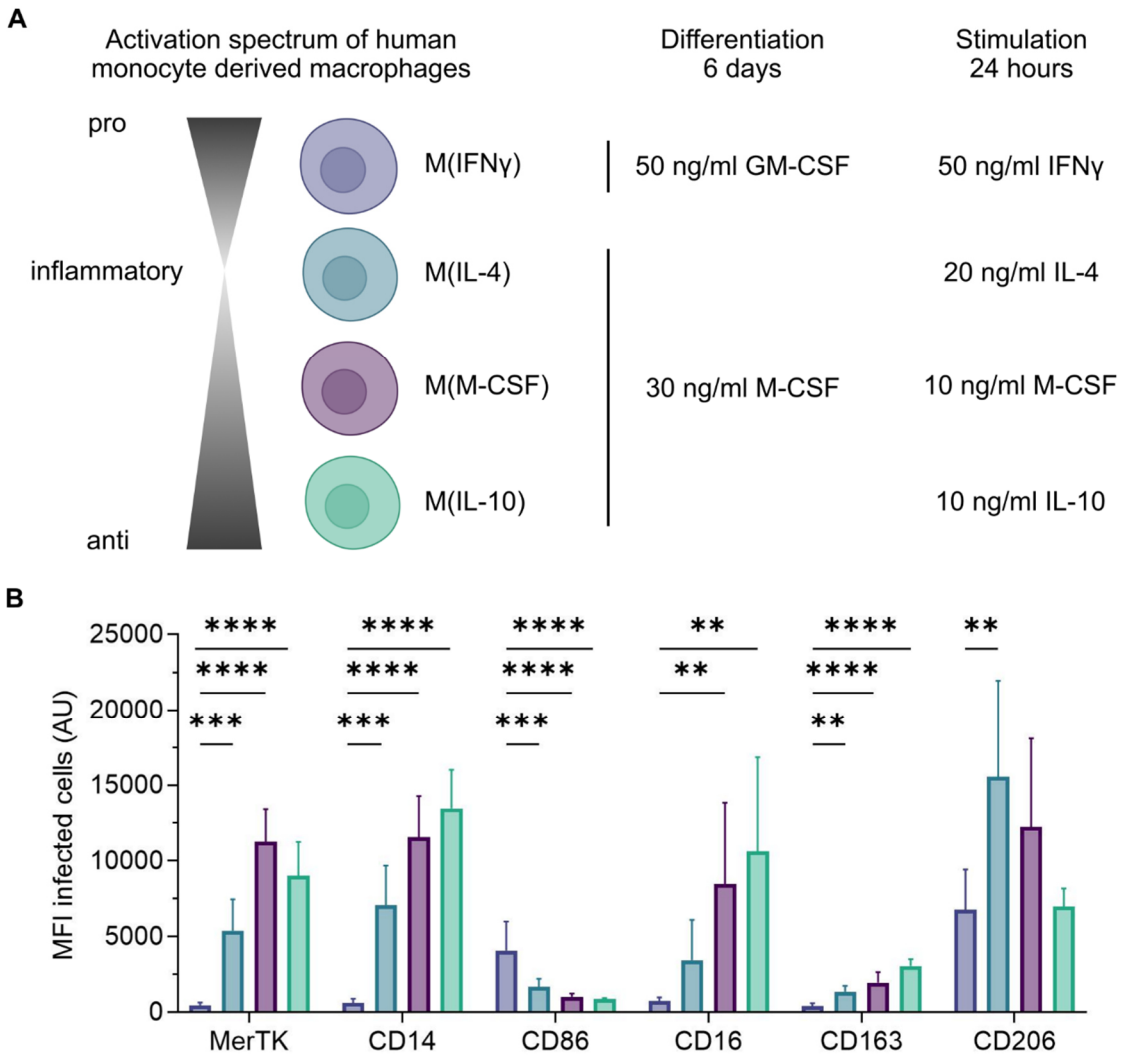

Figure 32: hMDMs stimulated with pro- and anti-inflammatory cytokines gave distinct surface marker profiles.
(A) Overview on the activation scale after differentiation of CD14⁺ primary monocytes and applied stimuli according to the nomenclature proposed by Murray *et al.* 2014 [41]. **(B)** Surface marker expression profile by immunofluorescence staining and subsequent flow cytometry analysis of M(IFNγ), M(IL-4), M(M-CSF) and M(IL-10). Samples were infected by *Lm*^{DsRed} axenic amastigotes after stimulation and stained by the respective antibody 44 h after infection. The experiment was compensated for spectral overlap by compensation beads. The MFIs of each marker were derived from single, viable and infected cells. Shown is the mean value + SD from six individual donors, N=3. Significance was determined by ordinary one-way ANOVA with multiple comparison correction by Dunnet test, $^{**}p < 0.01$., $^{***}p < 0.001$, $^{****}p < 0.0001$.

M(IFNγ) showed low expression of MerTK, CD14, CD16 and CD163 in comparison to the more anti-inflammatory group of M-CSF derived hMDMs. The expression of CD86 was significantly increased compared to the anti-inflammatory spectrum of the cells, while the CD206 expression was on the same level as M(IL-10) but lower than in M(IL-4). For M-CSF derived hMDMs, M(M-CSF) and M(IL-10) had a more similar profile with only a substantial difference in the expression of CD206. M(IL-4) showed an intermediate expression profile between the pro-inflammatory M(IFNγ) and the more anti-inflammatory M(M-CSF) and M(IL-10) for most markers, except for CD206, which was the most abundant in these cells (Figure 32 B). Also,

the cell surface marker expression was compared to uninfected subpopulation within samples from each stimulus, to test whether the infection by axenic amastigotes had effect on the phenotype. In addition, the different stimuli were further characterized by the capability for the uptake of amastigotes (Figure 33).

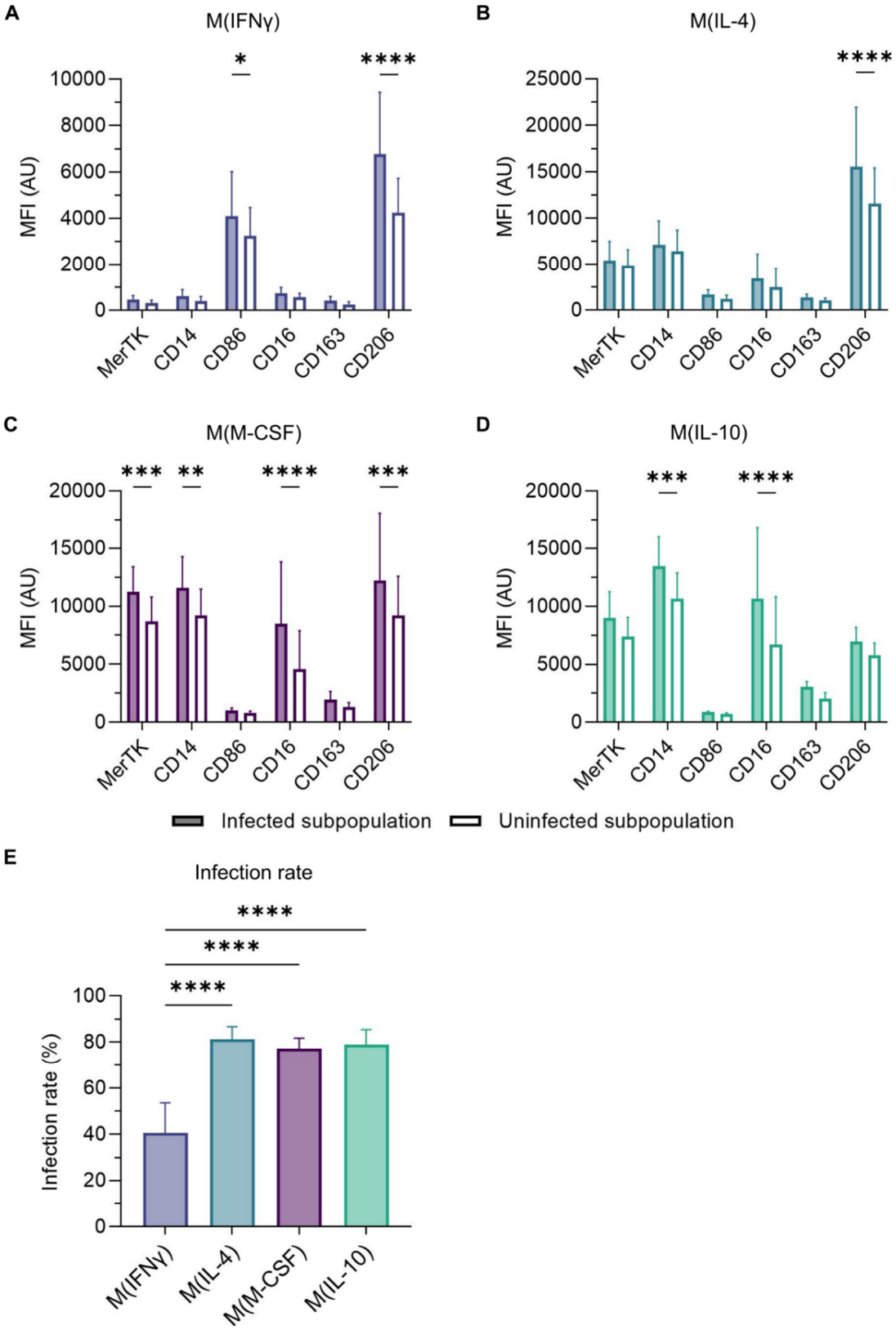

Figure 33: Infection rate of the different hMDM phenotypes and differences in the cell surface marker profile between infected versus uninfected cell subpopulations.

To Fig. 33 – **(A-D)** Cell surface marker expression in infected (also shown in Figure 32) and uninfected subpopulations of infected samples from M(IFNγ) **(A)**, M(IL-4) **(B)**, M(M-CSF) **(C)** and M(IL-10) **(D)** of the experiment shown in Figure 32. The MFIs of each marker were derived from single, viable cells divided into infected and uninfected populations. **(E)** Share of infected cells for each of the phenotypes 44 h pI. Shown as the mean value + SD from six individual donors, N=3. Significance was determined by two-tailed unpaired t-test **(A-D)** or ordinary one-way ANOVA with multiple comparison correction by Dunnet test **(E)**, **p* < 0.05, ***p* < 0.01, ****p* < 0.001, *****p* < 0.0001.

Interestingly, all stimuli showed an increased expression of CD206 in the infected subpopulation as compared to the uninfected subpopulation, except for M(IL-10) (Figure 33 A-D). Moreover, infected M(IFNγ) had a significantly higher expression of CD86 (Figure 33 A). While there were no further differences in the expression of cell surface markers in infected and uninfected M(IL-4), M(M-CSF) also had higher expression of MerTK, CD14, CD16 in the infected subpopulation (Figure 33 B, C). M(IL-10) infected subpopulations presented a significantly elevated expression of CD14 and CD16 (Fig. D). The share of the infected subpopulation per sample after 44 h of infection was uniformly for all M-CSF derived hMDMs and averaged 81.4 ± 5.4 % for M(IL-4), 77.2 ± 5.0 % for M(M-CSF) and 78.9 ± 6.6 % for M(IL-10). For M(IFNγ) the share of infected cells nearly halved and also presented a larger variation between individual donors with a mean of 40.5 ± 13.0 % (Figure 33 E). Overall, the differentiation, stimulation and infection of hMDMs resulted in distinct phenotypes of hMDMs characterized by the presented set of markers and the infection rate by axenic amastigotes. Therefore, the characteristics of proliferation after infection in these cell types were of great interest.

6.5.2 Analysis of amastigote proliferation within different host cell phenotypes

As in previous experiments, the parasite proliferation rate and the share of high proliferators in the different macrophage phenotypes was examined utilizing $Lm^{mKikume}$ axenic amastigote infections after a FRAC of 24 h and an analysis at 44 h pI. In addition, parasite burden was measured with Lm^{DsRed} derived from their DsRed MFI of intracellular parasites (Figure 34).

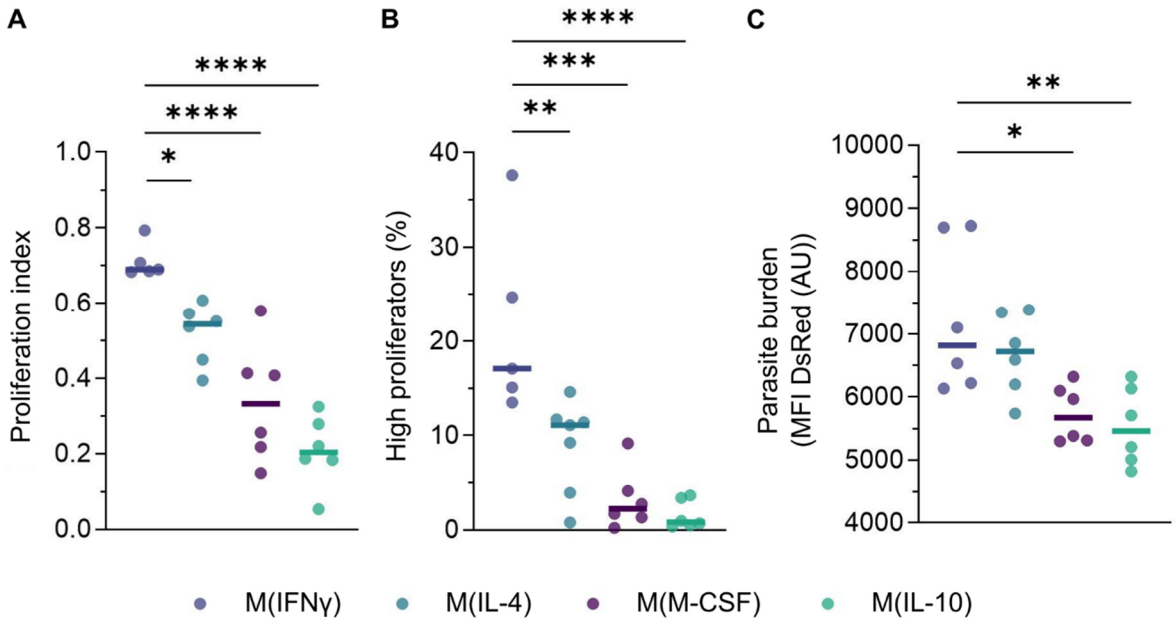

Figure 34: Parasite proliferation and burden in pro- or anti-inflammatory hMDMs.
Flow cytometry analysis of parasite proliferation by proliferation reporter mKikume and of parasite burden by MFI of the parasites' DsRed. **(A, B)** Cells were stimulated to M(IFNγ), M(IL-4), M(M-CSF) and M(IL-10) and infected by *Lm*^{mKikume}, photoconverted 20 h pI and the proliferation was analyzed 44 h pI (24 h FRAC). The proliferation index in infected cells was calculated by Formula (2) **(A)** and the share of high proliferating populations was analyzed according to gating in Figure 11 **(B)**. **(C)** Cells were stimulated to M(IFNγ), M(IL-4), M(M-CSF) and M(IL-10) and infected by *Lm*^{DsRed} and the DsRed MFI of intracellular parasites was analyzed 44 h pI. Shown are the mean values (colored line) and dots for each individual donor with a total of five to six donors, N=3. Significance was determined by 2way ANOVA with multiple comparison correction by Holm-Šidák test, *p < 0.05, **p < 0.01, ***p < 0.001, ****p < 0.0001.

The highest proliferation of amastigotes was observed in M(IFNγ) with a mean proliferation index of 0.71. Along the gradient of more anti-inflammatory hMDMs, the relative proliferation declined to 0.52, 0.34 and 0.21 for M(IL-4), M(M-CSF) and (M(IL-10), respectively (Figure 34 A). A similar trend was seen for the share of cells harboring high proliferating parasite populations (Figure 34 B). In M(IFNγ), the median of this share was 21.6 % and a maximum value of 37.6 % for one of the donors. For M(IL-4), the percentage of high proliferating parasite populations was 9.0 % in the median that was vastly reduced for two donors. M(M-CSF) and M(IL-10) barely showed a high proliferating parasite population at 44 h pI, which is interesting as the overall proliferation index in M(M-CSF) was increased compared to M(IL-10) (Figure 34 A, B). In well accordance with the data from the proliferation analysis, the parasite burden of M(IFNγ) and M(IL-4) was higher than in both other hMDM phenotypes (Figure 34 C). While this value can also be changed by the initial uptake of parasites during infection and not necessarily is a result from proliferation, the high proliferation indices coincide with increased parasite burden. This highly suggests that pro-inflammatory human hMDMs allow a more efficient parasite proliferation in *in vitro* infection experiments (Figure 34 A-C). To analyze,

whether this increased proliferation also translates to elevated exit rates, the co-incubation assay was performed with the range of different hMDM phenotypes.

6.5.3 Parasite exit in dependence of the hMDM phenotype and proliferation

The parasite exit rates were measured after 44 h of infection by *Lm*^{DsRed} axenic amastigotes and 20 h of co-incubation with M-CSF M(-), while the respective stimuli of each phenotype was retained. To determine whether observed effects were *Lm*-specific, a second set of hMDMs was loaded with fluorescent latex beads instead of parasites and the cell-to-cell transfer of beads was measured accordingly (Figure 35).

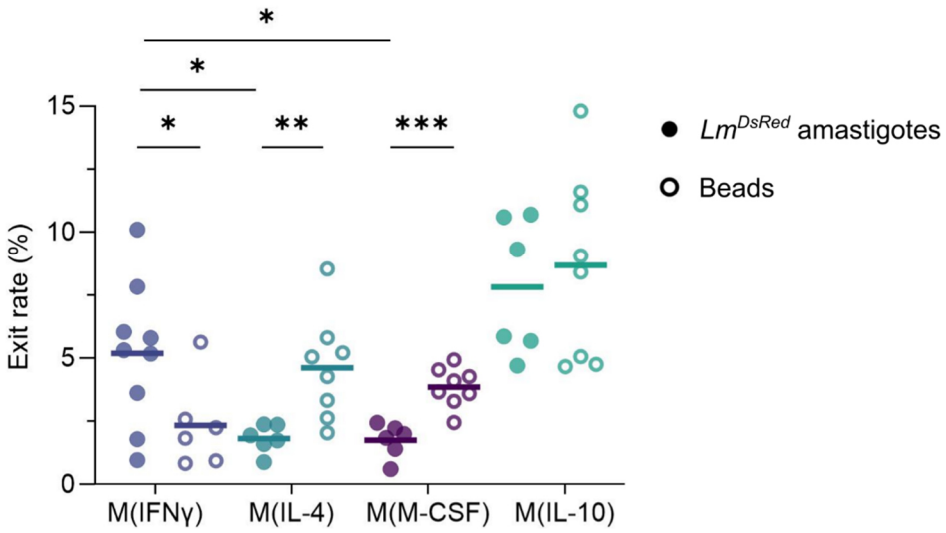

Figure 35: Parasite exit is elevated from pro-inflammatory hMDMs.
Quantification of the parasite exit by the co-incubation assay, in comparison between pro- and anti-inflammatory hMDMs and amastigotes versus latex beads. Cells were either infected by *Lm*^{DsRed} or incubated with red fluorescent latex beads and then co-incubated at 24 h pI with ViaFluor405^{+} M(-) of the same donor for 20 h. Shown is the exit rate as the percentage of total infections with dots for each individual donor and the mean value (colored line) with a total of six to eight donors, N=4. Significance was determined by 2-way ANOVA with multiple comparison correction by Holm-Šidák test for comparisons between different stimuli or by two-tailed unpaired t-test for comparisons between amastigote and beads cell-to-cell transfer events, *p < 0.05 **p < 0.01, ***p < 0.001, ****p < 0.0001.

Under the stimulation with IFNγ, the exit rates averaged 5.2 % (Figure 35). Therewith, the exit was significantly higher than the cell-to-cell transfer rate of 2.3 % observed in the samples with beads and in amastigote infected hMDM stimulated by IL-4 (1.8 %) or M-CSF (1.8 %). Intriguingly, the cell-to-cell transfer rates of beads were significantly increased for M(IL-4) and M(M-CSF), averaging 4.6 % and 3.9 %, respectively, compared to the parasite transmission rates. Also notable, the exit rates between individual donors varied greatly, ranging from 10.1 % to 1.0 %. For M(IL-10) *Lm*^{DsRed} and beads showed equally high transfer rates of 7.8 % and 8.7 %, indicating a non-parasite specific mechanism behind the cell-to-cell transfer under this condition.

6.5.4 Occurrence of regulated cell death during infection of pro- and anti-inflammatory stimulated hMDM

As hallmarks of apoptosis were observed in previous infection experiments with M(-), the occurrence of apoptotic cell death was examined for the different hMDM phenotypes, also, to verify if the initial hypothesis that the underlying mechanism for exit is a regulated form of cell death holds true for pro- and anti-inflammatory stimulated cells.

Apoptotic cell death was analyzed by the activation of caspase-3 during infection measured by the caspase-3 substrate NucView405, whereby positive events were assorted to early apoptotic cells which still had an intact cell membrane and late apoptotic cells with a compromised membrane positively stained for the live/dead stain Zombie NIR. Externalization of PtdSer was additionally detected by a specific antibody (Figure 36). Because M(IL-10) showed no parasite specific effects in regard of exit, they were left out of the following experiments.

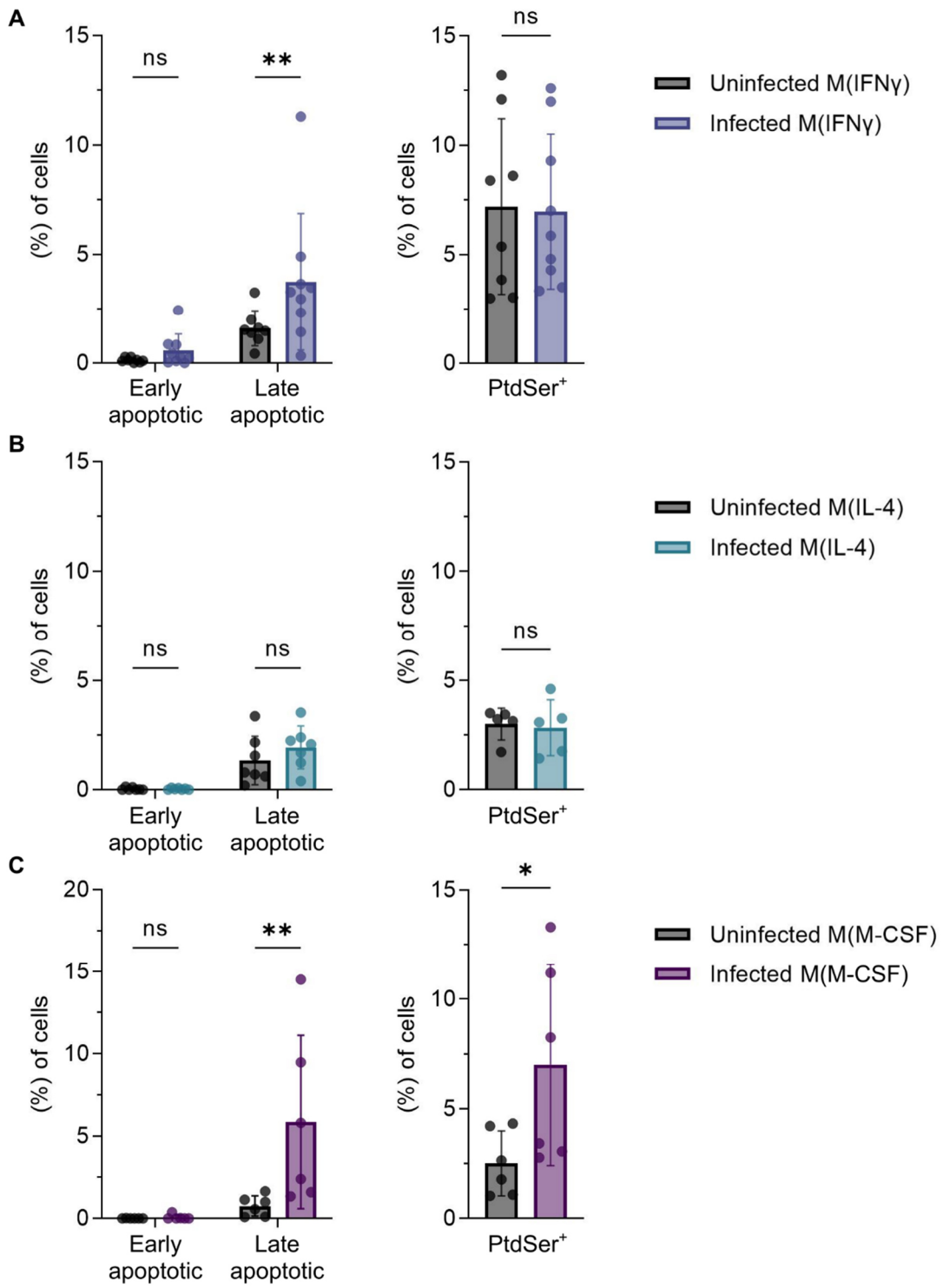

Figure 36: Detection of apoptosis hallmarks in infected M(IFNγ), M(IL-4) and M(M-CSF).
(A-C) Caspase-3 activity and PtdSer presentation of M(IFNγ) **(A)**, M(IL-4) **(B)** and M(M-CSF) **(C)** during infection was assessed by flow cytometry. Cells were infected by *Lm*^{DsRed} axenic amastigotes. At 24 h pI, 2.5 µM caspase-3 substrate NucView405 was added to the culture, incubated for 20 h and cells were harvested 44 h pI with subsequent staining by the PtdSer antibody Apotracker green and live/dead stain Zombie NIR prior to flow cytometry analysis. Single and infected cells were categorized to early apoptotic (NucView405$^+$, Zombie NIR$^-$), late apoptotic (NucView405$^+$, Zombie NIR$^+$) or PtdSer$^+$ (Apotracker green$^+$). Shown are bar graphs of the mean value + SD and dots for each individual donor with a total of six donors, N=3. Significance was determined by 2-way ANOVA with multiple comparison correction by Holm-Šidák test for late and early apoptotic or by ordinary one-way ANOVA with multiple comparison correction by Dunnet test, *p < 0.05 **p < 0.01, ***p < 0.001, ****p < 0.0001.

M(IFNγ) barely showed late apoptotic cells at 44 h pI, independent of the infection by *Lm*^{DsRed} axenic amastigotes. Yet, a significant difference was observed in the population of early apoptotic cells, where 3.8 ± 3.1 % of infected M(IFNγ) were positive for caspase-3 activity but only 1.6 ± 0.8 % of the uninfected sample. Again, a vast donor variation was seen for the infected samples, which was less apparent in uninfected cells (Figure 36 A, left graph). The share of PtdSer$^+$ cell was equally distributed between infected and uninfected M(IFNγ) with 7.2 ± 4.0 % and 7.0 ± 3.6 %, respectively, whereby variations were seen for both, infected and uninfected cells(Figure 36 A, right graph). In M(IL-4), no late apoptotic cells and limited shares of early apoptotic events were detected with 1.3 ± 1.1 % for uninfected and 1.9 ± 1.0 % for infected cells (Figure 36 B, left graph). Accordingly, the rates of PtdSer$^+$ cells were not significantly different in infected compared to the uninfected control (Figure 36 B, right graph). As for the other stimuli, no late apoptotic events were detected for M(M-CSF), yet the share of early apoptotic cells was significantly elevated for the infected sample with 5.9 ± 5.3 % versus 0.8 ± 0.6 % in the uninfected sample (Figure 36 C, left graph). Also, the share of PtdSer$^+$ cells was significantly higher for infected M(M-CSF) reaching 7.0 ± 4.6 % compared to the uninfected hMDMs with 2.5 ± 1.5 % (Figure 36 C, right graph).

Data sets from literature showed an activation of the NLRP3 inflammasome during infection by *L.* parasites, especially in pro-inflammatory hMDMs, which eventually results in pyroptotic cell death via the activation of caspase-1 [111,119]. Therefore, infected hMDMs were also analyzed towards signs of pyroptosis. In a similar approach, the differently stimulated hMDMs were tested for caspase-1 activity and pyroptosis by using the fluorescent caspase-1 substrate 660-YVAD-FMK for caspase-1 activity (Figure 37). It was differentiated between caspase-1$^+$ events that were positive for caspase-1 activity but had an intact membrane and pyroptotic cells that were positive for caspase-1 activity and a disrupted membrane integrity.

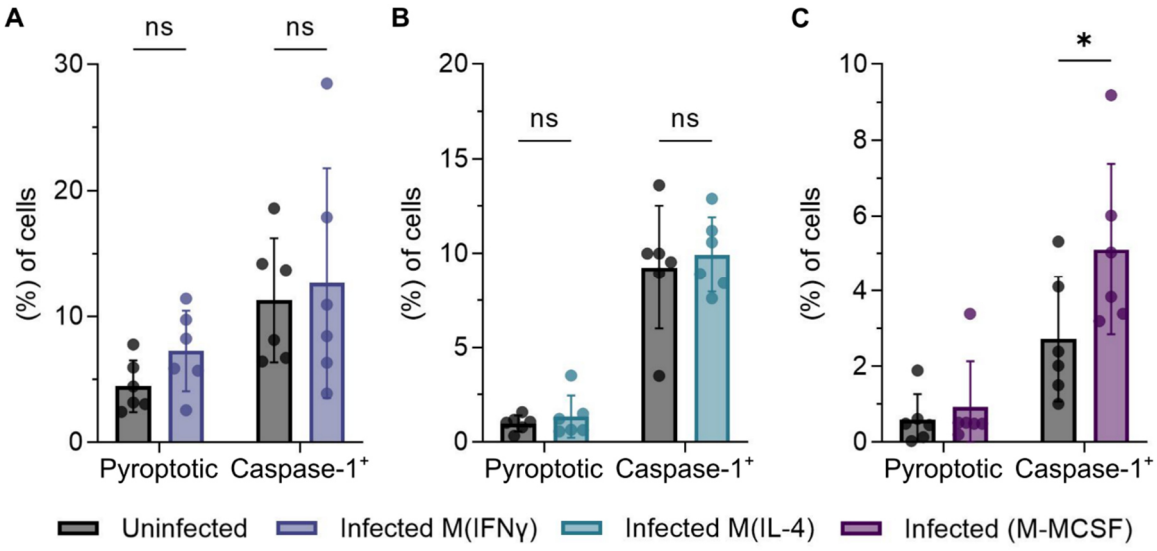

Figure 37: Detection of caspase-1 activity in hMDMs.

To Fig. 37 – **(A-C)** Caspase-1 activity of infected M(IFNγ) **(A)**, M(IL-4) **(B)** and M(M-CSF) **(C)** was analyzed by flow cytometry. Cells were infected by *Lm*^{DsRed} axenic amastigotes. At 36 h pI, 1 µM caspase-1 activity reagent 660-YVAD-FMK was added to the culture, incubated for 8 h and cells were harvested 44 h pI with subsequent staining live/dead staining using Zombie Aqua prior to flow cytometry analysis. Single and infected cells were categorized to caspase-1$^+$ (660-YVAD-FMK$^+$, Zombie NIR$^-$) or pyroptotic (660-YVAD-FMK $^+$, Zombie NIR$^+$) events. Shown are bar graphs of the mean value + SD and dots for each individual donor with a total of six donors, N=3. Significance was determined by 2-way ANOVA with multiple comparison correction by Holm-Šidák test for late and early apoptotic or by ordinary one-way ANOVA with multiple comparison correction by Dunnet test, **p* < 0.05 ***p* < 0.01, ****p* < 0.001, *****p* < 0.0001.

At 44 h pI, 7.2 ± 3.2 % of infected M(IFNγ) were pyroptotic, which was a slight but not significant increase to the uninfected control with 4.5 ± 2.0 %. The share of caspase-1$^+$ cells under the IFNγ stimulation was elevated, but equally distributed for infected and uninfected cells. Additionally, a pronounced variation between individual donors was seen again (Figure 37 A). In the IL-4 stimulated samples, neglectable shares of pyroptotic cells were detected, independent of the infection. The caspase-1$^+$ population was equally increased for infected with 9.9 ± 2.0 % and with 9.2 ± 3.3 % for uninfected cells to a comparable ratio as the M(IFNγ) (Figure 37 B). For M(M-CSF) pyroptotic events were barely detectable in the infected and uninfected sample, but interestingly the caspase-1$^+$ cell population was elevated in the infected sample compared to the uninfected control with an average of 5.1 ± 2.3 % versus 2.7 ± 1.7 % (Figure 37 C).

As pyroptosis is a lytic form of cell death, the share of lysed cells can indicate its occurrence by the detection of the release of the protein Lactatdehydrogenase (LDH) (Figure 38).

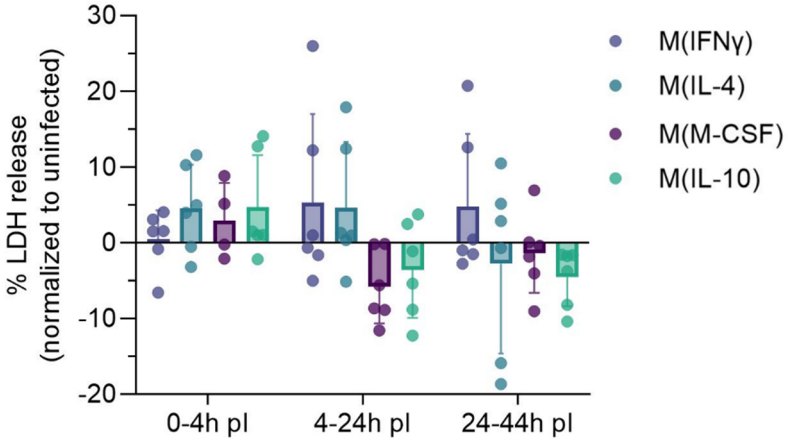

Figure 38: LDH release by lytic cell death varies between donors for activated and infected hMDM.
LDH release was assessed in a colorimetric assay for infected samples of pro- and anti-inflammatory hMDMs. Samples of stimulated cells were infected by *Lm*^{DsRed} axenic amastigotes. The medium was changed at the beginning of the indicated time-intervals and the released LDH into the medium during that interval was analyzed afterwards. Values were normalized to the minimum LDH release (untreated sample) and the maximum LDH release (chemically lysed sample) according to Formula (4). Shown is a bar graph of the mean value + SD and dots for each individual donor with a total of six individual donors, N=3. This experiment was conducted by Bianca Walber under my supervision.

The share of LDH release is determined by normalization of an entirely lysed sample and an untreated sample. A significant increase of LDH release over time was not observed for any of the stimuli (Figure 38). For M(IFNγ), hardly any LDH release was detected in the initial time interval from 0 to 4 pI. Over the course of infection, no substantial change in the LDH release was seen for four of the six donors but two donors showed highly increased LDH release rates with 12.2 % and 26.0 % from 4 h to 24 h pI and 12.6 % and 20.7 % form 24 h to 44 h pI. In samples with M(IL-4), M(M-CSF) and M(IL-10) the LDH release averaged 4.5 ± 5.8 %, 2.9 ± 5.0 % and 4.7 ± 6.8 % from 0 h to 4 h pI, whereby certain donors showed elevated shares of LDH release and others none. Under the stimulation of IL-4, two donors presented elevated LDH release ratios of 12.5 % and 17.9 % at 24 h pI, comparable to the IFNγ stimulation. At 24 h to 44 h pI the different donors resulted in opposing levels of LDH release, two even less than the untreated normalization control and three slightly elevated rates above the baseline. M(M-CSF) and M(IL-10) had a uniformly low release of LDH, on average less than the untreated control for both time intervals from 4 h to 24 h pI and 24 h to 44 h pI.

In summary, hMDMs stimulated by IFNγ were a permissive host cell for increased parasite proliferation and hosted high proliferating *Lm* population, compared to hMDM stimulated by IL-4, M-CSF and IL-10. Accordingly, the exit rate of parasites was increased for M(IFNγ) and latex beads controls demonstrated that the exit was parasite specific. Interestingly, individual donors showed a large variation in their allowance of *Lm* cell-to-cell transfer, a trend that was also observed in the detection of apoptotic and pyroptotic cell death. Opposingly, M(IL-4) specifically controlled parasite transmission despite elevated parasite proliferation rates and no divergence in the occurrence of regulated cell death in comparison to uninfected controls was apparent. M(M-CSF) allowed only basal parasite proliferation that agreed with reduced detection of parasite exit, yet the measurement of regulated cell death showed an upregulation of early apoptotic and caspase-1$^+$ cells after infection compared to uninfected samples. The stimulation by IL-10 also resulted in low *Lm* proliferation but notable increases in the cell-to-cell transfer of infection amastigotes. Increased transfer rates of ingested beads suggested a non-parasite specific process behind this upregulation of exit.

6.6 Downregulation of the kynurenine pathway is a trigger for *Lm* parasite exit

From the large variation that was observed in the parasite exit for individual donors of M(IFNγ), a chance arose to unravel exit pathway in more detail by searching for determinants causing these differences. Because exit was inhibited in anti-inflammatory stimulated hMDMs, we hypothesized that the extent and subversion of pro-inflammatory activation after infection could determine whether cells are susceptible for parasite exit. A previous study showed that variations, especially in the response to pro-inflammatory stimulation is commonly observed for individuals, and can be traced by probing the gene expression of enzymes in the arginine

catabolism pathway especially *NOS2* and arginase (*ARG*), as well as the cytokine subunit *IL12p40* [140]. Of interest in *L.* infection context and the regulation of the pro-inflammatory response is TGFβ and in human infection models, enzymes catalyzing the tryptophan catabolism kynurenine pathway for the generation of NAD^+, IDO1 and KYNU [62,160].

6.6.1 TGFβ relative gene expression is upregulated, and enzymes of kynurenine pathway are downregulated during infection

By qPCR, the changes in the gene expression of the genes *NOS2, ARG, IL12p40, TGFβ, IDO1* and *KYNU* was tested 24 h and 44 h after infection of M(IFNγ). For *NOS2, ARG* and *IL12p40* cycle threshold (C_t) values were nigh on equal to controls without a template, therefor no gene expression could be detected in infected samples from the utilized primary human cell *in vitro* infection model. *TGFβ, IDO1* and *KYNU* had detectable levels of mRNA and the gene expression of infected samples relative to the state pre-infection was analyzed for 20 individual donors (Figure 39).

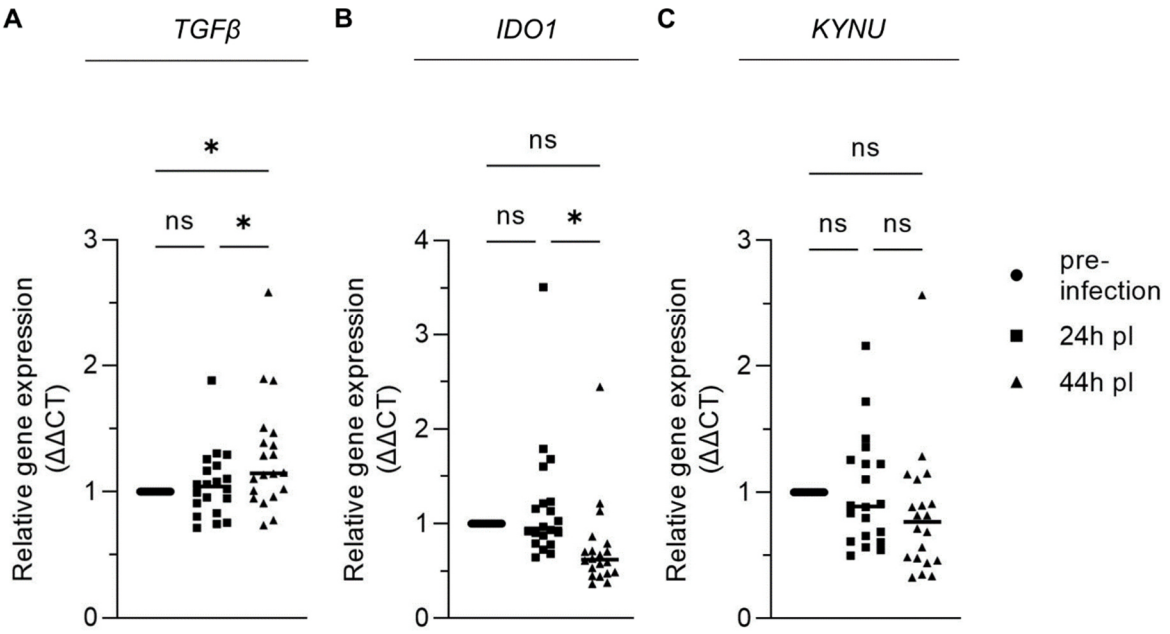

Figure 39: The relative expression of *TGFβ* is in- and the relative expression of *IDO1* and *KYNU* is decreased over the course of M(IFNγ) infection.
(A-C) The mRNA levels of *TGFβ* **(A)**, *IDO1* **(B)** and *KYNU* **(C)** were derived by qPCR from M(IFNγ) after 24 h of stimulation pre- and post-infection (24 h pI, 44 h pI) by Lm^{DsRed} axenic amastigotes. Gene expression was normalized to the housekeeping gene *HPRT1*. Shown is the mean value (black line) and dots for the ΔΔCT values derived from Formula (1) for each individual donor with a total of 20 donors, N=9. Significance was determined by ordinary one-way ANOVA with multiple comparison correction by Holm-Šidák test, ns – not significant, $*p < 0.05$. This experiment was conducted by Bianca Walber under my supervision.

The expression of *TGFβ* was upregulated over the course of infection, reaching 127 % of the initial expression before the infection. Yet, the expression level between the donors varied greatly from 258 % to 73 % of the normalization control (Figure 39 A). In contrast, the relative expression of *IDO1* decreased uniformly and significantly after 44 h of infection for nearly all

donors to 74 % of the pre-infection level. Only three donors showed increased expression of IDO1 after the infection (Figure 39 B). Similarly, the relative expression of *KYNU* declined on average after the same infection period but with more variation between donors, so the decrease remained insignificant (Figure 39 C).

To confirm that our primary human hMDM model is able to upregulate the key enzymes of the kynurenine pathway after IFNγ stimulation as published previously, the change in relative gene expression was tested after IFNγ stimulation relatively to the expression after the differentiation by GM-CSF (Figure 40)

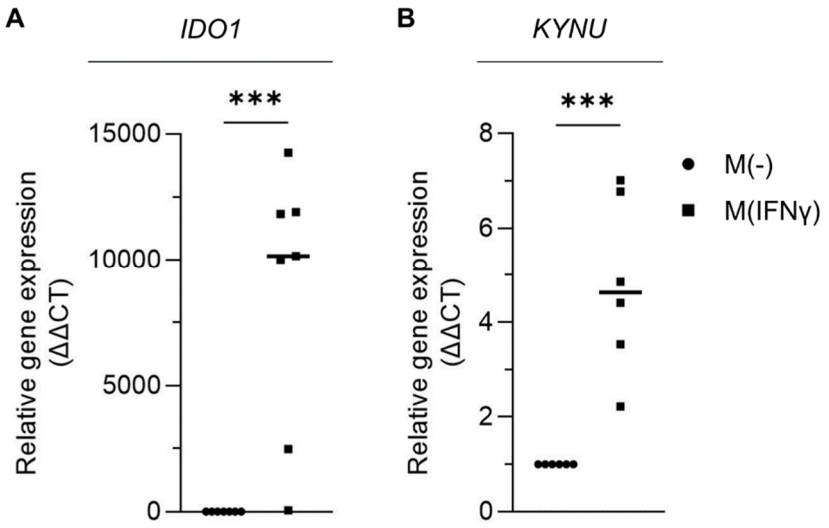

Figure 40: Kynurenine pathway enzymes *IDO1* and *KYNU* are strongly upregulated upon stimulation with IFNγ.
(A, B) The mRNA levels of *IDO1* **(A)** and *KYNU* **(B)** were analyzed by qPCR for GM-CSF derived hMDMs before (M(-)) and after stimulation with IFNγ (M(IFNγ)). Gene expression was normalized to the housekeeping gene *HPRT1*. Shown is the mean value (black line) and dots for the ΔΔCT values derived from Formula (1) for each individual donor with a total of six to seven donors, N=3. Significance was determined by two-tailed unpaired t-test, ***$p < 0.001$. This experiment was conducted by Bianca Walber under my supervision.

Indeed, the relative gene expression of enzymes catalyzing the kynurenine pathway were significantly upregulated upon stimulation. For *IDO1*, the expression was very strongly increased by a 10000-fold compared to prior to the stimulation (Figure 40 A). The expression of *KYNU* was upregulated by the simulation with IFNγ to the 4.8-fold of unstimulated hMDMs (Figure 40 B).

6.6.2 The *IDO1* and *KYNU* expression level is lower in donors susceptible to high exit rates

In order to test if the relative expression of the described genes associated with the parasite exit, the cell-to-cell transfer rate of *Lm*^{mKikume} axenic amastigotes was measured with the co-incubation from 24 h pI to 44 h pI with the same set of 20 donors. The donors were assigned to two groups of exit: high exit, for donors with an exit rate above the mean value of all

measured rates, or low exit, for donors below the mean value. The relative expression data for *TGFβ, IDO1* and *KYNU* from the experiment presented in Figure 39 of both groups were compared to find eventual differences correlating with high or low exit rates (Figure 40).

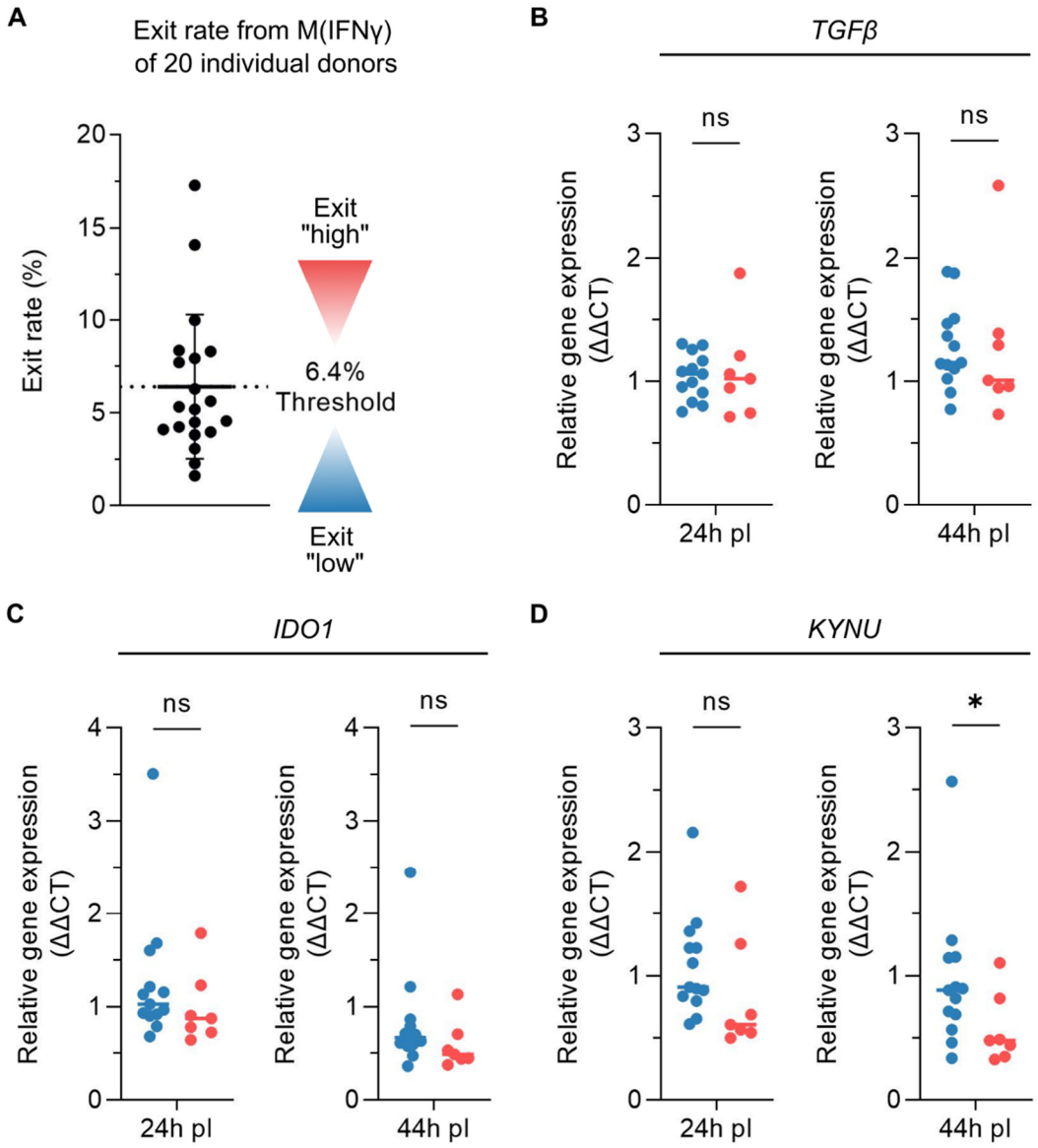

Figure 41: Individual donors susceptible for high parasite exit experience a stronger downregulation of the enzymes dedicated to the kynurenine pathway.
(A) Exit rates were measured by the co-incubation assay with the same set of donors shown in Figure 39. Therefore, M(IFNγ) were infected by *Lm*^{mKikune} axenic amastigotes with subsequent 20 h co-incubation of uninfected, ViaF405^{+} M-CSF derived M(-) and analysis by flow cytometry at 44 h pI. Shown is the mean value + SD and dots for each individual donor. The donors were grouped to exit high and exit low by being above or below the threshold exit rate, marked by the mean value (dotted line). **(B-D)** Relative gene expression of *TGFβ* **(B)**, *IDO1* **(C)** and *KYNU* **(D)** at 24 h and 44 h pI from Figure 39 for the individual donors, assigned to the exit low (blue) or exit high (red) group. Shown are dots for each donor and mean values (colored lines). Significance was determined by non-parametric Mann-Whitney test, ns – not significant, *$p < 0.05$. This experiment was conducted by Bianca Walber under my supervision.

The mean exit rate of the 20 donors was 6.4 ± 3.9 % which was set as the threshold, the variation observed in previous experiments was conserved. Seven donors grouped above and

thirteen donors below the threshold (Figure 41 A). The comparison of the *TGFβ* relative expression level in the high and low exit group showed no significant difference at 24 h pI and 44 h pI. For *IDO1* a slightly decreased yet not significant expression level was seen for the high exit donors, comparing a 1.00-fold expression at 24 h pI and 0.67-fold expression at 44 h pI in the low exit group, to 0.87-fold expression at 24 h pI and 0.49-fold expression at 44 h pI for the high exit group (Figure 41 B). This trend was even more pronounced for *KYNU* expression, where 24 h pI the relative gene expression was 0.91-fold in the low exit group and 0.61-fold in the high exit group and 0.91-fold in the low exit group and 0.30-fold in the high exit group for 44 h pI, which was a significant difference in the latter (Figure 41 C). In conclusion, the expression of the enzymes IDO1 and KYNU was downregulated for M(IFNγ) from donors susceptible to exit.

6.6.3 Inhibition of the kynurenine pathway reduces the parasite burden and induces exit

Because the kynurenine pathway is not only an indicator for the activation state of hMDMs, but its downregulation can have direct implications on intracellular parasites by diminishing the levels of available NAD^+, the impact of the IDO1 inhibitor 1-MT on the parasites' proliferation and exit rate was tested subsequently (Figure 42).

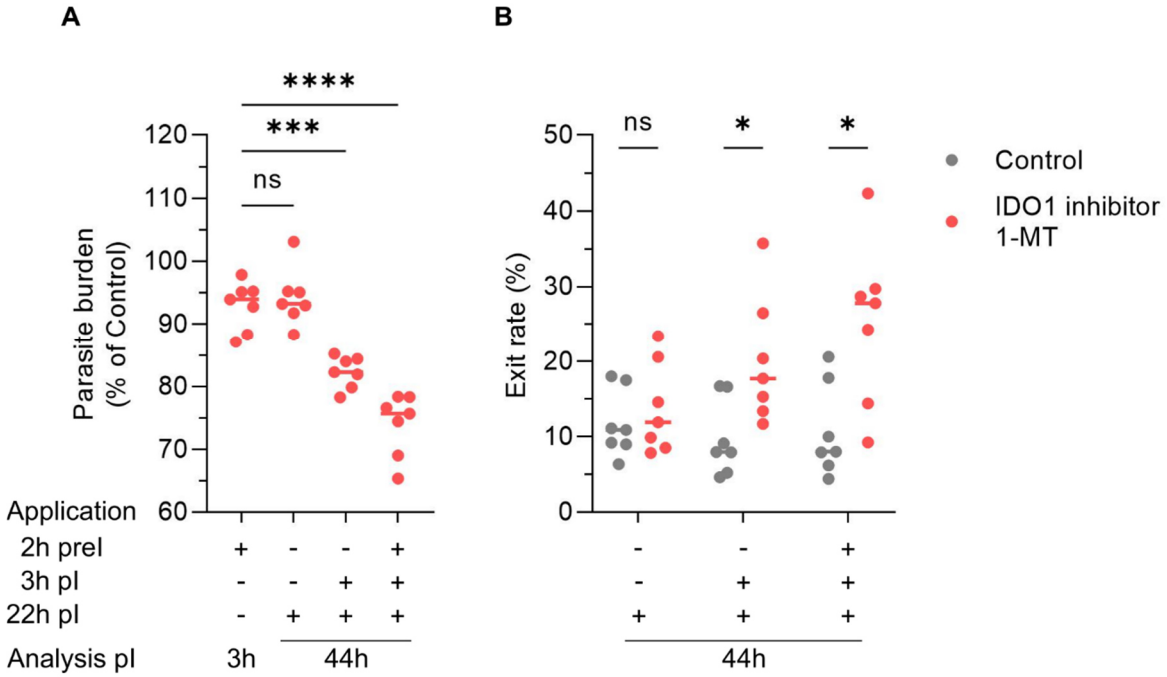

Figure 42: Parasite proliferation dampens and exit rate rises by kynurenine pathway inhibition.

To Fig. 42 – For the parasite burden and exit rate, M(IFNγ) were infected by Lm^{DsRed} axenic amastigotes and IDO1 enzyme activity was inhibited by 200 µM 1-MT per application. The inhibitor was applied as described below the graphs, (pre infection = preI). As control, cells were treated with NaOH which was used as solvent for 1-MT. **(A)** For the parasite burden, primary infected cells were analyzed flow cytometry for the DsRed MFI of intracellular parasites at 3 h pI or 44 h pI. Shown is the parasite burden in the inhibited samples relative to the burden reached in the controls, with dots for each individual donor and the mean value, N=3 **(B)** For the exit rate, uninfected ViaF405$^+$ M-CSF derived M(-) were added at 24 h pI for 20 h of co-incubation. Shown are dots for each individual donor and the mean value, N=3. Significance was determined by 2way ANOVA with multiple comparison correction by Holm-Šidák test **(A)** or two-tailed unpaired t-test **(B)**, ns – not significant, *$p < 0.05$, ***$p < 0.001$, ***$p < 0.0001$. This experiment was conducted by Bianca Walber under my supervision.

A single dose of 1-MT had a minor effect, the parasite burden was 92.9 % and 94.3 % at 3 h and 44 h pI, respectively, relative to the control. Significant lower parasite burdens were observed after additional applications of 1-MT after infection, decreasing the parasite burdens to 82.3 % after two doses and even 74.0 % after three doses compared to controls (Figure 42 A). In well accordance, the exit rate was not changed with a single dose of 1-MT compared to the control, and remained at 13.8 % and 11.7 %, respectively. A second application of the inhibitor resulted in a significant difference in exit with 20.1 % to 9.7 % in the control that was even more increased to 25.2 % by a third dose of 1-MT (Figure 42 B).

By making use of natural donor variation in the exit rate in IFNγ stimulated hMDMs, it was possible to unravel that a susceptibility to *L.* parasite exit is in line with a downregulation of the kynurenine pathway responsible for the NAD^+ *de novo* synthesis. The inhibition of the rate limiting initial step by IDO1 affected the parasites proliferation ability and consequently increased the measured cell-to-cell transfer. Thus, the metabolic host cell pathway has an impact on parasite proliferation and parasite exit.

6.7 BLaER1 hMDM cell line is a suitable infection model to dissect parasite exit under inflammatory inducing conditions

The BLaER1 cell line is a cell model for human hMDMs that has been established recently as a suitable *L.* infection system *in vitro,* supporting the parasites' transformation from pro- to amastigote and its intracellular replication [154]. *L.* infections can trigger the activation of the NLRP3 inflammasome, a process that eventually results in pyroptotic cell death [119,161]. To analyze if pyroptosis in addition to apoptosis, is a possible pathway for parasite cell-to-cell transfer, the ability of BLaER1 cells for genetic modification was utilized in the already established co-incubation assay under inflammasome inducing conditions. For that, the aim of this subproject was to test the pyroptosis resistance of the $BLaER1^{GSDMD-/-}$ mutant in comparison to the wildtype BLaER1 cell and subsequently establish a time interval for the co-incubation of wildtype BLaER1 cells as donor of infecting parasites and recipient *GSDMD* knockout BLaER1 cells to measure parasite exit.

6.7.1 Transdifferentiation of BLaER1

The pre-B cell form of BLaER1 cells used for this work was transdifferentiated to BLaER1-derived macrophages by the supplements M-CSF, β-Estradiol and IL-3 to generate hMDM-like phagocytes (Figure 43 A). The different BLaER1 strains were available with and without a constitutive expression of *eGFP* that, if expressed, can be utilized as a viability marker during flow cytometry analysis (5.1.13). The efficiency of the differentiation process was tested periodically by the detection of cell surface markers CD19, CD14 and CD11b. For the representative efficiency test shown, the undifferentiated BLaER1 cell control sample was with 99.6 % almost completely positive for the B cell lineage marker CD19, but entirely negative for the monocyte and hMDM markers CD14 and CD11b. Opposingly, the transdifferentiated cell sample had only a share of 4.7 % cells positive for CD19, yet 98.2 % were positive for CD14 and 89.9 % positive for CD11b (Figure 43 B)

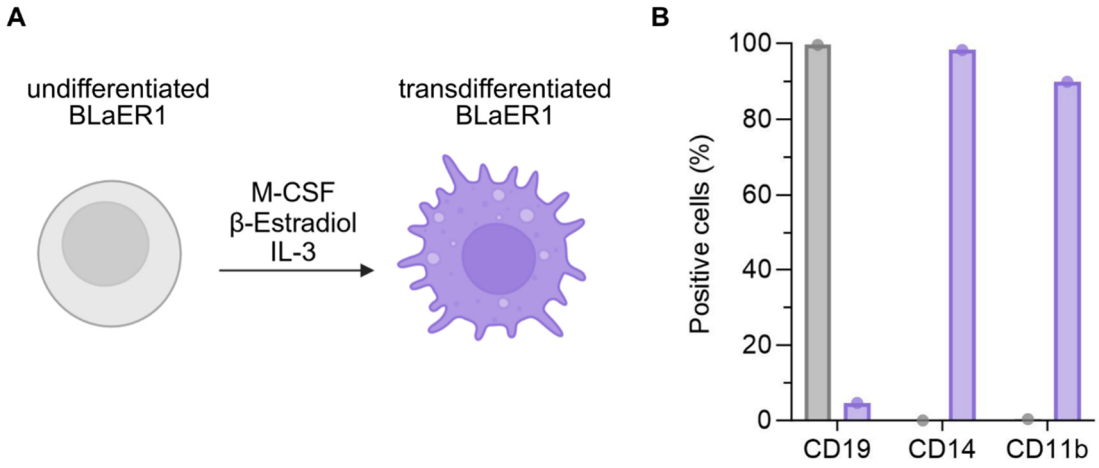

Figure 43: Transdifferentiation of BLaER1 cells.
(A) Transdifferentiation scheme for the BLaER1 cell model. **(B)** Confirmation of transdifferentiation by flow cytometry analysis of the cell surface markers CD19, CD14 and CD11b. Fluorescent channels were compensated using compensation beads. Single and viable (GFP^+) cells of undifferentiated (grey) and differentiated (violet) samples were stained with the respective antibodies and were analyzed by flow cytometry, including FMO controls for each marker. Shown is a representative sample as bar graph, testing the transdifferentiation efficiency. This experiment was conducted by Vivien Vankann under my supervision.

6.7.2 BLaER1$^{GSDMD-/-}$ are more resistant to pyroptosis induction

To characterize the susceptibility to pyroptosis induction, wildtype BLaER1 cells and BLaER1$^{GSDMD-/-}$ mutants were treated with LPS and nigericin to activate the NLRP3 inflammasome and induce pyroptosis, while their viability, PtdSer display and IL-1β release were monitored within the first 4 h post-treatment (Figure 44).

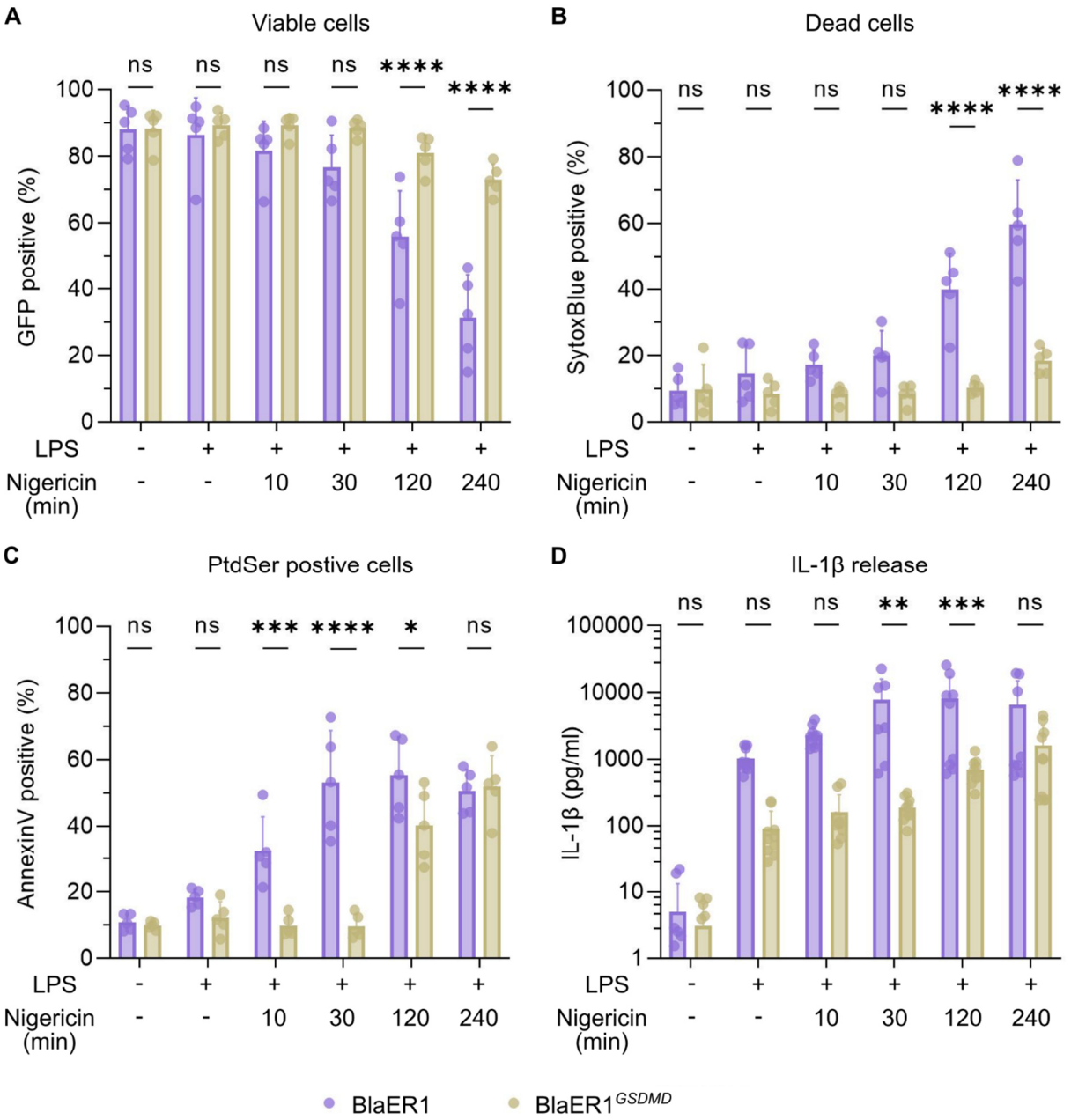

Figure 44: Knockout of *GSDMD* in BLaER1 cells results in resistance to pyroptosis.
(A-D) Pyroptosis was induced in BLaER1 and BLaER1$^{GSDMD-/-}$ cells by addition of 200 ng/mL LPS for 3 h 45 min and subsequent treatment with 4 µM nigericin for 10 to 240 min. After treatment, the cells were stained with SytoxBlue live/dead stain and AF647 conjugated AnnexinV and were analyzed by flow cytometry. For BLaER1 and BLaER1$^{GSDMD-/-}$ single cells the intrinsic eGFP fluorescence **(A)**, SytoxBlue signal **(B)** and Annexin V positivity **(C)** were measured**.** The IL-1β release was determined by an IL-1β specific ELISA using the cell supernatant at each respective time-point **(D)**. Shown are mean values + SD, N=5. Significance was determined by two-way ANOVA **(A-C)** or non-paramteric Mann–Whitney tests **(D)**. *$p < 0.05$, **$p < 0.01$, ***$p < 0.001$, ****$p < 0.0001$. Experiments conducted together with Kerren Volkmar.

The share of viable cells derived from the constitutively expressed GFP showed a significant decrease from 88.0 ± 7.0 % to 55.9 ± 13.8 % and 31.4 ± 13.0 % for the wildtype BLaER1 compared to 81.0 ± 5.4 % and 73.0 ± 4.6 % in the BLaER1$^{GSDMD-/-}$ sample at 120 min and 240 min post-induction, respectively (Figure 44 A). In well accordance, the ratio of dead cells, distinguished by the dead cell stain SytoxBlue, increased from 9.6 ± 4.8 % to 40.0 ± 10.9 %

and 59.7 ± 13.3 % at the same time points after treatment for the BLaER1 cells (Figure 44 B). In both approaches, the viability of cells was equal in untreated, LPS treated samples, as well as 10 min post-pyroptosis induction. At 30 min post-treatment a slight increase in the share of dead cells was observed for the wildtype BLaER1 (Figure 44 A, B). Quicker than the dead cells, the share of cells displaying PtdSer expanded for BLaER1 cells after the addition of nigericin from 10.8 ± 2.4 % in the untreated sample to 32.5 ± 10.3 % after 10 min and 53.1 ± 15.6 % after 30 min followed by a stagnation with 55.4 ± 11.4 % and 50.6 ± 6.4 % at 120 min and 240 min post-treatment. The share of PtdSer positive cells of BLaER1$^{GSDMD-/-}$ remained stable around 10 % until 30 min post-treatment, which was significantly lower than the wildtype BLaER1 cells. After 120 min of incubation with nigericin, the share increased to 40.2 ± 11.1 %, still significantly lower than the BLaER1 and further increased to 51.9 ± 9.4 % after 240 min of nigericin treatment and thereby equalized with the other sample (Figure 44 C). The IL-1β release was evenly low between BLaER1 and BLaER1$^{GSDMD-/-}$ without treatment, but strongly increased for the wildtype sample to 1019 ± 401 pg/mL after LPS stimulation and up to 8078 ± 8991 pg/mL and 6567 ± 8430 pg/mL and at 120 and 240 min after addition of nigericin, respectively. In comparison, BLaER1$^{GSDMD-/-}$ secreted significantly less amounts of IL-1β after LPS treatment at 120 and 240 min of nigericin treatment with 91 ± 74 pg/mL, 694 ± 292 pg/mL and 1600 ± 1581 pg/mL, respectively (Figure 44 D). In summary, the BLaER1$^{GSDMD-/-}$ strain was less susceptible to the pyroptosis induction than the wildtype BLaER1 strain.

6.7.3 Parasite release is delayed in pyroptosis resistant BLaER1$^{GSDMD-/-}$

Subsequently, it was tested whether the difference in the susceptibility to pyroptosis also confers to a difference in the release of parasites from an infected cell. Therefore, samples of BLaER1 and BLaER1$^{GSDMD-/-}$ were infected by *Lm*^{DsRed} promastigotes, treated with LPS and nigericin at 18 h pI and then tracked by live cell microscopy (Figure 45)

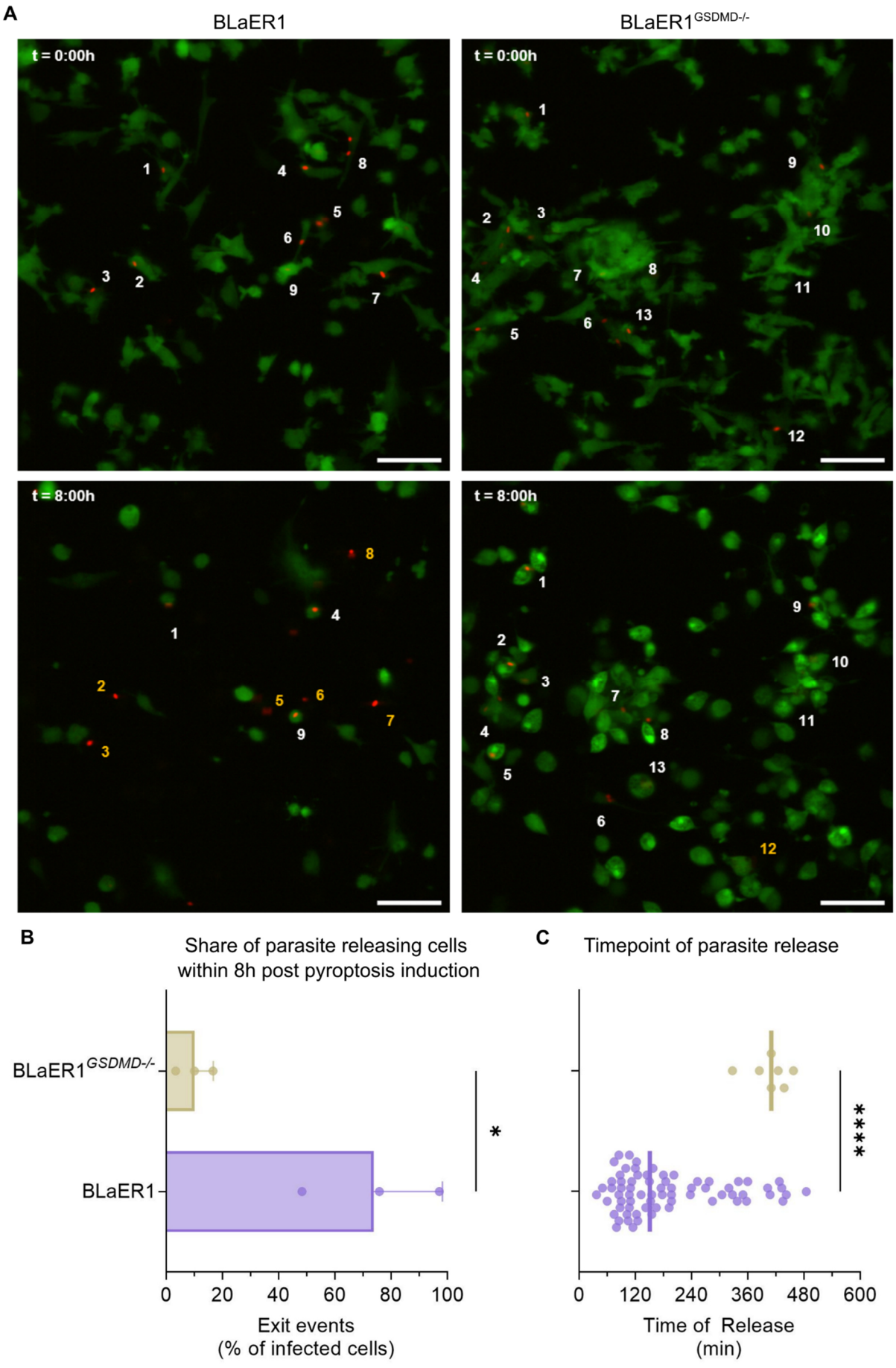

Figure 45: Parasite release from BLaER1$^{GSDMD-/-}$ is delayed after pyroptosis induction.

To Fig. 45 – Live-cell imaging analysis of *eGFP* expressing BLaER1 and BLaER1$^{GSDMD-/-}$ (green) infected by *Lm*^{DsRed} promastigotes (red) and treatment with 200 ng/mL LPS for 3 h 45 min and subsequent addition of 4 µM nigericin. Sample acquisition was started after the addition of nigericin (*t* = 0:00 h). Image series were acquired by laser scanning microscopy using a 40× objective and a time interval between individual images of 2.5 min. **(A)** Representative image series of infected BLaER1 and BLaER1$^{GSDMD-/-}$ after addition of nigericin, showing intracellular parasites (white numbers) and released parasites (orange numbers) at the beginning and the end of image acquisition. Scale bar equals to 20 µm. **(B)** Quantification of BLaER1 and BLaER1$^{GSDMD-/-}$ cells releasing parasites during acquisition within the first 8 h after nigericin addition. **(C)** Time of each parasite release event detected within the first 8 h after nigericin addition. For quantification three distinct positions were imaged per each sample and replicate, N=3. The graphs show mean values + SD **(B)** or values for each single cell **(C)**. Significance was determined by an unpaired *t*-test. **p* < 0.05, *****p* < 0.0001

Following the infected cells throughout the first 8 h post-treatment revealed parasite release events from the cells, whereby released parasites retained their red fluorescence during the recorded time-interval, indicating their viability (Figure 45 A). The share of infected cells having released parasites at the endpoint of the assay was with 73.8 ± 24.5 % in the wildtype BLaER1 sample highly increased over the 10.0 ± 6.7 % release events detected in the BLaER1$^{GSDMD-/-}$ sample (Figure 45 B). When comparing the timely distribution of release events, it became apparent that BLaER1$^{GSDMD-/-}$ cells released parasites significantly delayed than BLaER1 cells, with an average of 407.5 min to 189.5 min, respectively (Figure 45 C).

6.7.4 Induction of pyroptosis and LPS stimulation facilitate parasite cell-to-cell transfer of amastigotes

With the confirmation, that the BLaER1$^{GSDMD-/-}$ cells are less susceptible to pyroptosis and that the release of parasites is consequently delayed, the requirements were met to test if the release of parasites also results in secondary infections by released, viable *Lm*^{DsRed} and to establish BLaER1 cells as infection model for parasite exit in general (Figure 46).

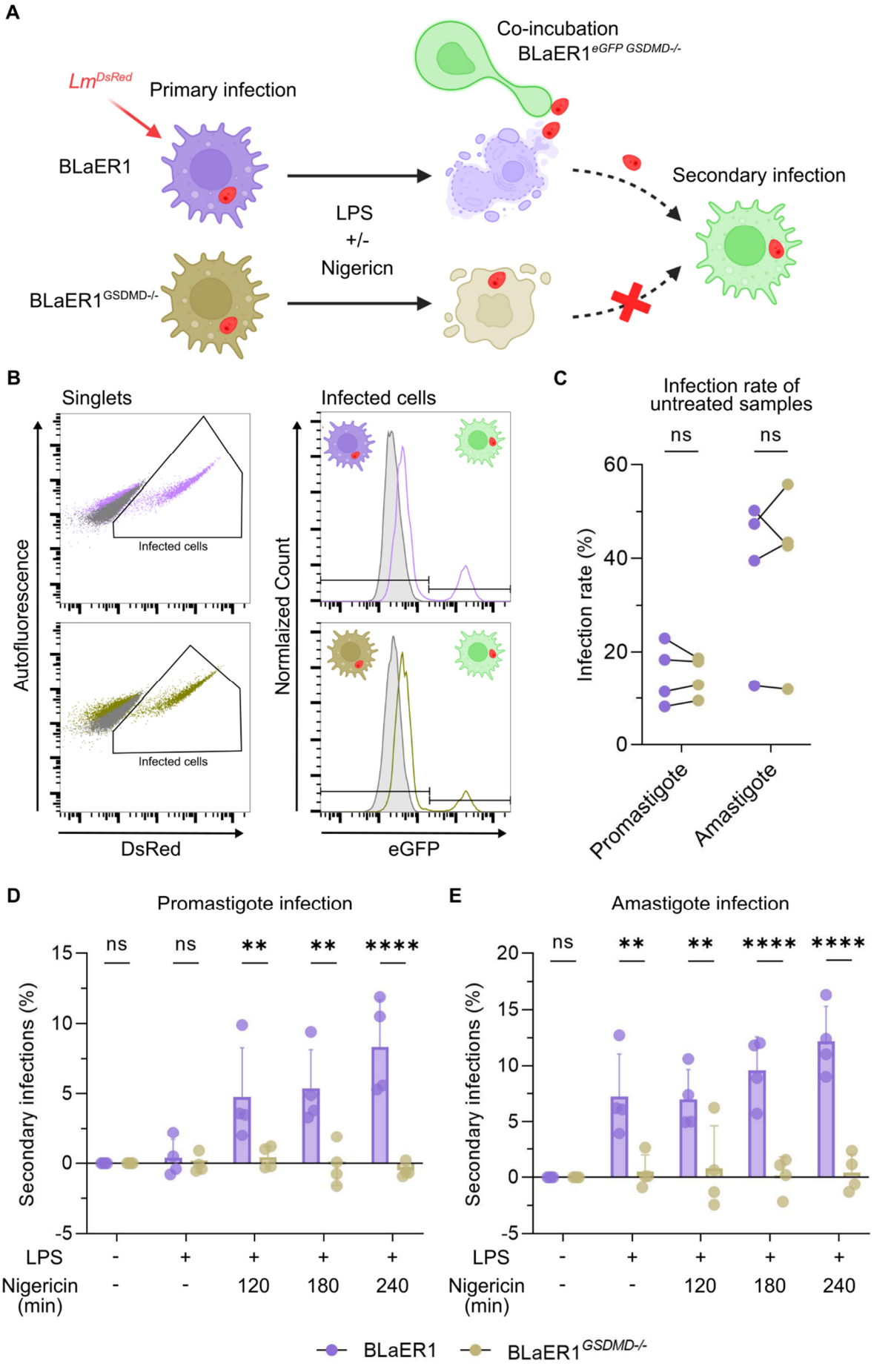

Figure 46: Cell-to-cell transfer can be measured under pyroptosis inducing conditions utilizing the BLaER1 infection model.

To Fig. 46 – **(A)** Scheme of parasite transfer from BlaER1 and BLaER1$^{GSDMD-/-}$ initially infected by *Lm*^{DsRed} promastigotes or amastigotes to uninfected BLaER1$^{GSDMD-/-}$ by nigericin and/or LPS stimulation using a co-incubation assay. **(B)** Gating strategy for the detection of infected cell populations by the DsRed fluorescence (left panel) with subsequent gating for primary infected cells (GFP^{-}) and co-incubated cells (GFP^{+}) to derive the secondary infection rate. **(C)** Primary infection rate of promastigote or amastigote infected BlaER1 and BLaER1$^{GSDMD-/-}$ cells. Connected dots represent samples infected by parasites from the same culture. **(D, E)** Secondary infection rate of co-incubated cells (GFP^{+}) after stimulation with LPS and nigericin for the indicated time during co-incubation, normalized to the secondary infection rate measured in the untreated control after primary infection by promastigotes **(D)** or amastigotes **(E)**. The graphs show the value of each experiment **(C)** or mean values + SD **(D, E)** of four independent experiments, N=4. Significance was determined by two-way ANOVA with multiple comparison correction by Holm-Šidák test, ns – not significant, $^{**}p < 0.01$, $^{****}p < 0.0001$.

BLaER1 and BLaER1$^{GSDMD-/-}$ were infected either with *Lm*^{DsRed} promastigotes or amastigotes and co-incubated with BLaER1$^{GSDMD-/-}$ constitutively expressing GFP during treatment with LPS with or without nigericin (Figure 46 A). The use of GFP negative and positive cells allowed the separate detection of primary and secondary infections, whereby the secondary infection rate is the ratio of infected and GFP positive cells as a share of all infected cells (Figure 46 B). The primary infection rate by pro- and amastigotes was equal within replicates of BLaER1 and BLaER1$^{GSDMD-/-}$ infected with the same batch of parasites (connected dots) and variations only occurred between biological replicates of the same cell type (Figure 46 C). After the initial infection of wildtype BLaER1 by *Lm*^{DsRed} promastigotes and upon pyroptosis induction, parasites caused elevated secondary infection rates of 4.8 ± 3.5 %, 5.4 ± 2.8 % and 8.3 ± 3.4 % from 120 to 240 min compared to the untreated sample. These rates were significantly higher than secondary infections caused by exit from BLaER1$^{GSDMD-/-}$, which showed no increase to its respective untreated control. Cells treated with LPS did not cause higher secondary infections rates above the background for both, BLaER1 and BLaER1$^{GSDMD-/-}$ cells (Figure 46 D). The same but more pronounced effect was observed in samples initially infected by axenic amastigote, resulting in 7.0 ± 2.7 %, 9.6 ± 3.0 % and 12.2 ± 3.0 % secondary infections above background in wildtype BLaER1 compared to unchanged secondary infection rates for BLaER1$^{GSDMD-/-}$ after 120, 180 and 240 min of LPS and nigericin treatment. Markedly, the sole treatment by LPS caused a significantly higher secondary infection rate of 7.2 ± 3.8 % in amastigote infected BLaER1 cells than in cells with an ablation of *GSDMD* which were on the background level (Figure 46 E). Thus, the exit of parasites from BLaER1 wildtype cells under inflammasome inducing conditions was increased compared to BLaER1$^{GSDMD-/-}$ cells. Additionally, the sole stimulation by LPS also resulted in a GSDMD dependent exit of parasites after an initial infection by axenic amastigotes.

7 Discussion

The intracellular proliferation and the transmission to new host cells of *L.* parasites in their amastigote stage is an essential mechanism to uphold and progress the infection. This work aimed to characterize and manipulate the *Lm* exit mechanism that facilitates cell-to-cell transfer between macrophages. Therefore, hMDM from individual donors and *in vitro* cultured *Lm* promastigotes and axenic amastigotes were employed as infection model. Firstly, the contribution of regulated cell death to this process in infected hMDM should be analyzed. Secondly, the role of parasite metabolism during infection and the phenotype of human host cells should be examined to further unravel how the interplay of *Leishmania* and the harboring cell tailor the appearance of exit events. In addition, the BLaER1 cell line ought to be tested to determine whether it is an applicable infection model to detect parasite cell-to-cell transmission by NLRP3 inflammasome induction, employing the advantages of gene modifications.

In order to gain an experimental approach to this task, a fluorescence-based co-incubation assay was established that successfully quantified exit events between hMDM and revealed a transfer of cellular material for the majority of events. Moreover, infected M-CSF derived M(-) displayed caspase-3 activity highly indicating the involvement of apoptosis in the process. The inhibition of apoptosis by caspase-3-specific and pan-caspase inhibitors was not able to change the occurrence of exit, yet both inhibitors lowered the viability of uninfected cells dependent on the individual donor. Employing the proliferation reporter strain $Lm^{mKikume}$ for the co-incubation assay proved that exit is dependent on parasite proliferation prior to an exit. Interestingly, the ability of *Lm* to proliferate intracellularly was strongly altered by the phenotype of infected cells. The inflammatory activation of hMDM with IFNγ resulted in vastly increased parasite proliferation, while stimulation with IL-4 reduced the proliferation slightly, and non-stimulated and IL-10-stimulated hMDM dampened the proliferation. Accordingly, the exit rates from pro-inflammatory M(IFNγ) were significantly increased over those measured in anti-inflammatory stimulated hMDM, yet large variations of the observed cell-to-cell transfer rates were apparent between replicates with individual donors for hMDM. A gene expression analysis of inflammatory M(IFNγ) from 20 individual donors revealed that the kynurenine pathway was downregulated in the group of donors exerting increased exit rates. Consequently, the inhibition of the rate-limiting step in that pathway induced a pronounced increase in exit events (Figure 47).

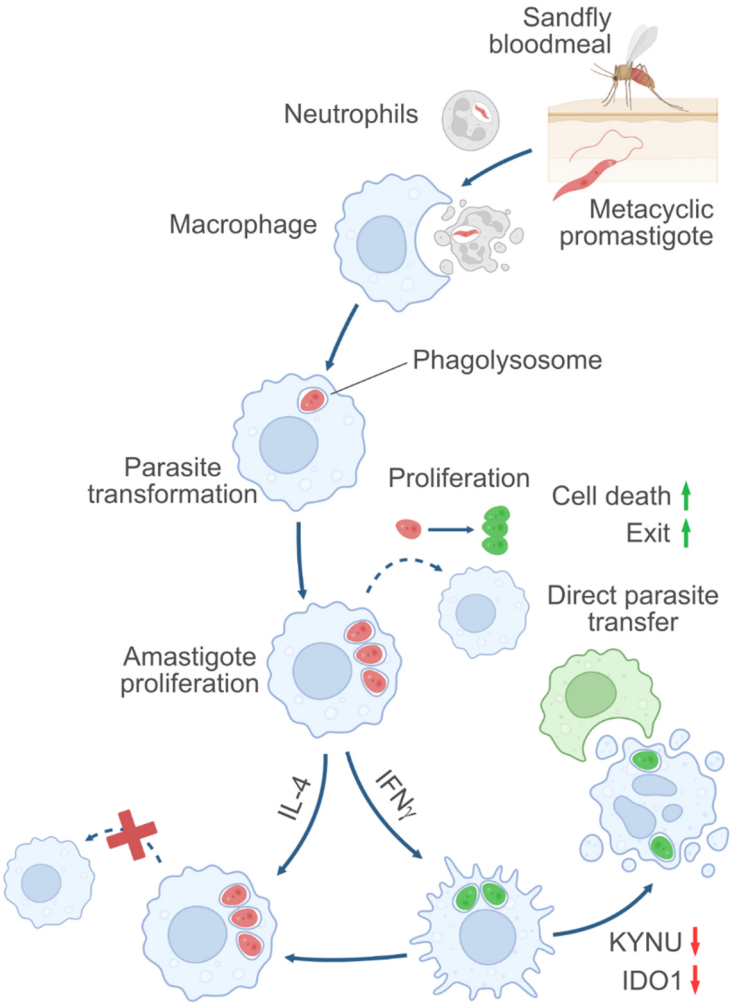

Figure 47: *Lm* lifecycle extract expanded by the results regarding an exit mechanism for the cell-to-cell transmission of parasites.

In cooperation with Kerren Volkmar, it was also possible to show that pyroptosis could be another pathway contributing to parasite exit. Here, an activation of the canonical activation pathway of the NLRP3 inflammasome in BLaER1 cells facilitated the cell-to-cell transfer of parasites to a recipient host cell in dependence on pyroptotic cell death. Interestingly, the priming by LPS during an amastigote infection of BLaER1 cells without a second stimulus already induced a cell-to-cell transmission of parasites by an inflammasome activation pathway that requires further characterization. In that context, the activity of caspase-1, a driver of pyroptotic cell death, was upregulated for some donors in IFNγ and M-CSF-stimulated hMDM.

7.1 Parasite exit in hMDM

Recruited monocytes and monocyte derived macrophages that invade the inflamed tissue are the central cell type involved in the infection progression during the acute phase of Lm infections [27]. Also, monocyte-derived Ly6C+CCR2+ phagocytes are the driver of parasite

proliferation and parasite cell-to-cell transmission during *in vivo* infections of mice [23]. Resident macrophages likely play a minor role in the spread of parasites due to their function as permissive reservoirs contributing to the long-term persistence of *L.* parasites and their relatively low numbers at the afflicted sites compared to recruited cells [53,54]. Hence, hMDM from individual donors were employed as a suitable infection model to further examine the characteristics of *Lm* parasite exit. The co-incubation assay is the fundament to address the exit of parasites from primary human cells *in vitro* and allows a relative quantification of infection events derived from exit compared to primary infection events. A comparable approach has been used to detect *Leishmania* parasite transmission to newly recruited monocytes in mice *in vivo* after an adoptive transfer with a progeny discrimination through the CD45.1/CD45.2 immunostaining and flow cytometry analysis [23]. To experimentally detect transfer of cellular material between cells, this method was even expanded by a combined staining with non-specific fluorescent dye of whole cells and CD45.1/CD45.2 labelling. Therewith, the pathogen transfer of *Mycobacterium tuberculosis* (*M. tuberculosis*) between cells alongside cellular material was observed using an *in vitro* microscopic analysis of infected BMDM [157]. These experimental approaches were used as a template for the co-incubation assay to detect *Lm* exit. Due to a missing cell surface marker that can be used to discriminate between two cell populations form identical human donors, I established the assay using irreversible fluorescent labelling of hMDM with SE-dyes. The labelling of the primary infected and the co-incubated cell batch with distinct fluorophores provided a reliable detection of both populations without fluorescent cross-labelling during the co-incubation time of samples (Figure 13). Additionally, this assay allowed the discrimination between secondary infections and infections with transfer of cellular material (Figure 14). It has to be mentioned that the co-incubation is only an indirect measure of exit because only exit events resulting in a transmission to co-incubated cells with a distinct fluorescence label were detected. Transmissions between cells with the same fluorescence label and parasites residing extracellularly after exit cannot be detected in this end-point analysis with flow cytometry. Still, the read out provides adequate results, as the relative exit rates were compared between conditions that suffered from the same described analytical drawbacks at all times. Since transmission events between cells of the primary infected cell batch were not detected, the overall exit rates might be rather underrepresented by the assay. Despite these limitations, the assay provided a compatibility of relative exit rates and allowed the comparison of various factors like differentiation method for the $CD14^+$ monocytes, the parasite's promastigote or amastigote stage and the time pI.

7.1.1 Dependence of exit on M-CSF or GM-CSF differentiation of hMDM

Considerable differences were observed between exit rates from M-CSF derived M(-) and GM-CSF derived M(-) after an infection by axenic amastigotes (Figure 15). The phenotypes of both M(-) might influence the outcome for a parasite exit. M-CSF and GM-CSF induce different

transcription factors [162] and a $CD14^+$ monocyte differentiation over 7 d results in expression variances of about 17 % of the genes [163]. Despite the rather low difference on the gene expression level, an apparent difference between the phenotypes was the parasite burden in primary infected cells, where M-CSF derived M(-) had the highest parasite load when being infected by axenic amastigotes. The parasite burden was drastically lower in the recipient cells, infected after exit. This effect was neither observed for axenic amastigote infected GM-CSF derived M(-) nor for all promastigote infections (Figure 16). A possible explanation could be that a single highly burdened cell spreads the infection to multiple co-incubated cells and thereby elevates the observed exit rates for M-CSF derived M(-), not due to increased parasite exit itself but due to the higher number of infected recipient cells per exit event. In addition, the observed differences in the parasite burden might have been caused by different proliferation rates of intracellular parasites. An analysis of the proliferative behavior of amastigotes in M-CSF derived M(-) in this work revealed especially high proliferation after an infection by axenic amastigotes within the first 48 h pI, which is the relevant time interval where the difference in exit was observed (Figure 24). The parasite proliferation is a described trigger for exit of *Lm* parasites in mouse and was also higher for parasites undergoing cell-to-cell transfer between hMDM (Figure 25) [23]. If the higher parasite burden in M-CSF derived M(-) compared to GM-CSF derived M(-) resulted from a more efficient proliferation after infection, this provides a reasoning for the increased exit rates.

7.1.2 Intracellular parasite proliferation in hMDM

As described, an identified trigger for *Lm* exit is the intracellular proliferation of parasites. [23,133]. To date, most of the data for *L.* infection progression or control on the cellular level are obtained from mice infections, especially in the analysis of the dynamic parasite proliferation process. On the cellular level, NO induction by macrophages controls the parasite proliferation and exerts parasite killing in murine cells *in vivo* as well as *in vitro* [44,56,128,129]. Several studies reported that macrophages from other mammals including porcine, cattle and human do not express NOS2 and do not produce NO during a microbial encounter [46,164–166]. As a consequence, *in vitro* cultured hMDM and macrophage-like cell lines cannot suppress and resolve *L.* infections [101,142]. Interestingly, also BMDM infected with *L. amazonensis* but without previous priming by LPS develop a chronic infection with high parasite burdens [167]. Yet, data on the proliferation in human macrophages *in vitro* is lacking. In this work, the mKikume proliferation reporter was successfully introduced to *Lm* parasites and used for the analysis of proliferation in M-CSF derived M(-) (Figure 23, Figure 24). Axenic amastigotes proliferated readily within the first 24 h pI, but their proliferation decreased significantly at the second and third day of infection before it stabilized at the fourth day. The high initial replication and the subsequent drop off are likely a result of the changing nutrient supply between the rich axenic culture and the phagolysosome of macrophage cells that exerts a harsh environment on residing pathogens [168]. The proliferation of intracellular parasites

after a *Lm* promastigote infection was more ambivalent. In some cases, no proliferation was detected within the first 24 h pI, while other samples showed proliferation at the same time interval. The proliferation lag can be explained by the transformation to amastigotes the parasites have to undergo prior to their ability for replication [169]. The transformation is completed within the first 24 h pI but is dependent on the infected cell type [170]. The observed proliferation rates within the first day of infection in some promastigote infected hMDM samples and its absence in others suggests that also individual donor variations influence the transformation process, as well as the subsequent proliferation rates (Figure 24).

7.1.3 Parasite proliferation as a trigger for exit

When using M-CSF derived M(-) for the primary infections, the exit rates were altered between the primary infection by promastigotes and amastigotes, as well as by the time interval pI that determined the beginning of the co-incubation with recipient cells (Figure 15). Both can be explained by the proliferation rates of the parasites at the respective time points that can be determining for an exit. Infecting axenic amastigotes had an increased intracellular proliferation from 24 h to 48 h pI compared to 72 h pI to 96 h pI and compared to promastigotes at both time points (Figure 24). Accordingly, the pronounced exit rates from M-CSF derived M(-) infected by axenic amastigotes at 24 h pI and 20 h of co-incubation coincide timely with the elevated proliferation rates. In comparison to promastigote infections, the proliferation rates were mostly higher for the axenic amastigote infections, likely due to the not required transformation before the intracellular replication [170].

Employing axenic amastigotes as the model for established infections with readily replicating parasites, proliferation was measured in primary infected cells and in cells infected after exit. Indeed, the observed proliferation rates in recipient cells was higher compared to primary infected cells (Figure 25). Moreover, the proliferation was increased prior to the exit and even more strikingly, the share of high proliferating parasite populations that varied between individual donors, correlated positively with the measured cell-to-cell transfer (Figure 26). The proliferation index, which is an averaged value of the parasite replication in all measured cells of a sample, showed no correlation to the exit rates. So, exit seemingly is not dependent on the overall proliferation allowed by a population of cells, but *Lm* requires highly replicating subpopulations to egress. These results confirm that parasite proliferation plays a similar role in the exit mechanism of intracellular *Lm* in non-activated human hMDM that was described for BMDM [23].

7.1.4 Attenuated *L.* parasites as control for exit

Attenuation of pathogens impairs the virulence of most pathogens and is a long time used technique to generate live vaccines [171,172]. As described, treatment of *L.* parasites with amotosalen and UV light can be used to generate KBMA parasites that are attenuated but infective *in vitro* and *in vivo* [130]. Because exit was shown to be dependent on proliferation of

intracellular parasites, it was expected that replication-deficient parasites would be hindered in their ability to induce a cell-to-cell transmission and provide a control to better characterize the relation between replication and exit. The KBMA treatment of amastigotes from axenic culture resulted in parasites unable to increase their numbers in axenic culture (Figure 28). Yet, contrary to the expectations, KBMA treated amastigotes were transferred to co-incubated cells just as untreated parasites (Figure 29). Therefore, the ability of KBMA treated amastigotes to proliferate was reevaluated using the proliferation reporter mKikume, which revealed an unchanged replication in axenic culture and after hMDM infection (Figure 30). In difference to our approach, previous studies used the promastigote form of the parasite to generate KBMA parasites, which could explain why the published protocols were not successful for axenic amastigotes. The latter appeared to be sensitive to increased concentrations of amotosalen, while lower concentrations did not block the replication in the axenic culture. The use of 4'-(aminomethyl)-4,5',8-trimethylpsoralen hydrochloride, a derivate of amotosalen, was utilized by other groups for the generation of *Lm* KBMA parasites and could provide a mitigation strategy for future attempts to generate KBMA axenic amastigotes [133].

An alternative approach to achieve an arrest of parasite replication that is even specific for the amastigote stage of the parasites, is the knockout of a specific *centrin* gene [131,134]. Interestingly, the loss of *centrin* induces the release of IL-12 and promotes a protective Th1 response in susceptible BALB/c mice in comparison with wildtype *L.* infections [135,136,173]. In a CRISPR/Cas9 based approach, the *Lm centrin* gene *LmjF22.1410* was knocked out successfully on one allele, yet the deletion on the second allele was not achieved (Figure 31). The heterozygous deletion was shown to not contribute to an attenuated parasite phenotype [134]. In order to achieve a knockout on both alleles, the experiment requires a replication, potentially exchanging the selective markers used to replace *LmjF22.1410* to achieve a better clone selection [174]. Replication deficient parasites could provide an additional tool to further analyze parasite exit mechanisms in hMDM and has been utilized already as such in mice [133].

7.2 Apoptosis induction as exit mechanism for parasite transmission

Apoptosis is a regulated cell death form serving as a homeostatic mechanism that ensures the recognition and uptake of dying cells without the induction of inflammatory responses by phagocytic cells like macrophages. Intracellular pathogens that preferably reside in phagocytic cells can subvert this process to infect new host cells. *Lm* uses host cell apoptosis to facilitate the transmission from neutrophils to macrophages in their promastigote stage and suppress an inflammatory response [20,146]. It is also evident that *Lm* amastigotes residing in macrophages utilize this mechanism to facilitate the cell-to-cell transfer between macrophages, triggered by the parasites' proliferation [23]. In the publication from Baars *et al.*

we were able to complement data from the mouse infection model with the present results from hMDM infections, together showing that amastigotes undergo a direct cell-to-cell transfer alongside cellular material of the initially infected cell. Moreover, infected M(-) displayed caspase-3 activity and fragmented DNA which was dependent on the ability of the parasite to proliferate [133].

7.2.1 Transfer of cellular material during the parasite transmission

The co-incubation assay established in this work allowed the detection and quantification of cell-to-cell transfer events with the transfer of cellular material to the parasite recipient cell (Figure 14). Infections with uptake of cellular material were the dominant form of parasite transmission for axenic amastigote and promastigote infections in M-CSF derived M(-) (Figure 17 A). The transfer of cellular material suggests a phagocytotic uptake of cell and parasite as a result of apoptosis, but also that parasites experience no or limited exposure to the extracellular space. This was underlined by the fact that the transferred material was detected within the same phagolysosome as the amastigote indicating their simultaneous transfer (Figure 17 B). To test whether the observed exit alongside cellular material might be a passive process or a parasite-induced process, the occurring exit rates after 24 h pI + 20 h co-incubation were correlated with the rate of phagocytosis of uninfected cells in co-incubated samples (Figure 18 D, E). Interestingly, the cell-to-cell transfer of parasites from initial infections by promastigotes highly correlated with the uptake of uninfected cells by the co-incubated cell batch, suggesting a passive transfer of infecting promastigotes. The transfer after amastigote infections was statistically independent of the transfer of cellular material from uninfected cells, indicating a distinct and amastigote-specific mechanism. The direct nature of the transmission event provides a shielding against the complement system and opsonization for the amastigote stage of the parasite prior to an uptake by macrophages, helping amastigote staged parasites to sustain clearance by the complement system. Amastigotes are more susceptible to an opsin-mediated uptake than promastigotes, because the metalloproteases GP63 and LPG, which confer to the protection against opsins, are differently expressed in amastigotes and show delocalization to the flagellar pocket [175–177]. The opsonization of amastigotes can result in a Ras-related C3 botulinum toxin substrate-1 (Rac-1)-mediated uptake which induces a microbicidal respiratory burst [178].

7.2.2 A connection between proliferation and apoptosis

M(-) infected by amastigotes but not promastigotes presented an upregulated caspase-3 activity at 44 h pI compared to uninfected cells (Figure 19). This is well in line with the increased exit observed after the infection with axenic amastigotes, compared to exit after primary infections by promastigotes, if apoptosis is the driver of parasite exit (Figure 15). Hallmarks for apoptotic cell death during *L.* infection are also described by other groups. *L. amazonensis* infections of BMDM result in an upregulation of the pro-apoptotic gene *Bax* and blebbing of

cells [101]. Similarly, the same *L. spp.* induced the catalytical activation of caspase-3, the externalization of PtdSer and the fragmentation of nucleic DNA [96]. Finally, intravital imaging of *Lm* infected C57BL/6 mice employing a fluorescence resonance energy transfer-based caspase-3 reporter substrate showed increased caspase-3 activity in infected compared to uninfected cells [133]. Measuring the caspase-3 activity in $Lm^{mKikume}$ infected hMDM revealed that the proliferation rate of parasites was increased in caspase-3^{+} cells (Figure 27). Accordingly, the parasite proliferation is elevated in $TUNEL^{+}$ cells, which stains fragmented nucleic DNA, during *in vitro* infections of BMDM by $Lm^{mKikume}$ [133]. This establishes a connection between the hypothesized mechanism driving parasite exit, the apoptotic cell death, and the previously described trigger for this process, the *Lm* proliferation [23].

The observed activation of apoptotic cell death as a process to spread *Lm* amastigotes likely complements a phase of apoptosis suppression reported for the initial infection of cells by promastigotes [97–100]. This temporal resolution of the cell death inhibition and subsequent induction is well established for neutrophils during *Lm* infections [20,146]. Therewith, the presented results provide a potent mechanism for parasite exit and contribute to our understanding of the infected macrophage host cell fate during acute infections.

7.3 Inflammasome activation and subsequent pyroptosis provides a functional pathway for exit

An activation of the inflammasome is widely approved for most *L. spp.* infections but results on a subsequent demise of infected cells to a pyroptotic cell death is scarce. In difference to apoptosis, pyroptosis is not a homeostatic process but a mechanism of the innate immune response to induce inflammatory processes by the release of IL-1β, IL-18 and DAMPs during the GSDMD and NINJ1 mediated disintegration of the cellular membrane [105,110]. Although, like apoptosis, pyroptosis can be subverted by intracellular pathogens to serve as an exit mechanism [70]. By employing the macrophage-like cell line BLaER1, it was possible to show that the activation of the inflammasome with LPS and nigericin is an effective mechanism to release viable *Lm* parasites by a pyroptotic cell death and that parasites were able to reinfect primary uninfected cells. Strikingly, the priming of amastigote infected cells by LPS also resulted in a GSDMD dependent transmission between cells [179].

7.3.1 Inflammasome activation and pyroptosis in BLaER1 and BLaER1$^{GSDMD-/-}$ cells

According to the literature, the canonical activation of the inflammasome by LPS and nigericin in BLaER1 cells led to IL-1β release and a GSDMD dependent cell death was observed within 2 h after the second signal by nigericin (Figure 44) [108]. GSDMD is essential for the induction of a pyroptotic cell death subsequent to a NLRP3 inflammasome assembly and activation [180]. Despite an initial protection against a lytic cell death by a GSDMD deletion, also the

BLaER1$^{GSDMD-/-}$ strain showed a temporally delayed release of IL-1β and increasing shares of dead cells. This could be a result of an caspase-3/7/8 mediated apoptosis activation described for BMDM and RAW264.7 cells and the same treatment due to the interrupted pyroptosis induction [180]. Even though apoptosis is not a lytic form of cell death and would not explain a release of IL-1β in the absence of GSDMD, apoptotic cells can, if they remain uncleared by phagocytes, segue into a secondary necrosis, characterized by a loss of membrane integrity and a release of cytosolic content [181,182]. Also, the sole stimulation with LPS of BLaER1 cells triggered the release of IL-1β but no pyroptosis occurred, as it was shown for the alternative inflammasome activation mechanism (Figure 44) [116]. As a consequence, the stimulation of promastigote infected BLaER1 cells with LPS and nigericin conferred to an efficient release of intracellular parasites, while the GSDMD KO strain of BLaER1 was less sensitive for the treatment and parasite release (Figure 45). Likely, *Lm* were not directly released by GSDMD but during the disintegration of the cellular membrane by NINJ1, as the pores formed by GSDMD are too narrow for parasites [110].

7.3.2 Parasite transmission by different inflammasome activation pathways

The release of parasites also contributed to an effective transfer of parasites to new recipient host cells, dependent on GSDMD and the canonical activation of the NLRP3 inflammasome by LPS and nigericin (Figure 46). The parasites appeared to be viable post-transmission derived from their intact intrinsic DsRed fluorescence, which is also described for the parasite release of cells treated by the canonical inflammasome inducer LPS and exogenous ATP [124]. In addition, the stimulation with LPS alone also led to a GSDMD dependent transfer of *Lm* parasites after an infection by axenic amastigotes, but not promastigotes (Figure 46). Interestingly, the GSDMD-dependent induction of pyroptotic cell death was shown to be subverted at the onset of *L. amazonensis* promastigotes infection of BMDM by an alternated cleavage of GSDMD inhibiting pore-formation assembly of the NLRP3 inflammasome by the non-canonical pathway [161]. This provides a protection against an inflammasome activation and pyroptosis at the onset of infection and could contribute to hinderance of a parasite exit before an effective replication by amastigotes is established intracellularly [161,170]. The strong and abrupt canonical activation via LPS and nigericin nevertheless overcame the promastigote inhibition of the pore formation, suggesting that both pathways are competitive for the available GSDMD. Vice versa, The ablation of GSDMD also conferred to exacerbated infections during *in vivo* infections of C57BL/6 mice with self-healing strains *Lm* and *L. braziliensis*, as well as *L. amazonensis* and *L. mexicana*, indicating a protective role through a functional activation of GSDMD at later stages of the infection. ASC-specks that indicate a successful assembly of the NLRP3 inflammasome were present in lesions of infected mice and CL patients [183]. Also, caspase-1/11 ablations increased parasite burdens and infection rates 72 h pI, suggesting that pyroptosis plays a role later during infection [161]. Therefore, the

induction of a GSDMD-dependent cell-to-cell transmission by amastigote during infections observed *in vitro* might also occur during *in vivo* infections.

The stimulation of human cell lines and hMDM with LPS induces the alternative activation of the NLRP3 inflammasome without an assembly of the whole machinery and devolving into pyroptosis [116]. Yet, the efficient transfer of amastigotes during the stimulation of cells with LPS can be attributed to a pyroptotic cell death as it appeared to be GSDMD dependent (Figure 46) [180]. This raises the question how the intracellular amastigotes contributed to an inflammasome activation with subsequent pyroptosis and parasite release. *Lm* is shown to non-canonically activate the inflammasome in an uncharacterized interaction between virulence factors like LPG from the parasite and the caspase-4/5 or caspase-11 [154,184]. A non-canonical activation of the inflammasome subsequent to the upregulation of cellular NLRP3 through the TLR4 and NF-κB signaling primed by LPS may have strengthened the pyroptosis induction resulting in increased exit rates [106]. A missing link is the inducing virulence factor for caspase-4/5, as the activation of the ortholog caspase-11 during infection is attributed to LPG by previous reports [184]. Amastigotes can retain an expression of LPG up to 72 h pI [170,185]. It should be subject to further research whether axenic amastigotes express LPG that potentially activates the inflammasome via the non-canonical pathway, or whether another virulence factor is capable to do so. In conclusion, also the pyroptotic cell death pathway provides a mechanism for parasites to transfer between cells under inflammasome inducing conditions.

Again, life stage dependent differences of the parasite were crucial for the induction of pyroptosis and the transmission between host cells. The combination of ASC-specks observed in CL patient lesions and the *IL-1β* expression levels that correlated positively with a worsened disease outcome for *L. braziliensis* and *L. mexicana* infected patients suggest a contribution of the inflammasome activation to the infection progression [120,121,161]. As a consequence, it can be speculated that also the pyroptosis driven release and transmission of parasites between cells negatively impacts the course of infection.

7.4 The determining role of the host cell phenotype for *Lm* replication and exit

The host cell phenotype affects the ability of infecting *L.* parasites to replicate intracellularly [23]. Yet, data on the intracellular proliferation of *L.* in hMDM, especially under different stimulations, is scarce. The signaling of the inflammatory cytokine IFNγ and regulatory cytokines like IL-4 and IL-10 shape the landscape of macrophages during the infection and have severe implications on the disease progression [2]. On the cellular level, the stimulation with IFNγ renders host cells that are permissive for the parasite proliferation until the replication is controlled by NO in mice and the systemic recruitment of monocytes is limited [27,129]. The

stimulation of macrophages with IL-10 allows the formation of a reservoir associated with long persisting parasites [53,125,133]. IL-4 contributes on the systemic level by limiting monocyte recruitment but dampening the activation of microbicidal effector mechanisms [27,52]. Due to the different roles of macrophages and monocytes during the infection induced by an anti- or pro-inflammatory stimulation, the effect of these stimuli on the parasite proliferation and the cell-to-cell transmission was tested with the previously established methods.

7.4.1 Influence of inflammatory and regulatory stimulation on the intracellular replication and exit of parasites in hMDM

The used set of surface markers confirm that the applied differentiation and stimulation confers to the macrophage phenotypes described, but due to the rather unspecific classification of macrophage phenotypes by a small set of cell surface markers, they are termed by their respective stimuli [41,147,186–188]. Interestingly, the cell surface marker abundance of CD206 was reduced in all infected cells in comparison to the uninfected cells from the same donor. Previous study showed that CD206 can facilitate the reception of *L.* parasites [189]. It can be speculated that the lower abundance of CD206 might therefore result from a CD206 dependent recognition and uptake of *Lm* axenic amastigotes (Figure 33 A-D). Moreover, the decreased CD206 expression by M(IFNγ) could also reason the lower infection rate in comparison to the other hMDM (Figure 33 E).

The infection of M(IFNγ) by *Lm*^{mKikume} axenic amastigotes revealed that the parasite proliferation is very strongly upregulated in comparison to M(M-CSF) and M(IL-10) (Figure 34 A). Also, the share of high proliferating parasite subpopulations was the most pronounced in M(IFNγ), which resulted also in increased parasite burdens (Figure 34 B, C). Here, it is to mention that the proliferation limiting agent NO is diminished or absent in *in vitro* cultured hMDM [165]. Despite a functional iNOS mechanism, increased proliferation rates are described also for inflammatory Ly6C^{+}CCR2^{+} monocytes in infection of the resistant mouse strain C57BL/6 in well accordance to our results in hMDM [23]. Additionally, the iNOS inducing signalling by IFNγ during a Th1 response is unable to exert efficient control of *L. amazonensis* infections within the first three weeks of C57BL/6 infections. Rather opposingly, IFNγ facilitates the recruitment of Ly6C^{+}CCR2^{+} monocytes which then constitute high numbers of infected cells [27]. In line with previous results of this work, the elevated proliferation rate of intracellular parasites and the presence of high proliferators in M(IFNγ) led to an increased and *Lm* specific cell-to-cell transmission compared to regulatory stimulated hMDM (Figure 35). Thereby, the exit from M(IFNγ) might contribute to the uncontrolled infection phase in the first 3 weeks pI, functionally linking the extensive recruitment of monocytes during an IFNγ signalling and the resulting high shares of infected monocyte-derived macrophages [27]. M(IL-4) allowed a slightly lower intracellular parasite proliferation than M(IFNγ), but increased rates compare to M-CSF and IL-4 activated hMDM (Figure 34 A). Also, high proliferating parasite populations

were observed (Figure 34 B). Strikingly, M(IL-4) were able to specifically prevent parasite exit, as inert latex beads showed higher transmission rates to uninfected cells than *Lm* amastigotes (Figure 35). As the opposing scenario of the IFNγ signaling during a Th1 response, IL-4 release in a Th2 response is connected with a non-resolving course of the disease [52,190]. Yet, IL-4 confers protection during the early phase of an infection by limiting the recruitment of permissive host cells [27]. The specific retention of intracellular parasites by M(IL-4) could help providing the control over the infection progression by reducing the parasite transmission rates.

IL-10 and also M-CSF strongly controlled the parasite proliferation after infection and high proliferators were barely observed (Figure 34 A, B). Conversely to the low proliferation, the M(IL-10) showed vastly increased exit rates to co-incubated cells (Figure 35). Yet, the cell-to-cell transfer of latex beads was equally high under the same conditions, indicating that the administration of IL-10 results in a rather unspecific transmission of parasites. A reasoning for this event remains vague to date, IL-10 signaling is associated with intracellular parasite survival and long term persistence in the literature due to the counter-regulation of microbicidal effector mechanisms [125,126]. Interestingly, the low proliferation rates in M(IL-10) and also M(M-CSF) are in better line with the formation of host cell reservoirs. At least the M-CSF stimulated hMDM presented reduced transmission of intracellular parasites, alike M(IL-4) (Figure 35). Similarly, the continuous stimulation of BMDM with M-CSF after an infection with amastigotes supported the long-term residency and growth of *L. amazonensis* [167]. It can be speculated that the link between parasite proliferation and exit tailored by the phenotype of the infected host cell contributes to the determination whether persistence or transmission of parasites dominates in the macrophage population. A balance between persistence and transmission regulated by the pathogen proliferation is described as a co-evolutionary process, important to maximize the parasites fitness provably shown for multiple pathogens [191,192]. For *Lm* parasites, this is further supported by findings from mice showing that long term infections are rather dependent on low proliferation rates of parasites than on parasite burdens [133].

7.4.2 Regulation of the parasite proliferation on the cellular level

How the susceptibility or control of parasite proliferation is mediated on the cellular level is an open question for *L.* infections. A determinant for amastigote growth is the nutrient and metabolite availability in the phagolysosome of the hosting cell [193]. The upregulation of the kynurenine pathway under stimulation of IFNγ is well described in the literature and was also measured for M(IFNγ) in the present work (Figure 40) [194]. This pathway supplies the cell with *de novo* synthesized NAD^+, a metabolite needed by *L.* parasites to proliferate and that can only be salvaged from the hosting cell which could therefore explain an upregulation of parasite replication due to the upregulation of the kynurenine pathway [58,61]. Indeed, an inhibition of the pathway by 1-MT resulted in a lower parasite burden relative to an untreated

control indicating a dampening of the parasites' replication by a limited NAD^+ *de novo* synthesis (Figure 42 A). At the same time, *NOS2* expression was not detected by qPCR in M(IFNγ) under the *in vitro* culture conditions (data not shown), whereby NO is not generated to control the proliferation [129]. Yet, the role of NO in human cell infections is still under vivid discussion [164]. The biopsy material from CL patients infected by *L. braziliensis* showed no increase in NO by NOS2 expression compared to a non-diseased patient material [45]. An increased proliferation of parasites and the absence of NO in inflammatory stimulated macrophages might reflect *in vivo* infection progressions in human patients. Also, and as described previously, inflammatory $Ly6C^+CCR2^+$ monocytes constitute a replicative niche for infecting parasites, despite a functional iNOS effector mechanism [23,27].

In regards to the infections by axenic amastigotes, the uptake of *L. amazonensis* amastigotes was recently shown to activate the Mitogen-activated protein/Extracellular signal regulated kinases (MAPK/ERK) pathway, which is associated with parasite survival and the reduction of ROS activation, potentially also protecting the replication of *Lm* amastigotes post infection [195,196]. The kynurenine pathway is downregulated by IL-4, but the arginase catabolism pathway by Arg1 is activated, supplying the intracellular parasite with polyamines that have been shown to be important for the support of amastigote proliferation, which can explain the only marginal reduction of proliferation in M(IL-4) compared to M(IFNγ) (Figure 34) [60,187,197]. The broad suppression of pathogen replication in M(M-CSF) and M(IL-10) partly contradicts the current literature and requires further analysis, as both regulatory stimuli are associated with the support of amastigote growth by a downregulation in effector mechanisms and the upregulation of Arg1 [125,167,197]. Yet, it is somewhat conform with reports showing that low proliferation rates are associated with *Lm* residency in anti-inflammatory macrophage phenotypes that convey parasite persistence in *in vivo* infections [23,53,133].

7.4.3 Activation of regulated cell death

Low to medium cell death rates were observed for all phenotypes of uninfected hMDM, which result from their *in vitro* cultivation as primary cells (Figure 36, Figure 37). The occurrence of a certain regulated cell death of infected cells is therefore seen as a relative increase compared to the basal occurrence in uninfected cells. In line with previous results and literature correlating increased proliferation and exit with an induction of apoptosis, the share of early apoptotic cells displaying caspase-3 activity was increased for infected M(IFNγ) compared to uninfected samples (Figure 36 A) [23,133]. The share of PtdSer-positive cells was not increased in infected cells, yet the permanent presence of phagocytic cells expressing PtdSer receptors like MerTK in the examined *in vitro* culture probably accounts for an efficient uptake of cells displaying "eat me" signals [86]. Therefore, and despite a low abundance of PtdSer-positive cells, the chance of their clearance hinders a detection of differences, which overall troubles the detection of apoptotic cell death in phagocyte cell cultures. The caspase-1 activity

was not significantly upregulated for M(IFNγ), yet infections of certain donors displayed increased caspase-1 activity and also the release of cellular contents typical for lytic cell death (Figure 37 A, Figure 38). As demonstrated, also pyroptosis is a pathway to facilitate parasite transmission, while the results for M(IFNγ) on pyroptosis induction are not significant, a contribution cannot be excluded. According to the low parasite transmission in M(IL-4), neither hallmarks for apoptosis nor pyroptosis were upregulated during infection compared to uninfected cells (Figure 36 B, Figure 37 B). Interestingly, hMDM stimulated with M-CSF showed an increase for both, caspase-1 and capase-3 activity for infected cells, despite the diminished rates of transmission measured in the previous experiment (Figure 36 B, Figure 37 B). The upregulation of caspase-1 did not confer to an increase of lytic cell death, though the transfer of parasites from BLaER1 cells after pyroptosis induction related on the cell lysis, explaining why no effect on the exit rates was seen for M(M-CSF) (Figure 45, Figure 35). Interestingly, the sustained stimulation with M-CSF may have a direct impact on the activation of caspase-3. The interaction of M-CSF and the M-CSF receptor during the differentiation of blood monocytes results in the transient activation of caspase-8 and caspase-3 without causing cell death [198]. This transient activation relies on an oscillating PI3K/Akt and ERK/MAPK signaling in the cells, pathways which are both engaged by infecting *L.* parasites, in the case of PI3K/Akt especially shown for amastigotes infections [195,196,199,200]. The combination of infection by *Lm* amastigotes and M-CSF stimulation might therefore account for a transient activation of caspases without inducing an exit of parasites by apoptosis.

7.4.4 Donor variations and the role of the kynurenine pathway in exit

An apparent feature of M(IFNγ) in experiments measuring exit and the occurrence of regulated cell death was a high variation between individual donors (Figure 35, Figure 36 A, Figure 37 A). Replicates measured in parallel from two independent donors presented opposing results, despite being infected by axenic amastigotes from the same culture and uniform experimental treatment. It was shown that the capacity of macrophages for an inflammatory activation is dependent on the individual person and differences between individuals underly natural variations [140]. As carved out, the proliferation and transmission of parasites is associated with pro-inflammatory stimulation. Therefore, several inflammatory markers were tested and correlated with exit from hMDM from the same donor (Figure 39). A relation of exit was only observed for the gene expression of *IDO1* and *KYNU* that encode the enzymes catalyzing the initial steps of the kynurenine pathway, whose activity is strongly upregulated by a stimulation with IFNγ (Figure 40) [194]. In the group of donors presenting high exit, *IDO1* but especially *KYNU* expression was reduced compared to the group showing low exit rates (Figure 41). In perfect accordance, the inhibition of IDO1 enzymatic activity resulted in elevated exit rates, although it also dampened the amastigote growth (Figure 42). The reduced growth might be a result of a hindered *de novo* synthesis of NAD^+ by the kynurenine pathway inhibition, a metabolite that is essential for the parasite proliferation and that needs to be salvaged from

the hosting cell by *L.* [61]. The slower gain of a parasite burden and the concomitant increase of exit contrasts previous results from this work proving a relation between parasite replication and transmission. Though, the inhibition of the kynurenine pathway and a strong parasite proliferation may have a common denominator causing cell death, the depletion of NAD^+ for the cell which is required to cover the energy consumption during inflammatory activation [57,58,61]. Another explanatory approach is derived from the finding that attenuated parasites were shown to inhibit the tryptophan catabolism by blocking IDO1, which allows a speculation of a proliferation-independent exit mechanism engaged via the kynurenine pathway [136]. The depletion of NAD^+ can trigger regulated cell death via necroptosis, which was shown to be engaged by *M. tuberculosis* in host cells [201]. The regulation of parasite growth by the kynurenine pathway is mostly associated with a T cell suppression during *L.* infection by an upregulation of IDO in the current literature [65,66]. The inhibition of IDO1 in M(IFNγ) in the present work reveals an undescribed cellular function of this pathway as suppressor for *Lm* expansion and is a previously unknown factor for parasite transmission.

7.5 Conclusion and outlook

The presented results confirm the initially formulated hypothesis and demonstrate a strong connection of the parasite metabolism in terms of proliferation, the activation of regulated cell death and parasite exit from infected host cells. Moreover, the phenotype of hMDM tailored both, the intracellular proliferation, likely due to the availability of metabolites and nutrients rather than by the activation of effector mechanisms, and the exit of parasites. This work thereby contributes to the understanding of *Lm* parasite exit and cell-to-cell transmission as part of its life cycle. The evidence for a conserved inflammasome activation during infection by multiple *L. spp.* infections observed in multiple studies and the present findings that the canonical inflammasome activation, as well as the sole priming by LPS induces parasite transmission, suggests that at least two forms of regulated cell death might co-exist as exit strategies for intracellular *Lm* amastigotes. In this work, exit from hMDMs occurred dominantly but was not restricted to pro-inflammatory host cells stimulated with IFNγ, providing a mechanistic link between the increased recruitment of inflammatory monocytes and their high infection rates during the systematic release of IFNγ by the Th1 adaptive immune response as previously described in mice. Vice versa, the restriction of exit by IL-4 might convey to the control of the infection progression during Th2 immune responses observed in the first three weeks of mouse infections. By utilizing natural human variations in the inflammatory capacity of individual donors for hMDM, it was possible to unravel that the downregulation of the kynurenine pathway is a modulator of intracellular parasite proliferation and cell-to-cell transmission from M(IFNγ) on the cellular level. This here newly described participation of the kynurenine pathway in the *Lm* infection progression and exit is a promising target for further research. Parasite exit might be associated with the *de novo* synthesis of NAD^+ that required

by the host cell and the infecting parasite and has the potential to mechanistically link parasite proliferation with host cell death.

Derived from the discussed results and the current literature, proliferation appears to be a process highly dependent on the interplay of the infecting parasites and the host cell, both in human and mouse models. The dynamic balance between high proliferating populations in inflammatory hMDM and lowered replication under regulatory stimuli allows the parasite to progress the infection in the parasitized tissue on one hand, and on the other ensures the formation of persistent parasite reservoirs. The connection of an exit mechanism with uncontrolled parasite replication shown in this work emphasizes for its relevance in the infection progression. It highlights the importance of the proliferation and exit for the pathogenicity and infection progression by *Lm*, which, to comprise a more comprehensive understanding, requires furthers research but yields the potential to be engaged by medication and to control the course of infection in patients.

On the basis of this work, future experiments should focus on the generation of replication-deficient variant of *Lm* parasites by the knockout of *centrin* to further dissect the role of proliferation for parasite exit [131,134]. Not only would this provide a specific control condition, the ablation of *centrin* and the resulting attenuation of parasites has been shown to inhibit IDO1, a pathway that was connected with exit in this work [136]. Besides the analysis of immediate parasite proliferation by employing $Lm^{mKikume}$ under 1-MT inhibition to confirm its reduction. Furthermore, the NAD^+ level during infections by vital and attenuated *Lm* should be tested to learn about the NAD^+ availability in cells, in dependence on the ability of parasites to proliferate [202]. Also, the potential role of necrosis should be experimentally analyzed with the detection of receptor-interacting serine/threonine-protein kinase 3 (RIP3K) and mixed lineage kinase domain like pseudo kinase (MLKL) protein in *Lm* infected cells under IDO1 inhibition by Western blot analysis [201,203]. Further, the BLaER1 model and its potential for genome editing should be utilized to examine the inflammasome activation and pyroptosis induction during *Lm* axenic amastigote infection and LPS stimulation [154,179]. Initial experiments to visualize the inflammasome assembly on the basis of speck formation by microscopy were negative for specks (data not shown). Probably, the use of Z-VAD to arrest the formed inflammasome and stop pyroptosis by an inhibition of caspase-1 troubled the detection in this scenario as Z-VAD also inhibits caspase-4 activity that might be essential for the non-canonical inflammasome activation pathway during *Lm* infection [41]. Consequently, a $BLaER1^{Caspase\text{-}1\text{-}/\text{-}}$ strain should be used to test more specifically for speck formation. The control strains $BLaER1^{Caspase\text{-}1\text{-}/\text{-}\ x\ Caspase\text{-}4\text{-}/\text{-}}$ and $BLaER1^{Caspase\text{-}1\text{-}/\text{-}\ x\ Caspase\text{-}8\text{-}/\text{-}}$ shall be included in the speck detection experiments, as well as in co-incubation assays to unravel the role of the non-canonical and the alternative inflammasome activation in *Lm* exit [115,116].

8 References

[1] M. Maroli, M.D. Feliciangeli, L. Bichaud, R.N. Charrel, L. Gradoni, Phlebotomine sandflies and the spreading of leishmaniases and other diseases of public health concern, Medical and veterinary entomology 27 (2013) 123–147.

[2] P. Scott, F.O. Novais, Cutaneous leishmaniasis: immune responses in protection and pathogenesis, Nat Rev Immunol 16 (2016) 581–592. https://www.nature.com/articles/nri.2016.72.

[3] Leishmaniasis, 2024.000Z. https://www.who.int/news-room/fact-sheets/detail/leishmaniasis. Accessed 22 April 2024.803Z.

[4] S. Scarpini, A. Dondi, C. Totaro, C. Biagi, F. Melchionda, D. Zama, L. Pierantoni, M. Gennari, C. Campagna, A. Prete, M. Lanari, Visceral Leishmaniasis: Epidemiology, Diagnosis, and Treatment Regimens in Different Geographical Areas with a Focus on Pediatrics, Microorganisms 10 (2022).

[5] Leishmaniasis, 2024.000Z. https://www.cdc.gov/parasites/leishmaniasis/. Accessed 22 April 2024.284Z.

[6] R.K. Madusanka, H. Silva, N.D. Karunaweera, Treatment of Cutaneous Leishmaniasis and Insights into Species-Specific Responses: A Narrative Review, Infectious diseases and therapy 11 (2022) 695–711.

[7] I. Abadías-Granado, A. Diago, P.A. Cerro, A.M. Palma-Ruiz, Y. Gilaberte, Cutaneous and Mucocutaneous Leishmaniasis, Actas Dermo-Sifiliográficas (English Edition) 112 (2021) 601–618. https://www.sciencedirect.com/science/article/pii/S1578219021001712.

[8] J. Alvar, S. Yactayo, C. Bern, Leishmaniasis and poverty, Trends in parasitology 22 (2006) 552–557.

[9] I. Okwor, J. Uzonna, Social and Economic Burden of Human Leishmaniasis, The American Journal of Tropical Medicine and Hygiene 94 (2016) 489–493.

[10] L.F. Oliveira, A.O. Schubach, M.M. Martins, S.L. Passos, R.V. Oliveira, M.C. Marzochi, C.A. Andrade, Systematic review of the adverse effects of cutaneous leishmaniasis treatment in the New World, Acta tropica 118 (2011) 87–96.

[11] A. Ponte-Sucre, F. Gamarro, J.-C. Dujardin, M.P. Barrett, R. López-Vélez, R. García-Hernández, A.W. Pountain, R. Mwenechanya, B. Papadopoulou, Drug resistance and treatment failure in leishmaniasis: A 21st century challenge, PLoS neglected tropical diseases 11 (2017).

[12] A.E. Shearley, The societal value of vaccination in developing countries, Vaccine 17 Suppl 3 (1999) S109-12.

[13] B. Greenwood, The contribution of vaccination to global health: past, present and future, Philosophical Transactions of the Royal Society B: Biological Sciences 369 (2014).

[14] R. Dinc, Leishmania Vaccines: the Current Situation with Its Promising Aspect for the Future, The Korean journal of parasitology 60 (2022) 379–391.

[15] K.R. Matthews, Controlling and Coordinating Development in Vector-Transmitted Parasites, Science (New York, N.Y.) 331 (2011).

[16] S.M. Gossage, M.E. Rogers, P.A. Bates, Two separate growth phases during the development of Leishmania in sand flies: implications for understanding the life cycle, International journal for parasitology 33 (2003) 1027–1034.

[17] P. Prasanna, A. Upadhyay, Heat Shock Proteins as the Druggable Targets in Leishmaniasis: Promises and Perils, Infection and immunity 89 (2021). https://pubmed.ncbi.nlm.nih.gov/33139381/.

[18] M.E. Rogers, T. Ilg, A.V. Nikolaev, M.A.J. Ferguson, P.A. Bates, Transmission of cutaneous leishmaniasis by sand flies is enhanced by regurgitation of fPPG, Nature 430 (2004) 463–467.

[19] E. Aga, D.M. Katschinski, G. van Zandbergen, H. Laufs, B. Hansen, K. Müller, W. Solbach, T. Laskay, Inhibition of the spontaneous apoptosis of neutrophil granulocytes by the intracellular parasite Leishmania major, Journal of immunology (Baltimore, Md. : 1950) 169 (2002) 898–905.

[20] G. van Zandbergen, M. Klinger, A. Mueller, S. Dannenberg, A. Gebert, W. Solbach, T. Laskay, Cutting edge: neutrophil granulocyte serves as a vector for Leishmania entry into macrophages, Journal of immunology (Baltimore, Md. : 1950) 173 (2004) 6521–6525.

[21] E. Handman, D.V.R. Bullen, Interaction of Leishmania with the host macrophage, Trends in parasitology 18 (2002) 332–334.

[22] P.E. Kima, The amastigote forms of Leishmania are experts at exploiting host cell processes to establish infection and persist, International journal for parasitology 37 (2007) 1087–1096.

[23] S. Heyde, L. Philipsen, P. Formaglio, Y. Fu, I. Baars, G. Höbbel, C.L. Kleinholz, E.A. Seiß, J. Stettin, P. Gintschel, A. Dudeck, P. Bousso, B. Schraven, A.J. Müller, CD11c-expressing Ly6C+CCR2+ monocytes constitute a reservoir for efficient Leishmania proliferation and cell-to-cell transmission, PLoS pathogens 14 (2018) e1007374.

[24] T.V. Piscopo, C. Mallia Azzopardi, Leishmaniasis, Postgraduate medical journal 83 (2007) 649–657.

[25] P. Kaye, P. Scott, Leishmaniasis: complexity at the host-pathogen interface, Nature reviews. Microbiology 9 (2011) 604–615.

[26] M. Rossi, N. Fasel, How to master the host immune system? Leishmania parasites have the solutions!, International immunology 30 (2018) 103–111.

[27] M.B. Carneiro, M.E. Lopes, L.S. Hohman, A. Romano, B.A. David, R. Kratofil, P. Kubes, M.L. Workentine, A.C. Campos, L.Q. Vieira, N.C. Peters, Th1-Th2 Cross-Regulation Controls Early Leishmania Infection in the Skin by Modulating the Size of the Permissive Monocytic Host Cell Reservoir, Cell host & microbe 27 (2020) 752-768.e7.

[28] D. Hirayama, T. Iida, H. Nakase, The Phagocytic Function of Macrophage-Enforcing Innate Immunity and Tissue Homeostasis, International journal of molecular sciences 19 (2018) 92. https://www.mdpi.com/1422-0067/19/1/92.

[29] S. Akira, S. Uematsu, O. Takeuchi, Pathogen recognition and innate immunity, Cell 124 (2006) 783–801.

[30] D. Li, M. Wu, Pattern recognition receptors in health and diseases, Signal transduction and targeted therapy 6 (2021) 291.

[31] J. Pugin, I.D. Heumann, A. Tomasz, V.V. Kravchenko, Y. Akamatsu, M. Nishijima, M.P. Glauser, P.S. Tobias, R.J. Ulevitch, CD14 is a pattern recognition receptor, Immunity 1 (1994) 509–516.

[32] R.A. Paveley, S.A. Aynsley, J.D. Turner, C.D. Bourke, S.J. Jenkins, P.C. Cook, L. Martinez-Pomares, A.P. Mountford, The Mannose Receptor (CD206) is an important pattern recognition receptor (PRR) in the detection of the infective stage of the helminth Schistosoma mansoni and modulates IFNγ production, International journal for parasitology 41 (2011) 1335–1345.

[33] K.E. Iles, H.J. Forman, Macrophage signaling and respiratory burst, Immunologic research 26 (2002) 95–105.

[34] D.M. Mosser, J.P. Edwards, Exploring the full spectrum of macrophage activation, Nat Rev Immunol 8 (2008) 958–969. https://www.nature.com/articles/nri2448.

[35] S. Gordon, Alternative activation of macrophages, Nature reviews. Immunology 3 (2003) 23–35.

[36] E. Mass, F. Nimmerjahn, K. Kierdorf, A. Schlitzer, Tissue-specific macrophages: how they develop and choreograph tissue biology, Nature reviews. Immunology 23 (2023) 563–579.

[37] C.D. Mills, Anatomy of a Discovery: M1 and M2 Macrophages, Frontiers in immunology 6 (2015).

[38] M. Orecchioni, Y. Ghosheh, A.B. Pramod, K. Ley, Macrophage Polarization: Different Gene Signatures in M1(LPS+) vs. Classically and M2(LPS-) vs. Alternatively Activated Macrophages, Frontiers in immunology 10 (2019) 1084.

[39] Y. Yao, X.-H. Xu, L. Jin, Macrophage Polarization in Physiological and Pathological Pregnancy, Frontiers in immunology 10 (2019).

[40] A.N. Orekhov, V.A. Orekhova, N.G. Nikiforov, V.A. Myasoedova, A.V. Grechko, E.B. Romanenko, D. Zhang, D.A. Chistiakov, Monocyte differentiation and macrophage polarization, VP 2019 (2019).

[41] P.J. Murray, J.E. Allen, S.K. Biswas, E.A. Fisher, D.W. Gilroy, S. Goerdt, S. Gordon, J.A. Hamilton, L.B. Ivashkiv, T. Lawrence, M. Locati, A. Mantovani, F.O. Martinez, J.-L. Mege, D.M. Mosser, G. Natoli, J.P. Saeij, J.L. Schultze, K.A. Shirey, A. Sica, J. Suttles, I.

Udalova, J.A. van Ginderachter, S.N. Vogel, T.A. Wynn, Macrophage activation and polarization: nomenclature and experimental guidelines, Immunity 41 (2014) 14–20.

[42] N.C. Peters, J.G. Egen, N. Secundino, A. Debrabant, N. Kimblin, S. Kamhawi, P. Lawyer, M.P. Fay, R.N. Germain, D. Sacks, In vivo imaging reveals an essential role for neutrophils in leishmaniasis transmitted by sand flies, Science (New York, N.Y.) 321 (2008) 970–974.

[43] M.M. Chaves, S.H. Lee, O. Kamenyeva, K. Ghosh, N.C. Peters, D. Sacks, The role of dermis resident macrophages and their interaction with neutrophils in the early establishment of Leishmania major infection transmitted by sand fly bite, PLoS pathogens 16 (2020) e1008674.

[44] S.J. Green, M.S. Meltzer, J.B. Hibbs, C.A. Nacy, Activated macrophages destroy intracellular Leishmania major amastigotes by an L-arginine-dependent killing mechanism, J Immunol 144 (1990) 278–283.

[45] F.O. Novais, B.T. Nguyen, D.P. Beiting, L.P. Carvalho, N.D. Glennie, S. Passos, E.M. Carvalho, P. Scott, Human classical monocytes control the intracellular stage of Leishmania braziliensis by reactive oxygen species, The Journal of infectious diseases 209 (2014) 1288–1296.

[46] P.P. Carneiro, J. Conceição, M. Macedo, V. Magalhães, E.M. Carvalho, O. Bacellar, The Role of Nitric Oxide and Reactive Oxygen Species in the Killing of Leishmania braziliensis by Monocytes from Patients with Cutaneous Leishmaniasis, PloS one 11 (2016).

[47] G. Gupta, S. Oghumu, A.R. Satoskar, Mechanisms of immune evasion in leishmaniasis, Advances in applied microbiology 82 (2013) 155–184.

[48] C. Matte, G. Maion, W. Mourad, M. Olivier, Leishmania donovani-induced macrophages cyclooxygenase-2 and prostaglandin E2 synthesis, Parasite immunology 23 (2001) 177–184.

[49] M. Olivier, D.J. Gregory, G. Forget, Subversion Mechanisms by Which Leishmania Parasites Can Escape the Host Immune Response: a Signaling Point of View, Clinical Microbiology Reviews 18 (2005) 293–305.

[50] F.Y. Liew, Y. Li, S. Millott, Tumor necrosis factor-alpha synergizes with IFN-gamma in mediating killing of Leishmania major through the induction of nitric oxide, J Immunol 145 (1990) 4306–4310.

[51] F. Mattner, J. Magram, J. Ferrante, P. Launois, K. Di Padova, R. Behin, M.K. Gately, J.A. Louis, G. Alber, Genetically resistant mice lacking interleukin-12 are susceptible to infection with Leishmania major and mount a polarized Th2 cell response, Eur. J. Immunol. 26 (1996) 1553–1559.

[52] R. Chatelain, K. Varkila, R.L. Coffman, IL-4 induces a Th2 response in Leishmania major-infected mice, J Immunol 148 (1992) 1182–1187.

[53] S.H. Lee, M. Charmoy, A. Romano, A. Paun, M.M. Chaves, F.O. Cope, D.A. Ralph, D.L. Sacks, Mannose receptor high, M2 dermal macrophages mediate nonhealing Leishmania major infection in a Th1 immune environment, The Journal of experimental medicine 215 (2018) 357–375.

[54] A. Romano, M.B.H. Carneiro, N.A. Doria, E.H. Roma, F.L. Ribeiro-Gomes, E. Inbar, S.H. Lee, J. Mendez, A. Paun, D.L. Sacks, N.C. Peters, Divergent roles for Ly6C+CCR2+CX3CR1+ inflammatory monocytes during primary or secondary infection of the skin with the intra-phagosomal pathogen Leishmania major, PLoS pathogens 13 (2017) e1006479.

[55] Cesar Terrazas, Sanjay Varikuti, Steve Oghumu, Heidi M. Steinkamp, Nurittin Ardic, Jennifer Kimble, Hira Nakhasi, Abhay R. Satoskar, Ly6Chi inflammatory monocytes promote susceptibility to Leishmania donovani infection, Scientific reports 7 (2017). https://www.ncbi.nlm.nih.gov/pmc/articles/PMC5665970/.

[56] P. Formaglio, M. Alabdullah, A. Siokis, J. Handschuh, I. Sauerland, Y. Fu, A. Krone, P. Gintschel, J. Stettin, S. Heyde, J. Mohr, L. Philipsen, A. Schröder, P.A. Robert, G. Zhao, S. Khailaie, A. Dudeck, J. Bertrand, G.F. Späth, S. Kahlfuß, P. Bousso, B. Schraven, J. Huehn, S. Binder, M. Meyer-Hermann, A.J. Müller, Nitric oxide controls proliferation of Leishmania major by inhibiting the recruitment of permissive host cells, Immunity 54 (2021) 2724-2739.e10.

[57] B. Groth, P. Venkatakrishnan, S.-J. Lin, NAD+ Metabolism, Metabolic Stress, and Infection, Frontiers in molecular biosciences 8 (2021) 686412.

[58] A.M. Cameron, A. Castoldi, D.E. Sanin, L.J. Flachsmann, C.S. Field, D.J. Puleston, R.L. Kyle, A.E. Patterson, F. Hässler, J.M. Buescher, B. Kelly, E.L. Pearce, E.J. Pearce, Inflammatory macrophage dependence on NAD+ salvage is a consequence of reactive oxygen species-mediated DNA damage, Nature immunology 20 (2019) 420–432.

[59] C.R. MacKenzie, R.G. González, E. Kniep, S. Roch, W. Däubener, Cytokine mediated regulation of interferon-gamma-induced IDO activation, Advances in experimental medicine and biology 467 (1999) 533–539.

[60] A.C.L. Chaves, I.P. Cerávolo, J.A.S. Gomes, C.L. Zani, A.J. Romanha, R.T. Gazzinelli, IL-4 and IL-13 regulate the induction of indoleamine 2,3-dioxygenase activity and the control ofToxoplasma gondii replication in human fibroblasts activated with IFN-γ, Eur. J. Immunol. 31 (2001) 333–344.

[61] E. Gazanion, D. Garcia, R. Silvestre, C. Gérard, J.F. Guichou, G. Labesse, M. Seveno, A. Cordeiro-Da-Silva, A. Ouaissi, D. Sereno, B. Vergnes, The Leishmania nicotinamidase is essential for NAD+ production and parasite proliferation, Molecular Microbiology 82 (2011) 21–38.

[62] S. Divanovic, N.M. Sawtell, A. Trompette, J.I. Warning, A. Dias, A.M. Cooper, G.S. Yap, M. Arditi, K. Shimada, J.B. DuHadaway, G.C. Prendergast, R.J. Basaraba, A.L. Mellor,

D.H. Munn, J. Aliberti, C.L. Karp, Opposing biological functions of tryptophan catabolizing enzymes during intracellular infection, The Journal of infectious diseases 205 (2012) 152–161.

[63] V. Rodrigues, S. André, H. Maksouri, T. Mouttaki, S. Chiheb, M. Riyad, K. Akarid, J. Estaquier, Transcriptional Analysis of Human Skin Lesions Identifies Tryptophan-2,3-Deoxygenase as a Restriction Factor for Cutaneous Leishmania, Frontiers in cellular and infection microbiology 9 (2019) 338.

[64] D.H. Munn, M.D. Sharma, D. Hou, B. Baban, J.R. Lee, S.J. Antonia, J.L. Messina, P. Chandler, P.A. Koni, A.L. Mellor, Expression of indoleamine 2,3-dioxygenase by plasmacytoid dendritic cells in tumor-draining lymph nodes, The Journal of clinical investigation 114 (2004) 280–290.

[65] L.H.C. Makala, B. Baban, H. Lemos, A.R. El-Awady, P.R. Chandler, D.-Y. Hou, D.H. Munn, A.L. Mellor, Leishmania major attenuates host immunity by stimulating local indoleamine 2,3-dioxygenase expression, The Journal of infectious diseases 203 (2011) 715–725.

[66] L.H.C. Makala, The role of indoleamine 2, 3 dioxygenase in regulating host immunity to leishmania infection, Journal of Biomedical Science 19 (2012) 5.

[67] M.J. Donovan, V. Tripathi, M.A. Favila, N.S. Geraci, M.C. Lange, W. Ballhorn, M.A. McDowell, Indoleamine 2,3-dioxygenase (IDO) induced by Leishmania infection of human dendritic cells, Parasite immunology 34 (2012) 464–472.

[68] A. Traven, T. Naderer, Microbial egress: a hitchhiker's guide to freedom, PLoS pathogens 10 (2014) e1004201.

[69] N. Friedrich, M. Hagedorn, D. Soldati-Favre, T. Soldati, Prison Break: Pathogens' Strategies To Egress from Host Cells, Microbiol Mol Biol Rev 76 (2012) 707–720.

[70] A. Flieger, F. Frischknecht, G. Häcker, M.W. Hornef, G. Pradel, Pathways of host cell exit by intracellular pathogens, Microbial cell (Graz, Austria) 5 (2018) 525–544.

[71] D.S. Ridley, A histological classification of cutaneous leishmaniasis and its geographical expression, Transactions of the Royal Society of Tropical Medicine and Hygiene 74 (1980) 515–521.

[72] E. Handman, D.T. Spira, Growth of Leishmania amastigotes in macrophages from normal and immune mice, Zeitschrift fur Parasitenkunde (Berlin, Germany) 53 (1977) 75–81.

[73] M.G. Rittig, K. Schröppel, K.H. Seack, U. Sander, E.N. N'Diaye, I. Maridonneau-Parini, W. Solbach, C. Bogdan, Coiling phagocytosis of trypanosomatids and fungal cells, Infection and immunity 66 (1998) 4331–4339.

[74] M.G. Rittig, C. Bogdan, Leishmania-host-cell interaction: complexities and alternative views, Parasitology today (Personal ed.) 16 (2000) 292–297.

[75] Y. Belkaid, S. Mendez, R. Lira, N. Kadambi, G. Milon, D. Sacks, A natural model of Leishmania major infection reveals a prolonged "silent" phase of parasite amplification in the skin before the onset of lesion formation and immunity, Journal of immunology (Baltimore, Md. : 1950) 165 (2000) 969–977.

[76] F.S. Noronha, F.J. Ramalho-Pinto, M.F. Horta, Cytolytic activity in the genus Leishmania: involvement of a putative pore-forming protein, Infection and immunity 64 (1996) 3975–3982.

[77] F.S. Noronha, J.S. Cruz, P.S. Beirão, M.F. Horta, Macrophage damage by Leishmania amazonensis cytolysin: evidence of pore formation on cell membrane, Infection and immunity 68 (2000) 4578–4584.

[78] A.M. deCathelineau, P.M. Henson, The final step in programmed cell death: phagocytes carry apoptotic cells to the grave, Essays in biochemistry 39 (2003) 105–117.

[79] Q. Lu, G. Lemke, Homeostatic regulation of the immune system by receptor tyrosine kinases of the Tyro 3 family, Science (New York, N.Y.) 293 (2001) 306–311.

[80] M. Enari, H. Sakahira, H. Yokoyama, K. Okawa, A. Iwamatsu, S. Nagata, A caspase-activated DNase that degrades DNA during apoptosis, and its inhibitor ICAD, Nature 391 (1998) 43–50.

[81] S. Krahling, M.K. Callahan, P. Williamson, R.A. Schlegel, Exposure of phosphatidylserine is a general feature in the phagocytosis of apoptotic lymphocytes by macrophages, Cell death and differentiation 6 (1999) 183–189.

[82] R. Singh, A. Letai, K. Sarosiek, Regulation of apoptosis in health and disease: the balancing act of BCL-2 family proteins, Nature reviews. Molecular cell biology 20 (2019) 175–193.

[83] C.-C. Wu, S.B. Bratton, Regulation of the intrinsic apoptosis pathway by reactive oxygen species, Antioxidants & redox signaling 19 (2013) 546–558.

[84] K. Segawa, S. Kurata, Y. Yanagihashi, T.R. Brummelkamp, F. Matsuda, S. Nagata, Caspase-mediated cleavage of phospholipid flippase for apoptotic phosphatidylserine exposure, Science (New York, N.Y.) 344 (2014) 1164–1168.

[85] J. Suzuki, E. Imanishi, S. Nagata, Exposure of phosphatidylserine by Xk-related protein family members during apoptosis, The Journal of biological chemistry (2014) 30257–30267.

[86] S. Nagata, Apoptosis and Clearance of Apoptotic Cells, Annual review of immunology 36 (2018) 489–517.

[87] K. Asano, M. Miwa, K. Miwa, R. Hanayama, H. Nagase, S. Nagata, M. Tanaka, Masking of phosphatidylserine inhibits apoptotic cell engulfment and induces autoantibody production in mice, The Journal of experimental medicine 200 (2004) 459–467.

[88] R. Hanayama, M. Tanaka, K. Miwa, A. Shinohara, A. Iwamatsu, S. Nagata, Identification of a factor that links apoptotic cells to phagocytes, Nature 417 (2002) 182–187.

[89] T. Nakano, Y. Ishimoto, J. Kishino, M. Umeda, K. Inoue, K. Nagata, K. Ohashi, K. Mizuno, H. Arita, Cell adhesion to phosphatidylserine mediated by a product of growth arrest-specific gene 6, The Journal of biological chemistry 272 (1997) 29411–29414.

[90] H.A. Anderson, C.A. Maylock, J.A. Williams, C.P. Paweletz, H. Shu, E. Shacter, Serum-derived protein S binds to phosphatidylserine and stimulates the phagocytosis of apoptotic cells, Nature immunology 4 (2003) 87–91.

[91] Q. Lu, M. Gore, Q. Zhang, T. Camenisch, S. Boast, F. Casagranda, C. Lai, M.K. Skinner, R. Klein, G.K. Matsushima, H.S. Earp, S.P. Goff, G. Lemke, Tyro-3 family receptors are essential regulators of mammalian spermatogenesis, Nature 398 (1999) 723–728.

[92] R.S. Scott, E.J. McMahon, S.M. Pop, E.A. Reap, R. Caricchio, P.L. Cohen, H.S. Earp, G.K. Matsushima, Phagocytosis and clearance of apoptotic cells is mediated by MER, Nature 411 (2001) 207–211.

[93] T.D. Camenisch, B.H. Koller, H.S. Earp, G.K. Matsushima, A novel receptor tyrosine kinase, Mer, inhibits TNF-alpha production and lipopolysaccharide-induced endotoxic shock, Journal of immunology (Baltimore, Md. : 1950) 162 (1999) 3498–3503.

[94] P. Sen, M.A. Wallet, Z. Yi, Y. Huang, M. Henderson, C.E. Mathews, H.S. Earp, G. Matsushima, A.S. Baldwin, R.M. Tisch, Apoptotic cells induce Mer tyrosine kinase-dependent blockade of NF-kappaB activation in dendritic cells, Blood (2007) 653–660.

[95] C.V. Rothlin, S. Ghosh, E.I. Zuniga, M.B.A. Oldstone, G. Lemke, TAM receptors are pleiotropic inhibitors of the innate immune response, Cell 131 (2007) 1124–1136.

[96] J.P. DaMata, B.P. Mendes, K. Maciel-Lima, C.A.S. Menezes, W.O. Dutra, L.P. Sousa, M.F. Horta, Distinct Macrophage Fates after in vitro Infection with Different Species of Leishmania: Induction of Apoptosis by Leishmania (Leishmania) amazonensis, but Not by Leishmania (Viannia) guyanensis, PloS one 10 (2015) e0141196.

[97] A. Ruhland, N. Leal, P.E. Kima, Leishmania promastigotes activate PI3K/Akt signalling to confer host cell resistance to apoptosis, Cellular microbiology 9 (2007) 84–96.

[98] P. Gupta, S. Srivastav, S. Saha, P.K. Das, A. Ukil, Leishmania donovani inhibits macrophage apoptosis and pro-inflammatory response through AKT-mediated regulation of β-catenin and FOXO-1, Cell death and differentiation 23 (2016) 1815–1826.

[99] R.K. Pandey, S. Mehrotra, S. Sharma, R.S. Gudde, S. Sundar, C. Shaha, Leishmania donovani-Induced Increase in Macrophage Bcl-2 Favors Parasite Survival, Frontiers in immunology 7 (2016) 456.

[100] J. Giri, S. Srivastav, M. Basu, S. Palit, P. Gupta, A. Ukil, Leishmania donovani Exploits Myeloid Cell Leukemia 1 (MCL-1) Protein to Prevent Mitochondria-dependent Host Cell Apoptosis, The Journal of biological chemistry 291 (2016) 3496–3507.

[101] F. Real, P.T.V. Florentino, L.C. Reis, E.M. Ramos-Sanchez, P.S.T. Veras, H. Goto, R.A. Mortara, Cell-to-cell transfer of Leishmania amazonensis amastigotes is mediated

by immunomodulatory LAMP-rich parasitophorous extrusions, Cellular microbiology 16 (2014) 1549–1564.

[102] P. Yu, X. Zhang, N. Liu, L. Tang, C. Peng, X. Chen, Pyroptosis: mechanisms and diseases, Signal transduction and targeted therapy 6 (2021) 128.

[103] C.A. Dinarello, A clinical perspective of IL-1β as the gatekeeper of inflammation, European journal of immunology 41 (2011) 1203–1217.

[104] T. Strowig, J. Henao-Mejia, E. Elinav, R. Flavell, Inflammasomes in health and disease, Nature 481 (2012) 278–286.

[105] Y. Huang, W. Xu, R. Zhou, NLRP3 inflammasome activation and cell death, Cell Mol Immunol 18 (2021) 2114–2127.

[106] F.G. Bauernfeind, G. Horvath, A. Stutz, E.S. Alnemri, K. MacDonald, D. Speert, T. Fernandes-Alnemri, J. Wu, B.G. Monks, K.A. Fitzgerald, V. Hornung, E. Latz, Cutting edge: NF-kappaB activating pattern recognition and cytokine receptors license NLRP3 inflammasome activation by regulating NLRP3 expression, Journal of immunology (Baltimore, Md. : 1950) 183 (2009) 787–791.

[107] B.F. Py, M.-S. Kim, H. Vakifahmetoglu-Norberg, J. Yuan, Deubiquitination of NLRP3 by BRCC3 critically regulates inflammasome activity, Molecular Cell 49 (2013) 331–338.

[108] R. Muñoz-Planillo, P. Kuffa, G. Martínez-Colón, B.L. Smith, T.M. Rajendiran, G. Núñez, K^+ efflux is the common trigger of NLRP3 inflammasome activation by bacterial toxins and particulate matter, Immunity 38 (2013) 1142–1153.

[109] S. Kesavardhana, R.K.S. Malireddi, T.-D. Kanneganti, Caspases in Cell Death, Inflammation, and Pyroptosis, Annual review of immunology 38 (2020) 567–595. https://www.ncbi.nlm.nih.gov/pmc/articles/PMC7190443/.

[110] N. Kayagaki, O.S. Kornfeld, B.L. Lee, I.B. Stowe, K. O'Rourke, Q. Li, W. Sandoval, D. Yan, J. Kang, M. Xu, J. Zhang, W.P. Lee, B.S. McKenzie, G. Ulas, J. Payandeh, M. Roose-Girma, Z. Modrusan, R. Reja, M. Sagolla, J.D. Webster, V. Cho, T.D. Andrews, L.X. Morris, L.A. Miosge, C.C. Goodnow, E.M. Bertram, V.M. Dixit, NINJ1 mediates plasma membrane rupture during lytic cell death, Nature 591 (2021) 131–136. https://www.nature.com/articles/s41586-021-03218-7.

[111] J. Shi, Y. Zhao, K. Wang, X. Shi, Y. Wang, H. Huang, Y. Zhuang, T. Cai, F. Wang, F. Shao, Cleavage of GSDMD by inflammatory caspases determines pyroptotic cell death, Nature 526 (2015) 660–665.

[112] N. Kayagaki, S. Warming, M. Lamkanfi, L. Vande Walle, S. Louie, J. Dong, K. Newton, Y. Qu, J. Liu, S. Heldens, J. Zhang, W.P. Lee, M. Roose-Girma, V.M. Dixit, Non-canonical inflammasome activation targets caspase-11, Nature 479 (2011) 117–121.

[113] P.J. Baker, D. Boucher, D. Bierschenk, C. Tebartz, P.G. Whitney, D.B. D'Silva, M.C. Tanzer, M. Monteleone, A.A.B. Robertson, M.A. Cooper, S. Alvarez-Diaz, M.J. Herold, S. Bedoui, K. Schroder, S.L. Masters, NLRP3 inflammasome activation downstream of

cytoplasmic LPS recognition by both caspase-4 and caspase-5, European journal of immunology 45 (2015) 2918–2926.

[114] N. Kayagaki, I.B. Stowe, B.L. Lee, K. O'Rourke, K. Anderson, S. Warming, T. Cuellar, B. Haley, M. Roose-Girma, Q.T. Phung, P.S. Liu, J.R. Lill, H. Li, J. Wu, S. Kummerfeld, J. Zhang, W.P. Lee, S.J. Snipas, G.S. Salvesen, L.X. Morris, L. Fitzgerald, Y. Zhang, E.M. Bertram, C.C. Goodnow, V.M. Dixit, Caspase-11 cleaves gasdermin D for non-canonical inflammasome signalling, Nature 526 (2015) 666–671.

[115] J.L. Schmid-Burgk, M.M. Gaidt, T. Schmidt, T.S. Ebert, E. Bartok, V. Hornung, Caspase-4 mediates non-canonical activation of the NLRP3 inflammasome in human myeloid cells, European journal of immunology 45 (2015) 2911–2917.

[116] M.M. Gaidt, T.S. Ebert, D. Chauhan, T. Schmidt, J.L. Schmid-Burgk, F. Rapino, A.A.B. Robertson, M.A. Cooper, T. Graf, V. Hornung, Human Monocytes Engage an Alternative Inflammasome Pathway, Immunity 44 (2016) 833–846.

[117] D. Delfino, M.S. Chiofalo, G. Riggio, M.C. Angelici, M. Gramiccia, L. Gradoni, D. Iannello, Induction of interleukin 1 alpha in murine macrophages infected in vitro with different species and strains of Leishmania, Microbial pathogenesis 18 (1995) 73–80.

[118] D.S. Lima-Junior, D.L. Costa, V. Carregaro, L.D. Cunha, A.L.N. Silva, T.W.P. Mineo, F.R.S. Gutierrez, M. Bellio, K.R. Bortoluci, R.A. Flavell, M.T. Bozza, J.S. Silva, D.S. Zamboni, Inflammasome-derived IL-1β production induces nitric oxide-mediated resistance to Leishmania, Nature medicine 19 (2013) 909–915.

[119] M. Charmoy, B.P. Hurrell, A. Romano, S.H. Lee, F. Ribeiro-Gomes, N. Riteau, K. Mayer-Barber, F. Tacchini-Cottier, D.L. Sacks, The Nlrp3 inflammasome, IL-1β, and neutrophil recruitment are required for susceptibility to a nonhealing strain of Leishmania major in C57BL/6 mice, European journal of immunology 46 (2016) 897–911.

[120] E.A. Fernández-Figueroa, C. Rangel-Escareño, V. Espinosa-Mateos, K. Carrillo-Sánchez, N. Salaiza-Suazo, G. Carrada-Figueroa, S. March-Mifsut, I. Becker, Disease Severity in Patients Infected with Leishmania mexicana Relates to IL-1β, PLoS neglected tropical diseases 6 (2012).

[121] F.O. Novais, L.P. Carvalho, S. Passos, D.S. Roos, E.M. Carvalho, P. Scott, D.P. Beiting, Genomic profiling of human Leishmania braziliensis lesions identifies transcriptional modules associated with cutaneous immunopathology, The Journal of investigative dermatology 135 (2015) 94–101.

[122] D. Santos, T.M. Campos, M. Saldanha, S.C. Oliveira, M. Nascimento, D.S. Zamboni, P.R. Machado, S. Arruda, P. Scott, E.M. Carvalho, L.P. Carvalho, IL-1β Production by Intermediate Monocytes Is Associated with Immunopathology in Cutaneous Leishmaniasis, The Journal of investigative dermatology 138 (2018) 1107–1115.

[123] I. Jorgensen, E.A. Miao, Pyroptotic cell death defends against intracellular pathogens, Immunological reviews 265 (2015) 130–142.

[124] T. Rosazza, H. Lecoeur, T. Blisnick, M. Moya-Nilges, P. Pescher, P. Bastin, E. Prina, G.F. Späth, Dynamic imaging reveals surface exposure of virulent Leishmania amastigotes during pyroptosis of infected macrophages, Journal of cell science 134 (2020).

[125] M.M. Kane, D.M. Mosser, The role of IL-10 in promoting disease progression in leishmaniasis, J Immunol 166 (2001) 1141–1147.

[126] Y. Belkaid, K.F. Hoffmann, S. Mendez, S. Kamhawi, M.C. Udey, T.A. Wynn, D.L. Sacks, The Role of Interleukin (IL)-10 in the Persistence of Leishmania major in the Skin after Healing and the Therapeutic Potential of Anti–IL-10 Receptor Antibody for Sterile Cure, The Journal of experimental medicine 194 (2001) 1497–1506.

[127] A.M. Carvalho, L.H. Guimarães, R. Costa, M.G. Saldanha, I. Prates, L.P. Carvalho, S. Arruda, E.M. Carvalho, Impaired Th1 Response Is Associated With Therapeutic Failure in Patients With Cutaneous Leishmaniasis Caused by Leishmania braziliensis, The Journal of infectious diseases 223 (2020) 527–535.

[128] R. Olekhnovitch, B. Ryffel, A.J. Müller, P. Bousso, Collective nitric oxide production provides tissue-wide immunity during Leishmania infection, The Journal of clinical investigation 124 (2014) 1711–1722.

[129] A.J. Müller, S. Aeschlimann, R. Olekhnovitch, M. Dacher, G.F. Späth, P. Bousso, Photoconvertible pathogen labeling reveals nitric oxide control of Leishmania major infection in vivo via dampening of parasite metabolism, Cell host & microbe 14 (2013) 460–467.

[130] K.W. Bruhn, R. Birnbaum, J. Haskell, V. Vanchinathan, S. Greger, R. Narayan, P.-L. Chang, T.A. Tran, S.M. Hickerson, S.M. Beverley, M.E. Wilson, N. Craft, Killed but metabolically active Leishmania infantum as a novel whole-cell vaccine for visceral leishmaniasis, Clinical and vaccine immunology : CVI 19 (2012) 490–498.

[131] A. Selvapandiyan, R. Duncan, A. Debrabant, S. Bertholet, G. Sreenivas, N.S. Negi, P. Salotra, H.L. Nakhasi, Expression of a mutant form of Leishmania donovani centrin reduces the growth of the parasite, The Journal of biological chemistry 276 (2001) 43253–43261.

[132] Amotosalen: Allogeneic Cellular Immunotherapies system, INTERCEPT Plasma System, INTERCEPT Platelet System, S 59, BioDrugs : clinical immunotherapeutics, biopharmaceuticals and gene therapy 17 (2003) 66–68.

[133] I. Baars, M. Jaedtka, L.-A. Dewitz, Y. Fu, T. Franz, J. Mohr, P. Gintschel, H. Berlin, A. Degen, S. Freier, S.M. Rygol, B. Schraven, S. Kahlfuss, G. van Zandbergen, A.J. Müller, Leishmania major drives host phagocyte death and cell-to-cell transfer depending on intracellular pathogen proliferation rate, JCI insight (2023).

[134] A. Selvapandiyan, A. Debrabant, R. Duncan, J. Muller, P. Salotra, G. Sreenivas, J.L. Salisbury, H.L. Nakhasi, Centrin Gene Disruption Impairs Stage-specific Basal Body

Duplication and Cell Cycle Progression in Leishmania*, Journal of Biological Chemistry 279 (2004) 25703–25710. https://www.sciencedirect.com/science/article/pii/S002192582066481X.

[135] G. Volpedo, T. Pacheco-Fernandez, E.A. Holcomb, W.-W. Zhang, P. Lypaczewski, B. Cox, R. Fultz, C. Mishan, C. Verma, R.H. Huston, A.R. Wharton, R. Dey, S. Karmakar, S. Oghumu, S. Hamano, S. Gannavaram, H.L. Nakhasi, G. Matlashewski, A.R. Satoskar, Centrin-deficient Leishmania mexicana confers protection against New World cutaneous leishmaniasis, NPJ vaccines 7 (2022) 32.

[136] T. Oljuskin, N. Azodi, G. Volpedo, P. Bhattacharya, H.L. Markle, S. Hamano, G. Matlashewski, A.R. Satoskar, S. Gannavaram, H.L. Nakhasi, Leishmania major centrin knock-out parasites reprogram tryptophan metabolism to induce a pro-inflammatory response, iScience 26 (2023).

[137] R. Sharma, F. Avendaño Rangel, J.L. Reis-Cunha, L.P. Marques, C.P. Figueira, P.B. Borba, S.M. Viana, T. Beneke, D.C. Bartholomeu, C.I. de Oliveira, Targeted Deletion of Centrin in Leishmania braziliensis Using CRISPR-Cas9-Based Editing, Frontiers in cellular and infection microbiology 11 (2022).

[138] S. Habuchi, H. Tsutsui, A.B. Kochaniak, A. Miyawaki, A.M. van Oijen, mKikGR, a monomeric photoswitchable fluorescent protein, PloS one 3 (2008) e3944.

[139] J. Mestas, C.C.W. Hughes, Of mice and not men: differences between mouse and human immunology, J Immunol 172 (2004) 2731–2738.

[140] K. Buscher, E. Ehinger, P. Gupta, A.B. Pramod, D. Wolf, G. Tweet, C. Pan, C.D. Mills, A.J. Lusis, K. Ley, Natural variation of macrophage activation as disease-relevant phenotype predictive of inflammation and cancer survival, Nature communications 8 (2017) 16041.

[141] P. Crauwels, R. Bohn, M. Thomas, S. Gottwalt, F. Jäckel, S. Krämer, E. Bank, S. Tenzer, P. Walther, M. Bastian, G. van Zandbergen, Apoptotic-like Leishmania exploit the host's autophagy machinery to reduce T-cell-mediated parasite elimination, Autophagy 11 (2015) 285–297.

[142] P. Crauwels, E. Bank, B. Walber, U.A. Wenzel, B. Agerberth, M. Chanyalew, M. Abebe, R. König, U. Ritter, N. Reiling, G. van Zandbergen, Cathelicidin Contributes to the Restriction of Leishmania in Human Host Macrophages, Frontiers in immunology 10 (2019) 2697.

[143] E.R. Stanley, D.M. Chen, H.S. Lin, Induction of macrophage production and proliferation by a purified colony stimulating factor, Nature 274 (1978) 168–170.

[144] U.A. Wenzel, E. Bank, C. Florian, S. Förster, N. Zimara, J. Steinacker, M. Klinger, N. Reiling, U. Ritter, G. van Zandbergen, Leishmania major parasite stage-dependent host cell invasion and immune evasion, FASEB journal : official publication of the Federation of American Societies for Experimental Biology 26 (2012) 29–39.

[145] R.L. Ihalamulla, U.S. Rajapaksa, N.D. Karunaweera, Microculture for the isolation of Leishmania parasites from cutaneous lesions -- Sri Lankan experience, Annals of tropical medicine and parasitology 99 (2005) 571–575.

[146] G. van Zandbergen, A. Bollinger, A. Wenzel, S. Kamhawi, R. Voll, M. Klinger, A. Müller, C. Hölscher, M. Herrmann, D. Sacks, W. Solbach, T. Laskay, Leishmania disease development depends on the presence of apoptotic promastigotes in the virulent inoculum, Proceedings of the National Academy of Sciences of the United States of America 103 (2006) 13837–13842.

[147] G. Zizzo, B.A. Hilliard, M. Monestier, P.L. Cohen, Efficient clearance of early apoptotic cells by human macrophages requires M2c polarization and MerTK induction, Journal of immunology (Baltimore, Md. : 1950) 189 (2012) 3508–3520.

[148] F.R. Bertani, P. Mozetic, M. Fioramonti, M. Iuliani, G. Ribelli, F. Pantano, D. Santini, G. Tonini, M. Trombetta, L. Businaro, S. Selci, A. Rainer, Classification of M1/M2-polarized human macrophages by label-free hyperspectral reflectance confocal microscopy and multivariate analysis, Sci Rep 7 (2017) 8965. https://www.nature.com/articles/s41598-017-08121-8.

[149] H. Bosshart, M. Heinzelmann, THP-1 cells as a model for human monocytes, Annals of translational medicine 4 (2016) 438.

[150] M. Gatto, P.A. Borim, I.R. Wolf, T. Fukuta da Cruz, G.A. Ferreira Mota, A.M. Marques Braz, B. Casella Amorim, G. Targino Valente, M. de Assis Golim, J. Venturini, J.P. Araújo Junior, A. Pontillo, A. Sartori, Transcriptional analysis of THP-1 cells infected with Leishmania infantum indicates no activation of the inflammasome platform, PLoS neglected tropical diseases 14 (2020).

[151] H. Shiratori, C. Feinweber, S. Luckhardt, B. Linke, E. Resch, G. Geisslinger, A. Weigert, M.J. Parnham, THP-1 and human peripheral blood mononuclear cell-derived macrophages differ in their capacity to polarize in vitro, Molecular immunology 88 (2017) 58–68.

[152] F. Rapino, E.F. Robles, J.A. Richter-Larrea, E.M. Kallin, J.A. Martinez-Climent, T. Graf, C/EBPα induces highly efficient macrophage transdifferentiation of B lymphoma and leukemia cell lines and impairs their tumorigenicity, Cell reports 3 (2013) 1153–1163.

[153] M.M. Gaidt, F. Rapino, T. Graf, V. Hornung, Modeling Primary Human Monocytes with the Trans-Differentiation Cell Line BLaER1, Methods in molecular biology (Clifton, N.J.) 1714 (2018) 57–66.

[154] K. Volkmar, Use of genome editing in human phagocytic cells to elucidate the role of the NLRP3 inflammasome in L. major infection. Doctoral Thesis, Johannes Gutenberg-Universität Mainz, 2023.

[155] T. Beneke, R. Madden, L. Makin, J. Valli, J. Sunter, E. Gluenz, A CRISPR Cas9 high-throughput genome editing toolkit for kinetoplastids, Royal Society open science 4 (2017) 170095.

[156] J. Schindelin, I. Arganda-Carreras, E. Frise, V. Kaynig, M. Longair, T. Pietzsch, S. Preibisch, C. Rueden, S. Saalfeld, B. Schmid, J.-Y. Tinevez, D.J. White, V. Hartenstein, K. Eliceiri, P. Tomancak, A. Cardona, Fiji: an open-source platform for biological-image analysis, Nat Methods 9 (2012) 676–682. https://www.nature.com/articles/nmeth.2019#citeas.

[157] C.J. Martin, M.G. Booty, T.R. Rosebrock, C. Nunes-Alves, D.M. Desjardins, I. Keren, S.M. Fortune, H.G. Remold, S.M. Behar, Efferocytosis is an innate antibacterial mechanism, Cell host & microbe 12 (2012) 289–300.

[158] P. Italiani, D. Boraschi, From Monocytes to M1/M2 Macrophages: Phenotypical vs. Functional Differentiation, Frontiers in immunology 5 (2014) 514.

[159] F. Tomiotto-Pellissier, B.T.S. Da Bortoleti, J.P. Assolini, M.D. Gonçalves, A.C.M. Carloto, M.M. Miranda-Sapla, I. Conchon-Costa, J. Bordignon, W.R. Pavanelli, Macrophage Polarization in Leishmaniasis: Broadening Horizons, Frontiers in immunology 9 (2018) 2529.

[160] F. Zhang, H. Wang, X. Wang, G. Jiang, H. Liu, G. Zhang, H. Wang, R. Fang, X. Bu, S. Cai, J. Du, TGF-β induces M2-like macrophage polarization via SNAIL-mediated suppression of a pro-inflammatory phenotype, Oncotarget 7 (2016) 52294–52306.

[161] K.S.G. de Sá, L.A. Amaral, T.S. Rodrigues, A.Y. Ishimoto, W.A.C. de Andrade, L. de Almeida, F. Freitas-Castro, S.S. Batah, S.C. Oliveira, M.T. Pastorello, A.T. Fabro, D.S. Zamboni, Gasdermin-D activation promotes NLRP3 activation and host resistance to Leishmania infection, Nature communications 14 (2023) 1049.

[162] F.O. Martinez, S. Gordon, The M1 and M2 paradigm of macrophage activation: time for reassessment, F1000prime reports 6 (2014) 13.

[163] D.C. Lacey, A. Achuthan, A.J. Fleetwood, H. Dinh, J. Roiniotis, G.M. Scholz, M.W. Chang, S.K. Beckman, A.D. Cook, J.A. Hamilton, Defining GM-CSF- and macrophage-CSF-dependent macrophage responses by in vitro models, Journal of immunology (Baltimore, Md. : 1950) 188 (2012) 5752–5765.

[164] M. Schneemann, G. Schoedon, Species differences in macrophage NO production are important, Nature immunology 3 (2002) 102.

[165] T.W. Jungi, H. Adler, B. Adler, M. Thöny, M. Krampe, E. Peterhans, Inducible nitric oxide synthase of macrophages. Present knowledge and evidence for species-specific regulation, Veterinary immunology and immunopathology 54 (1996) 323–330.

[166] K.R. Gantt, T.L. Goldman, M.L. McCormick, M.A. Miller, S.M. Jeronimo, E.T. Nascimento, B.E. Britigan, M.E. Wilson, Oxidative responses of human and murine

macrophages during phagocytosis of Leishmania chagasi, Journal of immunology (Baltimore, Md. : 1950) 167 (2001) 893–901.

[167] Hervé Lecoeur, Sheng Zhang, Hugo Varet, Rachel Legendre, Caroline Proux, Capucine Granjean, Philippe Bousso, Eric Prina, Gerald F. Späth, Leishmania amazonensis controls macrophage-regulated cell death to establish chronic infection in vitro and in vivo, bioRxiv (2022) 2022.09.14.507851. https://www.biorxiv.org/content/10.1101/2022.09.14.507851v1.full.

[168] J. Clos, J. Grünebast, M. Holm, Promastigote-to-Amastigote Conversion in Leishmania spp.—A Molecular View, Pathogens 11 (2022).

[169] M.J. McConville, D. de Souza, E. Saunders, V.A. Likic, T. Naderer, Living in a phagolysosome; metabolism of Leishmania amastigotes, Trends in parasitology 23 (2007) 368–375.

[170] M.A. Mandell, W.L. Beatty, S.M. Beverley, Quantitative single-cell analysis of Leishmania major amastigote differentiation demonstrates variably extended expression of the lipophosphoglycan (LPG) virulence factor in different host cell types, PLoS neglected tropical diseases 16 (2022).

[171] P.D. Minor, Live attenuated vaccines: Historical successes and current challenges, Virology 479-480 (2015) 379–392.

[172] T.W. Dubensky, J. Skoble, P. Lauer, D.G. Brockstedt, Killed but metabolically active vaccines, Current Opinion in Biotechnology 23 (2012) 917–923. https://www.sciencedirect.com/science/article/pii/S0958166912000675.

[173] A. Selvapandiyan, R. Dey, S. Nylen, R. Duncan, D. Sacks, H.L. Nakhasi, Intracellular replication-deficient Leishmania donovani induces long lasting protective immunity against visceral leishmaniasis, Journal of immunology (Baltimore, Md. : 1950) 183 (2009) 1813–1820.

[174] D.J. Freedman, S.M. Beverley, Two more independent selectable markers for stable transfection of Leishmania, Molecular and biochemical parasitology 62 (1993) 37–44.

[175] C. Yao, Major surface protease of trypanosomatids: one size fits all?, Infection and immunity 78 (2010) 22–31.

[176] L.H. Franco, S.M. Beverley, D.S. Zamboni, Innate immune activation and subversion of Mammalian functions by leishmania lipophosphoglycan, Journal of parasitology research 2012 (2012) 165126.

[177] B.R. Voth, B.L. Kelly, P.B. Joshi, A.C. Ivens, W.R. McMaster, Differentially expressed Leishmania major gp63 genes encode cell surface leishmanolysin with distinct signals for glycosylphosphatidylinositol attachment, Molecular and biochemical parasitology 93 (1998) 31–41.

[178] J. Morehead, I. Coppens, N.W. Andrews, Opsonization Modulates Rac-1 Activation during Cell Entry by Leishmania amazonensis, Infection and immunity 70 (2002) 4571–4580.

[179] K. Volkmar, M. Jaedtka, I. Baars, B. Walber, M.-S. Philipp, K. Bagola, A.J. Müller, H. Heine, G. van Zandbergen, Investigating pyroptosis as a mechanism of L. major cell-to-cell spread in the human BLaER1 infection model, Molecular Microbiology (2023).

[180] W.-t. He, H. Wan, L. Hu, P. Chen, X. Wang, Z. Huang, Z.-H. Yang, C.-Q. Zhong, J. Han, Gasdermin D is an executor of pyroptosis and required for interleukin-1β secretion, Cell research 25 (2015) 1285–1298.

[181] T. Vanden Berghe, N. Vanlangenakker, E. Parthoens, W. Deckers, M. Devos, N. Festjens, C.J. Guerin, U.T. Brunk, W. Declercq, P. Vandenabeele, Necroptosis, necrosis and secondary necrosis converge on similar cellular disintegration features, Cell death and differentiation 17 (2010) 922–930.

[182] S. He, Y. Liang, F. Shao, X. Wang, Toll-like receptors activate programmed necrosis in macrophages through a receptor-interacting kinase-3-mediated pathway, Proceedings of the National Academy of Sciences of the United States of America 108 (2011) 20054–20059.

[183] F. Hoss, V. Rolfes, M.R. Davanso, T.T. Braga, B.S. Franklin, Detection of ASC Speck Formation by Flow Cytometry and Chemical Cross-linking, Methods in molecular biology (Clifton, N.J.) 1714 (2018) 149–165.

[184] R.V.H. de Carvalho, W.A. Andrade, D.S. Lima-Junior, M. Dilucca, C.V. de Oliveira, K. Wang, P.M. Nogueira, J.N. Rugani, R.P. Soares, S.M. Beverley, F. Shao, D.S. Zamboni, Leishmania Lipophosphoglycan Triggers Caspase-11 and the Non-canonical Activation of the NLRP3 Inflammasome, Cell reports 26 (2019) 429-437.e5.

[185] T.A. Glaser, S.F. Moody, E. Handman, A. Bacic, T.W. Spithill, An antigenically distinct lipophosphoglycan on amastigotes of Leishmania major, Molecular and biochemical parasitology 45 (1991) 337–344. https://www.sciencedirect.com/science/article/pii/016668519190102C.

[186] D. Duluc, Y. Delneste, F. Tan, M.-P. Moles, L. Grimaud, J. Lenoir, L. Preisser, I. Anegon, L. Catala, N. Ifrah, P. Descamps, E. Gamelin, H. Gascan, M. Hebbar, P. Jeannin, Tumor-associated leukemia inhibitory factor and IL-6 skew monocyte differentiation into tumor-associated macrophage-like cells, Blood 110 (2007) 4319–4330.

[187] E. Hickman, T. Smyth, C. Cobos-Uribe, R. Immormino, M.E. Rebuli, T. Moran, N.E. Alexis, I. Jaspers, Expanded characterization of in vitro polarized M0, M1, and M2 human monocyte-derived macrophages: Bioenergetic and secreted mediator profiles, PloS one 18 (2023).

[188] T. Rőszer, Understanding the Mysterious M2 Macrophage through Activation Markers and Effector Mechanisms, Mediators of Inflammation 2015 (2015).

[189] O.E. Akilov, R.E. Kasuboski, C.R. Carter, M.A. McDowell, The role of mannose receptor during experimental leishmaniasis, Journal of leukocyte biology 81 (2007) 1188–1196.

[190] B. Poudel, M.S. Yorek, L. Mazgaeen, S.A. Brown, T.-D. Kanneganti, P. Gurung, Acute IL-4 Governs Pathogenic T Cell Responses during Leishmania major Infection, ImmunoHorizons 4 (2020) 546–560.

[191] S.A. Frank, Models of parasite virulence, The Quarterly review of biology 71 (1996) 37–78.

[192] J.J. Bull, A.S. Lauring, Theory and empiricism in virulence evolution, PLoS pathogens 10 (2014). https://pubmed.ncbi.nlm.nih.gov/25340792/.

[193] Malcolm J. McConville, David de Souza, Eleanor Saunders, Vladimir A. Likic, Thomas Naderer, Living in a phagolysosome; metabolism of Leishmania amastigotes, Trends in Parasitology 23 (2007) 368–375.

[194] B.D. Hissong, G.I. Byrne, M.L. Padilla, J.M. Carlin, Upregulation of interferon-induced indoleamine 2,3-dioxygenase in human macrophage cultures by lipopolysaccharide, muramyl tripeptide, and interleukin-1, Cellular immunology 160 (1995) 264–269.

[195] U. Barrie, K. Floyd, A. Datta, D.M. Wetzel, MAPK/ERK Activation in Macrophages Promotes Leishmania Internalization and Pathogenesis, Microbes and infection (2024) 105353. https://www.sciencedirect.com/science/article/pii/S1286457924000832.

[196] P.A. Martinez, C.A. Petersen, Chronic infection by Leishmania amazonensis mediated through MAPK ERK mechanisms, Immunologic research 59 (2014) 153–165.

[197] P. Kropf, J.M. Fuentes, E. Fähnrich, L. Arpa, S. Herath, V. Weber, G. Soler, A. Celada, M. Modolell, I. Müller, Arginase and polyamine synthesis are key factors in the regulation of experimental leishmaniasis in vivo, FASEB journal : official publication of the Federation of American Societies for Experimental Biology 19 (2005) 1000–1002.

[198] O. Sordet, C. Rébé, S. Plenchette, Y. Zermati, O. Hermine, W. Vainchenker, C. Garrido, E. Solary, L. Dubrez-Daloz, Specific involvement of caspases in the differentiation of monocytes into macrophages, Blood 100 (2002) 4446–4453.

[199] A. Jacquel, N. Benikhlef, J. Paggetti, N. Lalaoui, L. Guery, E.K. Dufour, M. Ciudad, C. Racoeur, O. Micheau, L. Delva, N. Droin, E. Solary, Colony-stimulating factor-1-induced oscillations in phosphatidylinositol-3 kinase/AKT are required for caspase activation in monocytes undergoing differentiation into macrophages, Blood 114 (2009) 3633–3641.

[200] R. Vázquez-López, J. Argueta-Donohué, A. Wilkins-Rodríguez, A. Escalona-Montaño, M. Aguirre-García, L. Gutiérrez-Kobeh, Leishmania mexicana amastigotes inhibit p38 and JNK and activate PI3K/AKT: role in the inhibition of apoptosis of dendritic cells, Parasite immunology 37 (2015) 579–589.

[201] D. Pajuelo, N. Gonzalez-Juarbe, U. Tak, J. Sun, C.J. Orihuela, M. Niederweis, NAD+ Depletion Triggers Macrophage Necroptosis, a Cell Death Pathway Exploited by Mycobacterium tuberculosis, Cell reports 24 (2018) 429–440.

[202] Y. Yang, A.A. Sauve, Assays for Determination of Cellular and Mitochondrial NAD+ and NADH Content, Methods in molecular biology (Clifton, N.J.) 2310 (2021) 271–285.

[203] M.J. Morgan, Y.-S. Kim, Roles of RIPK3 in necroptosis, cell signaling, and disease, Experimental & molecular medicine 54 (2022) 1695–1704.

Acknowledgements

Declaration of Authorship

I hereby certify that I have written the present dissertation with the title

Parasite proliferation and host cell phenotype drive *Leishmania* exit from infected macrophages

independently, using no other aids then those I have cited. I have clearly mentioned the source of the passages that are taken word for word or paraphrased from other works.

The presented thesis has not been submitted in this or any other form to another faculty or examination institution.

Eidesstattliche Versicherung

Hiermit versichere ich, dass ich die vorgelegte Dissertation mit dem Titel

Parasite proliferation and host cell phenotype drive *Leishmania* exit from infected macrophages

Selbstständig verfasst habe und keine anderen als die angegebenen Quellen und Hilfsmittel verwendet habe. Die Stellen der Dissertation, die anderen Werken oder Veröffentlichungen dem Wortlaut oder dem Sinn nach entnommen wurden, sind durch Quellenangaben gekennzeichnet.

Diese Dissertation wurde in der jetzigen oder in ähnlicher Form noch an keiner anderen Hochschule eingereicht und hat noch keinen sonstigen Prüfungszwecken gedient.

Frankfurt am Main

Moritz Jaedtka

Curriculum Vitae

Publications

Jaedtka M, Dewitz LA, Philipp MS, Walber B, Baars I, Bagola K, Müller AJ, van Zandbergen G (2024), Parasite proliferation and exit is tailored by the host cell phenotype of human primary macrophages. (Manuscript in preparation)

Jaedtka M*, Volkmar K*, Baars I, Walber B, Philipp MS, Bagola K, Müller AJ, Heine H, van Zandbergen G. Investigating pyroptosis as a mechanism of *L. major* cell-to-cell spread in the human BLaER1 infection model. Mol Microbiol. 2024 Mar;121(3):453-469. doi: 10.1111/mmi.15142. Epub 2023 Aug 23. PMID: 37612878. (*contributed equally)

Baars I, **Jaedtka M**, Dewitz LA, Fu Y, Franz T, Mohr J, Gintschel P, Berlin H, Degen A, Freier S, Rygol S, Schraven B, Kahlfuß S, van Zandbergen G, Müller AJ. *Leishmania major* drives host phagocyte death and cell-to-cell transfer depending on intracellular pathogen proliferation rate. JCI Insight. 2023 Jul 24;8(14):e169020. doi: 10.1172/jci.insight.169020. PMID: 37310793

Oral presentations

2024	27th Symposium: “Infection and Immune Defense”,Rothenfels Castle
2023	Paul-Ehrlich-Institut “Retreat on Biomedical Research”, Ronneburg
	75. Jahrestagung der DGHM 2023, Lübeck
	EXIT Symposium 2023 SPP2225 (DFG), Brühl
	26th Symposium: “Infection and Immune Defense”, Rothenfels Castle
2022	Status Workshop SPP2225 (DFG), Aachen

Poster presentations

2022	3rd International Caparica Conference on Leishmaniasis 2022, Portugal
2021	Academy for Immunology “Autumn School”, Merseburg